Universidade de Aveiro Departamento de Química
Ano 2012

Catherine Marichy

Deposição de Camadas Atómicas de óxido de Metais por Sol-Gel Não-Aquoso

Atomic Layer Deposition of Metal Oxide by Non-aqueous Sol-Gel Chemistry

Universidade de Aveiro Departamento de Química
Ano 2012

Catherine Marichy

Deposição de Camadas Atómicas de óxido de Metais por Sol-Gel Não-Aquoso

Atomic Layer Deposition of Metal Oxide by Non-aqueous Sol-Gel Chemistry

Tese apresentada à Universidade de Aveiro para cumprimento dos requisitos necessários à obtenção do grau de Doutor em Química, realizada sob a orientação científica do Doutor Nicola PINNA, Investigador Coordenador do Departamento de Química da Universidade de Aveiro

Apoio financeiro da FCT no âmbito do III Quadro Comunitário de Apoio.

o júri

presidente

Prof. Aníbal Guimarães da Costa
Professor catedrático da Universidade de Aveiro

Prof. Vitor Brás de Sequeira Amaral
Professor catedrático da Universidade de Aveiro

Prof. Elvira Maria Correia Fortunato
Professora associada da Faculdade de Ciências e Tecnologica da Universidade Nova de Lisboa

Prof. António Jorge Duarte de Castro Silvestre
Professor coordenator do Istituto Superior de Engenharia de Lisboa

Prof. Andrei Leonidovitch Kholkine
Investigador coordenator da Universidade de Aveiro

Prof. Mato Knez
Research professor da CIC Nano GUNE Consolider, Tolosa Hiribidea, San Sebastian

Prof. Nicola Alessandro Pinna
Investigador coordenator da Universidade de Aveiro

agradecimentos

I would like to thank, first and foremost, my supervisor, Prof. Nicola Pinna for giving me the great opportunity to realize this PhD, his guidance, support and advices among others. I am really grateful for everything you did and amazing possibilities that you offered me.

I thank Prof. Elvira Fortunato and Prof. Mato Knez for accepting to be the external examiners of this PhD and their interest on this manuscript. I am also grateful for accepting to chair this examination committee to Prof. Aníbal Guimarães da Costa and for their reviewing to all the member of the jury, Prof. António Jorge Silvestre, Dr. Andrei Kholkin, and specially Prof. Vitor Amaral who, additionally to his participation to the examination committee, kindly agreed to be my co-supervisor for the last 3 months.

This work being realized with several collaborations, I would like to share the credit of this work with the people that contribute to it and I am grateful for the time they dedicated to it. I thank Prof. Serge Ravaine and Renaud Vallée for the joint work on opal infiltration, bringing starting materials and theoretical simulations, respectively, as well as productive discussions. Prof. Jean-Philippe Tessonnier is acknowledged for his contribution and fruitful discussions on the CNTs work. I am indebted to Prof. Giovanni Neri and his group for their important contribution to this work by performing all the sensing experiments. I am grateful to Prof. Yves Chabal for his welcoming at the UT Dallas where IR in-situ studies were carried out. Karla and Wilfredo are thanked as well for their welcoming and help. I would like to acknowledge Dr. Sara Cavaliere for the electrocatalysis tests.

In addition, I would like to thank the people at the University of Aveiro who provided largely appreciated help. In particular Dr. Rosario Soares, Marta Ferro and Dr. Rute Ferreira are acknowledged for their contribution in XRR, electron microscopy and optical measurements, respectively.
Dr Marc Willinger is sincerely thanked for his contribution in many aspects, providing for instance help in electron microscopy, discussion and support.

I would like also to thank all the previous and present members of the group in Aveiro and at the SNU, in particular Ricardo and Kyeong-Hwan for their contribution to the ALD work as well as Valentina and Gianvito. Good luck on the next steps. A special thank is addressed to Andrea and Guylhaine for the joint work realized, their support and help in many ways.

Finally, Gareth, Kristof, Kamila, Maria and Mercedes are thanked for their good temper and friendship.

This work received the financial support from FCT (Fundação para a Ciência e a Tecnologia) and the University of Aveiro.

palavras-chave

Deposição de Camadas Atómicas, Óxido de Metais, Filmes Finos, Hetero-estruturas, SnO_2, TiO_2, Nanotubos de carbono, Sensores de gases, Sol-Gel Não-Aquoso, Revestimento, Funcionalização da superfície, Opalas.

resumo

O trabalho apresentado neste manuscrito foi desenvolvido no âmbito do programa doutoral intitulado “Deposição de Camadas Atómicas (ALD) de óxido de metais por sol-gel não-aquoso”. O objectivo deste trabalho foi a preparação de hetero-estruturas funcionais por ALD e a sua caracterização. Foi desenvolvido um novo processo de deposição de óxido de estanho a temperatura baixa-moderada, utilizando um método ALD não-aquoso, o qual foi aplicado com sucesso ao revestimento controlado das paredes internas e externas de nanotubos de carbono. Uma vez que a preparação de nanomateriais funcionais requer uma elevada exatidão do processo de deposição, foi demonstrada a deposição precisa de filmes que se adaptem à forma do substrato ou de filmes nano-estruturados constituídos por partículas em vários substratos. Além disso, foram depositados com grande exatidão vários óxidos de metal em nanotubos de carbono e demonstrou-se a possibilidade de ajustar o revestimento feito por ALD através do controlo da funcionalização da superfície do substrato nano-estruturado de carbono. As hetero-estruturas obtidas foram posteriormente aplicadas como sensores de gases. O melhoramento verificado na sensibilidade foi atribuído à formação de heterojunções p-n entre o filme de óxido de metais e o suporte. O trabalho desenvolvido tendo como objetivo o controlo do revestimento por ALD através da funcionalização da superfície do suporte é certamente de interesse para o design de hetero-estruturas funcionais baseadas em substratos de carbono. De facto, durante o último período do programa de doutoramento, este conceito foi alargado à funcionalização e revestimento com óxidos de metal de fibras de carbono preparadas por “electrospinning”, de forma a melhorar a estabilidade e a atividade eletrocatalítica de catalisadores à base de Pt.

Este trabalho foi realizado maioritariamente na Universidade de Aveiro mas também na Universidade Nacional de Seul e beneficiou de várias colaborações internacionais devido à natureza multidisciplinar da área de investigação em que está inserido.

keywords

Atomic Layer Deposition, Metal oxides, Thin film, Heterostructures, SnO_2, TiO_2, Carbon nanotubes, Gas sensors, Non-aqueous sol-gel chemistry, Coating, Surface functionalization, Opals.

abstract

The studies discussed in this manuscript have been carried out under the PhD program entitled “Atomic Layer Deposition of metal oxide by non-aqueous sol-gel chemistry”. The aim of this work was the elaboration by ALD and characterization of functional heterostructures. A novel low-mild temperature tin dioxide deposition process has been developed using a non-aqueous ALD approach and successfully applied to the conformal and controlled coating of the inner and outer walls of carbon nanotubes. Because a high deposition accuracy is required for the elaboration of functional nanomaterials, the precise deposition of conformal or nanostructured films made of particles onto various substrates was demonstrated. Moreover, various metal oxides have been deposited onto carbon nanotubes in an accurate manner and we have demonstrated the capability to tailor the ALD coating by controlled surface functionalization of the nanostructured carbon-based substrate. The heterostructures obtained were subsequently applied to gas sensing. The improvement of the sensitivity recorded was attributed to the formation of a p-n heterojunction between the metal oxide thin film and its support. The work aimed to control the ALD coating through the surface functionalization is certainly of interest for designing functional heterostructures based on carbon-based substrates. As a matter of fact, during the last period of the PhD program, this concept was extended to the metal oxide functionalization and coating of electrospun carbon fibers for the enhancement of Pt-based electrocatalyst activity and stability.

This work was mainly carried out at the University of Aveiro, but also at the Seoul National University, and benefits of several international collaborations due to the multidisciplinar nature of the research field.

Table of contents

List of figures

List of tables

Acronyms & Symbols

Acronyms:

AAO	Anodic Aluminum Oxide
AFM	Atomic Force Microscopy
ALD	Atomic Layer Deposition
ALE	Atomic Layer Epitaxy
BSU	Basic Structural Units
CF	Carbon Fiber
CNT	Carbon NanoTube
CV	Cyclic Voltammetry
CVD	Chemical Vapor Deposition
EDS	Energy Dispersive X-ray Spectrometry
EELS	Electron Energy Loss Spectroscopy
FDTD	Finite Difference Time-Domain
FFT	Fast Fourier Transform
FTIR	Fourier Transform Infra-Red
GC-MS	Gas Chromatography – Mass Spectrometry
GPC	Growth per Cycle
HAADF	High Angle Annular Dark-Field imaging
HRTEM	High-Resolution Transmission Electron Microscopy
LB	Langmuir-Blodgett
MOR	Methanol Oxidation Reaction
MOS	Metal Oxide Semiconductor
MO_x	Metal Oxide
MWCNT	Multi-Walls Carbon NanoTube
NHSG	Non-Hydrolytic Sol-Gel
NP	NanoParticle
PBG	Photonic Band Gap

PC	Photonic Crystal
PEMFC	Proton Exchange Membrane Fuel Cell
PPBG	Photonic Pseudo Band Gap
QCM	Quartz Crystal Microbalance
QMS	Quadrupole Mass Spectrometry
RMS	Root Mean Square
RT	Room Temperature
SEM	Scanning Electron Microscopy
SG	Sol-Gel
STEM	Scanning Transmission Electron Microscopy
STM	Scanning Tunneling Microscopy
SWCNT	Single-Wall Carbon NanoTube
TEM	Transmission Electron Microscopy
TG-MS	ThermoGravimetry Mass Spectroscopy
TMA	TriMethyl Aluminum
UV	Ultra-Violet
XPS	X-ray Photoelectron Spectroscopy
XRD	X-Ray Diffraction
XRR	X-Ray Reflectometry

Symbols:

E	Energy or electric potential
E_g	Energy Band Gap
F(R)	Kubelka-Munk function
i	Electric current
n	Refractive index
R	Reflectance (in UV-Visible spectroscopy) or Electric resistance
S	Sensitivity
ε	Dielectric constant
λ	Wavelength

Introduction

One of the challenges in the elaboration of functional nanomaterials is to combine one material that provides ideal support properties such as high surface area, good chemical and mechanical stability, with the desired properties of a second material. This requires a synthesis approach that is capable of controlling the decoration or deposition on a support at atomic scale whilst preserving the supports characteristic properties. Thin film technology finds an important place in the synthesis of such heterostructures. It consists on the elaboration of a material layer with a thickness ranging from few angstroms, to several micrometers. Various techniques can be used for this purpose and can be divided in chemical and physical deposition techniques.

Chemical deposition techniques involve the chemical reaction of a precursor on the substrate surface leading to the film formation, with the following being the most commonly employed.

- Chemical solution techniques, such as the sol-gel routes
- Metal-Organic Chemical Vapor Deposition (MOCVD)
- Plasma Enhanced CVD
- Atomic Layer Deposition (ALD)
- Electrochemical methods

Physical vapor deposition techniques involve the condensation of a vaporized form of the desired film material rather than a chemical reaction at the surface to be coated.

- Thermal evaporation, in particular the molecular beam epitaxy
- Sputtering
- Pulsed laser deposition
- Cathodic arc deposition

Amongst all the deposition processes, atomic layer deposition[1, 2] appears to be one of the most promising techniques due to its simplicity, reproducibility and the high conformality of the obtained films. High aspect ratio structures, nanoparticles, nanowires, nanotubes, soft materials, biological materials can be precisely coated by ALD.[1-4] The obtained heterostructures have a large range of applications, in catalysis, microelectronics, energy storage and conversion, sensing, *etc*.[1-4]

The aim of the study presented in this manuscript is the elaboration and characterization of functional heterostructured materials. The obtained structures were subsequently applied to gas

sensing and catalysis. During this PhD, we focused on the deposition of metal oxide due to their important interest for energy and environmental applications. Using a non-aqueous approach previously developed in our group, titanium- and tin-oxide were deposited onto various substrates, e.g. silicon wafer, carbon nanotubes/nanofibers, boron nitride nanotubes and silica opals. An important part of the work focused on the coating of carbon nanotubes (CNTs) with metal oxides, such as TiO_2, SnO_2 or ZnO. The study of the influence of the CNTs surface functionalization toward the coating morphology was carried out. The obtained MO_x@CNTs were investigated as gas sensors. Finally, preliminary experiments on the modification of the electrocatalytic activity and stability of platinum nanoparticles supported onto carbon fibers by metal oxide ALD coating are reported. In order to control the morphology of the ALD film, the density and nature of surface functional groups of the support was modified by thermal and chemical treatments.

The manuscript is organized as follows:

The first chapter consists of an introduction of the ALD technique and its use for the elaboration of heterostructures. The main principles are presented as well as the chemistry involved for the deposition of metal oxides. The state of the art on the fabrication of nanostructures and especially the coating of carbon nanotubes is also described. Finally, the interest of ALD for nanostructured materials fabrication targeting gas sensing and catalysis applications is highlighted. The next four chapters present and discuss the results obtained during the PhD work. Chapter II deals with the development of a novel low- to mid- temperature tin dioxide deposition process. Subsequently, the robustness of our ALD approach is highlighted in chapter III, in which silica opals, elaborated by Langmuir-Blodgett, were infiltrated with titanium dioxide in a controlled manner by steps of 1.2 nm. The good agreement between the experimental results and the theory demonstrates the accuracy and high reproducibility of our process. Based on the versatility and accuracy of the ALD process used, chapters IV and V are devoted to the coating of carbon nanotubes by non-aqueous ALD processes and their application as gas sensors, respectively. In chapter IV, we demonstrate the capability of ALD to monitor the surface defects and to tailor the morphology of the metal oxide coating by surface engineering of the support. In chapter V, the gas sensing mechanism is discussed as well as the influence of the thickness and morphology of the active layer and type of the CNTs used. Finally, after concluding, a perspective work is presented, introducing some preliminary findings on the functionalization and controlled coating of electrospun carbon fibers and their application in electrocatalysis.

References

1. S. M. George, *Chem. Rev.*, 2010, **110**, 111-131.
2. M. Knez, K. Niesch and L. Niinistö, *Adv. Mater.*, 2007, **19**, 3425-3438.
3. M. Leskelä and M. Ritala, *Angew. Chem. Int. Ed.*, 2003, **42**, 5548-5554.
4. N. Pinna and M. Knez, *Atomic Layer Deposition of Nanostructured Materials*, Wiley-VCH, 2011.

Chapter I:

Introductive part

Contents:

This PhD thesis deals with the deposition of metal oxides by Atomic Layer Deposition (ALD) and the elaboration of functional nanostructures, applied to gas sensing and catalysis. In the first part of the introduction, the definition of the ALD technique and some general concepts concerning the film growth will be presented. Subsequently, the reaction mechanism involved in the metal oxide formation will be introduced. Briefly, the formation of a metal oxide thin film involves the reaction between a metal precursor (e.g. metal halide, metal alkoxide, *etc.*) and an oxygen source.[1] While water is the most common oxygen source, oxygen (i.e. O_2 molecular, radical or plasma), ozone or oxygen peroxide are also used. Under hydrolytic conditions, the formation of M-O-M bonds (oxo-metal bonds) is separated into the two successive reactions: (i) a hydrolysis step during the water pulse forming -OH groups and oxo-metal bonds, and (ii) a condensation step in which the resulting hydroxyl groups react with the metal oxide precursor supplied by the next pulse. Therefore, the metal oxide is obtained through hydrolysis and condensation steps as in traditional solution sol-gel (SG) process. More details and comparison with the SG in solution will be presented in the section II.

In the section III and IV, the elaboration of heterostructures, specially the coating/decoration of carbon nanotubes (CNTs) and the application of ALD nanostructures to gas sensing and catalysis will be discussed. Indeed, ALD can be used for the deposition of thin films onto various supports.[1-3] Especially, in view of the development of new functional nanostructures, where desired properties of one material acting as a support are combined with complementary and desired properties of a second material, ALD is a highly suitable technique. It allows the coating of flat surfaces and complex structures in a conformal and homogeneous manner with a precise control of the thickness of the deposited film in the range of a few angstroms.[4] These characteristics, combined with the versatility in terms of materials that can be deposited, make ALD a technique of choice for the fabrications of complex heterostructures for energy and environmental applications for instance. The last section will briefly describe the different ALD tools used during the work presented in this dissertation.

I. Atomic layer deposition: general concepts

Atomic layer deposition was originally known as Atomic Layer Epitaxy (ALE). The group of Aleskovskii developed in 1960s[1] a technique named molecular layering which is based on the chemical reactions of precursors with functional surface groups of a support in order to build thin films by repeated sequences.[5] In 1970s, Suntola *et al*. elaborated a thin film deposition technique, i.e. the ALE, to fabricate electro-luminescent flat panel displays.[6] Interest for this method starts to

expand in the mid-1990s, related to the manufacturing of microelectronic devices.[3, 7] Its take off occurred in the 2000s, motivated by the need of accurate coating of high-aspect ratio materials. A modified process, the molecular layer deposition, was also developed to deposit organic and hybrid polymers.[8, 9]

Atomic layer deposition is a unique technique for the deposition of conformal and homogeneous thin films. Due to its simplicity, reproducibility and the high conformality of the as-deposited films, it appears to be a promising deposition technique.[2-4] It is based on a reaction between precursor materials, which are separated into successive surface reactions. In this manner, the reactants are kept separated and react with surface species in a self-limiting process, i.e. without the presence of a gas phase reaction. Each surface reaction is separated by a purge step to remove the unreacted precursor and the by-product. The sequence of self-limited reactions and purges constitute a cycle (Figure I.1). The growth per cycle (GPC) is defined as the thickness of the film deposited in one full cycle. Due to the self-limited reactions in ALD, the thickness of the as-deposited film is simply controlled by the number of cycles.[1]

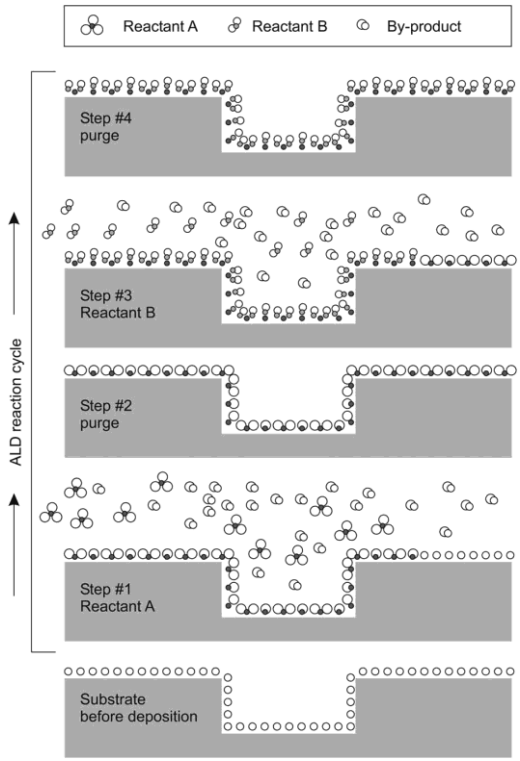

Figure I.1. Schematic of an ALD cycle. Step 1: pulse of the reactant A leading to its absorption on the surface. Step 2: purge of the unreacted precursor A and of the by-products. Step 3: pulse of the reactant B, which reacts with the surface species created by precursor A. Step 4: purge of the unreacted precursor B and of the by-products. Taken from Ref.[1]

I.1. ALD precursors

ALD processes exist for a large variety of material classes, such as metals, oxides, nitrides, sulfides and phosphates. The chemistry taking place in ALD is rather rich as well. The detailed treatment of the self-limited surface chemical reactions involved in the metal oxide thin film deposition will be detailed in the following section and the readers can refer to recent reviews on the subject, especially concerning the deposition of other materials.[1, 2, 7, 10-14]

The precursors can be classified into three classes, i.e. inorganic precursors, organometallic compounds and non-metal precursors.[13] They can be gaseous, liquid or solid; however some general requirements have to be fulfilled. Indeed, the ALD precursors must have a sufficient volatility and a good thermal stability over the deposition temperature range. No thermal decomposition should occur. The reactant should not react with itself but must adsorb or react with the surface species and have a sufficient reactivity towards the counter precursor to ensure a reasonable deposition rate. Etching of the surface and of the growing film by the incoming reactant is unwanted.[13, 15, 16] Finally, a non-toxicity, good availability and low cost are also sought after.[13, 16]

The inorganic precursors are most commonly metal halides, especially metal chlorides, oxygen-coordinated compounds, such as metal alkoxide and β-diketonates, and nitrogen-coordinated compounds. Organometallic compounds are widely used and can be divided into two categories: the metal alkyls and the cyclopentadienyl-compounds. Finally reducing agents like hydrogen, oxygen sources, such as water, hydrogen peroxide, oxygen, ozone, alcohols and carboxylic acids, and nitrogen sources (i.e. NH_3, N_2H_4 and amine) represent the principal non-metal precursors used in ALD.[1, 13, 15] A recent book chapter[13] reviews in detail the various precursors used for ALD processes.

In this PhD work, we focused on the deposition of metal oxides by reacting metal alkoxides with carboxylic acids, i.e. acetic acid.

I.2. Influence of the parameters on the growth per cycle: the ALD window

ALD is defined by a self-limiting growth process based on gas-surface reactions. Adsorption phenomena, especially the chemisorption, are therefore involved in the film formation. One of the parameters influencing the GPC is the partial pressure or amount of the precursor reacting on the surface. Indeed, it should be in a sufficient quantity to form a full monolayer and the following purge long enough to remove all the by-products and unreacted precursor in order to avoid unwanted gas phase reactions. Nevertheless, reactant excess does not affect the growth due to its inertia toward itself. Depending on the surface reactivity, a reaction time can be needed.[1]

A determining parameter of the growth rate is the deposition temperature. Figure I.2 represents its influence on the GPC. The so-called “ALD-window” is the temperature range where the thin film

formation occurs under self-limiting conditions. It consists on the temperature range to obtain a true steady ALD regime. Outside this temperature range, the growth is limited by various factors such as an insufficient reactivity and physisorption in case of temperatures lower than the ALD window and a diminution of the number of surface active sites, desorption phenomena or precursor decomposition for higher temperatures.[1, 16]

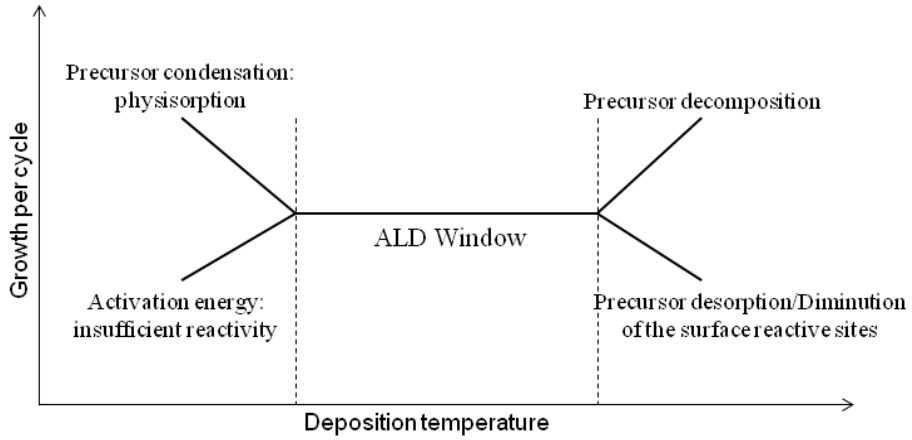

Figure I.2. Scheme of the ALD window. Influence of the deposition temperature on the growth per cycle.

Other factors can affect the growth like the steric hindrance of the precursor ligands, which can block the access to active surface sites. In this case, less than one monolayer is generally formed.[1, 14]

I.3. The growth modes

At the beginning of the growth, the relationship between the number of cycles and the GPC (Figure I.3a) can be categorized into three groups i.e. a linear, a surface-enhanced and a surface-inhibited growth.[1, 17] Actually, the linear relationship is a sign of a steady regime and therefore to a perfect ALD growth. If the GPC is higher during the first cycles, a surface-enhanced growth occurs due to a higher amount of anchoring sites on the substrate than on the deposited layer before to reach a steady regime. Moreover, a precursor solubility into the support and the equilibrium between the precursor desorption and the ligand exchange reaction takes place, which can be modified by the nature of the substrate, lead in some cases to a substrate-enhanced growth. If the number of surface reactive sites is lower on the substrate, at the first cycles a lower increase of the film thickness is observed, leading to a surface-inhibited growth.

Moreover, the deposition can occur in three different ways as shown in Figure I.3b.[1] The 2D growth consists on the completion of a monolayer prior the formation of a second one. It is the mode mostly sought after. The island growth consists on the deposition of the new material on the

top of the previously deposited one. This mode is often due to an insufficient number of anchoring sites, but can be in some cases intrinsic to the mechanism involved in the material formation. Depending on the film thickness, intermediate cases can be observed, the growth mode may be first island growth, and once the islands have coalesced to form a continuous layer a 2D growth may occur. Finally an unusual random growth, that is statistical deposition, was also reported.[18-20]

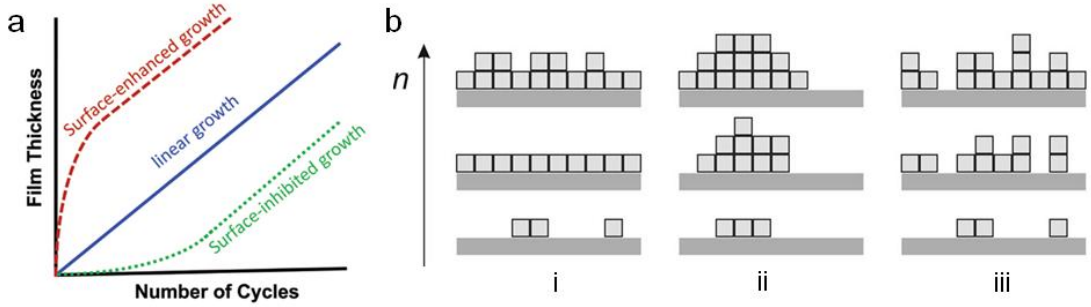

Figure I.3. a) Film thickness as a function of the number of cycles, taken from Ref.[17] b) Scheme of the 3 different modes of growth, i) 2 dimensional growth, ii) island growth and iii) random growth, taken from Ref.[1]

I.4. Advantages and limitations

The main ALD features, i.e. the self-limiting growth, the separated gas-surface reactions and the presence of an often wide ALD window, lead to the following advantages: An accurate control of the film thickness is achieved by the simple control of the number of cycles. The reactant flux does not need to be fully homogeneous to obtain a good conformality and large area uniformity of the as-deposited layer, allowing a good reproducibility, an easy scale up and no specific requirement for the reactor design. Dense, pinhole free and good quality films can be elaborated, with an atomic level control of the material composition. Doping, sharp interface, interface modification and multilayer and multi-compounds materials are also achievable. Moreover, no gas phase reaction occurs, allowing the use of highly reactive precursor and a sufficient time can be provided to reach the completion of each step. Nevertheless, the precursor has to be sufficiently stable over the time. Finally low deposition temperature processes are possible.[7, 16, 21]

On the other hand, some limitations have also to be highlighted. The industrial scale up of the process is an important challenge faced nowadays by the ALD. Indeed, one of its features is that it is a slow process and often homogeneous coating of significant amount of nanomaterials is difficult to be obtained. As a matter of fact, just few milligrams of nanostructured materials can be generally processed in typical laboratory equipments. Nevertheless, the ALD community is already actively studying the possibility of scaling up and/or accelerating the processes. For example, the use of fluidized bed reactors[22-25] in ALD or the design of novel reactors such as rotary reactors[26-28] already

showed the ability to process multigram quantities of nanoparticles and nanotubes without impacting the self-limited surface reactions. Moreover, batch processing,[29] inline atmospheric pressure ALD[30, 31] and roll-to-roll reactors[32, 33] have been developed allowing faster processes for industrial applications.[34] Another challenge in ALD is related to the chemistry and the requirements that ALD reactions impose, implying that ALD processes for some materials are difficult or might be even impossible to be developped. This was set by M. Leskelä as one of the most important challenges for ALD.[35] Furthermore, although various approaches have been recently reported,[36, 37] it is still challenging to control the deposition of multimetals and doped oxides because of the complex dosing and reactivity of different metal precursors.

II. Sol-gel chemistry applied to ALD

II.1. Aqueous and non-aqueous sol-gel in solution

As the name suggests, sol-gel is a process in which an inorganic network is formed from a homogeneous solution of precursors through the formation of a sol (colloidal suspension) and then of a gel (crosslinked solid network surrounding a continuous liquid phase) by inorganic polymerization.[38, 39] Basically, the principle of a sol-gel reaction is the formation of an inorganic polymer by hydrolysis and condensation reactions generally induced by water, with or without the presence of an acid/base; the precursor being either a metal salt or a metal organic compound. Metal alkoxides are the most convenient precursors used, reacting readily with water and known for almost all metals.[40] The characteristics, structure, and properties of a sol-gel inorganic network, depend on the factors that affect the rate of hydrolysis and condensation reactions, for example, pH, temperature and time of reaction, reagent concentrations, nature of the solvent, catalyst, aging temperature and time, and drying.[38, 39]

Because of its mild conditions, sol-gel chemistry offers a versatile access to new hybrid organic-inorganic materials.[41-44] Furthermore, a series of related processes using the sol-gel chemistry, have also been developed. For example, by a careful control of sol preparation and processing, colloids or monodispersed nanoparticles of various oxides and organic-inorganic hybrids can be synthesized.[45, 46] Another intriguing approach is the “surface sol-gel process” which is, basically, an ALD process in solution. In this technique, an ultrathin film of metal oxide,[47-53] phosphate[54, 55] or organic-inorganic hybrid[56] is grown, layer by layer, by successive dip coatings of a substrate into the reactant solutions, each step being separated by a rinse in order to purge the surface off of unreacted precursors.[50]

While the sol-gel approach is extremely successful in the case of silica, it was found to be less attractive for the synthesis of transition metal oxides, as transition metal oxide precursors are generally much more reactive towards water preventing an accurate control over the growth of metal oxides.[40, 57] Therefore the use of organic additives such as, functional alcohols, carboxylic acids or β-diketones for example, which modify the precursor and thereby its reactivity, was thoroughly studied.[40, 57] An alternative approach is to contain the hydrolysis of the metal oxide precursors by controlling the local concentration of water by chemical or physical processes, like by *in situ* water generation or slow dissolution of water from the gas-phase in the solvent.[58-61]
Finally, another approach to gain a better control over the formation of inorganic network is to completely avoid the use of water. The sol gel chemistry under non aqueous conditions is known as non-aqueous or non-hydrolytic sol-gel (NHSG).

During the last decades, the use of non-aqueous conditions has proven to be an elegant approach, eliminating the main drawbacks of aqueous sol-gel chemistry and offering advantages such as a high reproducibility and a better control of the composition and homogeneity of multi-component oxides.[62-66] Following this approach, a large variety of metal oxide gels were synthesized and reported as well as organic-inorganic hybrids.[62, 64, 66] In the NHSG chemistry, the M-O-M bonds are formed without a hydrolysis step, the oxygen being provided by other molecular species such as, the solvent (alcohol, ether, ketone) or by the metal precursor itself (alkoxide, acetate, acetylacetonate).[64, 66-69] It is interesting to note that, besides the number of possible precursor and/or solvent combinations, there are few different reaction pathways responsible for the metal-oxygen-metal bond formation. For instance, the formation of the metal oxide network can involve only a condensation step, occurring between ligands coordinated to two different metal centers under the elimination of organic molecules. It is possible to summarize most of these condensation reactions in only three distinct mechanisms: alkyl halide, ether, or ester eliminations.[62, 64, 65, 70] It is important to notice that in the case of these direct condensation reactions no intermediate formation of an OH group is involved. When the NHSG approaches engage the reaction between a metal precursor and an organic solvent, the different reaction mechanisms possible are: a ligand exchange followed by one of the condensation reactions mentioned above, a hydroxylation reaction of the metal complex leading to the formation of a hydroxyl group (non-hydrolytic hydroxylation reactions[66]) which further reacts with a metal precursor or another hydroxyl group, and finally more complex mechanisms such as, Guerbet-like reactions or aldol condensations.[62, 64, 65, 68, 70]
NHSG processes were extensively applied to the synthesis of oxide nanoparticles because the as-synthesized oxides are generally characterized by a high crystallinity and allow the control of the crystal growth without the use of any additional ligands.[62-65] Furthermore, as mentioned before, an

advantage of non-hydrolytic sol-gel processes, especially in comparison to aqueous systems, is the accessibility of multi-metal oxide and doping. Indeed, the reactivity of metal oxide precursors is often significantly reduced under water exclusion, making it easier to match the reactivity of different metal precursors to obtain single-phase multi-component oxides.[62, 64, 65]

II.2. Sol-gel and ALD: an overview

ALD of metal oxides involves the reaction of a metal oxide precursor with an oxygen source. Water is the most commonly used oxygen precursor; the formation of M-O-M bonds (oxo-metal bonds) being separated into the two successive reactions: (i) a hydrolysis step during the water pulse forming -OH groups and oxo-metal bonds, and (ii) a condensation step in which the resulting hydroxyl groups react with the metal oxide precursors supplied by a new pulse. The formation of the oxide is therefore obtained through hydrolysis and condensation steps as in traditional solution-based sol-gel processes. Recently, inspired by the success of non-aqueous sol-gel, similar non-aqueous conditions were developed for ALD. The evolution and strategies developed for the deposition of metal oxide thin films by ALD show similarities with the development of the sol-gel approach. Both techniques use common precursors such as metal halides, alkoxides, and diketonates and modifications of precursors were also pursued in ALD to enhance their efficiency by tuning their reactivity/stability/volatility.[15, 71] The ALD reactions can be divided into two approaches depending on whether a hydrolytic step is involved or not. First, we will focus on the hydrolytic route; the reaction mechanism involving water or hydrogen peroxide as oxygen sources will be presented, classified according to the various possible reagents. In a second part, an overview of the reaction taking place under non-aqueous conditions will be given.

II.2.1. Metal oxide formation via hydrolytic routes

The hydrolytic sol-gel route involves the formation of hydroxyl intermediate species. The oxygen source used is in general water but hydrogen peroxide is also common while, metal halides, metal alkoxides, and organometallic compounds can be employed as metal sources. Depending on the metal precursor, different reactions are responsible for the metal oxide formation. In the following, for each precursor family mentioned, the general mechanism observed will be illustrated through a non-exhaustive overview of *in situ* studied depositions.

II.2.1.1. Reaction with metal halides

Metal halides have been used in ALD as precursor for the deposition of many oxides.[1] An early *in situ* study of this reaction dealt with the deposition of titania, from titanium chloride and water, investigated by FTIR spectroscopy. A ligand exchange during both precursor pulses was

observed.[72] Later on, this reaction was examined by *in situ* QMS and QCM while using D_2O. During both the $TiCl_4$ and D_2O pulses, DCl is released, confirming the results of the previously published study, i.e. the formation of the metal oxide occurs via –OH to $–OTiCl_x$ and –Cl to –OH surface exchanges.[73] Moreover, the authors observed a decrease of the amount of DCl released while increasing the temperature. It has been proposed that this phenomenon is caused by a dehydroxylation of the surface at high temperatures, which reduced the number of active sites, by molecular adsorption of $TiCl_4$ and/or readsorption of DCl.[73] Rahtu *et al.*[74] investigated the mechanism of ZrO_2 deposition from $ZrCl_4$ and H_2O by *in situ* QCM and QMS. They observed an identical reaction mechanism as for titania. However, they quantified that, at high temperatures, only one HCl was released during the metal precursor pulse to form a Zr-O bond and three during the water pulse while, at moderate temperatures (300-325 °C), two equivalents of HCl were released during each half-sequence.[74] A similar behavior was observed for HfO_2 deposition with hafnium halide precursors.[74] Another example of a reaction with a metal halide is the deposition of SnO_2 using $SnCl_4$ and either H_2O or H_2O_2. The reaction with hydrogen peroxide should be thermodynamically more favorable than the one with water as shown by the calculated enthalpies of the overall reactions (-34.6 kcal/mol and 4.5 kcal/mol in the cases of H_2O_2 and water, respectively),[75] and effectively, a decrease of the deposition temperature and an increase of the growth per cycle by changing the oxygen source from water to hydrogen peroxide, was demonstrated.[75]

Generally, the reaction pathway observed consists of the hydrolysis of the surface by the oxygen source with formation of hydrogen halide as by-product (eq.1). The resulting OH terminated surface reacts then with the incoming metal halides to form M-O-M bonds under elimination of hydrogen halide (eq.2).[76]

$$\equiv OMX_x + xH_2O \rightarrow \equiv OM(OH)_x + xHX \quad (1)$$

$$\equiv OH + MX_x \rightarrow \equiv OMX_{x-1} + HX \quad (2)$$

II.2.1.2. Reaction with metal alkoxide

In solution, one of the most widely used sol-gel approaches to form metal oxide is the reaction between metal alkoxide and water which releases the corresponding alcohol as by-product. In ALD, the related reaction can be represented by the two following half-equations (eq.3, 4):

$$\equiv OM(OR)_x + xH_2O \rightarrow \equiv OM(OH)_x + xROH \quad (3)$$

$$\equiv OH + M(OR)_x \rightarrow \equiv OM(OR)_{x-1} + ROH \quad (4)$$

Various metal oxide depositions via this approach have been investigated. For example, tantalum oxide deposition from $Ta(OC_2H_5)_5$ and water was studied by *in situ* QCM. The two possible mechanisms considered were either a growth via a molecular adsorption of the metal precursor or

via the formation of intermediate hydroxyl species by exchange reactions. The mass gain and surface mass exchange ratio, determined by QCM monitoring, pointed out an exchange reaction process as main reaction path.[77] Aarik *et al.*[78] studied the reaction mechanism of the titanium ethoxide/water process, as well as titanium isopropoxide/water and titanium isopropoxide/H_2O_2 processes,[79] by *in situ* QCM. For all the precursor combinations tested, the surface species changed from isopropoxide or ethoxide to hydroxyl species during the oxygen precursor pulses. However, the GPC appeared to be much lower with titanium ethoxide than with the isopropoxide. In fact, the authors observed that during the ethoxide precursor pulse, less than one ligand is released, the remaining ethanol being liberated during the water pulse. The resulting steric hindrance of the absorbed metal precursor was made responsible for the low GPC found.[78] A similar behavior was also observed for other metal ethoxides such as Ta or Nb.[78] Comparing the titanium isopropoxide/water and titanium isopropoxide/hydrogen peroxide processes, it appeared that a higher GPC has been obtained at low temperatures using H_2O_2 as a result of its greater ability to eliminate alkoxide ligands. At higher temperatures, the growth rate was independent of the oxygen precursor.

Basically, the main reaction pathway observed during depositions from metal alkoxide and water or hydrogen peroxide, consists of hydrolysis of the alkoxide surface species leading to a –OH terminated surface by the release of alcohol. The hydroxyl groups then react with the metal alkoxide from the gas phase to form the M-O-M bond under elimination of the corresponding alcohol. Moreover, phenomena of dehydroxylation of the surface at high temperatures can occur. Due to the decrease of OH surface groups, generally only one ligand is released during the metal pulse.[78, 80]

II.2.1.3. Reaction with organometallic compounds

Trimethyl aluminium (TMA) is probably the organometallic compound most widely employed in ALD, and its use with water for alumina deposition has been intensively studied.[1] The two half sequences of this process are exchange reactions releasing methane as by-product (eq.5, 6), as confirmed by *in situ* FTIR, QCM and QMS experiments.[1, 81, 82] *In situ* QCM studies were realized to investigate this reaction;[82] the mass gain per cycle provides information about the surface coverage.

$\equiv OAl(CH_3)_x + xH_2O \rightarrow \equiv OAl(OH)_x + xCH_4$ (5)

$\equiv OH + Al(CH_3)_3 \rightarrow \equiv OAl(CH_3)_2 + CH_4$ (6)

Furthermore, it has been proposed that dissociation reactions occur during both water and TMA pulses.[1] Being thermodynamically favorable, the formation of Al_2O_3 from TMA and H_2O can be achieved at temperatures as low as 33 °C, even though in this case the GPC is low, because of the

slow surface reaction kinetic.[83] A decrease of the GPC was also observed at high temperatures due to the diminution of the hydroxyl group concentration on the surface caused by dehydroxylation[81] leading to the diminution of the number of functional groups on the surface.[84] Beside alumina, zinc and indium oxides have also been deposited from a metal alkyl/water process (diethylzinc [85] and trimethylindium,[86] respectively). The reaction mechanisms found for these two processes were similar to the one involving TMA. However, in the case of In_2O_3 deposition, rough oxide films with a low GPC have been obtained resulting probably from low hydroxyl coverage of the surface.[86] Other organometallic precursors than metal alkyl were also used such as cyclopentadienyl-based metal compounds. As an example, Niinisto *et al.* have investigated the ALD deposition of ZrO_2 from $Cp_2Zr(CH_3)_2$ and H_2O by *in situ* QMS.[87] The by-products released during both pulses, were mostly methane and cyclopentadiene. Due to its higher reactivity, it appeared that the methyl ligand reacted first on the hydroxylated surface. The remained cyclopentadienyl groups cause a steric hindrance and lower the GPC.[87]

In conclusion, the main reaction pathway observed during metal oxide deposition from organometallic compounds and water is a ligand exchange reaction producing the corresponding ligand-H organic molecules as by-products.

II.2.2. Metal oxide deposition under non-aqueous conditions

During the last decade, non-aqueous conditions were attempted to be adapted to ALD.[11, 88] Various approaches were studied, including the use of alkoxides, alcohols or carboxylic acids as oxygen sources. In the following part, the elucidated or proposed reaction mechanisms under non-aqueous conditions will be grouped and discussed in view of the three main condensation mechanisms discussed previously in the non-hydrolytic sol-gel introduction, i.e. the halide, ether, and ester condensations. Some other approaches such as the depositions involving the use of organometallic compounds will be introduced, as well.

II.2.2.1 Alkyl halide elimination

In solution, the alkyl halide elimination corresponds to the condensation between metal chlorides and metal alkoxides (eq.7) or alcohols and is probably the most studied pathway.[62, 64, 66]

$$\equiv M\text{-}X + \equiv M\text{-}OR \rightarrow \equiv M\text{-}O\text{-}M\equiv + RX \qquad (7)$$

In ALD, the first example of NHSG process and first mechanistic study found in the literature is attributable to Brei *et al.*[89] In 1993, they proved that titanium silicate growth from $TiCl_4$ and $Si(OEt)_4$ takes place via an alkyl halide elimination condensation mechanism by monitoring the growth by IR and analyzing the by-products of the reaction by mass spectrometry. Later on, Rahtu *et al.*[90] studied the reaction mechanism for the deposition of $Zr_xTi_yO_z$ from $ZrCl_4$ and $Ti(O^iPr)_4$.

They also found out that the principal reaction responsible for the metal oxide formation is an alkyl halide elimination. However, in their study the deposition temperature was slightly too high (300 °C) to safely exclude thermal decomposition of $Ti(O^iPr)_4$. Ritala *et al.*[88] showed that this approach can be applied for the deposition of various metal oxide and silicate thin films. Up to now, Al_2O_3,[88] Ta_2O_5,[88] Hf, Ti and Zr aluminate,[88] $Ti_xHf_yO_z$,[88] $Ti_xZr_yO_z$;[88, 90] and Hf,[91] Zr[88, 92] and Ti[89, 93] silicates, were deposited from their corresponding metal alkoxides and halides. From these examples, it appears that the elevated deposition temperatures (300-500 °C) are higher than the temperatures required to form metal oxides in solution.

The approaches using a metal halide with an alcohol or an ether are expected, in solution, to proceed via an alkyl halide elimination condensation. Indeed, an alcoholysis/etherolysis takes place forming an alkoxy group on the metal center which can, further on, condensate with a halide ligand as in eq.7. However, the formation of hydroxyl groups is a competitive pathway especially if electron donor substituent groups are present in the alkyl radical of the alcohol (e.g tertiary and benzylic alcohols).[66] This approach was firstly applied in ALD at the beginning of the '90s for the formation of alumina from $AlCl_3$ and different alcohols.[94, 95] More recently, Evans *et al.*[96] showed that titania can be grown from $TiCl_4$ and tert-butyl alcohol or diisopropyl ether. Even though they did not discuss it, the idea behind these experiments arises directly from similar reactions performed in solution. In fact, the use of tert-butyl alcohol involves preferentially the formation of hydroxyl groups while the use of the di-isopropyl ether can only lead to the formation of alkoxy groups.[97] However, the authors concluded that their approaches do not bring clear advantages over traditional water-assisted depositions.[96]

II.2.2.2. Ether elimination

Another non-aqueous condensation step, in solution, is the ether elimination (eq.8). For example, the direct condensation of alkoxides was found to proceed via an ether elimination for multivalent early transition metals and leads to oxoclusters.[98] Mixed metal oxides can also be directly produced if a basic alkoxide is used.[99]

$$\equiv M\text{-}OR + \equiv M\text{-}OR' \rightarrow \equiv M\text{-}O\text{-}M\equiv + ROR' \qquad (8)$$

An equivalent approach that makes use of the same chemical principle consists on the reaction of a metal alkoxide with an alcohol. This route was extensively used in solution for the formation of metal oxides.[64, 65] In ALD, the growth of metal oxides using only one metal alkoxide source was already tested.[88, 100] Naturally, no deposition was observed to take place at temperatures below the thermal self-decomposition of the metal precursors. There are only few reports on the reaction of alkoxides and alcohols, and no mechanistic studies have been carried out.[94] The deposition of

titania using $Ti(O^iPr)_4$ and methanol or ethanol has been already tested.[101] However, under similar experimental conditions, water leads to a growth per cycle larger than in the case of alcohols.

II.2.2.3. Ester elimination

The third possible route involves the condensation between metal carboxylates and alkoxides under the elimination of esters (eq.9).

≡M-OR + ≡M-OOCR' → ≡M-O-M≡ + R'COOR (9)

The mechanism of the ester elimination is similar to acid-catalyzed transesterification where the electropositive metal center acts as a Lewis acid by coordinating to the carbonyl oxygen atom.[102] This coordination decreases the electron density at the carbonyl carbon, allowing for nucleophilic attack of the oxygen of the alkoxide ligand. The transfer of the alkoxide ligand to the carbonyl carbon leading to the formation of the ester was demonstrated by labeling experiments on the oxygen of the alkoxy groups by Caruso *et al*.[102] Metal oxides have also been prepared, in solution, by reacting metal alkoxides and carboxylic acids for the production of titania clusters and nanoparticles, for example.[59, 103] In those cases, the metal precursor is hydrolyzed by water generated *in situ* by the reaction between the carboxylic acid and the alcohols resulting from ligand exchanges. However, a competitive mechanism in which a direct esterification takes place in the coordination sphere of the metal was also proposed but could not be verified in liquid phase.[103, 104] More recently, another approach based on the reaction between a metal acetate and an alcohol, was used for the formation of zinc oxide[105, 106] and indium oxide.[107]

One application of this NHSG route to ALD has been reported by our group.[100] Indeed, it was demonstrated that the deposition of titania and hafnia from simple metal alkoxides and acetic acid reaches acceptable GPC at temperatures as low as 50 °C, and a self-limiting growth was observed through a large temperature range (e.g. the ALD window for TiO_2 is 150-200 °C). The proposed reaction mechanism for this process, supported by GC-MS and kinetic studies, involved an ester elimination condensation. During the carboxylic acid pulse, the alkoxy ligands at the surface are replaced by carboxylate groups under the elimination of alcohol while during the metal alkoxide pulse, a reaction between the carboxylate surface species and the metal alkoxide occurs under the elimination of an ester. In this experiment no water was formed, therefore proving a direct condensation mechanism between alkoxide and acetate species. Later on, this process was also applied to the deposition of V_2O_4.[108] During the PhD work presented in this manuscript, this approach was extended to the SnO_2 ALD deposition (cf. Chapter 2).[109]

II.2.2.4 Other reactions

Further non-aqueous routes can also be considered, like for example, the reaction of organometallic compounds with alcohols or metal alkoxides. In solution these routes have not been extensively studied, as organometallic compounds are generally very reactive and therefore would not permit the control of gel formation or particle growth. In ALD, however, their high reactivity might be an advantage and therefore depositions of alumina[88, 110] and aluminosilicates[111] were investigated. It was suggested for the TMA/aluminium triisopropoxide process, that the reaction involved the elimination of tert-butane.[88] The ALD from TMA and isopropyl alcohol should proceed by a similar chemistry.[110] Indeed, the reaction of a metal alkyl and an alcohol usually leads to the formation of alkoxy species by ligand exchange.[98] Jeon *et al.*[110] made a direct comparison of the alumina deposition using this combination of precursors or water as oxygen source. In contrast to the traditional approach, no oxide interface between the Si substrate and the metal oxide film was observed under non-aqueous conditions. Finally, inspired by NHSG, other reactions can be tested in ALD. For example, ketones and aldehydes were applied in solution for the synthesis of metal oxide nanoparticles.[64] In particular, titania nanoparticles were synthesized in various ketones and aldehydes via an aldol condensation mechanism.[112] Although a similar NHSG approach was not yet reported for ALD, preliminary tests for the deposition of titania from $Ti(OiPr)_4$ and acetone show a GPC at 200 ºC slightly lower than in the case of water.[101] So far no mechanistic studies were performed.

II.2.3. Alternative reactions and remarks

In this section an overview of some relevant reactions taking place in ALD was given. However, it is important to mention that there exist several alternative ALD processes that were not taken into account here, for example, the ones using strong oxidizing agents such as ozone or radical oxygen as oxygen sources. From the few mechanistic studies on these oxygen sources found in the literature, it seems that similar condensation reactions like those reported above are engaged. Indeed, depending on the metal precursor used and the flow rate, ozone leads to the formation of OH-terminated surfaces[113, 114] or to the formation of carbonate and formate species in addition to the hydroxyl groups[115-118] or alkoxide species.[119] For example, according to Goldstein *et al.*,[115] a large amount of formate surface species was formed by a reaction between trimethylaluminium and O_3. Similar findings were established for reactions between titanium tetraisopropoxide and ozone or O_2-plasma by Rai *et al.*[120] These surface species are the active sites for the next precursor pulse reaction and so, the expected mechanisms are different to the ones from hydrolyzed surfaces.[36, 115, 118, 119] Unfortunately, the reactions responsible for the oxide growth from these species are still not clearly identified.[116, 117] On the other hand, the reaction of ozone can produce water as a by-product

leading to a hydroxyl terminated surface.[121, 122] Thus, in those cases, the following metal precursor half-reactions are similar to the ones of processes applying H_2O or H_2O_2 sources.

In the metal oxide ALD deposition from water or hydrogen peroxide, the main reaction pathway consists of the hydrolysis of surface species leading to OH surface group formation. The resulting OH-terminated surface then reacts with the incoming vapor phase metal precursor species to form the M-O-M bond. Therefore, in the hydrolytic ALD approaches, the mechanisms involved in the M-O-M bond formation are proven to be similar to the pathways present in solution, i.e. hydrolysis and condensation. Even though the number of mechanistic studies of NHSG conditions applied to ALD is still limited, it seems evident that, here again, similar reactions are accountable for the metal oxide formation in solution and in ALD. Nevertheless, depending on the temperature, the contribution of dehydroxylation phenomena of the surface and/or readsorption of by-product, as well as the metal precursor self-decomposition should be taken into account while analyzing reaction mechanisms.

Concerning the metal oxide film formation by NHSG, the approaches did not, up to now, demonstrate significant advantages compared to water assisted processes. Although one of the foreseen advantages offered by this approach was the possibility to obtain sharp silicon-metal oxide interfaces in the case of metal oxides grown on silicon, it was so far only demonstrated for alumina depositions.[88, 110] An interesting aspect of NHSG approaches is the possibility to deposit metal oxide films without intermediate hydroxyl group formation. Furthermore, in the case of the direct condensation some benefits can be listed. Notably, the growth per cycle can be twice as large as compared to traditional depositions since both reactants can contain a metal. Moreover, during the reaction between alkoxy and halide precursors the formation of mineral acids, which could subsequently damage the freshly formed oxide film, is avoided in contrast to the reaction of metal halides with water or alcohols.

II.3. Conclusion

Sol-gel technology is a well developed domain and was employed for decades for the synthesis of various oxides, phosphates, hybrids and composites. Inorganic polymerization (hydrolysis and condensation reactions), aqueous chemistry of metal cations, chemistry of metal alkoxides, as well as physical chemistry (phenomena of aggregation, gelation and drying), are keys to the sol-gel science. Hence, the knowledge gained by the sol-gel community is broad, encompassing diverse fields of chemistry and physics.

In view of what was discussed above, it emerges that similar chemistry is responsible for the metal oxide formation in ALD and in solution even though some differences exist. Therefore, ALD could greatly profit from the established knowledge and experience of sol–gel chemistry. Nevertheless

there are some notable differences between oxide formation in solution and by ALD. First of all, the nature of the reactions is obviously different. In sol-gel, the reactions occurring in solution are step growth condensation polymerizations. The precursors/monomers and already formed dimers and oligomers condense to give larger colloidal species under the elimination of simple molecules. In ALD, the metal oxide growth is based on subsequent self-terminating heterogeneous reactions between the surface species and the monomers coming from the gas phase. The latter thereby undergo irreversible chemisorption. Another important difference concerns the time scales of these two processes, the typical pulse length in ALD being a few seconds compared to some hours/days for sol-gel. Indeed, to better control the metal oxide formation in a sol-gel process, it is important to curb hydrolysis and/or condensation reactions. On the contrary, in ALD, fast reactions are sought after in order to obtain short deposition times. For example, non-hydrolytic conditions were introduced in sol-gel chemistry because in these cases the reactions are slower. Although this suggests that non-hydrolytic conditions are not favorable for ALD of metal oxides, they bring some significant benefits. Similarly, the modification of precursors in both techniques is not pursuing the same purpose due to the very different expected requirements for sol-gel and ALD precursors in terms of reactivity, volatility, thermal stability and solubility.[57, 71, 123]

However, it is important to keep in mind that in ALD the reactions are naturally separated due to the alternating introduction of the two reactants. In contrast, in solution, solvolysis, exchange reactions and condensations occur simultaneously between the precursors as well as with intermediate species, making it difficult to investigate their respective mechanisms. Therefore, due to the divided steps, the *in situ* study of mechanisms in ALD is an attractive approach to better understand reactions performed in solution during oxide growth or in sol-gel chemistry and that might also be interesting for surface chemistry such as in heterogeneous catalysis, for example. ALD can be viewed as a tool operating at the frontier between surface science (i.e. studies performed in UHV on model systems such as single crystals) and industrially relevant heterogeneous reaction conditions (i.e. performed at atmospheric pressure or above). Therefore, ALD might experimentally bridge the apparent gap between the two fields if *in situ* analytical techniques such as FTIR, XPS, NEXAFS and mass spectrometry are applied. Furthermore, the use of *in situ* techniques in ALD allows to better control and understand thin film deposition and to study chemical phenomena which are difficult to be investigated in solution or under conventional working conditions.

III. Elaboration of nanostructured materials by ALD

Heterostructured materials are typically composite materials consisting of several distinct phases, each contributing to a different function. One important aspect is that coupling between different phases induced by electrical/magnetic/mechanical/optical interactions can result in new functionalities which cannot be found in conventional materials. The synthesis of heterostructured materials through the combination of structurally or chemically different materials on a confined space of few nanometers is still very challenging. Certainly, one of the challenges in the synthesis of novel nanostructured materials is to combine one material that provides ideal support properties, such as a high surface area and a good chemical and mechanical stability, with the desired properties of a second material. This requires a synthesis approach that is capable of controlling the decoration or the deposition on a support at the atomic scale, whilst preserving the support characteristic properties. Amongst all the deposition processes, ALD[2-4] appears to be one of the most promising techniques due to its simplicity, reproducibility and the high conformality of the obtained films. As a matter of fact, ALD was already chosen by the microelectronic industry as the technique of choice for the fabrication of next generation metal-insulator-metal capacitors in DRAMs and to deposit gate oxide in CMOS transistors.[124] High aspect ratio structures, nanoparticles, nanowires, nanotubes, soft materials, biological materials can be precisely coated by ALD.[2-4, 125] The obtained heterostructures have a large range of applications, such as in catalysis, microelectronics, energy storage and conversion, sensing, *etc*.[2-4, 125]

The PhD work, presented in this manuscript, focuses mainly on the elaboration of heterostructures based on CNTs. Therefore, in this section, a brief overview on the fabrication of nanostructures will be presented before to focus on the coating of carbon nanotubes by ALD.

III.1. Nanostructure fabrication

The precise control of the thickness of the ALD layers combined with the high step coverage permitted to introduce new approaches for nanostructures fabrication.[88, 126-138] For instance, using nanopaterning by area selective ALD,[139] porous[140] and nanostructured templates,[141] novel nanostructured materials can be elaborated by ALD. Up to now, only few review articles[2, 4, 142-145] focused on the different strategies for nanostructure elaboration. While an early review of Ritala *et al.* highlighted the potentiality of the ALD for obtaining heterostructures,[145] Leskela *et al*.[144] and Knez *et al.*[4] reviewed in detail the use of ALD for the preparation of complex nanostructures. Later on, Kim *et al.*[143] detailed the "application of atomic layer deposition to nanofabrication and emerging nanodevices". An overview of the different existing approaches is presented by these main papers. In a comprehensive overview of ALD, George[2] also briefly presented the main

fabrication strategies. Finally, several chapters of the recently published book on "atomic layer deposition of nanostructured materials"[125] discuss in detail the different approaches for nanostructure elaboration by ALD.

The ALD coating of nanotubes, nanowires and nanoparticles[141] has been reported as well as the use of templates, such as porous membranes, fibers or biomaterials, for the preparation of nanostructures. An early work presented the coating of boron nitride particles with Al_2O_3 ALD.[146] Various nano-objects, such as carbon nanotubes,[147] electrospun fibers, semiconductor nanorods, *etc.* have been coated by ALD by now. The main purpose was the protection of the substrate with an insulating layer preventing oxidation and electrical conduction and the modification of its physical properties (e.g. optical, mechanical properties).[2, 141] The substrates have also been used as sacrificial templates removed by annealing, chemical or physical etching after coating by ALD. For this purpose, biological[148] and soft materials[149] present a considerable interest due to their easier removal compared to inorganic supports.[143] Furthermore, chemical transformation of the nanostructured substrates can also be induced by ALD. For example, the coating of ZnO[150] or MgO[151] nanowires with Al_2O_3, followed by thermal treatment, induces the formation of zinc or magnesium aluminate spinel structures. The elaboration of semiconductor nanowires by Vapor-Liquid-Solid growth can be better controlled when combined with ALD.[4]

Porous and high aspect ratio materials have been widely coated by this technique.[140] They are of particular interest for nanotube/nanowire preparation. Although the first depositions into porous materials were realized into porous silicon,[152, 153] one of the first attempts dealt with a polycarbonate filter acting as template. Free standing metal oxide nanotubes were fabricated via its infiltration with TiO_2 and ZrO_2 followed by the dissolution of the filter.[154] Anodic Aluminum Oxide (AAO) is the most common porous template used and serves currently for model studies.[2, 4, 143] Dense, well-aligned and uniform arrays of nanotubes can be obtained[155] by infiltration and removal of AAO. Step coverage models[156] are currently developed for the determination of the ALD processing parameters (e.g. exposure and purge time). In this context, AAO[157] represents an ideal model structure for high aspect ratio materials, due to its well-defined and controlled porous structure.[2] The utilization of soft templates allows the fabrication of original inorganic nanostructures, for example ALD on self-assembled polymer led to the fabrication of "complex ZnO nanorods containing helical motifs".[158, 159] Moreover, ALD infiltration of periodic structures, such as opal, has been widely investigated for the tuning of their optical properties as well as to elaborate inverse opals and more complex structures, e.g. by using a sacrificial ALD layer.[160]

Finally, strategies for achieving area selective ALD were also studied[139] following different approaches[4] such as the use of an overcoating (e.g. a polymer)[161-164] to protect the surface from

ALD or of self-assembled monolayers[165-169] bearing different chemical species for promoting or preventing the initiation of the ALD growth at different locations.[143]

III.2. Coating of carbon nanotubes

Carbon nanotubes offer a high surface area, good thermal and electrical conductivity, and mechanical as well as chemical stability. As such, they are ideally suited as support for a second material that can be deposited onto their surface either as particles or as a thin film. Such heterostructures find applications in catalysis, energy storage, or gas sensing, where it is essential to expose the active phase on a large surface area. Due to the small dimensions, interactions between the deposited material and the tubes at the interface can significantly alter the properties of the composite. This is specifically the case for semiconducting materials when the dimensions are in the range of the Debye length, i.e. the dimension of the space charge region. Therefore, the modification of CNTs is of outmost scientific and technological importance. Many reports dealing with the synthesis, characterization, and properties of such structured materials can be found in the recent literature.[170] By using different material combinations and synthesis procedures, MO_x/CNT composites, MO_x-coated CNTs, or MO_x-filled CNTs have been prepared and their electrical, electrochemical, (photo)catalytic, field emission, or gas sensing properties investigated.[170] Studying such synergetic phenomena and size-dependent properties in a systematic way relies on a method that allows a precise control of the particle or film growth during the deposition. Nevertheless, the common features of almost all the techniques used are the nonhomogeneity of the metal oxide coating and often only partial covering of the entire surface of the tubes, resulting in discontinuous films or islands of inorganic coatings. Moreover, control and reproducibility of the film thickness are often difficult or impossible to obtain. Among the techniques available, ALD is specifically suited for the production of such heterostructures but its drawback is the difficulty to process a large amount of CNTs. However, this problem was recently addressed by making use of fluidized bed[22-25] or rotary ALD reactors.[26-28]

III.2.1 Purification and surface functionalization of carbon nanotubes

In order to decorate and coat CNTs, it is primordial to characterize and modify their surface chemistry. Although CNTs can be synthesized using several techniques and routes, in all the cases, the pristine CNTs contain a variety of impurities ranging from other forms of carbon (i.e., fullerenes, graphite, and amorphous carbon) to metal nanoparticles used as catalyst to promote the CNT growth. Numerous procedures have been used to purify CNTs (cf. Ref.[171]).

Two types of functionalizations can be distinguished: covalent and noncovalent.[172] The most common ways involve covalent functionalization by gas- and liquid-phase oxidative treatments.

Even if the chemical functionalization permits to obtain a fine dispersion and a relatively selective separation, unfortunately no way to purify the product without damaging the nanotubes or changing the original morphology can be achieved.

On the one hand, covalent functionalization by treatment of pristine CNTs with strong acids such as HNO_3 or other strong oxidizing agents (e.g. O_3) permits to generate oxygenated functional groups such as alcohol, ketone, ether, carboxylic acid, and ester.[173, 174] This first chemical modification of the CNT surface paves the way to an endless possibility of further attachments.

On the other hand, noncovalent functionalization is mainly based on supramolecular complexation using various adsorptive and anchoring forces, such as van der Waals and π-π interactions, hydrogen bonding, and electrostatic forces. One of the main advantages of the noncovalent functionalization, besides the use of mild conditions, is that no serious changes in the electrical and mechanical properties of the pristine CNTs occur. Indeed, the carbon sp^2 structure and the conjugation of carbon atoms are preserved. This functionalization can be achieved, for instance, by the adsorption or anchoring of various functional molecules such as polymers or surfactants.[175] In order to coat freestanding SWCNTs by Al_2O_3 ALD, Farmer and Gordon[176] showed that the in situ physisorption of NO_2 on SWCNTs permitted to initiate the metal oxide growth. Due to the reversible and nondissociative adsorption of NO_2, the surface modification had to be performed *in situ* and it is not applicable to liquid phase.

III.2.2 Atomic layer deposition on carbon nanotubes

The coating of MWCNTs with Al_2O_3, by ALD, from trimethylaluminum and water was already reported in 2003.[177] Multilayer coatings on MWCNTs could be obtained by the sequential Al_2O_3 and W ALD processes as described by Herrmann *et al.*[178] TMA/H_2O and WF_6/Si_2H_6 cycles were used for the Al_2O_3 and tungsten deposition, respectively. The obtained "coaxial cables" are constituted by rather conformal ALD layers. This multistep approach permits to produce multifunctional nanostructures with interesting flexibility in terms of type of materials that can be deposited and their combination at the nanoscale.

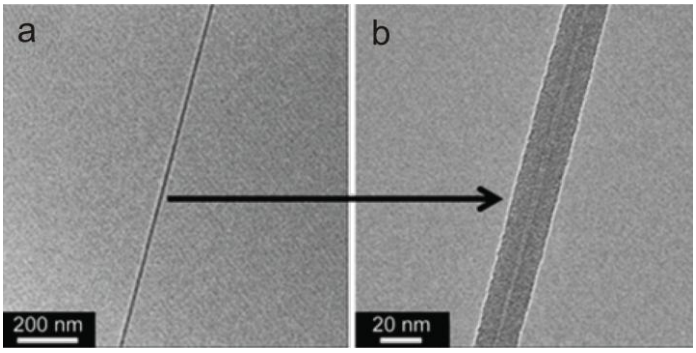

Figure I.4. ALD coating of suspended NO_2/TMA functionalized SWCNTs. a) TEM micrograph of an Al_2O_3-coated SWCNT. b) Higher magnification of the 2 nm nanotube reveals the 10 nm coating to be uniform and continuous.[176]

Suspended SWCNTs could be conformally coated with Al_2O_3, after a NO_2 pretreatment.[176] NO_2 reversibly physisorbs on the SWCNTs acting as anchoring site for further oxide growth. One of the most relevant advantages of this approach is that the SWCNTs are not modified with chemical groups that would alter their physical properties. This is particularly important for the application of the freestanding coated SWCNTs as field effect transistors. The noncovalent functionalization was achieved by several NO_2 and TMA cycles prior to TMA and water cycles. Such a pretreatment produces a stable complex that does not desorb from the nanotube sidewalls at room temperature and allows the subsequent coating of SWCNTs by ALD. TEM micrographs (Figure I.4a,b) revealed the resulting coating to be uniform and continuous. The oxide layer thickness of 10 nm was in perfect agreement with the one expected from the number of ALD cycles carried out. Therefore, there is no evidence of inhibition or delay in nucleation of ALD Al_2O_3 onto the NO_2–TMA pretreated SWCNTs.

The idea of the alumina growth onto NO_2-treated SWCNTs arose from a previous paper of the same group, in which Al_2O_3 and HfO_2 were grown onto SWCNTs functionalized with aniline and nitroaniline.[179] The treated SWCNTs presented surface phenyl and nitrophenyl groups, respectively, as depicted in Figure I.5 (left). Depending on the surface species, aluminum and hafnium oxide depositions onto the SWCNTs exhibited either localized nucleation or continuous coating, as clearly shown in the TEM images (Figure I.5, right). The Al_2O_3 spheres measured between 15 and 20 nm and the diameter of the Al_2O_3 wire was 22 nm corresponding to a typical growth per cycle of 0.1 nm for the TMA/H_2O process at 225 ºC. This finding once again proved the absence of evident inhibition or delay in the nucleation of Al_2O_3 onto surface nitryl species.

Min *et al.*[180] used MWCNT arrays grown on porous anodic alumina as templates for the growth of Ru thin films. The deposition took place after dissolution of the alumina matrix by phosphoric acid, which also permitted to open the CNT tips, leading to a coating on the inner and outer surfaces.

After thermal treatment in oxygen at 500 ºC, ruthenium was oxidized into RuO_2 and the MWCNTs burned off producing freestanding RuO_2 nanotube arrays.

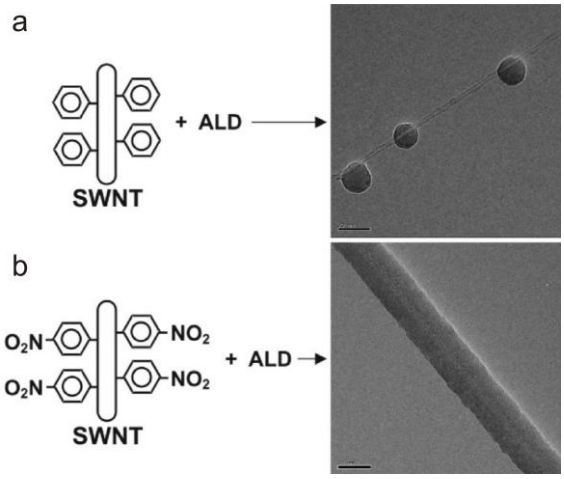

Figure I.5. Reaction schematic and TEM images of functionalized suspended SWCNTs exposed to 100 ALD cycles of Al_2O_3. a) SWCNTs functionalized using aniline. b) SWCNTs functionalized using nitroaniline. Scale bar: 20 nm.[179]

Gomathi *et al.*[181] coated HNO_3-treated MWCNTs with SiO_2, TiO_2, and Al_2O_3 from the respective metal chloride and water at either 80 or 150 ºC. In this work, an unconventional glass reactor was used. It consisted of two glass chambers for the precursors connected to the reaction chamber by high-vacuum stopcocks, which were manually operated. Despite the simplicity of the setup, the quality and conformality of the coatings were surprisingly good. The as-deposited hydroxides needed to be annealed to 350 ºC to form the oxide.

Javey *et al.*[182] deposited zirconium oxide thin films (~8 nm), as gate dielectrics for nanotube field effect transistors, on top of individual single-walled carbon nanotubes. Individual semiconducting SWCNTs, bridging metal source and drain electrodes (spacing ~3 mm), were lying onto a SiO_2/Si substrate. Helbling *et al.*[183] also investigated SWCNT-based field effect transistors and showed that their encapsulation by approximately 100 nm Al_2O_3 ALD leads to stable device operation for 260 days and reduces the sensitivity to the environment. Recently, Nakashima *et al.*[184] and Shen *et al.*[185] coated CNTs with HfO_2 for CNT field effect transistors applied to biosensors and for nanoelectrodes based on a single CNT, respectively.

Noncovalent wrapping of SWCNTs with poly-T DNA improved the nucleation of HfO_2 ALD.[186] Indeed, for SWCNTs on SiO_2 substrates with DNA functionalization, concurrent ALD growth on both nanotubes and SiO_2 surfaces was observed. Actually, a quasi continuous and conformal layer was obtained. For SWCNTs without DNA functionalization, no HfO_2 nucleation and growth directly on the "defect-free" tube surface took place.

Kim *et al.*[187] fabricated coaxial nanotubes with a highly conformal ZnO film, by employing an intermediate Al_2O_3 coating on the nanotubes. Indeed, the structure of the zinc oxide being strongly dependent of the surface properties of the support, the direct coating with ZnO led to highly irregular ZnO shells, while the Al_2O_3 shell forming a uniform coating on the nanotubes allows the deposition of a conformal ZnO layer.

In a recent study, Al_2O_3 ALD (from TMA and H_2O) on SWCNTs was studied in a viscous flow reactor and in a fluidized bed reactor.[188] The SWCNTs were pretreated with ethanol or with sodium dodecyl sulfate (SDS) prior to deposition. As expected, neither continuous nor conformal ALD films could be achieved on non-functionalized SWCNTs. Only nucleation at defective sites was observed, leading to a pearl necklace-like morphology. However, after a simple ethanol pretreatment, SWCNT ropes could be coated with continuous, although not conformal, Al_2O_3 layers (Figure I.6), proving that physisorbed ethanol promotes Al_2O_3 nucleation and that the density of nucleation sites is much higher than in the case of the unfunctionalized SWCNTs. The SDS-based surfactant dispersion technique permitted to successfully promote a conformal Al_2O_3 shell that contained no visible nodules or particles. The advantage of the functionalization with SDS is that no covalent chemical modification is required, which, as already discussed, considerably alters the physical properties of the pristine SWCNT.

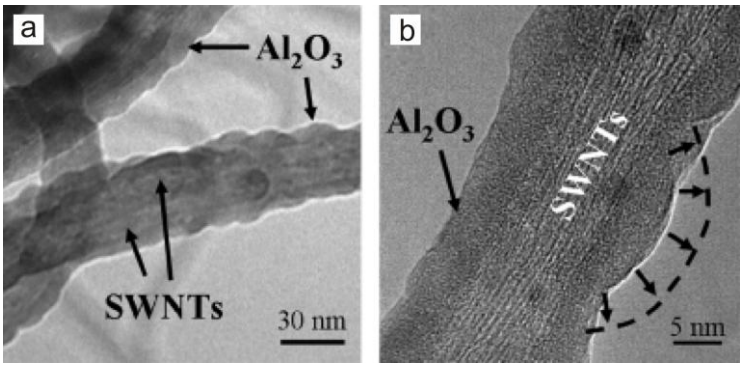

Figure I.6. a) TEM image of Al_2O_3 ALD on ethanol-dispersed SWCNT bundles, detailing continuous Al_2O_3 growth on bulk quantities of SWCNTs. b) High-resolution TEM image of the same, showing radial growth from closely packed nodules that form a continuous film.[188]

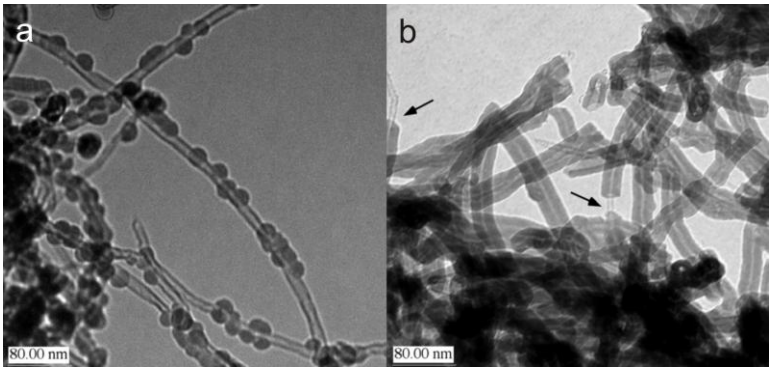

Figure I.7. a) TEM image of untreated MWCNTs after 50 ALD cycles of Al_2O_3. b) TEM image of NO_2/TMA functionalized MWCNTs after 50 ALD cycles.[189]

ALD of Al_2O_3 (from TMA and H_2O) on untreated NC7000 MWCNTs from Nanocyl in a rotary reactor resulted in the growth of Al_2O_3 nanospheres forming a pearl necklace-like morphology. A TEM micrograph of these spherical and monodisperse nanospheres after 50 ALD cycles is shown in Figure I.7a.[189] The TEM images suggested that Al_2O_3 nucleated at defects on the MWCNT surface during the initial Al_2O_3 ALD cycles. The nanospheres then grew isotropically with the number of ALD cycles to yield fairly monodisperse sphere diameters. To grow conformal Al_2O_3, prefunctionalization of the MWCNT, similar to that proposed previously,[176] from NO_2 and TMA was carried out at room temperature prior to the Al_2O_3 deposition at 180 ºC. The TEM image after 50 ALD cycles proved that a smooth and conformal film can be grown under these conditions (Figure I.7b).[189]

In our group, CNTs have been coated via a non-hydrolytic approach applied to ALD, by using metal alkoxides and carboxylic acids as reactants.[100, 190] Based on this procedure, hafnium-, titanium-, and vanadium oxide thin films of controlled thickness have been deposited onto the surface of functionalized CNTs. In the TEM images (Figure I.8a,b), the contrast-rich, darker regions on the outer and inner walls of the CNTs correspond to the metal oxide layers deposited by the ALD process. In the energy filtered TEM images, the lighter regions correspond to the metal oxide (Figure I.8c,d). The coating, only a few nanometers thick, was uniform along the whole surface of the tubes and presents approximately the same thickness on the inner and outer surfaces. Only the inner cavities in the bamboo-like tubes remain inaccessible for the precursor vapor and hence uncoated as it can be clearly seen in the energy filtered images (Figure I.8c). The film thickness abstracted from TEM measurements on the coated tubes was in agreement with reflectometry measurements performed on silicon wafers coated during the same deposition experiments. High-resolution TEM and electron diffraction experiments showed that the as-deposited films are amorphous and can be directly grown on the graphitic surface of the nitric acid-treated CNTs.[108, 191]

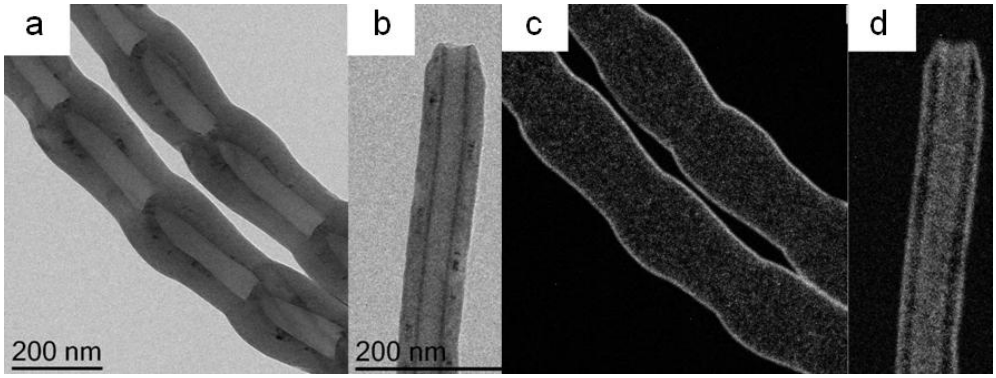

Figure I.8. a,b) TEM images recorded from CNTs coated with V_2O_5 and c,d) corresponding energy filtered images showing the distribution of vanadium on the surface.

Finally, these various examples show that ALD permits, by controlling the surface chemistry and the density of nucleation sites, to produce complex nanostructures (e.g., conformal coating or pearl necklace-like) and therefore to tune the functionalities and/or the properties of the final material.

A general drawback of the ALD processing of nanoparticles or CNTs is the low amount of material that can be homogeneously coated. As a matter of fact, the studies discussed above were made on single CNT or just few milligrams deposited by drop coating on a substrate. For the production of commercially viable CNT-based composites, bulk quantities of CNTs per batch must be used.[192] For this purpose, fluidized bed reactors[22-25] or rotary reactors[26-28] can be used as in the case of nanoparticles.

Zhan *et al*.[188] used an ALD fluidized bed reactor composed of a small fluidized bed holding (4 cm in diameter) for the Al_2O_3 ALD coating of SWCNTs. The bed was fluidized using N_2 as the gas source at a pressure around 100 Pa. The Al_2O_3 deposition was carried out at 450 K using TMA and H_2O pulses of 750 s each separated by 120 s purge times. By using a "large" reactor (15 cm in diameter), 100 g of SWCNTs per batch could be processed. The main drawback of fluidized bed reactors is that long precursor pulses are required leading to a large amount of reactants lost to the vacuum pump. Rotary reactors can overcome this drawback due to their possibility of static reactant exposures.[26] Cavanagh *et al.*[189] used a rotary reactor for the coating of gram quantities of MWCNTs with Al_2O_3 and WO_3.

IV. ALD of functional heterostructures for gas sensing and catalysis application.

Recently, ALD has widely been used to elaborate functional heterostructures for environment and energy applications. Since the heterostructures presented in the following chapters are essentially applied for gas sensing and electrocatalysis, this section will focus only on the ALD of functional materials for gas sensing and catalysis applications. The reader can refer to recent review papers for more exhaustive applications of such structures.[193, 194]

IV.1. Gas sensors

Based on the modification of their physical properties (e.g. electrical, optical) in presence of a target species, chemical sensors find important applications in everyday life. Indeed, they are widely applied to household security, industrial emission control, biomedical and agricultural domains, and to the control of the emission and engine combustions of vehicles.[195, 196] In general, metal oxide semiconductors are used as active layers in resistive sensors, with SnO_2 being the most studied one.[197-199] Due to the strong correlation between grain size and sensor response,[200] nanostructured and/or heterostructured materials lead to an enhancement of the gas sensing response.

In this context, films made of nanoparticles deposited by ALD have been investigated as gas sensors since many years already.[201-209] In 2003, Rosental *et al.*[207] demonstrated the ALD deposition of a crystalline SnO_2 granular film on a flat α-Al_2O_3 substrate from tin tetrachloride or tin iodide and O_2 or H_2O_2 precursors, respectively. They noticed an effect of the metal precursor on the sensor response, due to a difference on oxygen vacancy density of the obtained films. An increase of the oxygen vacancies leads to a higher electronic conductivity of the nanoparticulate film, which causes an improvement of the sensitivity towards CO. The ALD process using iodine precursors demonstrated a 10-fold improvement compared to the chlorine approach.

Later on, Du *et al.*[203] deposited tin oxide on a flat hotplate template from $SnCl_4$ and H_2O_2. The importance of the film thickness was highlighted by CO sensing experiments. The best sensitivity was obtained for film thicknesses in the range of the Debye length of the material (~3 nm for SnO_2)[200] due to the full depletion of the sensing layer during the target gas adsorption (Figure I.9a).[203] Platelet-like granular SnO_2 films (Figure I.9b), deposited by the chloride approach described above, were also investigated for acrylonitrile, acetone and ethanol sensing. A fast increase of the conductance was observed for the two first gases, in agreement with an adsorption/desorption kinetic of the 1st order, while ethanol sensing presents a 2nd kinetic order, related to complex reaction pattern. In all cases, fast response and full recovery were obtained (Figure I.9c,d).[206]

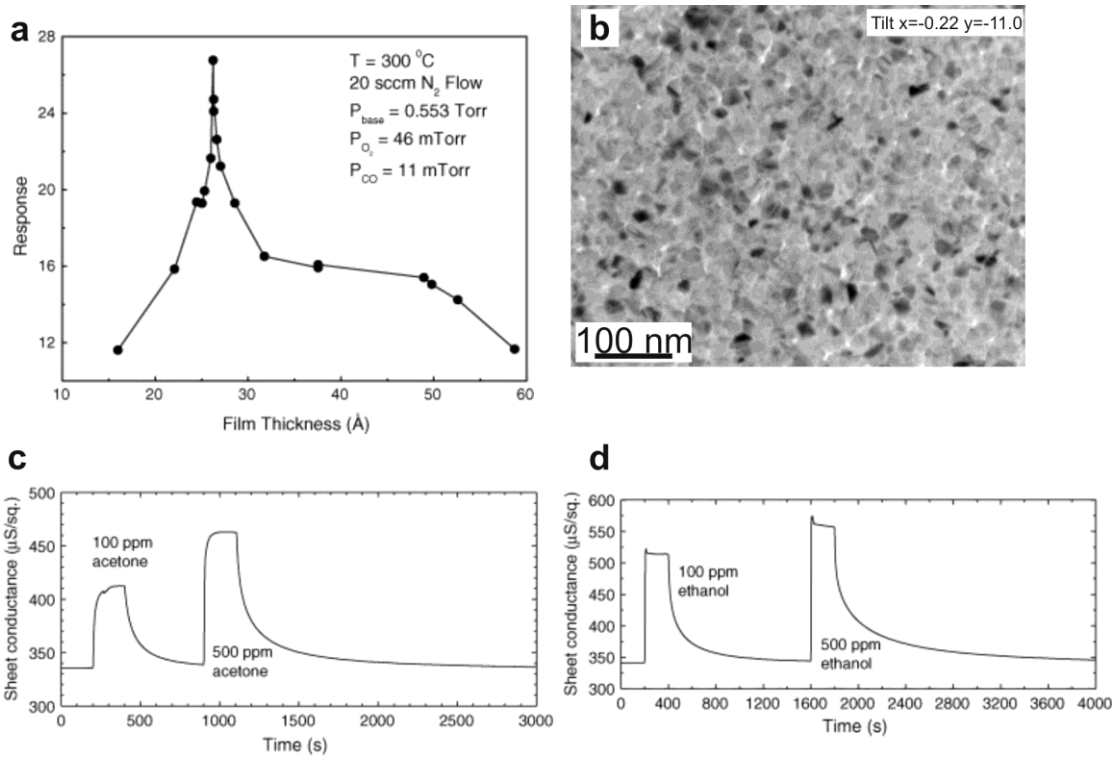

Figure I.9. a) Sensor response to CO gas for different thicknesses of SnO_2 grown on different flat hotplates.[203] The TEM image in b) reveals the grain structure of the ALD deposited SnO_2. Response of the device at 300 ºC to various c) acetone and d) ethanol concentrations.[206]

Heterostructures elaborated by ALD were also tested in gas sensing applications. Coating and decoration of particles or nanotubes by a metal[210, 211] or a metal oxide[108, 212-216] were studied in order to investigate the modification of the sensing properties of the support by the controlled deposition of a different material by ALD. As a matter of fact, the interaction between the deposited material and the support can significantly alter the properties of the composite. This is specifically the case for semiconducting materials when the dimensions are in the range of the Debye length (i.e. few nanometers for most metal oxide semiconductors). Studying such synergetic phenomena and size dependent properties in a systematic way relies on a method that allows a precise control of the particle or film growth during the deposition.

Offering a high surface area, good thermal and electric conductivity and mechanical as well as chemical stability, CNTs are ideally suited as support for a second material that can be deposited onto their surface either as particles or as a thin film.[147] Metal oxide-coated single-wall CNTs and multi-wall CNTs have been used as CO,[215] O_2, NO_2 sensors.[108] A non-aqueous sol-gel approach was successfully applied for the conformal and homogeneous coating of the inner and outer surface of carbon nanotubes (cf. section III.2.2. and Figure I.8).[100, 108, 191] ALD-coated tubes with thin layers of V_2O_4 as active component were investigated in gas-sensing devices.[108] Due to the formation of a

p-n heterojunction between the p-type conductive CNTs and the n-type thin film, an enhancement of the gas-sensing response was observed.

The role of the thickness and nanostructure of the deposited material on the properties of p-n heterojunctions was demonstrated by coating CNTs (p-type) by ZnO (n-type) ALD. ZnO crystalline nanoparticles are deposited forming a partial or full coating of the CNTs. The so-fabricated photodetector devices exhibit a semiconducting p-type character when the coating is incomplete and a n-type character for a continuous coating. This was attributed to the different nature of charge carriers, holes for the first and electrons for the latter case.[214]

Combining electrospinning and ALD, SnO_2 nanofibers coated with ZnO were elaborated (Figure I.10a-b) and tested as O_2, NO_2[212] and CO gas sensors.[216] The electrospun nanofibers presented an average diameter of 120 nm (Figure I.10a) and were covered by ZnO shells (Figure I.10b) of various thicknesses. A stable and reproducible sensing response was obtained. The response to NO_2 appeared faster compared to the one recorded for pure ZnO fibers.[212] In case of CO sensing, a comparison between ZnO and SnO_2 fibers showed a gas sensing enhancement of the ZnO@SnO_2 heterostructures. This was attributed to a fully depleted ZnO top layer and the formation of the n-n isotope heterojunction.[216]

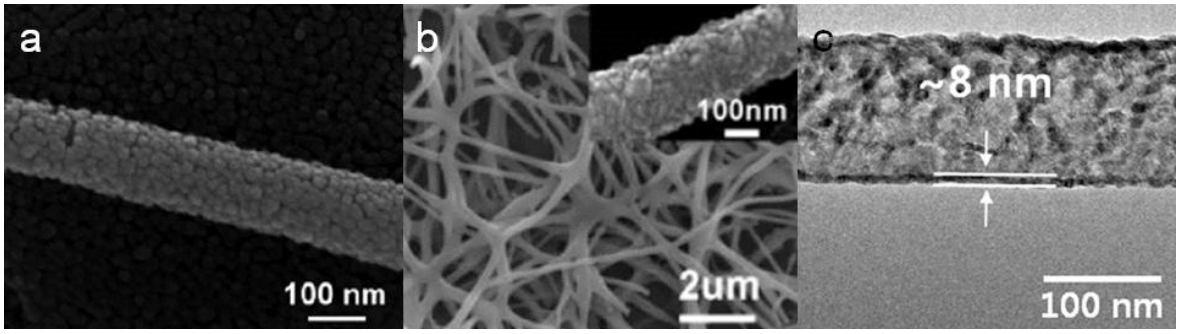

Figure I.10. Preparation process of a SnO_2-ZnO core-shell nanofiber sensor. a) SEM image of the electrospun SnO_2 fiber[216] and b) after ZnO ALD coating.[212] c) TEM image of SnO_2 nanotubes elaborated by subsequent coating and removal of polyacrylonitrile (PAN) electrospun fibers.[217]

SnO_2 nanofibers were also decorated by Pt nanoparticles deposited by ALD from $MeCpPtMe_3$ and O_2. An enhancement of the ethanol sensitivity, due to the presence of catalytic Pt nanoparticles on the surface, was observed.[210]

Syntheses of nanotubes/nanowires and porous materials[217-223] by template infiltration were achieved by ALD. SnO_2 nanotube networks[217] and ZnO nanowires arrays[220] were elaborated by ALD coating and template removal of electrospun polyacrylonitrile (PAN) fibers and patterned sacrificial silicon oxide, respectively. These nanostructures were investigated as O_2, CO, NO_2, NH_3 and ethanol sensors, and O_2 and CO sensors, respectively. In case of the tin oxide, a conservation of the nanostructured network was obtained even after stabilized-PAN fiber removal by calcination

(Figure I.10c). Indeed, a uniform coating made of interconnected crystalline nanoparticles was realized. A fast, reversible and stable response to ethanol was observed. Cross sensitivity tests showed a higher response to ethanol. As expected, the highest response was obtained for the thinnest wall thickness (~8 nm).[217]

Porous alumina, elaborated by ALD, was investigated as DNA[221, 222] and humidity sensors.[223] Ordered macroporous silicon, infiltrated by Ta_2O_5 was also used for relative humidity sensing.[223] As last example, infiltration of AAO by Pt/Ir permitted the non-enzymatic glucose detection. Platinum and iridium were deposited from $MeCpPtMe_3$, $Ir(acac)_3$ and O_2. By varying the ratio of Pt and Ir pulses, Pt/Ir alloys with various percentages were realized. The complete and conformal coating of the AAO pores enables the preparation of homogeneous controlled compositionally structured alloy films. Nanostructured Pt films were investigated as electrochemical electrodes for non-enzymatic glucose sensing. They presented a high selectivity to this compound and allowed to distinguish between glucose and interfering species, such as ascorbic acid and p-acetamidophenol. Indeed, a larger amperometric response to the target substance was observed compared to interfering species.[218] These nanostructured alloys can also find applications in the domain of catalysis and energy storage.

These examples suggest that ALD is probably the most suitable technique for the fabrication of chemical sensors because they require active materials of well controlled particle size, thickness of coating, morphology and composition.

IV.2. Catalysis and fuel cells

Materials for heterogeneous catalysis represent a crucial issue due to their large range of applications, in the chemical industry, automobile pollution control, fuel refinement and production, *etc.*[224] To increase the catalytic activity and reduce the production costs, nanostructured catalysts are relevant because of their high surface area and their potentially low active material loading.[224] Although the application of ALD in catalysis was early demonstrated for the deposition of oxide acting as support,[225] we mainly focus here on deposition and protection of metallic catalysts especially for fuel cell applications. The reader can also refer to two recent review papers.[226, 227] Particular attention is devoted to the development and improvement of fuel cell catalysts for e.g. methanol oxidation and oxygen reduction reactions. Since few years, ALD has proven to be a highly suitable technique to elaborate catalysts[128, 228-245] and has induced important progresses in fuel cell technology.[128, 238, 243, 246-255]

Feng *et al.*[232] infiltrated AAO with 1 nm ALD Al_2O_3 before loading it with VO_x by either wet impregnation or ALD. The catalysts prepared by ALD showed higher specificity toward the oxidative dehydrogenation of cyclohexane than those prepared by wet impregnation. Ma *et al.*[240]

modified the surface of Au/TiO_2 catalysts by SiO_2. 5 nm sized gold nanoparticles, homogeneously distributed on 20-50 nm titania particles, were encapsulated with an amorphous silica layer by ALD. Electron microscopy investigation showed that silica deposition takes place principally on TiO_2 and leaves Au nanoparticles at least partially uncovered (Figure I.11a). Despite the fact that the silica-stabilized sample exhibits a lower catalytic activity due to the partial coverage of gold particles with SiO_2, blocking some active catalytic sites, $SiO_2/Au/TiO_2$ showed an improved sintering resistance, maintaining a comparable activity toward the CO oxidation upon thermal treatment. The stabilization of porous gold by Al_2O_3 and TiO_2 ALD showed a threefold increase of the CO oxidation activity. This was attributed to the oxide-gold interaction and the improved thermal stability of the porous network (Figure I.11b,c).[228]

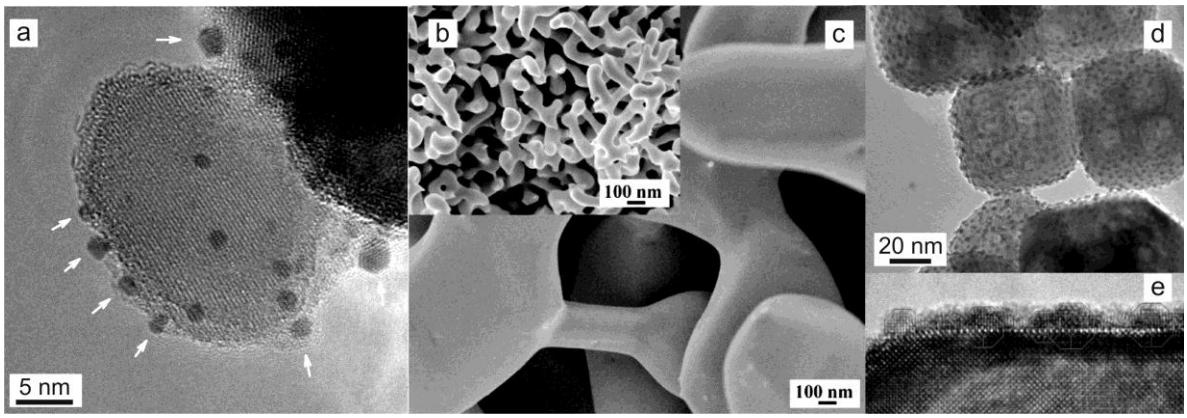

Figure I.11. a) TEM images of as-synthesized $SiO_2/Au/TiO_2$ catalyst, the arrows show the SiO_2 coated and uncoated Au nanoparticles[240] b) Al_2O_3-coated (10 cycles) and c) uncoated Au NP after annealing at 600 °C showing the protective effect of the ALD coating after annealing the porous structure.[228] d) Low-resolution TEM and e) HRTEM images of platinum NPs on strontium titanate nanocuboids.[231]

ALD was also used to directly deposit metal catalyst particles. The epitaxial growth of platinum nanoparticles on strontium titanate nanocubes leads to uniform 2-3 nm Pt nanoparticles with a 4-8 nm interparticle spacing (Figure I.11d,e).[128] Due to a cube on cube epitaxy the Pt particles are thermodynamically stable. By tuning the amount of Pt deposited, the shape of the deposited clusters could be controlled. The modification of the ratio of exposed Pt{111} to Pt{100} facets permits to study face-selective catalytic activities.[230] This effect was exploited for propane oxidation catalysis; a light off temperature (i.e. temperature for which 50% conversion is obtained) 50 ºC lower than the traditional Pt/Al_2O_3 catalyst with comparable Pt loading was recorded. Moreover, no deactivation was noticed and the activity appeared to be three orders of magnitude higher. The deactivation resistance improvement was related to Pt stabilization by the strong epitaxy with $SrTiO_3$ nanocubes, inhibiting the complete Pt oxidation.[231]

The surface of porous carbon aerogel was decorated by Pt nanocatalysts, prepared by ALD, from (methylcyclopentadienyl)trimethyl platinum ($MeCpPtMe_3$) and oxygen (dry air). A decrease of the average particle size was observed with increasing depth on the porous structure. Such a behavior was related to a non-ideal ALD process. High catalytic activity towards CO oxidation was observed even with a Pt loading as low as ~0.047 mg/cm^2, corresponding to 2 ALD cycles. Nearly full conversion was reached at a temperature as low as 150 ºC and equivalent activity was observed for 2 and 10 Pt ALD cycles.[238] Thus, ALD is highly suitable to synthesize supported catalysts with very low loading. From the same precursors, using a fluidized bed reactor, which allows processing of large amounts, Li *et al.*[239] investigated supported-Pt nanoparticles on porous silica catalysts for CO oxidation. Homogeneously dispersed on the outer and inner SiO_2 surface, Pt particles were deposited with a narrow size distribution.

In view of application in direct methanol fuel cells (DMCFs), bimetallic catalysts can improve the catalytic activity towards methanol oxidation. Christensen *et al.*[250] investigated the synthesis and activity towards methanol decomposition of supported Ru-Pt bimetallic NPs elaborated by ALD. $MeCpPtMe_3$ and 2,4-(dimethylpentadienyl)(ethylcyclopentadienyl) ruthenium and oxygen were used as precursors. Isolated crystalline 1.2 ± 0.3 nm sized Ru-Pt nanoparticles were deposited onto Al_2O_3 nanoparticles (Figure I.12a). By adjusting the ratio of Ru to Pt ALD cycles, a precise control of the composition was demonstrated. Methanol decomposition was performed on alumina supported bimetallic Ru-Pt and on a physical mixture of pure $Ru@Al_2O_3$ and $Pt@Al_2O_3$ catalysts. Above 210 ºC, with the bimetallic catalyst higher methanol conversion compared to the mixture of pure metallic particles was obtained.[250] Being well-known catalyst for CH_3OH oxidation, palladium nanoparticles fabricated by ALD were also investigated. From Pd(II) hexafluoroacetylacetonate and formaldehyde, Pd was deposited onto Al_2O_3 and ZnO surfaces.[233] The effect of the surface functional groups on the Pd nucleation was also studied in the case of the Al_2O_3 substrate.[244] Highly dispersed and uniform 1-2 nm Pd particles were deposited on porous silica, previously coated with a thin film of either Al_2O_3 or ZnO, allowing to tune the support surface composition without modifying its porosity and shape. After an incubation period, uniform Pd distribution over the whole support was obtained (Figure I.12c-d). $Pd\text{-}Al_2O_3$ presented a high activity with a nearly full conversion at 280 ºC and 100 % H_2 selectivity, while Pd-ZnO showed a fast deactivation due to the dissolution of the Pd into the support. This phenomenon could be suppressed by a simple thin Al_2O_3 overcoating acting as stabilization layer. Pd-ZnO overcoated by alumina showed an increase of catalytic activity, with a methanol conversion rising with the temperature, as well as no significant deactivation at 270 ºC after 6 h.[233] The high versatility of the ALD technique was also highlighted by the possibility to tune the average particle size. Pd particles from 0.8 nm to 2.2 nm

in size with a very narrow size distribution could be obtained, and an increase of catalyst activity with the decrease in particle size was noticed in methanol oxidation.[244]

Precious metal catalysts prepared by ALD for an oxygen reduction reaction (ORR) (i.e. for application as cathode catalysts in fuel cells) were also investigated. In 2009, Liu *et al.*[253] investigated the decoration of CNTs and carbon cloth by Pt for proton exchange membrane fuel cells (PEMFC). After Pt ALD on acid-treated-CNTs and -carbon cloth, conformal decoration with a 20-40 nm grain size Pt film was obtained (Figure I.12b). Pt@CNTs heterostructure used as cathode material in PEMFC showed high efficiency in ORR.

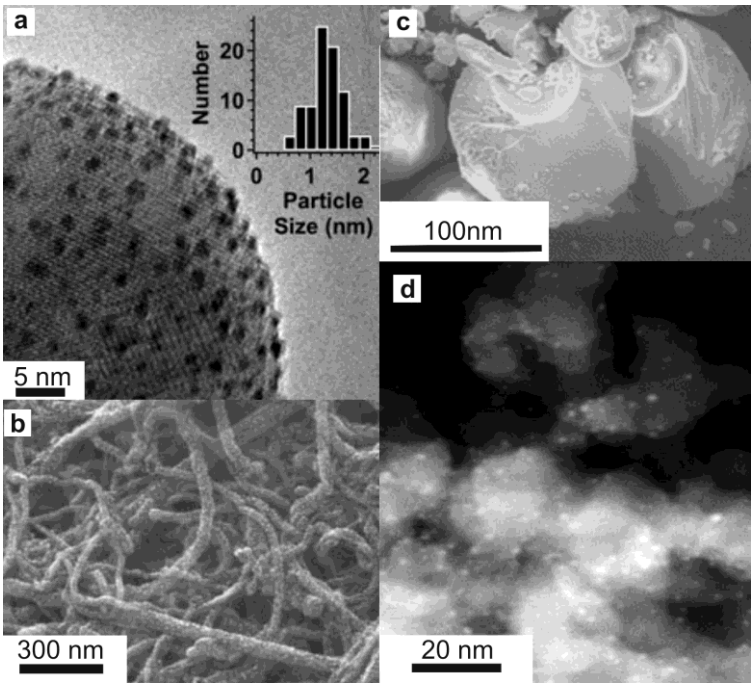

Figure I.12. a) TEM images of Ru-Pt nanoparticles deposited onto alumina. The histogram gives the nanoparticle size distribution measured from TEM with a mean particle diameter of 1.2 nm.[250] b) SEM cross-section view of the CNTs on Si wafer after 100 ALD cycles of Pt.[253] c) SEM image of the cross-section of a cleaved silica gel particle. d) TEM image of Pd particles supported on Al_2O_3.[233]

V. ALD set-ups used

The dissertation focuses on the deposition of titanium-, tin- and zinc oxide. Three different types of ALD tools were used. At the University of Aveiro, three home-made ALD reactors with two different set-ups (Figures I.13 and I.14) are available. One of those home-made set-ups was built during this PhD thesis.

Various designs of ALD reactors exist and can be divided into two types: the continuous flow reactor and the exposure mode one. When a reactor works in exposure mode, the precursors are pulsed into an isolated chamber from the pump using an intermediate valve between the chamber and the pumping system. After the precursor exposure, the unreacted precursor and the by-product are removed by opening this valve, and the reactor is thus purged. One can also let a residence time between the precursor pulse and the purge in order to let a sufficient time to the precursor to react with the surface. The total exposure time of the surface to the precursor consists thus in the pulse length and the residence time. On the other hand, the continuous flow reactor type consists in the precursor exposures with a carrier gas flowing continuously through the reactor to the pump. The ALD chamber is never isolated from the pump. The exposures to the different precursor are realized by successive their pulses separated by purging time.

The deposition of tin dioxide and a part of the experiments on titanium dioxide were realized in a home-made ALD reactor shown in the Figure I.13 working in exposure mode. The chamber consists of a stainless steel round plate-like reactor (outer diameter: 20 cm) with a lid, maintained at a particular temperature by an underneath heating plate. A scroll dry pump is connected to one side, while on the other side 2 precursor lines are set up with separated entrances. One stainless steel canister is assembled for the metal source and one for the oxygen source. In the manner to keep both reactants separated until the chamber, alternating precursor pulses occurred through 3 way pneumatic ALD valves. The chamber is isolated from the pump by an electromagnetic vacuum valve to allow a residence time of the reactants, if needed. The flow of the carrier gas, passing through the ALD valves until the chamber, is controlled by a mass flow controller. Finally, a pirani gauge placed between the chamber and the electromagnetic valve permits to monitor the dynamic pressure of the reactor. Typically, using 5 sccm of carrier gas, the pressure inside the chamber is, during the purge, $\sim 2.10^{-1}$ torrs and, just after the residence time, ~4-5 torrs. Each part of the apparatus is kept at a constant temperature by individual heaters.

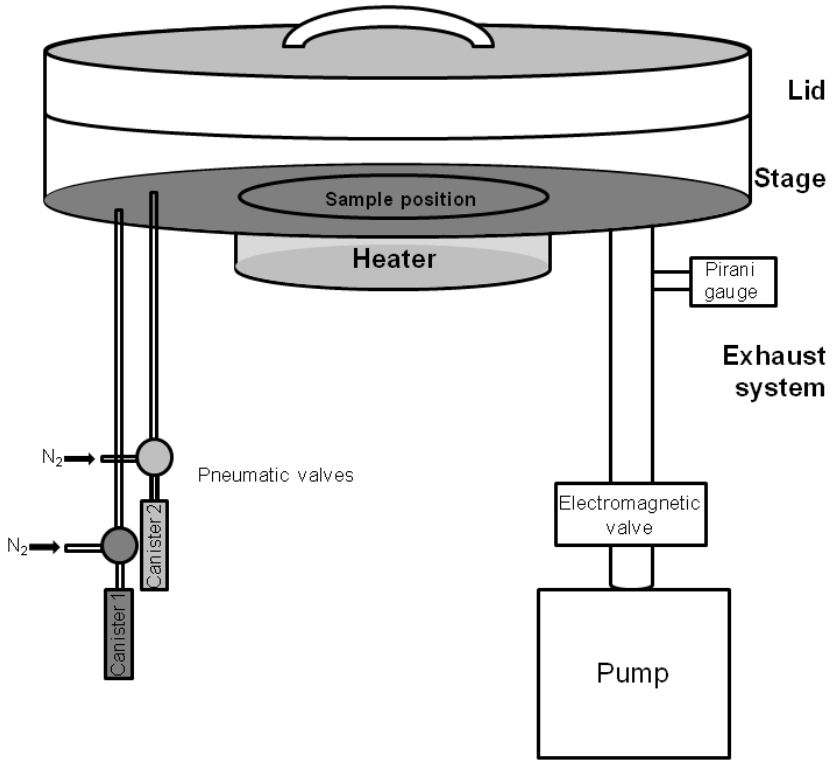

Figure I.13. Scheme of the ALD tool working in exposure mode, used for the deposition of SnO_2 and TiO_2.

In order to increase the amount of materials that can be coated, a second ALD tool operating in continuous flow has been constructed during this PhD work. The TiO_2 coating of carbon nanotubes and carbon fibers was partially realized in the reactor shown in Figure I.14. A split tubular furnace with a stainless steel tube is used as a deposition chamber. The furnace temperature is controlled by 3 external thermocouples in contact with the tube. Via a seal flange adaptor, an external thermocouple can also be added to measure the real temperature inside the chamber. On the one side an oil pump, a pirani gauge, for dynamic pressure monitoring, and either the external thermocouple or a blank flange are connected, and on the other side of the tube, the sample can be introduced and the precursor lines are connected. In this case, although the precursor lines merge before the entrance of the chamber, the reactants are kept separated thanks to 3 way pneumatic valves. One stainless steel canister is assembled for the metal source, one for the oxygen source and a third one is available for a second metal precursor. The flow of the carrier gas, i.e. N_2, passing through the ALD valves until the chamber, is controlled by a mass flow controller. The sample deposited in a rectangular crucible is introduced by a long rod having a hook for the sample removal at the end. During the deposition, a blank flange is used to close the sample entrance in order to keep the whole system under vacuum. The chamber is directly connected to the pump without intermediate valves allowing depositions only in continuous flow mode. The deposition

takes place at a pressure of ~1 torrs, with a flow of carrier gas of 100 sccm. Each part of the apparatus is kept at the desired temperature by an individual heater.

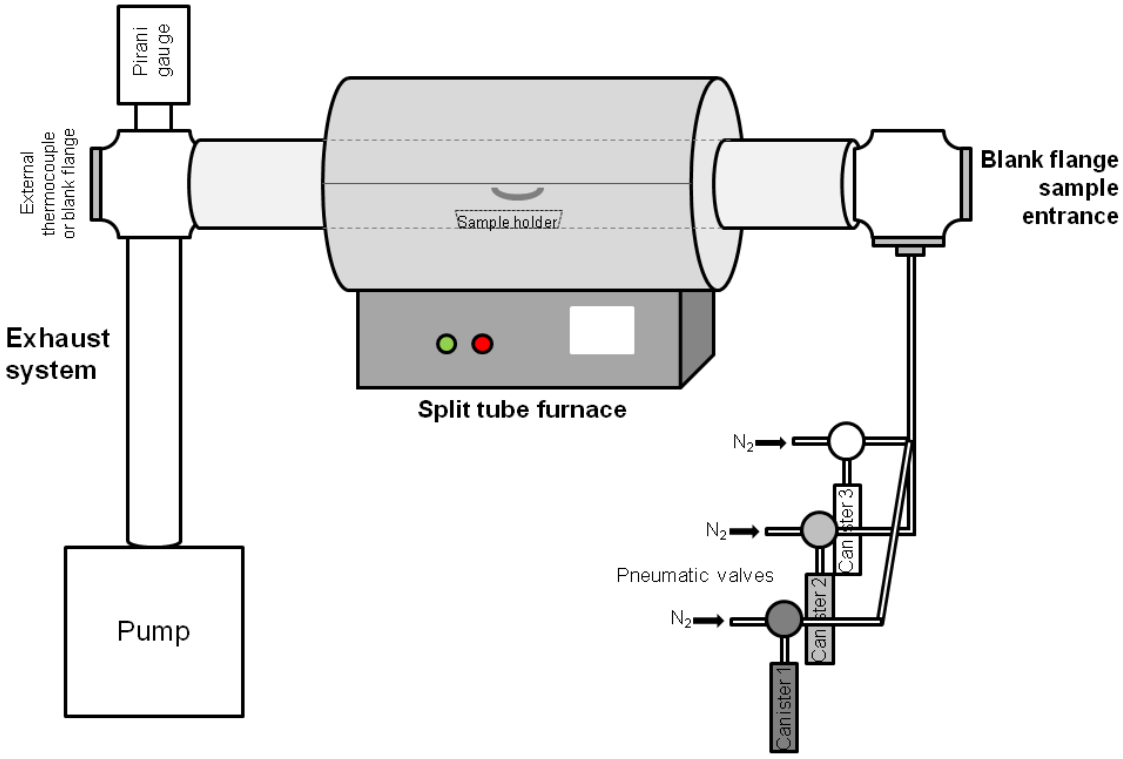

Figure I.14. Scheme of the ALD working in continuous flow mode used for the coating of the carbon nanotubes and carbon fibers.

Finally, the zinc oxide deposition was realized at the Seoul National University in a commercial ALD reactor, a CN1 model "atomic classic" operated in exposure mode.

VI. References

1. R. L. Puurunen, *J. Appl. Phys.*, 2005, **97**, 121301-121362.
2. S. M. George, *Chem. Rev.*, 2010, **110**, 111-131.
3. M. Leskelä and M. Ritala, *Angew. Chem. Int. Ed.*, 2003, **42**, 5548-5554.
4. M. Knez, K. Niesch and L. Niinistö, *Adv. Mater.*, 2007, **19**, 3425-3438.
5. A. A. Malygin, *J. Ind. Eng. Chem.*, 2006, **12**, 1-11.
6. T. Suntola and J. Antson, US 4,058,430, 1977.
7. F. Zaera, *J. Mater. Chem.*, 2008, **18**, 3521-3526.
8. S. M. George, B. Yoon and A. A. Dameron, *Acc. Chem. Res.*, 2009, **42**, 498-508.

9. S. M. George, B. Yoon, R. A. Hall, A. I. Abdulagatov, Z. M. Gibbs, Y. Lee, D. Seghete and B. H. Lee, in *Atomic Layer Deposition of Nanostructured Materials*, eds. N. Pinna and M. Knez, Wiley-VCH, 2011, pp. 83-108.
10. G. Clavel, C. Marichy and N. Pinna, in *Atomic Layer Deposition of Nanostructured Materials*, eds. N. Pinna and M. Knez, Wiley-VCH, 2011, pp. 61-82.
11. G. Clavel, E. Rauwel, M. G. Willinger and N. Pinna, *J. Mater. Chem.*, 2009, **19**, 454-462.
12. M. Leskelä, M. Ritala and O. Nilsen, *MRS Bull.*, 2011, **36**, 877-884.
13. M. Putkonen, in *Atomic Layer Deposition of Nanostructured Materials*, eds. N. Pinna and M. Knez, Wiley-VCH, 2011, pp. 41-59.
14. S. M. George, A. W. Ott and J. W. Klaus, *J. Phys. Chem.*, 1996, **100**, 13121-13131.
15. M. Leskelä and M. Ritala, *Thin Solid Films*, 2002, **409**, 138-146.
16. L. Niinistö, J. Paivasaari, J. Niinistö, M. Putkonen and M. Nieminen, *Phys. Status Solidi A*, 2004, **201**, 1443-1452.
17. J. Kim and T. Kim, *JOM*, 2009, **61**, 17-22.
18. M. de Ridder, P. C. van de Ven, R. G. van Welzenis, H. H. Brongersma, S. Helfensteyn, C. Creemers, P. Van Der Voort, M. Baltes, M. Mathieu and E. F. Vansant, *J. Phys. Chem. B*, 2002, **106**, 13146-13153.
19. R. L. Puurunen, *Chem. Vap. Deposition*, 2004, **10**, 159-170.
20. R. L. Puurunen, A. Root, P. Sarv, M. M. Viitanen, H. H. Brongersma, M. Lindblad and A. O. I. Krause, *Chem. Mater.*, 2002, **14**, 720-729.
21. L. Niinistö, M. Ritala and M. Leskelä, *Mater. Sci. Eng., B*, 1996, **41**, 23-29.
22. L. F. Hakim, S. M. George and A. W. Weimer, *Nanotechnology*, 2005, **16**, S375-S381.
23. D. M. King, J. A. Spencer, X. Liang, L. F. Hakim and A. W. Weimer, *Surf. Coat. Technol.*, 2007, **201**, 9163-9171.
24. X. H. Liang, D. M. King, P. Li and A. W. Weimer, *J. Am. Ceram. Soc.*, 2009, **92**, 649-654.
25. J. R. Wank, S. M. George and A. W. Weimer, *Powder Technol.*, 2004, **142**, 59-69.
26. J. A. McCormick, B. L. Cloutier, A. W. Weimer and S. M. George, *J. Vac. Sci. Technol., A*, 2007, **25**, 67-74.
27. J. A. McCormick, K. P. Rice, D. F. Paul, A. W. Weimer and S. M. George, *Chem. Vap. Deposition*, 2007, **13**, 491-498.
28. C. A. Wilson, J. A. McCormick, A. S. Cavanagh, D. N. Goldstein, A. W. Weimer and S. M. George, *Thin Solid Films*, 2008, **516**, 6175-6185.
29. E. Granneman, P. Fischer, D. Pierreux, H. Terhorst and P. Zagwijn, *Surf. Coat. Technol.*, 2007, **201**, 8899-8907.
30. D. H. Levy, D. Freeman, S. F. Nelson, P. J. Cowdery-Corvan and L. M. Irving, *Appl. Phys. Lett.*, 2008, **92**, 192101-192103.
31. P. Poodt, A. Lankhorst, F. Roozeboom, K. Spee, D. Maas and A. Vermeer, *Adv. Mater.*, 2010, **22**, 3564-3567.
32. K. Lahtinen, P. Maydannik, P. Johansson, T. Kääriäinen, D. C. Cameron and J. Kuusipalo, *Surf. Coat. Technol.*, 2011, **205**, 3916-3922.
33. P. S. Maydannik, T. O. Kääriäinen and D. C. Cameron, *Chem. Eng. J.*, 2011, **171**, 345-349.

34. W. M. M. E. Kessels and M. Putkonen, *MRS Bull.*, 2011, **36**, 907-913.
35. M. Leskelä, in *Atomic Layer Deposition of Nanostructured Materials*, eds. N. Pinna and M. Knez, Wiley-VCH, 2011, pp. 401-421.
36. H. J. Lee, M. H. Park, Y.-S. Min, G. Clavel, N. Pinna and C. S. Hwang, *J. Phys. Chem. C*, 2010, **114**, 12736-12741.
37. A. Yanguas-Gil, K. E. Peterson and J. W. Elam, *Chem. Mater.*, 2011, **23**, 4295-4297.
38. L. L. Hench and J. K. West, *Chem. Rev.*, 1990, **90**, 33-72.
39. J. Livage and C. Sanchez, *J. Non-Cryst. Solids*, 1992, **145**, 11-19.
40. J. Livage, M. Henry and C. Sanchez, *Prog. Solid State Chem.*, 1988, **18**, 259-341.
41. J. Livage, *Bull. Mater. Sci.*, 1999, **22**, 201-205.
42. C. Sanchez, B. Julian, P. Belleville and M. Popall, *J. Mater. Chem.*, 2005, **15**, 3559-3592.
43. U. Schubert, *J. Mater. Chem.*, 2005, **15**, 3701-3715.
44. J. Wen and G. L. Wilkes, *Chem. Mater.*, 1996, **8**, 1667-1681.
45. B. L. Cushing, V. L. Kolesnichenko and C. J. O'Connor, *Chem. Rev.*, 2004, **104**, 3893-3946.
46. J. Livage, M. Henry, J. P. Jolivet and C. Sanchez, *MRS Bull.*, 1990, **XV**, 18-25.
47. Y. Aoki, T. Kunitake and A. Nakao, *Chem. Mater.*, 2004, **17**, 450-458.
48. T. R. B. Foong, Y. Shen, X. Hu and A. Sellinger, *Adv. Funct. Mater.*, 2010, **20**, 1390-1396.
49. G. Freiman, P. Barboux, J. Perrière and K. Giannakopoulos, *Thin Solid Films*, 2009, **517**, 2670-2674.
50. I. Ichinose, H. Senzu and T. Kunitake, *Chem. Mater.*, 1997, **9**, 1296-1298.
51. N. I. Kovtyukhova, T. E. Mallouk and T. S. Mayer, *Adv. Mater.*, 2003, **15**, 780-785.
52. J. Huang and T. Kunitake, *J. Am. Chem. Soc.*, 2003, **125**, 11834-11835.
53. W. Yan, S. Mahurin, S. Overbury and S. Dai, *Top. Catal.*, 2006, **39**, 199-212.
54. G. Freiman, P. Barboux, J. Perriere and K. Giannakopoulos, *Chem. Mater.*, 2007, **19**, 5862-5867.
55. J. Zhang, Z. Ma, J. Jiao, H. Yin, W. Yan, E. W. Hagaman, J. Yu and S. Dai, *Langmuir*, 2009, **25**, 12541-12549.
56. I. Ichinose, T. Kawakami and T. Kunitake, *Adv. Mater.*, 1998, **10**, 535-539.
57. C. Sanchez, J. Livage, M. Henry and F. Babonneau, *J. Non-Cryst. Solids*, 1988, **100**, 65-76.
58. R. J. P. Corriu and D. Leclercq, *Angew. Chem. Int. Ed.*, 1996, **35**, 1420-1436.
59. M. Ivanda, S. Music, S. Popovic and M. Gotic, *J. Mol. Struct.*, 1999, **480-481**, 645-649.
60. H. Kominami, M. Kohno, Y. Takada, M. Inoue, T. Inui and Y. Kera, *Ind. Eng. Chem. Res.*, 1999, **38**, 3925-3931.
61. M. Monge, M. L. Kahn, A. Maisonnat and B. Chaudret, *Angew. Chem. Int. Ed.*, 2003, **42**, 5321-5324.
62. P. H. Mutin and A. Vioux, *Chem. Mater.*, 2009, **21**, 582-596.
63. M. Niederberger, *Acc. Chem. Res.*, 2007, **40**, 793-800.

64. M. Niederberger and N. Pinna, *Metal Oxide Nanoparticles in Organic Solvents: Synthesis, Formation, Assembly and Application* Springer, 2009.

65. N. Pinna and M. Niederberger, *Angew. Chem. Int. Ed.*, 2008, **47**, 5292-5304.

66. A. Vioux, *Chem. Mater.*, 1997, **9**, 2292-2299.

67. R. J. P. Corriu and D. Leclercq, *Comments Inorg. Chem.*, 1997, **19**, 245 - 262.

68. M. Niederberger and G. Garnweitner, *Chem. Eur. J.*, 2006, **12**, 7282-7302.

69. N. Pinna, G. Garnweitner, M. Antonietti and M. Niederberger, *J. Am. Chem. Soc.*, 2005, **127**, 5608-5612.

70. M. Niederberger, G. Garnweitner, N. Pinna and G. Neri, *Prog. Solid State Chem.*, 2005, **33**, 59-70.

71. A. C. Jones, H. C. Aspinall, P. R. Chalker, R. J. Potter, T. D. Manning, Y. F. Loo, R. O'Kane, J. M. Gaskell and L. M. Smith, *Chem. Vap. Deposition*, 2006, **12**, 83-98.

72. E. L. Lakomaa, S. Haukka and T. Suntola, *Appl. Surf. Sci.*, 1992, **60-61**, 742-748.

73. R. Matero, A. Rahtu and M. Ritala, *Chem. Mater.*, 2001, **13**, 4506-4511.

74. A. Rahtu and M. Ritala, *J. Mater. Chem.*, 2002, **12**, 1484-1489.

75. X. Du, Y. Du and S. M. George, *J. Vac. Sci. Technol., A*, 2005, **23**, 581-588.

76. R. L. Puurunen, *Chem. Vap. Deposition*, 2005, **11**, 79-90.

77. K. Kukli, J. Aarik, A. Aidla, H. Siimon, M. Ritala and M. Leskelä, *Appl. Surf. Sci.*, 1997, **112**, 236-242.

78. J. Aarik, A. Aidla, V. Sammelselg, T. Uustare, M. Ritala and M. Leskelä, *Thin Solid Films*, 2000, **370**, 163-172.

79. J. Aarik, A. Aidla, T. Uustare, M. Ritala and M. Leskelä, *Appl. Surf. Sci.*, 2000, **161**, 385-395.

80. A. Rahtu and M. Ritala, *Chem. Vap. Deposition*, 2002, **8**, 21-28.

81. M. Juppo, A. Rahtu, M. Ritala and M. Leskelä, *Langmuir*, 2000, **16**, 4034-4039.

82. R. A. Wind and S. M. George, *J. Phys. Chem. A*, 2010, **114**, 1281-1289.

83. M. D. Groner, F. H. Fabreguette, J. W. Elam and S. M. George, *Chem. Mater.*, 2004, **16**, 639-645.

84. A. W. Ott, J. W. Klaus, J. M. Johnson and S. M. George, *Thin Solid Films*, 1997, **292**, 135-144.

85. E. B. Yousfi, J. Fouache and D. Lincot, *Appl. Surf. Sci.*, 2000, **153**, 223-234.

86. A. W. Ott, J. M. Johnson, J. W. Klaus and S. M. George, *Appl. Surf. Sci.*, 1997, **112**, 205-215.

87. J. Niinistö, A. Rahtu, M. Putkonen, M. Ritala, M. Leskelä and L. Niinistö, *Langmuir*, 2005, **21**, 7321-7325.

88. M. Ritala, K. Kukli, A. Rahtu, P. I. Raisanen, M. Leskelä, T. Sajavaara and J. Keinonen, *Science*, 2000, **288**, 319-321.

89. V. V. Brei, V. A. Kaspersky and N. U. Gulyanitskaya, *React. Kinet. Catal. Lett.*, 1993, **50**, 415-421.

90. A. Rahtu and M. Ritala, *Langmuir*, 2002, **18**, 10046-10048.

91. K. Kukli, M. Ritala, M. Leskelä, T. Sajavaara, J. Keinonen, R. I. Hegde, D. C. Gilmer and P. J. Tobin, *J. Electrochem. Soc.*, 2004, **151**, F98-F104.

92. W. K. Kim, S. W. Kang and S. W. Rhee, *J. Vac. Sci. Technol., A*, 2003, **21**, L16-L18.

93. K. E. Prince, P. J. Evans, G. Triani, Z. Zhang and J. Bartlett, *Surf. Interface Anal.*, 2006, **38**, 1692-1695.

94. L. Hiltunen, H. Kattelus, M. Leskelä, M. Makela, L. Niinistö, E. Nykanen, P. Soininen and M. Tiitta, *Mater. Chem. Phys.*, 1991, **28**, 379-388.

95. M. Tiitta, E. Nykanen, P. Soininen, L. Niinistö, M. Leskelä and R. Lappalainen, *Mater. Res. Bull.*, 1998, **33**, 1315-1323.

96. P. J. Evans, P. H. Mutin, G. Triani, K. E. Prince and J. R. Bartlett, *Surf. Interface Anal.*, 2006, **38**, 740-743.

97. P. Arnal, R. J. P. Corriu, D. Leclercq, P. H. Mutin and A. Vioux, *J. Mater. Chem.*, 1996, **6**, 1925-1932.

98. D. C. Bradley, R. C. Mehrota, I. P. Rothwell and A. Singh, *Alkoxo and aryloxo derivatives of metals*, Academic Press, London, 2001.

99. V. G. Kessler, *Chem. Commun.*, 2003, 1213-1222.

100. E. Rauwel, G. Clavel, M. G. Willinger, P. Rauwel and N. Pinna, *Angew. Chem. Int. Ed.*, 2008, **47**, 3592-3595.

101. M. Knez and N. Pinna, *Unpublished results*.

102. J. Caruso, C. Roger, F. Schwertfeger, M. J. Hampdensmith, A. L. Rheingold and G. Yap, *Inorg. Chem.*, 1995, **34**, 449-453.

103. S. Doeuff, M. Henry and C. Sanchez, *Mater. Res. Bull.*, 1990, **25**, 1519-1529.

104. P. D. Cozzoli, A. Kornowski and H. Weller, *J. Am. Chem. Soc.*, 2003, **125**, 14539-14548.

105. G. Clavel, M. G. Willinger, D. Zitoun and N. Pinna, *Adv. Funct. Mater.*, 2007, **17**, 3159-3169.

106. J. Joo, S. G. Kwon, J. H. Yu and T. Hyeon, *Adv. Mater.*, 2005, **17**, 1873-1877.

107. A. Narayanaswamy, H. Xu, N. Pradhan, M. Kim and X. Peng, *J. Am. Chem. Soc.*, 2006, **128**, 10310-10319.

108. M. G. Willinger, G. Neri, E. Rauwel, A. Bonavita, G. Micali and N. Pinna, *Nano Lett.*, 2008, **8**, 4201-4204.

109. C. Marichy, N. Donato, M.-G. Willinger, M. Latino, D. Karpinsky, S.-H. Yu, G. Neri and N. Pinna, *Adv. Funct. Mater.*, 2011, **21**, 658-666.

110. W. S. Jeon, S. Yang, C. S. Lee and S. W. Kang, *J. Electrochem. Soc.*, 2002, **149**, C306-C310.

111. D. Hausmann, J. Becker, S. L. Wang and R. G. Gordon, *Science*, 2002, **298**, 402-406.

112. G. Garnweitner, M. Antonietti and M. Niederberger, *Chem. Commun.*, 2005, 397-399.

113. J. W. Elam, A. B. F. Martinson, M. J. Pellin and J. T. Hupp, *Chem. Mater.*, 2006, **18**, 3571-3578.

114. E. Langereis, J. Keijmel, M. de Sanden and W. M. M. Kessels, *Appl. Phys. Lett.*, 2008, **92**, 231904-231906.

115. D. N. Goldstein, J. A. McCormick and S. M. George, *J. Phys. Chem. C*, 2008, **112**, 19530-19539.

116. J. Kwon, M. Dai, M. D. Halls and Y. J. Chabal, *Chem. Mater.*, 2008, **20**, 3248-3250.

117. V. R. Rai, V. Vandalon and S. Agarwal, *Langmuir*, 2010, **26**, 13732-13735.

118. Y. Wang, M. Dai, M.-T. Ho, L. S. Wielunski and Y. J. Chabal, *Appl. Phys. Lett.*, 2007, **90**, 022906-022908.

119. J. Kwon, M. Dai, M. Halls, D. and Y. Chabal, J. , *Appl. Phys. Lett.*, 2010, **97**, 162903-162905.

120. V. R. Rai and S. Agarwal, *J. Phys. Chem. C*, 2009, **113**, 12962-12965.

121. K. Knapas and M. Ritala, *Chem. Mater.*, 2008, **20**, 5698-5705.

122. M. Rose, J. Niinistö, I. Endler, J. W. Bartha, P. Kücher and M. Ritala, *ACS Appl. Mater. Interfaces*, 2010, **2**, 347-350.

123. P. O'Brien and A. Sullivan, *J. Mater. Chem.*, 2004, **14**, E11-E15.

124. C. S. Hwang, in *Atomic Layer Deposition of Nanostructured Materials*, eds. N. Pinna and M. Knez, Wiley-VCH, 2011, pp. 161-192.

125. N. Pinna and M. Knez, *Atomic Layer Deposition of Nanostructured Materials*, Wiley-VCH, 2011.

126. J. Bachmann, J. Jing, M. Knez, S. Barth, H. Shen, S. Mathur, U. Gösele and K. Nielsch, *J. Am. Chem. Soc.*, 2007, **129**, 9554-9555.

127. J. Bachmann, R. Zierold, Y. T. Chong, R. Hauert, C. Sturm, R. Schmidt-Grund, B. Rheinlander, M. Grundmann, U. Gösele and K. Nielsch, *Angew. Chem. Int. Ed.*, 2008, **47**, 6177-6179.

128. S. T. Christensen, J. W. Elam, F. A. Rabuffetti, Q. Ma, S. J. Weigand, B. Lee, S. Seifert, P. C. Stair, K. R. Poeppelmeier, M. C. Hersam and M. J. Bedzyk, *Small*, 2009, **5**, 750-757.

129. E. R. Cleveland, P. Banerjee, I. Perez, S. B. Lee and G. W. Rubloff, *Acs Nano*, 2010, **4**, 4637-4644.

130. B. Hatton, V. Kitaev, D. Perovic, G. Ozin and J. Aizenberg, *J. Mater. Chem.*, 2010, **20**, 6009-6013.

131. H. Kim, E. Pippel, U. Gösele and M. Knez, *Langmuir*, 2009, **25**, 13284-13289.

132. H.-B.-R. Lee, G. H. Gu, J. Y. Son, C. G. Park and H. Kim, *Small*, 2008, **4**, 2247-2254.

133. R. B. Yang, J. Bachmann, M. Reiche, J. W. Gerlach, U. Gösele and K. Nielsch, *Chem. Mater.*, 2009, **21**, 2586-2588.

134. R. Zierold, Z. Wu, J. Biskupek, U. Kaiser, J. Bachmann, C. E. Krill and K. Nielsch, *Adv. Funct. Mater.*, 2011, **21**, 226-232.

135. M. Knez, *Mater. Matters*, 2008, **3**, 28-30.

136. M. Knez, A. Kadri, C. Wege, U. Gösele, H. Jeske and K. Nielsch, *Nano Lett.*, 2006, **6**, 1172-1177.

137. A. Szeghalmi, M. Helgert, R. Brunner, F. Heyroth, U. Gösele and M. Knez, *Adv. Funct. Mater.*, 2010, **20**, 2053-2062.

138. A. Szeghalmi, K. Sklarek, M. Helgert, R. Brunner, W. Erfurth, U. Gösele and M. Knez, *Small*, 2010, **6**, 2701-2707.

139. H.-B.-R. Lee and S. F. Bent, in *Atomic Layer Deposition of Nanostructured Materials*, eds. N. Pinna and M. Knez, Wiley-VCH, 2011, pp. 193-226.

140. J. W. Elam, in *Atomic Layer Deposition of Nanostructured Materials*, eds. N. Pinna and M. Knez, Wiley-VCH, 2011, pp. 227-250.

141. H. J. Fan and K. Nielsch, in *Atomic Layer Deposition of Nanostructured Materials*, eds. N. Pinna and M. Knez, Wiley-VCH, 2011, pp. 251-270.

142. C. Bae, H. Shin and K. Nielsch, *MRS Bull.*, 2011, **36**, 887-897.

143. H. Kim, H.-B.-R. Lee and W. J. Maeng, *Thin Solid Films*, 2009, **517**, 2563-2580.

144. M. Leskelä, M. Kemell, K. Kukli, V. Pore, E. Santala, M. Ritala and J. Lu, *Mater. Sci. Eng., C*, 2007, **27**, 1504-1508.

145. M. Ritala and M. Leskelä, *Nanotechnology*, 1999, **10**, 19.

146. J. D. Ferguson, A. W. Weimer and S. M. George, *Thin Solid Films*, 2000, **371**, 95-104.

147. C. Marichy, A. Pucci, M.-G. Willinger and N. Pinna, in *Atomic Layer Deposition of Nanostructured Materials*, eds. N. Pinna and M. Knez, Wiley-VCH, 2011, pp. 327-343.

148. M. Knez, in *Atomic Layer Deposition of Nanostructured Materials*, eds. N. Pinna and M. Knez, Wiley-VCH, 2011, pp. 301-326.

149. G. N. Parsons, in *Atomic Layer Deposition of Nanostructured Materials*, eds. N. Pinna and M. Knez, Wiley-VCH, 2011, pp. 271-300.

150. H. J. Fan, M. Knez, R. Scholz, D. Hesse, K. Nielsch, M. Zacharias and U. Gösele, *Nano Lett.*, 2007, **7**, 993-997.

151. H. Fan, M. Knez, R. Scholz, K. Nielsch, E. Pippel, D. Hesse, U. Gösele and M. Zacharias, *Nanotechnology*, 2006, **17**, 5157-5162.

152. C. Ducso, N. Q. Khanh, Z. Horvath, I. Barsony, M. Utriainen, S. Lehto, M. Nieminen and L. Niinistö, *J. Electrochem. Soc.*, 1996, **143**, 683-687.

153. M. Utriainen, S. Lehto, L. Niinistö, C. Ducso, N. Q. Khanh, Z. E. Horvath, I. Barsony and B. Pecz, *Thin Solid Films*, 1997, **297**, 39-42.

154. H. Shin, D. K. Jeong, J. Lee, M. M. Sung and J. Kim, *Adv. Mater.*, 2004, **16**, 1197-1200.

155. M. S. Sander, M. J. Côté, W. Gu, B. M. Kile and C. P. Tripp, *Adv. Mater.*, 2004, **16**, 2052-2057.

156. S. K. Panda and H. Shin, in *Atomic Layer Deposition of Nanostructured Materials*, eds. N. Pinna and M. Knez, Wiley-VCH, 2011, pp. 23-40.

157. J. W. Elam, D. Routkevitch, P. P. Mardilovich and S. M. George, *Chem. Mater.*, 2003, **15**, 3507-3517.

158. C. Bohley, M. Y. E. Yau, C. Erk, Y. Wang, R. B. Wehrspohn, S. Schlecht and M. Steinhart, *Phys. Status Solidi B*, 2010, **247**, 2470-2475.

159. Y. Wang, Y. Qin, A. Berger, E. Yau, C. He, L. Zhang, U. Gösele, M. Knez and M. Steinhart, *Adv. Mater.*, 2009, **21**, 2763-2766.

160. D. P. Gaillot and C. J. Summers, in *Atomic Layer Deposition of Nanostructured Materials*, eds. N. Pinna and M. Knez, Wiley-VCH, 2011, pp. 345-376.

161. E. Färm, M. Kemell, M. Ritala and M. Leskelä, *J. Phys. Chem. C*, 2008, **112**, 15791-15795.

162. E. Färm, M. Kemell, E. Santala, M. Ritala and M. Leskelä, *J. Electrochem. Soc.*, 2010, **157**, K10-K14.

163. A. Sinha, D. W. Hess and C. L. Henderson, *J. Electrochem. Soc.*, 2006, **153**, G465-G469.

164. A. Sinha, D. W. Hess and C. L. Henderson, *J. Vac. Sci. Technol., B*, 2006, **24**, 2523-2532.

165. R. Chen, H. Kim, P. C. McIntyre and S. F. Bent, *Chem. Mater.*, 2005, **17**, 536-544.

166. X. Jiang and S. F. Bent, *J. Phys. Chem. C*, 2009, **113**, 17613-17625.

167. X. Jiang, R. Chen and S. F. Bent, *Surf. Coat. Technol.*, 2007, **201**, 8799-8807.

168. J. P. Lee, Y. J. Jang and M. M. Sung, *Adv. Funct. Mater.*, 2003, **13**, 873-876.

169. E. K. Seo, J. W. Lee, H. M. Sung-Suh and M. M. Sung, *Chem. Mater.*, 2004, **16**, 1878-1883.

170. D. Eder, *Chem. Rev.*, 2010, **110**, 1348-1385.

171. T.-J. Park, S. Banerjee, T. Hemraj-Benny and S. S. Wong, *J. Mater. Chem.*, 2006, **16**, 141-154.

172. D. Tasis, N. Tagmatarchis, A. Bianco and M. Prato, *Chem. Rev.*, 2006, **106**, 1105-1136.

173. S. Banerjee, T. Hemraj-Benny and S. S. Wong, *Adv. Mater.*, 2005, **17**, 17-29.

174. A. Hirsch, *Angew. Chem. Int. Ed.*, 2002, **41**, 1853-1859.

175. M. J. O'Connell, P. Boul, L. M. Ericson, C. Huffman, Y. Wang, E. Haroz, C. Kuper, J. Tour, K. D. Ausman and R. E. Smalley, *Chem. Phys. Lett.*, 2001, **342**, 265-271.

176. D. B. Farmer and R. G. Gordon, *Nano Lett.*, 2006, **6**, 699-703.

177. J. S. Lee, B. Min, K. Cho, S. Kim, J. Park, Y. T. Lee, N. S. Kim, M. S. Lee, S. O. Park and J. T. Moon, *J. Cryst. Growth*, 2003, **254**, 443-448.

178. C. F. Herrmann, F. H. Fabreguette, D. S. Finch, R. Geiss and S. M. George, *Appl. Phys. Lett.*, 2005, **87**, 123110-123112.

179. D. B. Farmer and R. G. Gordon, *Electrochem. Solid State Lett.*, 2005, **8**, G89-G91.

180. Y. S. Min, E. J. Bae, K. S. Jeong, Y. J. Cho, J. H. Lee, W. B. Choi and G. S. Park, *Adv. Mater.*, 2003, **15**, 1019-1022.

181. A. Gomathi, S. R. C. Vivekchand, A. Govindaraj and C. N. R. Rao, *Adv. Mater.*, 2005, **17**, 2757-2761.

182. A. Javey, H. Kim, M. Brink, Q. Wang, A. Ural, J. Guo, P. McIntyre, P. McEuen, M. Lundstrom and H. Dai, *Nat. Mater.*, 2002, **1**, 241-246.

183. T. Helbling, C. Hierold, C. Roman, L. Durrer, M. Mattmann and V. M. Bright, *Nanotechnology*, 2009, **20**, 434010-434019.

184. Y. Nakashima, Y. Ohno, S. Kishimoto, M. Okochi, H. Honda and T. Mizutanu, *J. Nanosci. Nanotechnol.*, 2010, **10**, 3805-3809.

185. J. Shen, W. Wang, Q. Chen, M. Wang, S. Xu, Y. Zhou and X.-X. Zhang, *Nanotechnology*, 2009, **20**, 245307-245312.

186. Y. Lu, S. Bangsaruntip, X. Wang, L. Zhang, Y. Nishi and H. Dai, *J. Am. Chem. Soc.*, 2006, **128**, 3518-3519.

187. D. S. Kim, S. M. Lee, R. Scholz, M. Knez, U. Gösele, J. Fallert, H. Kalt and M. Zacharias, *Appl. Phys. Lett.*, 2008, **93**, 103108-103110.

188. G. D. Zhan, X. H. Du, D. M. King, L. F. Hakim, X. H. Liang, J. A. McCormick and A. W. Weimer, *J. Am. Ceram. Soc.*, 2008, **91**, 831-835.

189. A. S. Cavanagh, C. A. Wilson, W. Alan and S. M. George, *Nanotechnology*, 2009, **20**, 255602-255611.

190. E. Rauwel, M. G. Willinger, F. Ducroquet, P. Rauwel, I. Matko, D. Kiselev and N. Pinna, *J. Phys. Chem. C*, 2008, **112**, 12754-12759.

191. M. G. Willinger, G. Neri, A. Bonavita, G. Micali, E. Rauwel, T. Herntrich and N. Pinna, *Phys. Chem. Chem. Phys.*, 2009, **11**, 3615-3622.

192. D. M. King, X. Liang and A. W. Weimer, *ECS Trans.*, 2009, **25**, 163-190.

193. C. Marichy, M. Bechelany and N. Pinna, *Adv. Mater.*, 2012, **24**, 1017-1032.

194. M. Liu, X. Li, S. K. Karuturi, A. I. Y. Tok and H. J. Fan, *Nanoscale*, 2012, **4**.

195. G. Neri, *Sci. Adv. Mater.*, 2010, **2**, 3-15.

196. A. Tricoli, M. Righettoni and A. Teleki, *Angew. Chem. Int. Ed.*, 2010, **49**, 7632-7659.

197. W. Gopel and K. D. Schierbaum, *Sens. Actuators, B*, 1995, **26**, 1-12.

198. G. Korotcenkov, *Mater. Sci. Eng. R: Rep.*, 2008, **61**, 1-39.

199. G. Neri, A. Bonavita, G. Rizzo, S. Galvagno, N. Pinna, M. Niederberger, S. Capone and P. Siciliano, *Sens. Actuators, B*, 2007, **122**, 564-571.

200. C. Xu, J. Tamaki, N. Miura and N. Yamazoe, *Sens. Actuators, B*, 1991, **3**, 147-155.

201. M. Aronniemi, J. Saino and J. Lahtinen, *Thin Solid Films*, 2008, **516**, 6110-6115.

202. G. Choi, L. Satyanarayana and J. Park, *Appl. Surf. Sci.*, 2006, **252**, 7878-7883.

203. X. Du and S. M. George, *Sens. Actuators, B*, 2008, **135**, 152-160.

204. K. B. Jinesh, V. A. T. Dam, J. Swerts, C. de Nooijer, S. van Elshocht, S. H. Brongersma and M. Crego-Calama, *Sens. Actuators, B*, 2011, **156**, 276-282.

205. G. Natarajan and D. Cameron, *Appl. Phys. A*, 2009, **95**, 621-627.

206. A. J. Niskanen, A. Varpula, M. Utriainen, G. Natarajan, D. C. Cameron, S. Novikov, V.-M. Airaksinen, J. Sinkkonen and S. Franssila, *Sens. Actuators, B*, 2010, **148**, 227-232.

207. A. Rosental, A. Tarre, A. Gerst, J. Sundqvist, A. Harsta, A. Aidla, J. Aarik, V. Sammelselg and T. Uustare, *Sens. Actuators, B*, 2003, **93**, 552-555.

208. A. T. Rosental, A.; Gerst, A.; Uustare, T.; Sammelselg, V., *Sens. Actuators, B*, 2001, **77**, 297-300.

209. M. Utriainen, K. Kovacs, J. M. Campbell, L. Niinistö and F. Reti, *J. Electrochem. Soc.*, 1999, **146**, 189-193.

210. Y.-H. Lin, Y.-C. Hsueh, P.-S. Lee, C.-C. Wang, J. M. Wu, T.-P. Perng and H. C. Shih, *J. Mater. Chem.*, 2011, **21**, 10552-10558.

211. V. A. Sivakov, K. Höflich, M. Becker, A. Berger, T. Stelzner, K.-E. Elers, V. Pore, M. Ritala and S. H. Christiansen, *ChemPhysChem*, 2010, **11**, 1995-2000.

212. S.-W. Choi and et al., *Nanotechnology*, 2009, **20**, 465603-465608.

213. X. Du, Y. Du and S. M. George, *J. Phys. Chem. A*, 2008, **112**, 9211-9219.

214. Y.-H. Lin, P.-S. Lee, Y.-C. Hsueh, K.-Y. Pan, C.-C. Kei, M.-H. Chan, J.-M. Wu, T.-P. Perng and H. C. Shih, *J. Electrochem. Soc.*, 2011, **158**, K24-K27.

215. M. Mattmann, C. Roman, T. Helbling, D. Bechstein, L. Durrer, R. Pohle, M. Fleischer and C. Hierold, *Nanotechnology*, 2010, **21**, 185501-185509.

216. J. Y. Park, S.-W. Choi and S. S. Kim, *J. Phys. D: Appl. Phys.*, 2011, **44**, 205403-205406.

217. W.-S. Kim, B.-S. Lee, D.-H. Kim, H.-C. Kim, W.-R. Yu and S.-H. Hong, *Nanotechnology*, 2010, **21**, 245605-245611.

218. D. J. Comstock, S. T. Christensen, J. W. Elam, M. J. Pellin and M. C. Hersam, *Adv. Funct. Mater.*, 2010, **20**, 3099-3105.

219. J. T. Korhonen, P. Hiekkataipale, J. Malm, M. Karppinen, O. Ikkala and R. H. A. Ras, *ACS Nano*, 2011, **5**, 1967-1974.

220. H.-W. Ra, K.-S. Choi, J.-H. Kim, Y.-B. Hahn and Y.-H. Im, *Small*, 2008, **4**, 1105-1109.

221. B. M. Venkatesan, B. Dorvel, S. Yemenicioglu, N. Watkins, I. Petrov and R. Bashir, *Adv. Mater.*, 2009, **21**, 2771-2776.

222. B. M. Venkatesan, A. B. Shah, J.-M. Zuo and R. Bashir, *Adv. Funct. Mater.*, 2010, **20**, 1266-1275.

223. Y. Wang, S. Park, J. T. W. Yeow, A. Langner and F. Müller, *Sens. Actuators, B*, 2010, **149**, 136-142.

224. F. Raimondi, G. G. Scherer, R. Kötz and A. Wokaun, *Angew. Chem. Int. Ed.*, 2005, **44**, 2190-2209.

225. S. Haukka, E. L. Lakomaa and T. Suntola, in *Studies in Surface Science and Catalysis*, ed. A. Dabrowski, Elsevier, 1999, pp. 715-750.

226. C. Detavernier, J. Dendooven, S. Pulinthanathu Sree, K. F. Ludwig and J. A. Martens, *Chem. Soc. Rev.*, 2011, **40**, 5242-5253.

227. J. W. Elam, N. P. Dasgupta and F. B. Prinz, *MRS Bull.*, 2011, **36**, 899-906.

228. M. M. Biener, J. Biener, A. Wichmann, A. Wittstock, T. F. Baumann, M. Bäumer and A. V. Hamza, *Nano Lett.*, 2011, **11**, 3085-3090.

229. Y. W. Chen, J. D. Prange, S. Dühnen, Y. Park, M. Gunji, C. E. D. Chidsey and P. C. McIntyre, *Nat. Mater.*, 2011, **10**, 539-544.

230. J. A. Enterkin, K. R. Poeppelmeier and L. D. Marks, *Nano Lett.*, 2011, **11**, 993-997.

231. J. A. Enterkin, W. Setthapun, J. W. Elam, S. T. Christensen, F. A. Rabuffetti, L. D. Marks, P. C. Stair, K. R. Poeppelmeier and C. L. Marshall, *ACS Catal.*, 2011, **1**, 629-635.

232. H. Feng, J. W. Elam, J. A. Libera, M. J. Pellin and P. C. Stair, *J. Catal.*, 2010, **269**, 421-431.

233. H. Feng, J. W. Elam, J. A. Libera, W. Setthapun and P. C. Stair, *Chem. Mater.*, 2010, **22**, 3133-3142.

234. R. R. Hoover and Y. V. Tolmachev, *J. Electrochem. Soc.*, 2009, **156**, A37-A43.

235. I. J. Hsu, D. A. Hansgen, B. E. McCandless, B. G. Willis and J. G. Chen, *J. Phys. Chem. C*, 2011, **115**, 3709-3715.

236. M. Kemell, V. Pore, M. Ritala and M. Leskelä, *Chem. Vap. Deposition*, 2006, **12**, 419-422.

237. D. Kim, K.-D. Kim, H. Seo, N. Dey, M. Kim, Y. Kim, D. Lim and K. Lee, *Catal. Lett.*, 2011, **141**, 854-859.

238. J. S. King, A. Wittstock, J. Biener, S. O. Kucheyev, Y. M. Wang, T. F. Baumann, S. K. Giri, A. V. Hamza, M. Baeumer and S. F. Bent, *Nano Lett.*, 2008, **8**, 2405-2409.

239. J. Li, X. Liang, D. M. King, Y.-B. Jiang and A. W. Weimer, *Appl. Catal., B*, 2010, **97**, 220-226.

240. Z. Ma, S. Brown, J. Y. Howe, S. H. Overbury and S. Dai, *J. Phys. Chem. C*, 2008, **112**, 9448-9457.

241. M. J. Pellin, P. C. Stair, G. Xiong, J. W. Elam, J. Birrell, L. Curtiss, S. M. George, C. Y. Han, L. Iton, H. Kung, M. Kung and H. H. Wang, *Catal. Lett.*, 2005, **102**, 127-130.

242. J. R. Scheffe, M. D. Allendorf, E. N. Coker, B. W. Jacobs, A. H. McDaniel and A. W. Weimer, *Chem. Mater.*, 2011, **23**, 2030-2038.

243. J. H. Shim, X. Jiang, S. F. Bent and F. B. Prinz, *J. Electrochem. Soc.*, 2010, **157**, B793-B797.

244. H. Feng, J. A. Libera, P. C. Stair, J. T. Miller and J. W. Elam, *ACS Catal.*, 2011, **1**, 665-673.

245. R. Liu, Y. J. Lin, L. Y. Chou, S. W. Sheehan, W. S. He, F. Zhang, H. J. M. Hou and D. W. Wang, *Angew. Chem. Int. Ed.*, 2011, **50**, 499-502.

246. E. Ballee, A. Ringuede, M. Cassir, M. Putkonen and L. Niinistö, *Chem. Mater.*, 2009, **21**, 4614-4619.

247. C. Brahim, A. Ringuedé, M. Cassir, M. Putkonen and L. Niinistö, *Appl. Surf. Sci.*, 2007, **253**, 3962-3968.

248. M. Cassir, A. Ringuedé and L. Niinistö, *J. Mater. Chem.*, 2010, **20**, 8987-8993.

249. C.-C. Chao, C.-M. Hsu, Y. Cui and F. B. Prinz, *ACS Nano*, 2011, **5**, 5692-5696.

250. S. T. Christensen, H. Feng, J. L. Libera, N. Guo, J. T. Miller, P. C. Stair and J. W. Elam, *Nano Lett.*, 2010, **10**, 3047-3051.

251. X. R. Jiang, H. Huang, F. B. Prinz and S. F. Bent, *Chem. Mater.*, 2008, **20**, 3897-3905.

252. C.-W. Kwon, J.-W. Son, J.-H. Lee, H.-M. Kim, H.-W. Lee and K.-B. Kim, *Adv. Funct. Mater.*, 2011, **21**, 1154-1159.

253. C. Liu, C.-C. Wang, C.-C. Kei, Y.-C. Hsueh and T.-P. Perng, *Small*, 2009, **5**, 1535-1538.

254. J. S. Park, Y. B. Kim, J. H. Shim, S. Kang, T. M. Gür and F. B. Prinz, *Chem. Mater.*, 2010, **22**, 5366-5370.

255. J. H. Shim, C.-C. Chao, H. Huang and F. B. Prinz, *Chem. Mater.*, 2007, **19**, 3850-3854.

Chapter II:

Development of a low-moderate temperature SnO_2 deposition process

Contents:

A new low-moderate temperature atomic layer deposition process of tin dioxide films was developed. This approach, which is adapted from the non-hydrolytic sol-gel chemistry, permits to deposit SnO_2 at temperatures as low as 75 °C. At deposition temperature of 200 °C some initiation of crystallization can be observed. The microstructural and elemental characterizations reveal the formation of a granular film nearly free of carbon impurities having a band gap, determined by UV-visible spectroscopy, of 3.4 eV.

I. Introduction

I.1. SnO_2

Tin dioxide is a transparent and high direct band gap (~3.6 eV at 25 ºC)[1-3] n-semiconductor. It crystallizes principally into a tetragonal rutile structure, with a denser orthorhombic phase being formed at high pressures. Due to the dual valency of the Sn, i.e. Sn^{2+} and Sn^{4+}, SnO_2 can be reversibly reduced into SnO. Its electrical conductivity can be controlled by its stoichiometry and its oxygen vacancy concentration.[4] Tin dioxide is widely studied for its application e.g. as transparent conducting oxide, heterogeneous catalyst, Li-ion battery anode and solid-state gas sensor.[5] It has proven to be highly suited for the application as active layer in metal oxide semiconductor gas sensors.[6] Its electric resistance changes due to the charge carrier exchange between the adsorbed gas and the oxide surface.[7] Since the process takes place at the surface, it is crucial to have a large surface to volume ratio in order to achieve a high response.[8] Recently, many SnO_2-based nanostructures have been used for gas sensing applications.[9-11]

I.2. Deposition of SnO_2 thin films

Tin oxide thin films have been deposited onto various substrates by chemical and physical deposition processes.[12] They are currently prepared by aqueous and non-aqueous[13] sol-gel routes from tin halide,[14-16] tin alkoxide[17-20] or organotin,[21] using dip- or spin-coating. Various CVD approaches such as thermal-,[22-25] low pressure-,[26] plasma assisted-,[27, 28] induced plasma coupled,[29] laser assisted-,[30] atmospheric pressure-[31, 32] and aerosol assisted-[33] CVD are widely used with tin halides and organotin as metal precursor. Even though often high deposition temperatures are required, SnO_2 can also be prepared at room temperature e.g. by plasma enhanced CVD from tetramethyl tin.[34] The following section will describe the use of ALD to fabricate SnO_2 thin films.
Also physical deposition approaches such as pulsed laser deposition,[35-37] electron beam and thermal evaporation,[38-42] pyrolysis[40, 42-45] and sputtering[46-48] methods are also widely used to elaborate tin oxide films.

Many of the approaches used for SnO_2 thin film elaboration require a deposition temperature higher than 300 °C or are followed by a thermal treatment. By chemical and physical approaches, depending on the precursor and the deposition temperature, amorphous, crystallites embedded in an amorphous matrix, and polycrystalline films were obtained. Whenever a crystalline tin dioxide phase was synthesized, the tetragonal rutile phase was always obtained.

I.3. Atomic layer deposition of SnO_2

Thin films of tin oxide have already been deposited by ALD from tin chloride ($SnCl_4$) reacting with either water[49-53] or hydrogen peroxide[54-58] or from SnI_4 and either H_2O_2[55, 57] or O_2[28, 55, 57-59] at relatively high temperatures (180-700 °C). In order to decrease the deposition temperature and to avoid corrosive by-products and further to obtain amorphous as-deposited films, alternative pathways have been developed. An early work makes use of organotin, i.e. tetraethyl tin and tetramethyl tin, reacting with N_2O_4. Nevertheless, no low temperature deposition was achieved having ALD windows at 250-290 ºC and 400-450ºC, respectively. During the film nucleation, a participation of the substrate oxygen promotes the metal oxide growth, otherwise due to an initiation step a growth delay is noticed at the first cycles.[60] Furthermore, instead of halides, at moderate temperatures (200 ºC to 400 ºC), dibutyl tin acetate has been reacted with O_2.[61-65] Low-mild deposition temperatures were reached with an amino-tin precursor. Indeed, SnO_2 was deposited from tetrakis(ethylmethylamino)tin and oxygen plasma[66] and from tetrakis(dimethylamino)tin and water, hydrogen peroxide or ozone.[67] Recently, Gordon's group developed a low temperature approach based on a cyclic amide precursor, which reacts either with hydrogen peroxide[68] or recently with NO,[69] from 50 to 200 ºC and 130 to 250 ºC, respectively.
Often polycrystalline rutile SnO_2 is deposited. The microstructure and properties of ALD-grown epitaxial SnO_2 has been studied on α-Al_2O_3[28, 55, 57-59, 70, 71], n- and m- cut sapphire[63] and oriented TiO_2.[62] ALD processes were also applied to the coating of nanostructured and/or functional materials such as, porous silicon,[72, 73] AFM microprobes,[74] microhotplate gas sensors,[75, 76] AAO,[77] nanoparticles,[78, 79] nanowires,[80] polymer fibers,[64] CNTs[81, 82] or graphene nanosheets.[83, 84]

Considering the previously developed processes, very few low temperature approaches have been developed and involved oxygen sources with high oxidative power, such as oxygen plasma, O_3 and H_2O_2. It is certainly of interest to access SnO_2 by ALD at gentle deposition conditions, i.e. low or middle temperature (lower than 250-300 °C), low oxidative and corrosive character and low harmfulness of precursors and by-products towards the user. The successful application of a non-hydrolytic route for the deposition of titanium-, vanadium- and hafnium oxides has been reported by our group (see Chapter I).[85, 86] The use of carboxylic acids as oxygen source allows the coating

of moisture and/or oxidant sensitive substrates. During this PhD work, this approach was extended to tin dioxide.[87]

In this chapter, it will be shown that the use of a tin(IV) alkoxide and a carboxylic acid, as metal and oxygen source, is highly suitable for the deposition of tin dioxide films at temperatures as low as 75 ºC onto various substrates. The structural characterization in terms of microstructure, crystallinity and elemental composition of the as-deposited films will be presented. The SnO_2 approach presented in this chapter has also been employed for the coating of MWCNTs applied as gas sensors (cf. Chapters IV and V).

II. Reactions involved in the ALD process and methodology

The deposition of tin dioxide by a non-aqueous sol-gel route was realized in the home-made ALD reactor schematized in Figure I.13. The development of the low-mid temperature deposition of tin dioxide, presented here, is based on a reaction between a metal alkoxide and a carboxylic acid. SnO_2 was deposited from tin(IV) tetra-butoxide, $Sn(^tOBu)_4$, reacting with acetic acid following the two surface half-reactions (eq. 1 and 2).

During the acetic acid pulse, ligand exchange occurs between the surface alkoxy species and the evaporated carboxylic acid, under an alcohol elimination.

$$\equiv Sn\text{-}O^tBu + CH_3COOH \rightarrow \equiv Sn\text{-}OOCCH_3 + {}^tBuOH \qquad \text{(eq. 1)}$$

The following tin alkoxide pulse leads to an ester elimination corresponding to a condensation step with the formation of an oxo bond.

$$\equiv Sn\text{-}OOCCH_3 + Sn\text{-}O^tBu \rightarrow \equiv Sn\text{-}O\text{-}Sn\equiv + CH_3COO^tBu \qquad \text{(eq. 2)}$$

Comments on the precursors used:

Tin(IV) tetra-butoxide, is a colorless low-melting solid, moisture sensitive. Using a non-aqueous sol-gel approach, acetic acid ≥99.0% was employed and both canisters, metal and oxygen sources, were filled inside a glove box.

After proving the feasibility of the process with some preliminary films, the influence of the various parameters was scanned in order to define the ALD window of this new process. First of all, based on the typical deposition parameters for TiO_2 and HfO_2,[85, 86] thin films of SnO_2 were deposited on silicon substrates at 200 ºC, in exposure mode. In these standard conditions, the pulse durations of the oxygen and metal source, kept at 30 ºC and 80 ºC, were 0.03 s and 1 s, respectively. An exposure of 20 s and purging of 15 s were performed at each half-reaction. The ALD window was then roughly estimated and established between 175 and 200 ºC. Above 225-250

°C decomposition of the tin alkoxide occurs. A more systematic study of the ALD parameters is currently being carried out.

Although thin films were deposited at temperatures as low as 75 °C, in the following section only the films deposited at 200 °C will be presented.

III. Structural film characterizations

III.1. Microstructure of as-deposited SnO_2 thin films

Films deposited on Si wafer were characterized by X-ray reflectivity, SEM and EDS as well as AFM.

In Figure II.1, an SEM image recorded from the edge of a fractured silica wafer after depositing 22 nm thick SnO_2 during 200 ALD cycles at 200 °C is shown. As evidenced by the corresponding EDS map shown in Figure II.1b, tin is homogeneously distributed on the flat surface of the wafer.

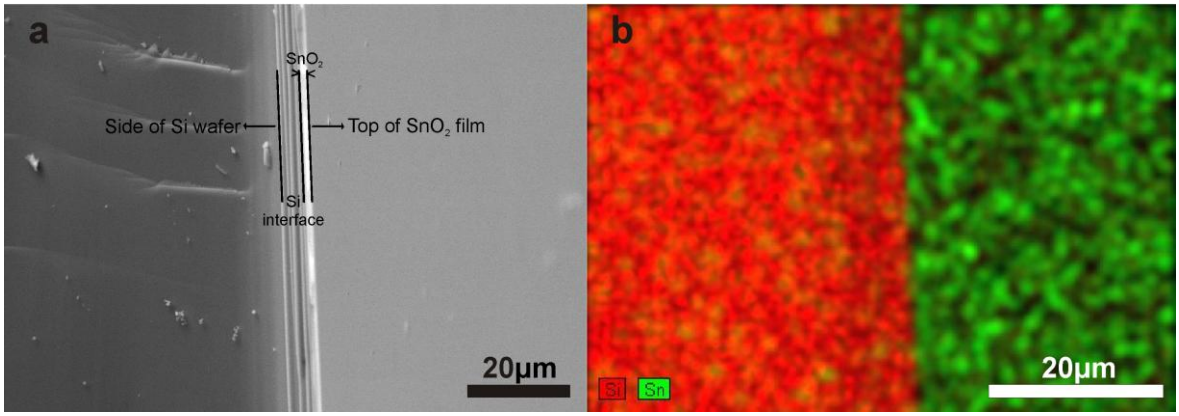

Figure II.1. a) SEM image showing the edge of a fractured silica wafer after thin film deposition. Vertical lines at the edge are due to the fracture of the wafer. b) Corresponding EDS map.

Observation in cross-section of a 120 nm thick film on a (100) Si wafer, after fracture, reveals a continuous and thickness uniform coating (Figure II.2a). At low magnification, one can notice a granular aspect confirmed in Figure II.2b at higher magnification, where small grains are visible. This observation is further confirmed by the AFM characterizations.

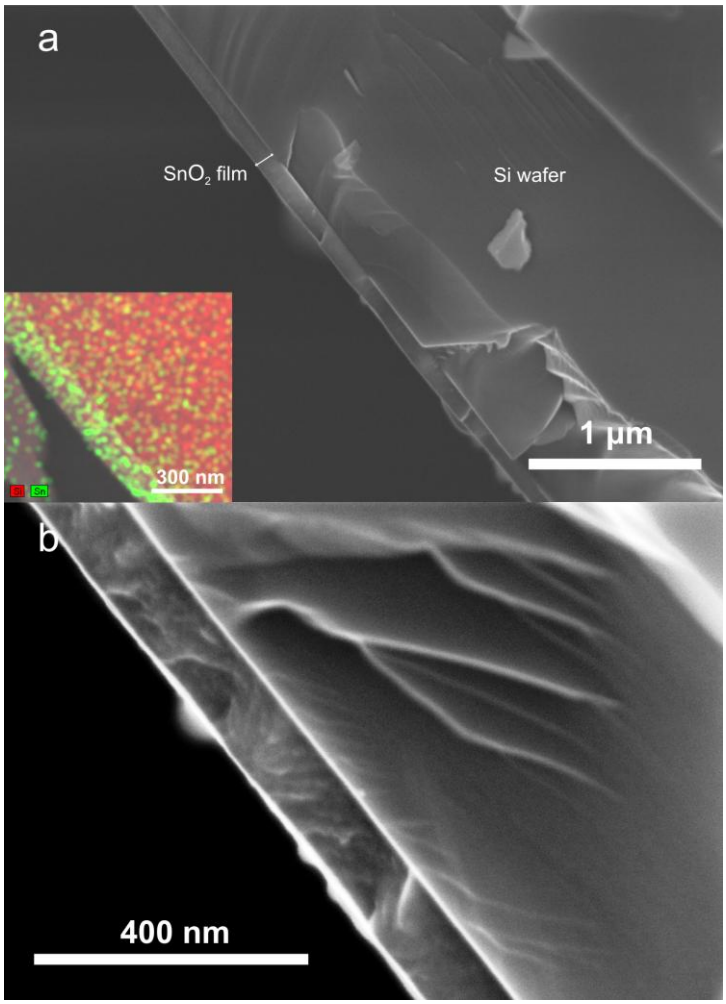

Figure II.2. Cross-section of a 120 nm thick SnO_2 film on silicon wafer, a) at low magnification, in inset the EDS map shows the presence of the film on the side. b) At higher magnification, the SEM image reveals a granular morphology of the film.

AFM images reveal a granular structure consisting of sub-10 nm nanoparticles (Figure II.3). One should take in consideration the convolution of the tip and sample leading to an over- or under-estimation of the particles diameter. The thickness of the film obtained by XRR measurements (Figure II.4) was 22 nm, therefore an average growth per cycle (GPC) of 0.11 nm can be derived. The root mean square (RMS) roughness extracted from the AFM images was around 0.40 nm. The RMS roughness of the bare Si wafer substrate (Figure II.3a) used in this work was 0.20 nm. Hence, the roughness of the deposited film is lower or equal to previous results reported for different ALD processes. For example, crystalline films formed from $SnCl_4$ and water on soda lime and corning glass substrates showed a RMS roughness of around 2-12 nm, depending on the film thickness.[71] In the case of H_2O_2 as oxygen source, amorphous films were obtained on Si wafer. Their RMS roughness was reported to range from 0.3 to 10 nm depending on the number of ALD cycles when

$SnCl_4$ was used as metal source,[54, 75] and 0.85 nm for 9.1 nm thick films grown using tetrakis(dimethylamino)tin.[67]

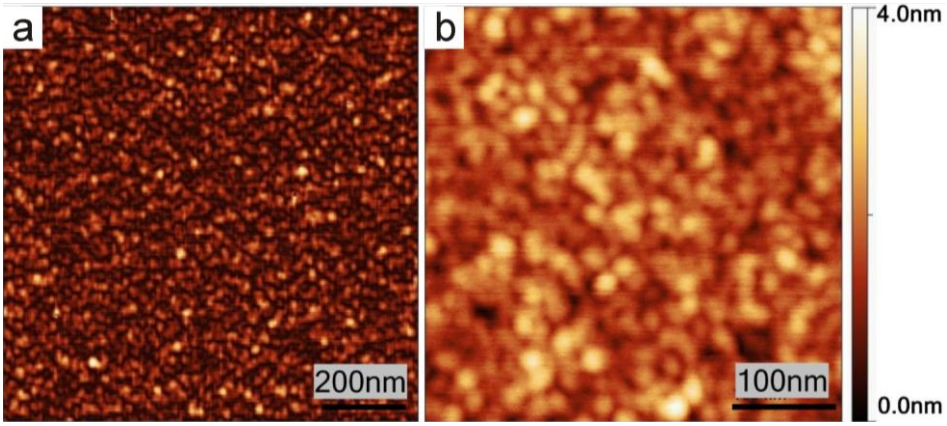

Figure II.3. Tapping mode AFM images recorded from SnO_2 thin film grown at 200 °C over an area of 1x1 µm and 400x400 nm are shown in a) and b), respectively.

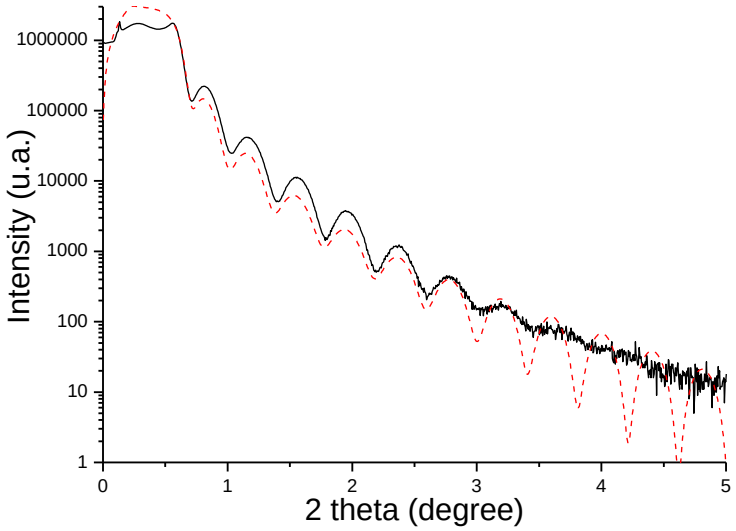

Figure II.4. XRR curve of SnO_2 films on Si wafer investigated by AFM (full black line) and the simulated curve of a film of 22 nm (dotted red line).

III.2. Crystallinity of as-deposited SnO_2

The crystalline aspect has been characterized by XRD and high-resolution TEM. On 35 nm thick SnO_2 film deposited on Si wafer, grazing incidence angle XRD (not shown) did not permit to obtain clear evidence of crystallinity. Coated carbon nanotubes (cf. chapter IV) were also investigated by electron microscopy in order to study the tin dioxide crystallinity. A particulate structure of the film is demonstrated by HRTEM images that were recorded in regions where the thickness of the supporting carbon structure is very thin. Close inspection reveals small contrast variations due to lattice fringes of nanometer sized crystalline SnO_2 particles (Figure II.5). In order

to better characterize the crystallinity of the particles, XRD patterns have been recorded on coated CNTs (not shown). Although the AFM and TEM images indicate the presence of sub-10 nm SnO_2 particles, the crystallite size appears to be insufficient to obtain diffraction peaks even with a long acquisition time. These findings can be explained by the weak and broad expected reflections of such small crystallites, which remain blended with the background. Only the HRTEM observations and Fourier filtered images show the presence of lattice fringes attributed to the rutile phase demonstrating a beginning of crystallization. The investigation of the nanocrystallinity of the film by HRTEM will be further developed more in detail in the Chapter IV, section IV.1.3.

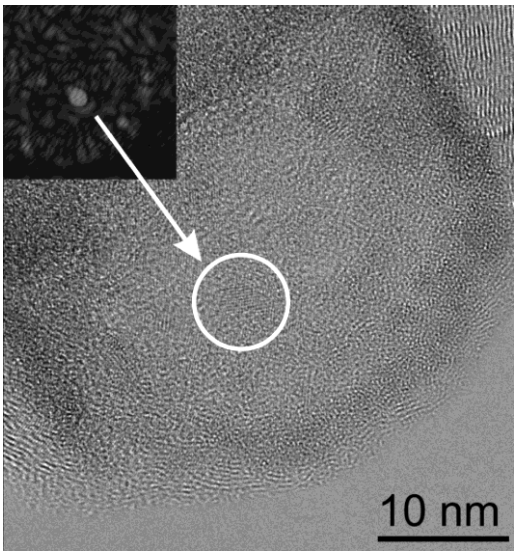

Figure II.5. In thin regions, where the background contrast due to the carbon substrate is weak, fringes of the crystalline SnO_2 nanoparticles can be observed. It is enhanced in the Fourier filtered inset of the panel, generated using the 200 d-spacing of rutile SnO_2. The deposition temperature was 200 °C.

III.3. Elemental composition of the ALD tin oxide

In order to obtain information about the elemental composition and chemical state of the film, X-ray photoelectron spectroscopy was performed. Prior to the measurements, the surface of the sample was sputter-cleaned with argon ions to remove carbon contaminations. The XPS survey spectrum obtained for the film deposited on Si wafer is shown in Figure II.6a. The spectrum is dominated by strong signals from Sn and O. A very small amount of carbon (284.6 eV), as shown in the narrow scan of C 1s (Figure II.6b), and a small quantity of silicon (99.3 eV for Si and 103.3 eV for SiO_2) can be observed. The narrow-scan XPS spectra of Sn 3d and O 1s are shown in Figures II.6c and II.6d, respectively. The Sn 3d photoelectron peaks at 487.3 eV and 495.7 eV are characteristic of Sn^{4+} in SnO_2. The O 1s peak can be divided into two peaks, which are in good agreement with the reference data and the literature.[88, 89] They correspond to the oxygen in SnO_2

(531.3 eV) and SiO_2 (532.8 eV), respectively. The small peak of SiO_2 is due to a surface oxide layer on the Si wafer. The XPS data reveal the high purity of the deposited film and demonstrate that the process results in SnO_2 that is almost free of carbon impurities.

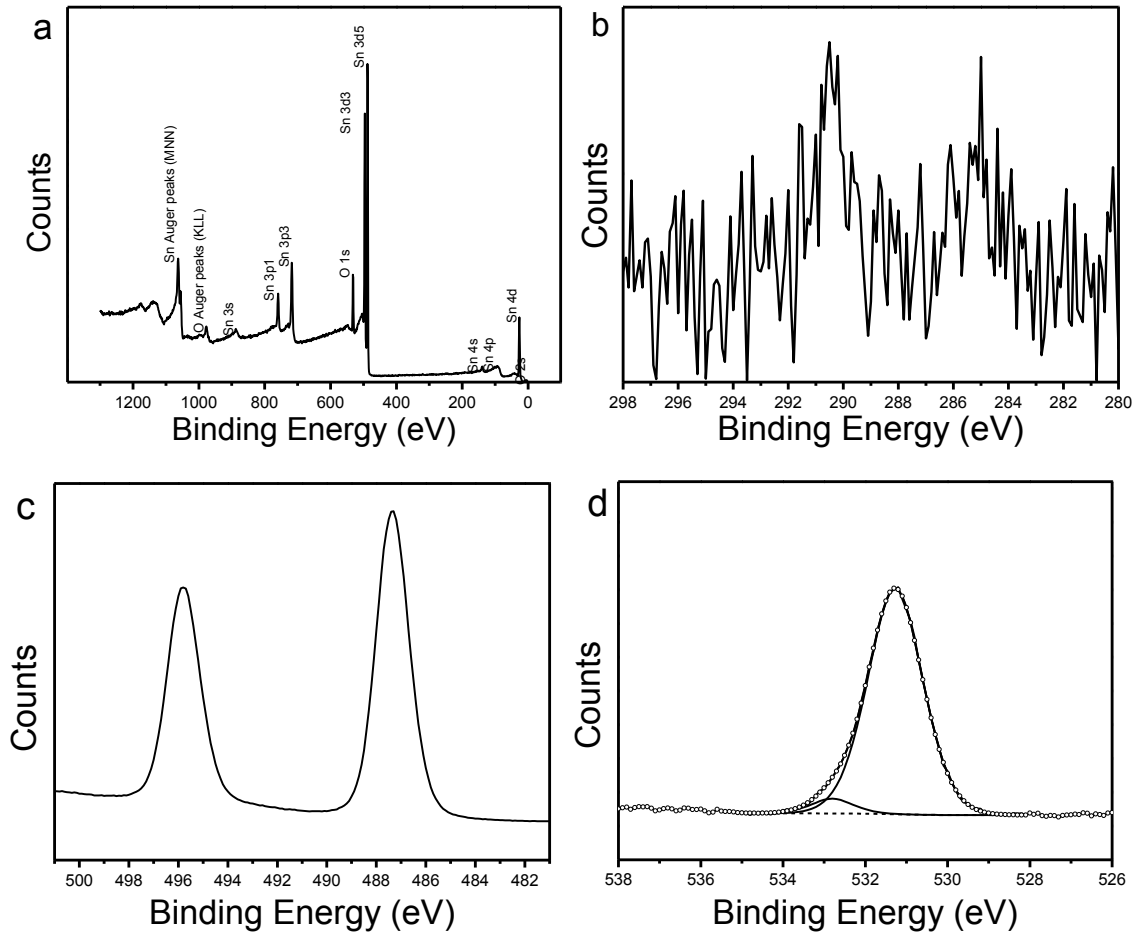

Figure II.6. XPS Spectra of the film deposited on Si wafer: a) survey scan, b) narrow scan of C 1s. c) and d) show high resolution scans across the Sn3d and O1s edges, respectively.

IV. Determination of the SnO_2 band gap

The band gap value, E_g, of the obtained SnO_2 thin film was determined using UV-Visible spectroscopy. The reflectance spectra of 30 and 120 nm thick films deposited on si wafer are shown in Figure II.7.

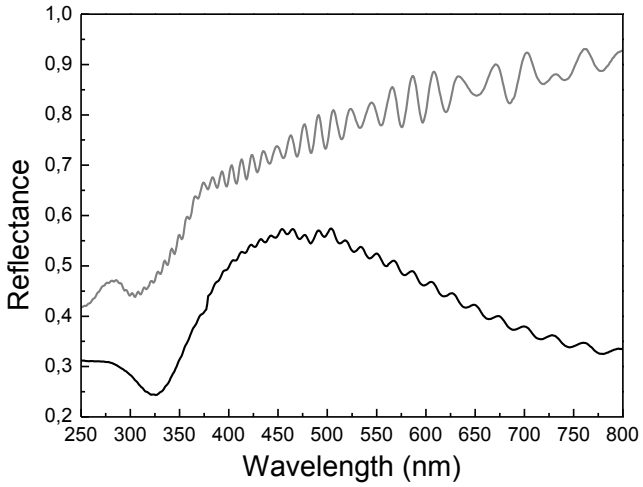

Figure II.7. UV-Visible reflectance spectra of a 30 nm (grey line) and 120 nm (black line) thick SnO_2 films on Si, after removal of the support contribution.

The presence of fringes is attributed to the interaction of the incident light with the ~2 nm-SiO_2 interface layer. An absorption between 250-400 nm is noted in both cases as well as a decrease of the reflectance for the thicker film.

Tin dioxide band gap is expected to be direct. Its value can therefore be obtained graphically by plotting $(F(R)*E)^2$ *vs.* E, where F(R) is the Kulbelka-Munk function: $F(R) = (1-R)^2/2R$, R being the reflectance value.[90] The E_g value is determined at the intersection of the linear fit with the energy axis for 0 coordinate. In fact, this method is valid for infinitely thick samples. However, by dividing the measured reflectance spectra of the supported film by reference spectra (as realized in Figure II.7), the support reflectance contribution is considered being sufficiently reduced.

The E_g extracted for the reflectance transformations, shown in Figure II.8, is 3.4 eV for both films. This value seems realistic, while slightly lower than the theoretical value for the SnO_2 bulk (3.6 eV). This could be explained by the dominant amorphous phase of the ALD tin dioxide and probably its lower compactness.

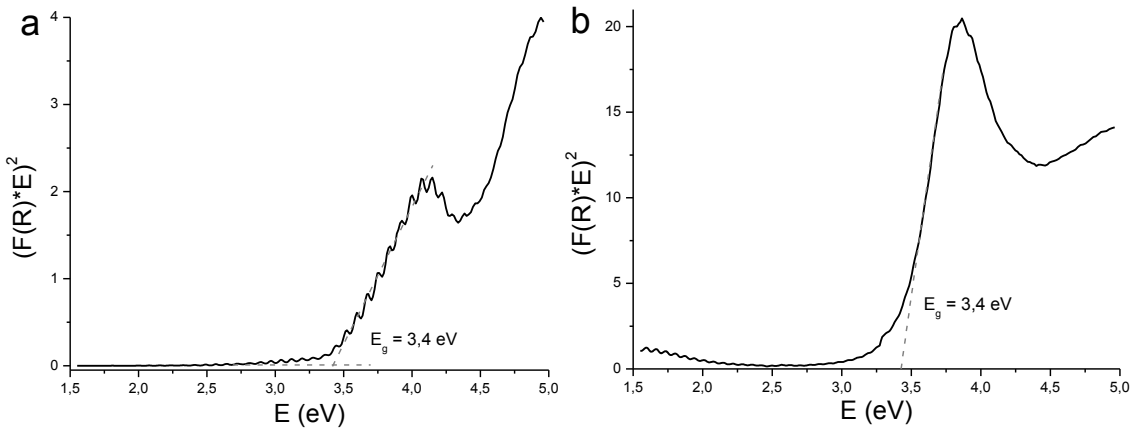

Figure II.8. Kulbelka-Munk transformed reflectance spectra and their linear fits for a) 30 nm and b) 120 nm SnO_2 thin films.

V. Conclusions

In this work, a novel ALD process for the deposition of nanocrystalline films of SnO_2 at low and moderate temperature is reported. Indeed, tin dioxide has been deposited at temperatures as low as 75 °C. The process is based on the reaction of tin(IV) tert-butoxide with acetic acid as metal and oxygen sources, respectively. The as-deposited films show a granular like structure composed of nanoparticles that measure few nanometers in diameter only. The presence of small crystallites embodied into an amorphous phase is noticed demonstrating a starting crystallization. The SnO_2 presents some crystalline rutile phase and is almost carbon free. Finally, the as-deposited SnO_2 shows a band gap of 3.4 eV, slightly lower than the theoretical band gap of the bulk metal oxide.
The implementation of this novel method for the elaboration of SnO_2@CNTs heterostructures will be described in Chapter IV.

VI. Experimental part

SnO_2 deposition

Tin dioxide was deposited on (100) silicon wafer and carbon nanotubes (Applied Science PR-24-PS, unfunctionalized and functionalized). Tin tert-butoxide (99.99% PURATREM, STREM and ≥99.99%, Aldrich) and acetic acid (Purum ≥99.0%, Fluka) were used as metal and oxygen precursors, respectively. The depositions took place between 75 °C and 250 °C in an exposure mode reactor. Metal precursor and carboxylic acid were introduced subsequently by pneumatic

ALD valves from their reservoirs, which were kept at 80 and 30 ºC, respectively. For the deposition, pure nitrogen was used as a carrier gas at a constant flow rate of 5 sccm. The ALD valves opened for 0.03 and 1 s for the oxygen source and tin precursor, respectively. The residence time after each precursor pulse was set to 20 s, followed by a nitrogen purge during 15 s.

Characterizations of the as-deposited film

The thickness of the as-deposited tin oxide films on the wafer substrates were measured by XRR using a Philips X'Pert MRD X-ray diffractometer with copper radiation and a graphite monochromator for the selection of pure Kα radiation. The X-ray tube was operated at 40 kV and 50 mA. A 1 mm slit was used in order to reduce the scattered X-ray intensity. Measurements were performed in low-resolution experimental set up with the following instrumental configuration: divergence slit at the incident beam: 1/8 in.; step width: 0.005°; acquisition time: 1 s. XRD characterization of films on Si wafer and CNTs (not shown) was performed with a Philips X'Pert MRD X'ray diffractometer (Cu Kα radiation at 40 kV and 50 mA) and in transmission mode on a STOE STADI MP equipped with IP-PSD image plate detector (Co Kα radiation), respectively. Using the high-resolution TEM, JEOL JEM220FS microscope, diffraction patterns were recorded on the coated CNTs to investigate the crystallinity of the SnO_2 coating. Coated wafers were further analyzed by SEM and EDS using a SU-70 (Hitachi) microscope equipped with a Bruker silicon drift detector. The surface morphology was studied by AFM in tapping mode using a commercial NSG 10 tip (tip curvature radius 10 nm guaranteed) with a constant force of 12 $N.m^{-1}$ and a resonant frequency of 220 kHz. The XPS experiments were performed on thick films in an UHV multipurpose surface analysis system (SIGMA PROBE, ThermoFisher Scientific, UK) operating at base pressures $<10^{-10}$ mbar. The photoelectron spectra were excited by an Al Kα (1486.6 eV) anode operating at constant power of 100 W (15 kV and 10 mA). During the spectra acquisition, the constant analyzer energy (CAE) mode was employed at a pass energy of 30 eV and a step of 0.1 eV. The sputtering process was carried out in the analysis chamber, using an argon ion sputtering gun at normal incidence. The etching process was performed using an argon ion beam (accelerating voltage 2 keV and 1 mA). UV-visible absorption spectra were recorded at room temperature, using a dual beam spectrophotometer Lambda 950, Perkin Elmer, with a 150 nm diameter integrating sphere. Spectra of thin film of 120 and 30 nm SnO_2 on Si wafer were recorded.

VII. References

1. P. Barbarat, S. F. Matar and G. Le Blevennec, *J. Mater. Chem.*, 1997, **7**, 2547-2550.
2. D. Fröhlich, R. Kenklies and R. Helbig, *Phys. Rev. Lett.*, 1978, **41**, 1750-1751.
3. K. G. Godinho, A. Walsh and G. W. Watson, *J. Phys. Chem. C*, 2009, **113**, 439-448.
4. C. X. Wang, L. W. Yin, L. Y. Zhang, D. Xiang and R. Gao, *Sensors*, 2010, **10**, 2088-2106.
5. M. Batzill and U. Diebold, *Prog. Surf. Sci.*, 2005, **79**, 47-154.
6. W. Gopel and K. D. Schierbaum, *Sens. Actuators, B*, 1995, **26**, 1-12.
7. V. Dermane and R. Sanjine, in *Gas sensors*, ed. G. Sberveglieri, Kluwer Academic Publishers, Netherlands, 1992, pp. 89-116.
8. P. Ivanov, E. Llobet, X. Vilanova, J. Brezmes, J. Hubalek and X. Correig, *Sens. Actuators, B*, 2004, **99**, 201-206.
9. A. Kolmakov, Y. Zhang, G. Cheng and M. Moskovits, *Adv. Mater.*, 2003, **15**, 997-1000.
10. M. Law, H. Kind, B. Messer, F. Kim and P. Yang, *Angew. Chem. Int. Ed.*, 2002, **41**, 2405-2408.
11. F. Li, J. Xu, X. Yu, L. Chen, J. Zhu, Z. Yang and X. Xin, *Sens. Actuators, B*, 2002, **81**, 165-169.
12. G. Sberveglieri, *Sens. Actuators, B*, 1992, **6**, 239-247.
13. M. Niederberger, G. Garnweitner, J. Buha, J. Polleux, J. H. Ba and N. Pinna, *J. Sol-Gel Sci. Technol.*, 2006, **40**, 259-266.
14. J. Ba, J. Polleux, M. Antonietti and M. Niederberger, *Adv. Mater.*, 2005, **17**, 2509-2512.
15. R. Rella, A. Serra, P. Siciliano, L. Vasanelli, G. De, A. Licciulli and A. Quirini, *Sens. Actuators, B*, 1997, **44**, 462-467.
16. D. Torres Martínez, R. Castanedo Pérez, G. Torres Delgado and O. Zelaya Angel, *J. Mater. Sci.:Mater. Electron.*, 2011, **22**, 684-689.
17. J. C. Giuntini, W. Granier, J. V. Zanchetta and A. Taha, *J. Mater. Sci. Lett.*, 1990, **9**, 1383-1388.
18. S.-S. Park and J. D. Mackenzie, *Thin Solid Films*, 1996, **274**, 154-159.
19. N. Pinna, G. Neri, M. Antonietti and M. Niederberger, *Angew. Chem. Int. Ed.*, 2004, **43**, 4345-4349.
20. S. de Monredon, A. Cellot, F. Ribot, C. Sanchez, L. Armelao, L. Gueneau and L. Delattre, *J. Mater. Chem.*, 2002, **12**, 2396-2400.
21. T. Liu, Z. Jin, J. Yang and L. Feng, *J. Am. Ceram. Soc.*, 2008, **91**, 1939-1944.
22. V. Caslavsk and R. Roy, *J. Appl. Phys.*, 1969, **40**, 3414.
23. J. Kane, H. P. Schweizer and W. Kern, *J. Electrochem. Soc.*, 1975, **122**, 1144-1149.
24. S. Mathur, V. Sivakov, H. Shen, S. Barth, C. Cavelius, A. Nilsson and P. Kuhn, *Thin Solid Films*, 2006, **502**, 88-93.
25. J. Sundqvist, M. Ottosson and A. Harsta, *Chem. Vap. Deposition*, 2004, **10**, 77-82.
26. C. F. Wan, R. D. McGrath, W. F. Keenan and S. N. Frank, *J. Electrochem. Soc.*, 1989, **136**, 1459-1463.

27. H. Natsuhara, T. Tatsuyama, M. Ushiro, M. Furuhashi, T. Fujii, F. Ohashi, N. Yoshida and S. Nonomura, *Thin Solid Films*, 2011, **519**, 4538-4541.

28. J. Sundqvist, J. Lu, M. Ottosson and A. Harsta, *Thin Solid Films*, 2006, **514**, 63-68.

29. H. Y. Lee, J. N. Kim, H. Kim, D. S. Jang and J. J. Lee, *Thin Solid Films*, 2008, **516**, 3538-3543.

30. J. Lancok, A. Santoni, M. Penza, S. Loreti, I. Menicucci, C. Minarini and M. Jelinek, *Surf. Coat. Technol.*, 2005, **200**, 1057-1060.

31. C. G. Borman and R. G. Gordon, *J. Electrochem. Soc.*, 1989, **136**, 3820-3828.

32. I. Volintiru, A. de Graaf, J. van Deelen and P. Poodt, *Thin Solid Films*, 2011, **519**, 6258-6263.

33. J. Zhao, S. Wu, J. Liu, H. Liu, S. Gong and D. Zhou, *Sens. Actuators, B*, 2010, **145**, 788-793.

34. D. S. Wavhal, S. Goyal and R. B. Timmons, *Chem. Mater.*, 2009, **21**, 4442-4447.

35. R. Dolbec, M. A. El Khakani, A. M. Serventi, M. Trudeau and R. G. Saint-Jacques, *Thin Solid Films*, 2002, **419**, 230-236.

36. R. Khandelwal, A. P. Singh, A. Kapoor, S. Grigorescu, P. Miglietta, N. E. Stankova and A. Perrone, *Opt. Laser Technol.*, 2009, **41**, 89-93.

37. S. K. Sinha, R. Bhattacharya, S. K. Ray and I. Manna, *Mater. Lett.*, 2011, **65**, 146-149.

38. P. Koshy, J. T. Abraham, P. S. Mukherjee and V. K. Vaidyan, *Phys. Status Solidi A*, 1997, **161**, 399-405.

39. M. H. Madhusudhana Reddy and A. N. Chandorkar, *Sens. Actuators, B*, 1992, **9**, 1-8.

40. S. H. Park, Y. C. Son, W. S. Willis, S. L. Suib and K. E. Creasy, *Chem. Mater.*, 1998, **10**, 2389-2398.

41. P. Parreira, J. Valente, G. Lavareda, C. Nunes de Carvalho, A. R. Ramos, E. Alves, P. Brogueira and A. Amaral, *Phys. Status Solidi A*, 2008, **205**, 1957-1960.

42. K. S. Shamala, L. C. S. Murthy and K. N. Rao, *Bull. Mater. Sci.*, 2004, **27**, 295-301.

43. G. Korotcenkov, V. Brinzari, J. Schwank, M. DiBattista and A. Vasiliev, *Sens. Actuators, B*, 2001, **77**, 244-252.

44. G. Korotcenkov, M. DiBattista, J. Schwank and V. Brinzari, *Mater. Sci. Eng., B*, 2000, **77**, 33-39.

45. D. Perednis and L. J. Gauckler, *J. Electroceram.*, 2005, **14**, 103-111.

46. H. P. Hübner and E. Obermeier, *Sens. Actuators*, 1989, **17**, 351-354.

47. R. Kohler, H. Besser, M. Hagen, J. Ye, C. Ziebert, S. Ulrich, J. Proell and W. Pfleging, *Microsyst. Technol.*, 2011, **17**, 225-232.

48. T. Suzuki, T. Yamazaki, H. Yoshioka, K. Takahashi and T. Kageyama, *J. Mater. Sci. Lett.*, 1987, **6**, 437-438.

49. R. Matero, A. Rahtu, M. Ritala, M. Leskelä and T. Sajavaara, *Thin Solid Films*, 2000, **368**, 1-7.

50. T. Takeuchi, K. Shoji, T. Tadano, I. Doteshita and S. Onodera, *Thin Solid Films*, 2003, **442**, 98-101.

51. A. Tarre, A. Rosental, V. Sammelselg and T. Uustare, *Appl. Surf. Sci.*, 2001, **175**, 111-116.

52. M. Utriainen, K. Kovacs, J. M. Campbell, L. Niinistö and F. Reti, *J. Electrochem. Soc.*, 1999, **146**, 189-193.

53. H. Viirola and L. Niinistö, *Thin Solid Films*, 1994, **249**, 144-149.

54. X. Du, Y. Du and S. M. George, *J. Vac. Sci. Technol., A*, 2005, **23**, 581-588.

55. J. Lu, J. Sundqvist, M. Ottosson, A. Tarre, A. Rosental, J. Aarik and A. Harsta, *J. Cryst. Growth*, 2004, **260**, 191-200.

56. G. Natarajan and D. Cameron, *Appl. Phys. A*, 2009, **95**, 621-627.

57. A. Rosental, A. Tarre, A. Gerst, J. Sundqvist, A. Harsta, A. Aidla, J. Aarik, V. Sammelselg and T. Uustare, *Sens. Actuators, B*, 2003, **93**, 552-555.

58. A. Tarre, A. Rosental, A. Aidla, J. Aarik, J. Sundqvist, A. Hårsta, *Vacuum*, 2002, **67**, 571-575.

59. A. Tarre, A. Rosental, J. Sundqvist, A. Harsta, T. Uustare and V. Sammelselg, *Surf. Sci.*, 2003, **532**, 514-518.

60. V. E. Drozd and V. B. Aleskovski, *Appl. Surf. Sci.*, 1994, **82-83**, 591-594.

61. G. Choi, L. Satyanarayana and J. Park, *Appl. Surf. Sci*., 2006, **252**, 7878-7883.

62. D. H. Kim, W.-S. Kim, S. B. Lee and S.-H. Hong, *Sens. Actuators, B*, 2010, **147**, 653-659.

63. D. H. Kim, J.-H. Kwon, M. Kim and S.-H. Hong, *J. Cryst. Growth*, 2011, **322**, 33-37.

64. W.-S. Kim, B.-S. Lee, D.-H. Kim, H.-C. Kim, W.-R. Yu and S.-H. Hong, *Nanotechnology*, 2010, **21**, 245605-245611.

65. W. Lee, K. Hong, Y. Park, N. H. Kim, Y. Choi and J. Park, *Electron. Lett.*, 2005, **41**, 475-477.

66. W.-S. Choi, *Trans. Electr. Electron. Mater.*, 2009, **10**, 200-202.

67. J. W. Elam, D. A. Baker, A. J. Hryn, A. B. F. Martinson, M. J. Pellin and J. T. Hupp, *J. Vac. Sci. Technol., A*, 2008, **26**, 244-252.

68. J. Heo, A. S. Hock and R. G. Gordon, *Chem. Mater.*, 2010, **22**, 4964–4973.

69. J. Heo, S. B. Kim and R. G. Gordon, *J. Mater. Chem.*, 2012, **22**, 4599-4602.

70. T. Takeuchi, I. Doteshita and S. Asami, *Surf. Interface Anal.*, 2004, **36**, 1133-1135.

71. M. Utriainen, H. Lattu, H. Viirola, L. Niinistö, R. Resch and G. Friedbacher, *Mikrochim. Acta*, 2000, **133**, 119-123.

72. C. Ducso, N. Q. Khanh, Z. Horvath, I. Barsony, M. Utriainen, S. Lehto, M. Nieminen and L. Niinistö, *J. Electrochem. Soc.*, 1996, **143**, 683-687.

73. M. Utriainen, S. Lehto, L. Niinistö, C. Ducso, N. Q. Khanh, Z. E. Horvath, I. Barsony and B. Pecz, *Thin Solid Films*, 1997, **297**, 39-42.

74. M. Utriainen, L. Niinistö and R. Matero, *Appl. Phys. A*, 1999, **68**, 339-342.

75. X. Du and S. M. George, *Sens. Actuators, B*, 2008, **135**, 152-160.

76. A. J. Niskanen, A. Varpula, M. Utriainen, G. Natarajan, D. C. Cameron, S. Novikov, V.-M. Airaksinen, J. Sinkkonen and S. Franssila, *Sens. Actuators, B*, 2010, **148**, 227-232.

77. X. Meng, Y. Zhang, S. Sun, R. Li and X. Sun, *J. Mater. Chem.*, 2011, **21**, 12321-12330.

78. X. Du, Y. Du and S. M. George, *J. Phys. Chem. A*, 2008, **112**, 9211-9219.

79. J. D. Ferguson, K. J. Buechler, A. W. Weimer and S. M. George, *Powder Technol.*, 2005, **156**, 154-163.

80. K. Baek, C. Jin, J. Lee, B.-Y. Jeong, W. Lee and C. Lee, *J. Mater Sci.*, 2010, **45**, 3851-3857.

81. Y. Chen, J. Wang, X. Meng, Y. Zhong, R. Li, X. Sun, S. Ye and S. Knights, *Int. J. Hydrogen Energy*, 2011, **36**, 11085-11092.

82. X. Meng, Y. Zhong, Y. Sun, M. N. Banis, R. Li and X. Sun, *Carbon*, 2011, **49**, 1133-1144.

83. X. Li, X. Meng, J. Liu, D. Geng, Y. Zhang, M. N. Banis, Y. Li, J. Yang, R. Li, X. Sun, M. Cai and M. W. Verbrugge, *Adv. Funct. Mater.*, 2012, **22**, 1647-1654.

84. X. Meng, D. Geng, J. Liu, M. N. Banis, Y. Zhang, R. Li and X. Sun, *J. Phys. Chem. C*, 2010, **114**, 18330-18337.

85. E. Rauwel, G. Clavel, M. G. Willinger, P. Rauwel and N. Pinna, *Angew. Chem. Int. Ed.*, 2008, **47**, 3592-3595.

86. E. Rauwel, M. G. Willinger, F. Ducroquet, P. Rauwel, I. Matko, D. Kiselev and N. Pinna, *J. Phys. Chem. C*, 2008, **112**, 12754-12759.

87. C. Marichy, N. Donato, M.-G. Willinger, M. Latino, D. Karpinsky, S.-H. Yu, G. Neri and N. Pinna, *Adv. Funct. Mater.*, 2011, **21**, 658-666.

88. M. Fuchs, D. Breitenstein, M. Fartmann, T. Grehl, S. Kayser, R. Koester, R. Ochs, S. Schlabach, D. V. Szabó and M. Bruns, *Surf. Interface Anal.*, 2010, **42**, 1131-1134.

89. J. F. Moulder, W. F. Stickle, P. E. Sobol, K. D. Bomben and J. J. Chastain; R. C. King, *Handbook of X-ray Phooelectron Spectroscopy* Eden Prairie, Minn., 1995.

90. R. S. Weber, *J. Catal.*, 1995, **151**, 470-474.

Chapter III:

ALD coating of films made of nanoparticles: proof of the process robustness

Contents:

Non-aqueous ALD was applied to the controlled coating of film made of particles. Using Langmuir-Blodgett technique, periodic 3-dimensional materials made of mono-dispersed silica particles were elaborated. The obtained opal was further accurately infiltrated by TiO_2 ALD.
Combining both electromagnetic simulations and experiments, it will be shown that the photonic pseudo band gap (PPBG) exhibited by a silica opal can be fully controlled by ALD of titania into the pores of the silica spheres constituting the opals. Different types of opals were assembled by the Langmuir–Blodgett (LB) technique: homogeneous closed packed structures set up of, respectively, 260 and 285 nm silica spheres, as well as opal heterostructures consisting of a monolayer of 430 nm silica spheres embedded within 10 layers of 280 nm silica spheres. For the stepwise infiltration of the opals with titania, titanium isopropoxide and acetic acid were used as metal and oxygen sources, in accordance with the non-aqueous approach to ALD published by our group. A shift of the direct PPBG, its disappearance, and the subsequent appearance and shifting of the inverse PPBG are observed as the opal is progressively filled. The close agreement between simulated and experimental results is striking, and promising in terms of predicting the properties of advanced photonic materials. This work demonstrates that the ALD process used is rather robust and can be applied to the coating and the elaboration of complex nanostructures.

I. Introduction

I.1. General consideration on opals and photonic crystals

Opals are densely packed periodic 3D materials which can be found in nature. Made of silica particles, natural opals are considered as gemstone due to their particular iridescence property, which is due to the interaction between the periodic low and high dielectric function (or refractive index) of the macroscopic material and the light, obeying to the Bragg law. Artificial opals can be considered as self-assembled colloidal crystals, presenting a dense packing,[1] typically face centered cubic (fcc) or hexagonal compact packing (hcp) lattices. They are of interest due to their particular optical properties, i.e. the inhibition of spontaneous emission rate and the strong localization of light,[2] and constitute then a typical example of photonic crystals (PC). A number of reviews report the characteristics, synthesis and application of these photonic structures.[1, 3-9]
The works of John[10] and Yablonovitch[11] set the ground for the scientific interest in photonic crystal structures and the study of their optical properties. The development of materials that are characterized by a periodically varying index of refraction enables improved control over the generation and propagation of light. Indeed, as in a crystal lattice where electron waves interfere with the periodic potential, electromagnetic waves interfere with the periodic dielectric function of

the PC material.[6, 12] Reflection of light by the photonic structure, as shown in Figure III.1, occurs following the Bragg's law, combined with Snell's law.[1] Bragg-Snell law along the [111] direction is defined by the relationship:

$$\lambda_{Bragg} = 2d_{111}\sqrt{\left(n_{eff}^2 - \sin^2\theta\right)}$$

where λ_{Bragg} is the Bragg peak, d_{111} the distance separating the [111] plane, equal to $d_{111} = \sqrt{2/3}D$ in case of a dielectric sphere of a diameter D, θ is the incident angle and finally n_{eff} is the effective refractive index, defined by the refractive indexes of the opal material and air and to the volume fraction of the opal, f, by the relationship: $n_{eff} = \sqrt{\left(fn_{opal}^2 + (1-f)n_{air}^2\right)}$.

For a certain energy range called stop band or photonic band gap (PBG), electromagnetic waves propagation is forbidden. The energy band structure is governed by the Floquet-Bloch theorem.[13]

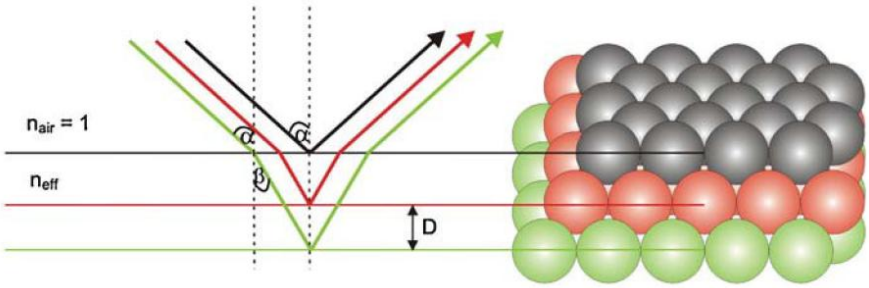

Figure III.1. Scheme of the optical path of incident light in an opal. Reproduced from Ref.[1].

The unique characteristics, i.e. the formation and directionality of the PBGs, can be manipulated in order to control the amount of losses in optical circuits and spontaneous emission. The engineering of a full PBG requires a periodic and high refractive index contrast in all (3D) spatial directions. PCs based on the infiltration and inversion of direct opals have been shown to be promising structures,[14-16] and a full PBG at infrared frequencies has been obtained in silicon inverse opals.[17, 18] Recently, it was shown that topological tuning, obtained by shifting the distribution and filling fraction of the high-index dielectric material through advanced architectures, such as multilayered inverse opals and non-close-packed (NCP) inverse opals,[19-25] can significantly change the photonic band properties.

I.2. Atomic layer deposition applied to inverse opal

Opal infiltration was motivated by the modification of the refractive index contrast of the original structure by its filling with high refractive index material to tune its optical properties. The structure presents some voids that can be homogeneously coated and filled leading to the tuning of the effective index contrast. Inverse opal elaboration has been achieved by several groups, using for

instance impregnation, sol-gel technique[26-29] or chemical vapor deposition.[17, 29-36] The group of López demonstrated the high suitability of the CVD technique for opal infiltration among other by ZnO,[32, 34] and VO_2[37] by tuning the PBG position as a function of the metal oxide deposited. A good agreement between theory and experiments was observed indeed in the case of polystyrene opals infiltrated with ZnO.[34] Due to its high accuracy and versatility, ALD appears as a technique of choice for inverse opal elaboration. It has already proven to be a suitable technique for the deposition of conformal films with submonolayer control, allowing one to reach filling fractions as good as 88% of the pore volume.[22-24, 38-40] A recent book chapter reviews the ALD application to the inverse opal fabrication.[2]

Rugge *et al.*[22] reported the first use of ALD for the formation of inverse opal, by infiltrating silica opal by WN ALD. In the same year, King *et al.*[41, 42] published the infiltration of silica opal with ZnS doped Mn. After this early work, they demonstrated the flexibility of the ALD by the opal infiltration with TiO_2[24, 43] and specially by the elaboration of ZnS:Mn/TiO_2 multilayer inverse opal.[44, 45] Reflectance UV-Visible spectra were recorded in order to follow the shift and disappearance / reappearance of the pseudo band gap.[24] Summers, King, Graugnard *et al.* brought a very important contribution to ALD applied to photonic crystals.[46-48] Indeed, using a sacrificial layer between the high refractive index material and the opal permits the obtaining of non-closed packed inverse opal.[23, 49, 50] Graugnard *et al.*[50] reported the coating of synthetic opal by either ZnS or Al_2O_3, acting as a buffer layer, prior to TiO_2 or ZnS ALD deposition, respectively. By etching, inverted opal are obtained and infiltrated once more by ALD. Simultaneously GaP inverse opal has as well been elaborated by ALD infiltration of silica opal. A high filling fraction of the deposited material was obtained.[51] ALD approach was also extended to various materials, as Ta_3N_5,[52] ZnO,[53-56] GaAs[57, 58] and W.[59] Infiltration of silica opal by Al_2O_3 ALD was used as a model system for PC, proving the well suitability of the technique. The high quality of the ALD infiltration was highlighted by the good agreement between the experimental and simulated optical behavior, i.e. shift and intensity modification of the Bragg peak function of the filling ratio.[40] Recently, opals were used as high aspect ratio templates to study the step coverage of a stop-flow TiO_2 ALD process, using $TiCl_4$ and H_2O as precursors. The filling fraction was determined from the PBG position.[60]

Finally, the tailoring of pore size and architecture of inverse opal were realized by Alessandri *et al.* After infiltration of polystyrene opal with CeO_2, and removal of the template, TiO_2 ALD was performed in order to tune the pores of the obtained inverse opal.[61]

These ALD elaborated heterostructures have found a wide range of application such as in dye sensitized solar cell,[62-64] solar cell,[38, 65] photocatalysis,[66] electrochromic photonic material[67] and surface enhanced Raman spectroscopy.[68-70]

In order to demonstrate the robustness of our ALD approach, the conformal coating of high aspect ratio substrates, such as films of nanoparticles, was realized. By combining a solution approach for the assembly of nanoparticles (Langmuir-Blodgett technique) with ALD, well calibrated particle thin film heterostructures have been elaborated. Indeed, homogeneous mono- or multi-layers of particles can be deposited on flat substrates by LB and subsequently homogeneously coated with a metal oxide by ALD. While the complete GaAs ALD infiltration of a LB engineered silica opal was already reported by Povey *et al*.,[57] the combination of the layer by layer Langmuir–Blodgett deposition method for the production of complex photonic crystals (e.g., opals containing defect layers)[71-73] with the subsequent and progressive coating of the nanostructure by ALD was not reported until the work presented in this manuscript.[74] In this context, the controlled infiltration of opals with TiO_2 and the precise tuning of their optical properties will be demonstrated. Combining both electromagnetic simulations and experiments, we showed that the PPBG exhibited by a silica opal can be fully controlled by ALD of titania into the pores formed by the silica spheres constituting the opal. The infiltration was applied to silica opals, deposited using the Langmuir-Blodgett technique, made of 260 and 285 nm silica spheres, and to heterostructures made of two stacks of 5 layers of 280 nm silica particles surrounding a defect layer constituted by a monolayer of 430 nm silica particles. With this work, realized in collaboration with Prof. Serge Ravaine (opal elaboration) and Dr. Renaud Vallée (simulations) at the CRPP in Bordeaux, France, the ALD process was demonstrated to be rather robust and suitable for the coating and elaboration of complex nanostructures. The fabrication of structured nanomaterials by ALD infiltration of such photonic crystals will be briefly introduced.

II. Tuning of the opal band gap by controlled ALD TiO_2 infiltration

The infiltration of silica opals was achieved by ALD using titanium isopropoxide and acetic acid as precursors.[74] The opals were synthesized with the LB technique, in Bordeaux, France. In the first set of experiments, simple opals made of either 5 or 10 layers of uniform sized particles, were investigated. In a second set, once the infiltration was optimized, opals containing one layer of defects embodied in a sandwich structure (5 layers, one defect layer, 5 layers) were studied.
The progressive infiltration was realized by steps of 1.2 nm and between each deposition the UV-Visible spectrum of the opal was recorded in order to follow the evolution of the optical properties and to highlight the high accuracy of our ALD process.

II.1. Case of silica opals without defects

II.1.1. Infiltration of the opals

Opals made of 5 and 10 layers of 260 and 285 nm diameter SiO_2 particles, respectively, were infiltrated by titania. Figure III.2a shows the SEM image of a monolayer of the infiltrated SiO_2 opals. A small amount of opal being taken and deposited onto a SEM holder revealed that the opal structure is not fully retained, which explains the large voids visible between the particles. Nevertheless, from this top view, interspaces between SiO_2 spheres appear almost completely filled. Almost no interstitials between the spheres (bright contrast in the image) can be noticed, being a sign of an effective and nearly complete infiltration of the opal. After silica removal, the TiO_2 inverse opal structure was recovered. The SEM top view (Figure III.2b) shows the presence of periodically aligned monodisperse pores, corresponding to the dark circles in the image. This typical porous arrangement, according to reference[75], can be correlated to a shell structure backfilling morphology of the fcc lattice.

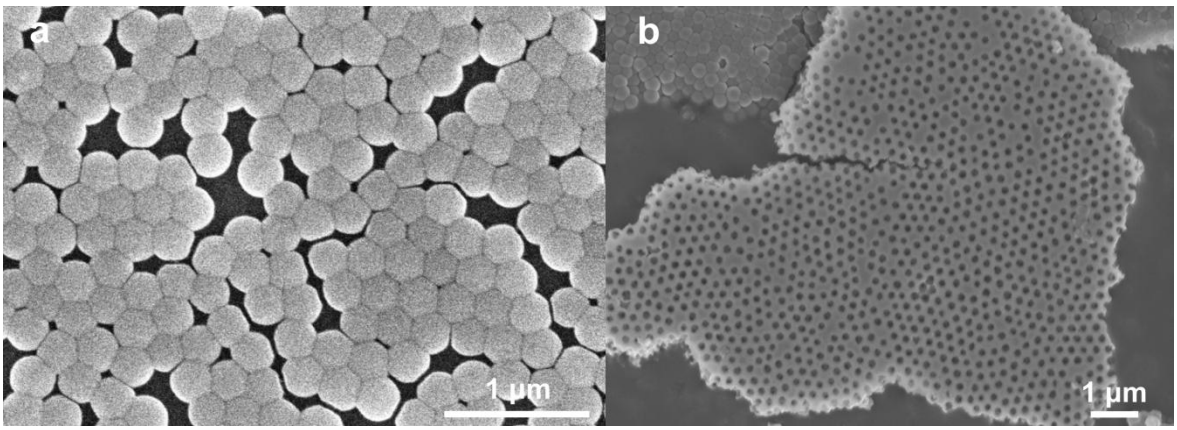

Figure III.2. SEM top views of a) TiO_2 infiltrated 240 nm SiO_2 opal. Filled particle interspaces are visible. b) TiO_2 inverse opal after removal of the SiO_2 scaffold.

SEM images of the ALD-processed silica opal reveal that the structure is homogeneously infiltrated with titania (Figure III.3a,b). At higher magnification, the titania coating can be distinguished from the silica spheres in regions where the titania film was detached during sample preparation for SEM (Figure III.3b). After dissolution of the silica template, the inverted opal structure is clearly visible (Figure III.3c). The smaller holes at the surface of the hollow spheres are caused by the contact region between silica spheres and are the typical signature of the formation of the inverted opal structure after dissolution of the template. TEM images acquired on fractured samples highlight the good conformality of the titania coating and the high filling ratio of the silica opal (Figure III.3d,e). Regions where the coating is missing due to contact between spheres are indicated by the arrows. The energy filtered TEM image recorded using the Ti L edges further

proves the presence of a conformal titania coating (Figure III.3f). TEM images of a cross section of the annealed opals before (Figure III.3g,h) and after removal of the silica template (Figure III.3i) denote the good preservation of the opal structure during annealing and removal of the silica template, as well as the induced densification and crystallization in the anatase phase.

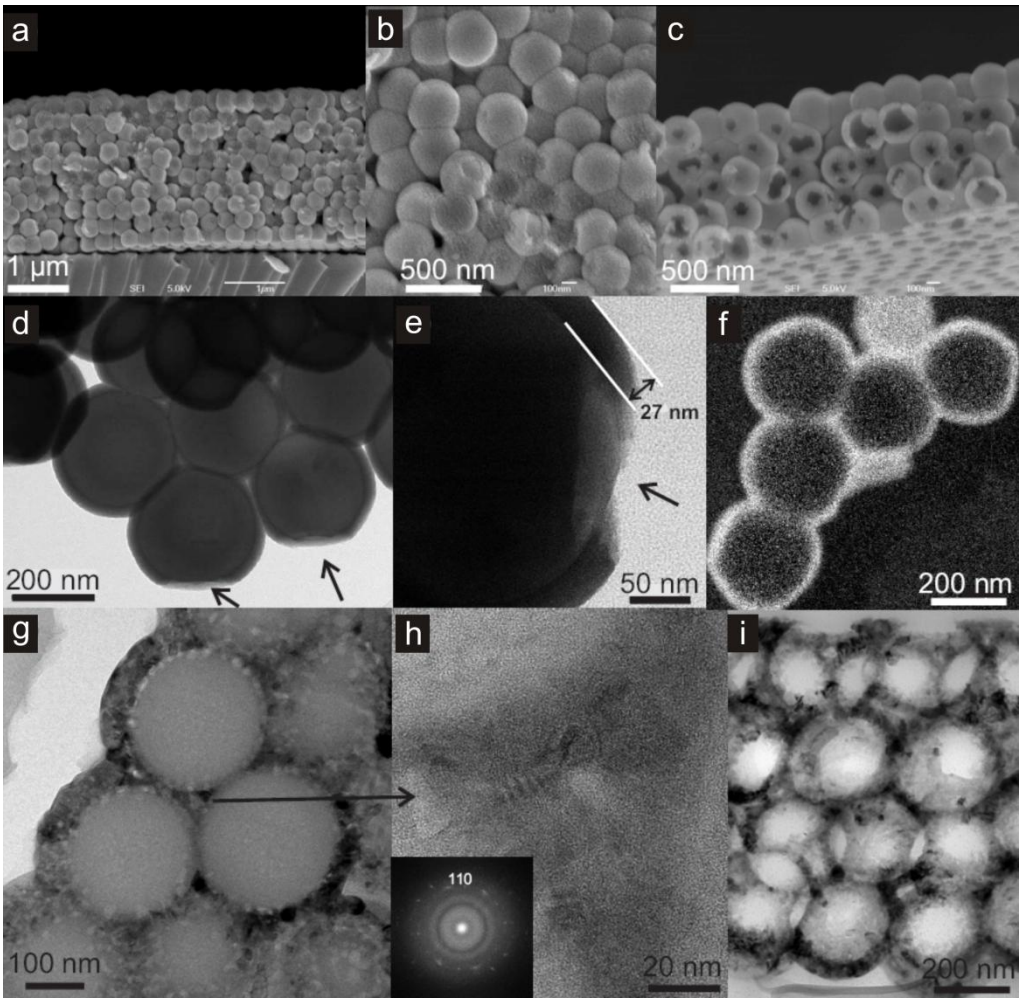

Figure III.3. SEM images of the a,b) 285 nm sphere diameter direct silica opal filled with titania, c) 260 nm sphere diameter inverse titania opal after removal of the template. d,e) TEM images of the 285 nm sphere diameter direct silica opal filled with titania (the arrows denote the contact point of the silica spheres during deposition) and f) energy filtered TEM images at the Ti 2p edge showing the conformality of the titania coating around the silica spheres. TEM images of cross section cuts of the annealed opal (260nm sphere diameter) g,h) before and i) after removal of the silica template. Inset: power spectrum of the HRTEM image in h).

II.1.2. Optical properties

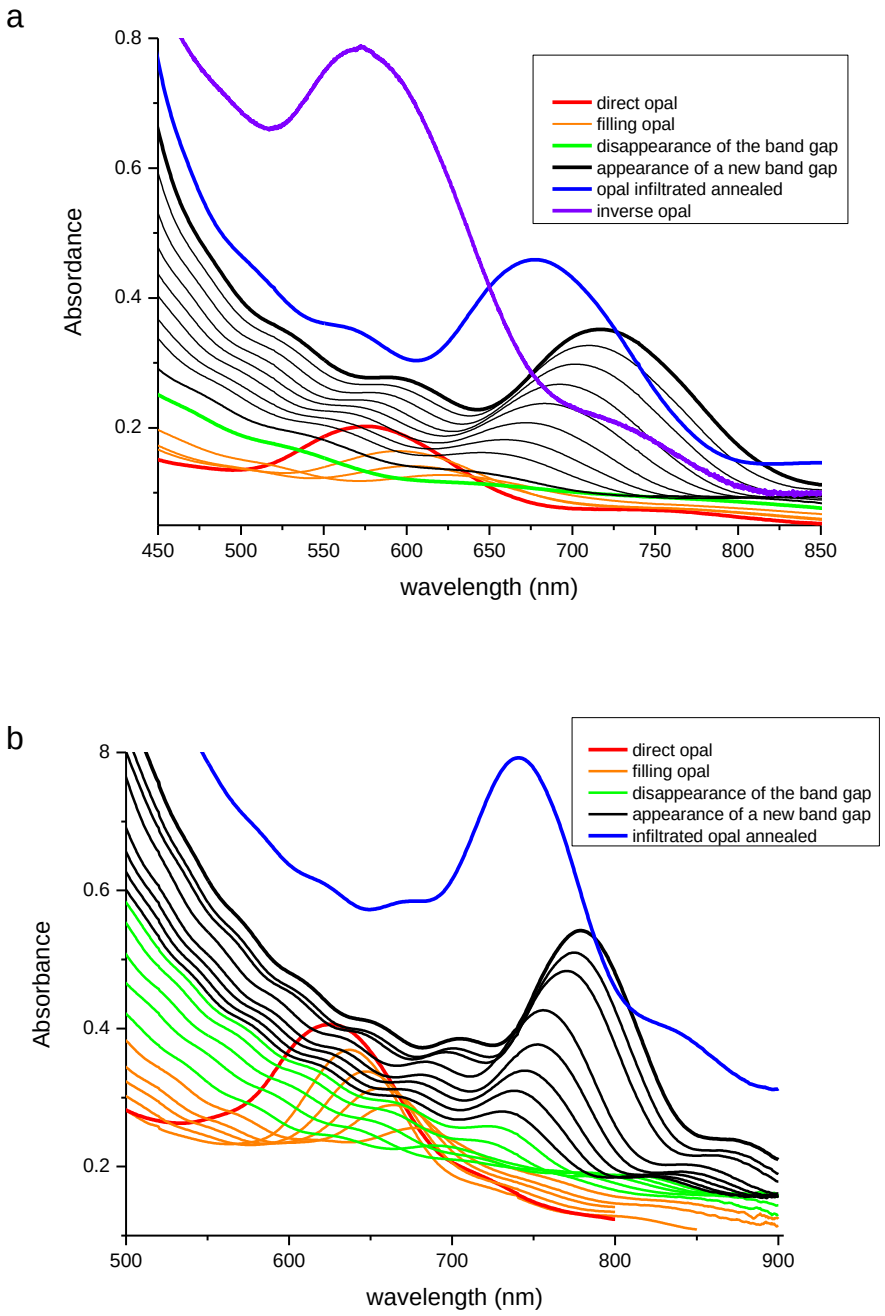

Figure III.4. Experimental extinction spectra of a) 260 nm and b) 285 nm sphere diameter direct silica opal progressively filled with titania by ALD. The red line corresponds to the pseudo-band gap of the direct opal before impregnation. The orange lines depict the progressive red shift and reduction of the photonic pseudo band gap after the first impregnation steps. The green line refers to its disappearance. The black lines depict the progressive red shift and increasing of the titania filled silica inverse opal PPBG. The blue line corresponds to the annealed infiltrated opal and the violet to the band gap of the inverse opal, after removal of the silica scaffold.

According to Bragg's law and its adapted relationship to opal: $\lambda_{Bragg} = 1.63 D n_{eff}$, where D is the sphere diameter and n_{eff} the effective refractive index, the extinction spectra of the pure silica opal structures studied in this work are expected to have a maximum at λ = 572 nm and λ = 627 nm for sphere diameters of D = 260 nm and D = 285 nm, respectively. This is experimentally obtained for the case of 260 nm and 285 nm spheres, as shown by the red curves in Figure III.4. In both cases, a similar trend is observed as a function of the TiO_2 infiltration (Figure III.4). Looking at the case of the opal made of 285 nm spheres, the increased filling of the pores with titania leads to a shift of the PPBG to longer wavelengths. Simultaneously to this shift, the peak amplitude decreases until it disappears at around 700 nm. Subsequently, the inverse PPBG starts to appear and grows in amplitude, while shifting to longer wavelengths until it reaches λ = 780 nm once the pores are completely filled.

The first step (disappearance of the peak, orange curves) corresponds to the modification of the band structure of the direct opal in such a way that the refractive index contrast between the constitutive spheres and the surroundings vanishes (green curves). In the present system, this happens at a filling fraction r = 6% (cf. section III). In the second step, the index contrast gets reversed as the surrounding pores are further filled with a higher index dielectric material, refractive index of 2.35 for amorphous TiO_2 compared to a value of 1.45 for the case of SiO_2. The band gap of the resulting inverse opal appears and converges once the opal is completely filled (black curves). It is important to notice that the increased extinction at wavelengths below the position of the PPBG originates from the increased incoherent diffusion as titania is progressively introduced into the structure.[76]

Once the opal filling was completed, an annealing was realized in order to crystallize the amorphous as-deposited titania into anatase. Despite an expected red-shifted position, due to the effective refractive index increase expected for anatase compared to amorphous titanium dioxide, a blue-shift and increase of the PPBG is noticed (blue curves). This is attributed to a shrinking of the structure, leading to the domination of the opposite effect.

Finally, HF etching of the SiO_2 scaffold was realized in order to obtain the inverted opal, as shown in Figure III.4b and 3c. A blue-shifted intense PPGB is observed (violet curve in Figure III.4a) in agreement with the occurrence of the reduction of the effective refractive index.

II.2. Case of silica opals containing defects

The controlled insertion of a defect causes a rupture in the periodicity of the photonic crystal and induces the appearance of localized states for photons within the gap. Recently, various techniques were developed to introduce a planar defect into 3D PCs.[71, 77, 78] The obtained heterostructures present a dip, also called a pass band, inside the stop band in the transmission spectrum. To the best

of our knowledge, neither the progressive titania filling by ALD of the direct template nor the inversion of such a heterostructure were previously reported. Moreover, the inversion process presents the advantage of increasing the quality factor of the pass band. Accordingly, due to the versatility of the Langmuir–Blodgett technique, allowing control of the deposition layer by layer, a photonic heterostructure made of two stacks of five layers of 280 nm diameter silica host particles surrounding a defect layer constituted by a monolayer of 430 nm diameter silica guest particles, was produced. In the next step, the silica template was filled with titania by ALD. Figure III.5 shows the extinction spectra experimentally obtained.

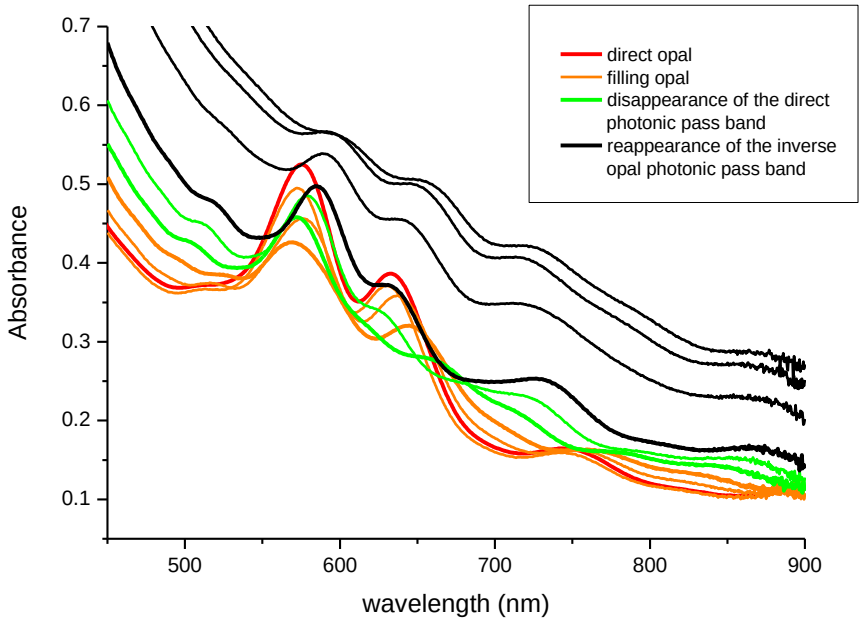

Figure III.5. Experimental extinction spectra of a direct silica opal, constituted of two stacks of five layers of 280 nm diameter silica host particles enclosing a planar defect layer made of a monolayer of 430 nm diameter particles, progressively filled with titania by ALD. The red line corresponds to the pseudo-band gap and the pass band of the direct opal. The orange lines depict the progressive red shift and reduction of the direct opal photonic pass gap. The green line refers to its disappearance. The black lines depict the progressive reappearance of the photonic pass band of the titania filled silica inverse opal.

As predicted by theory and simulations, the introduction of a defect layer introduces a pass band in the PPBG of the direct opal. This pass band manifests as a dip at ~610 nm, as seen in the extinction spectra. The progressive titania ALD filling of the template induces a red shift of the high wavelength edge of the PPBG together with its pass band (orange lines), followed by the disappearance of the pass band (green line). The low wavelength edge of the PPGB did not significantly move. Further filling induces a blue-shift reappearance of the pass band within the

PPBG in inverse geometry (black lines) prior to progressively shifting more to the red as the filling ratio further increases. In the inverse geometry both, the low and the high wavelength edges of the PPBG, move together with the pass band.

III. Theoretical calculation

In order to combine both electromagnetic simulations and experiments, theoretical calculations were realized using fully-vectorial eigenmodes of Maxwell's equations computing and finite-difference time-domain (FDTD) simulations. The FDTD modeling technique is a powerful tool to treat time-dependant Maxwell's equations by their fine discretization. This work was performed by Dr. Renaud Vallée of the CRPP, University Bordeaux 1 in France.

The studied opals elaborated by the Langmuir-Blodgett technique present a face centered cubic arrangement.[79] Considering a primitive fcc cell, opals can be then seen as a 3D-periodic lattice. The corresponding 1st Brillouin zone, volume defined by equidistant surfaces from one point of the system and its neighbors, schematized in Figure III.6, is characterized by the critical points: Γ, K, L, U, W and X.

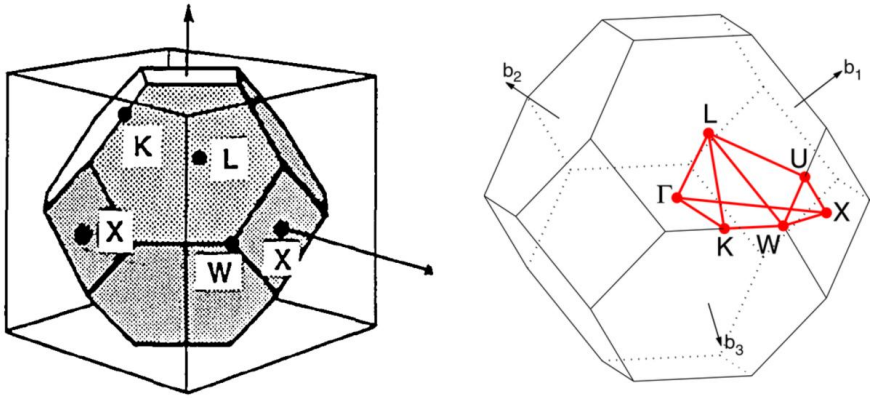

Figure III.6. Representation of the 1st Brillouin zone of a fcc lattice[80] and position of its characteristic points.[81]

The propagation of light through a periodic crystal is driven by the four macroscopic Maxwell's equations. Assuming the crystal being macroscopic and isotrope, the light interacts with the material structure similarly to electrons with atom lattice. Therefore, as a crystal presents periodic Coulomb's potential, the 3D structure can be seen as periodic variation of the dielectric function of the material. Shortly, by solving the Maxwell's equation as a function of time and space dependences, eigenvectors are calculated depending on the structure symmetry.[12] Hence, by

general symmetry consideration, the electromagnetic modes can be defined and the Bloch's theorem permits the determination of the photonic crystal band structure.[12]

Photonic band diagrams of the silica opals progressively filled with titania were simulated as a function of the filling ratio, expressed as the ratio r between the titania coating shell thickness and the silica sphere diameter. The diagrams are shown in Figure III.7 for four particular cases. The direct silica opal (Figure III.7a) exhibits a Γ*L* PPBG between the second and third bands with a width to position ratio of 5.22%, in agreement with values reported in the literature.[23] The progressive filling of the direct opal with titania, in a conformal type of growth, leads to a red shift of the Γ*L* PPBG, ranging from an adimensional frequency (in c/a, where c is the speed of light and a the lattice parameter) of 0.65 for the direct opal to 0.51 for the infiltrated opal with a ratio r = 13.1% (Figure III.7c). This is in agreement with the Bragg's law adapted to opals: $\lambda_{Bragg} = 2d_{111}n_{eff} = 1.63Dn_{eff}$. Simultaneously to this red shift, a flattening of the bands is observed. The latter is the result of the increased effective refractive index: $n_{eff} = \sqrt{\Phi_{SiO_2} n_{SiO_2}^2 + \Phi_{TiO_2} n_{TiO_2}^2 + \Phi_{air} n_{air}^2}$.

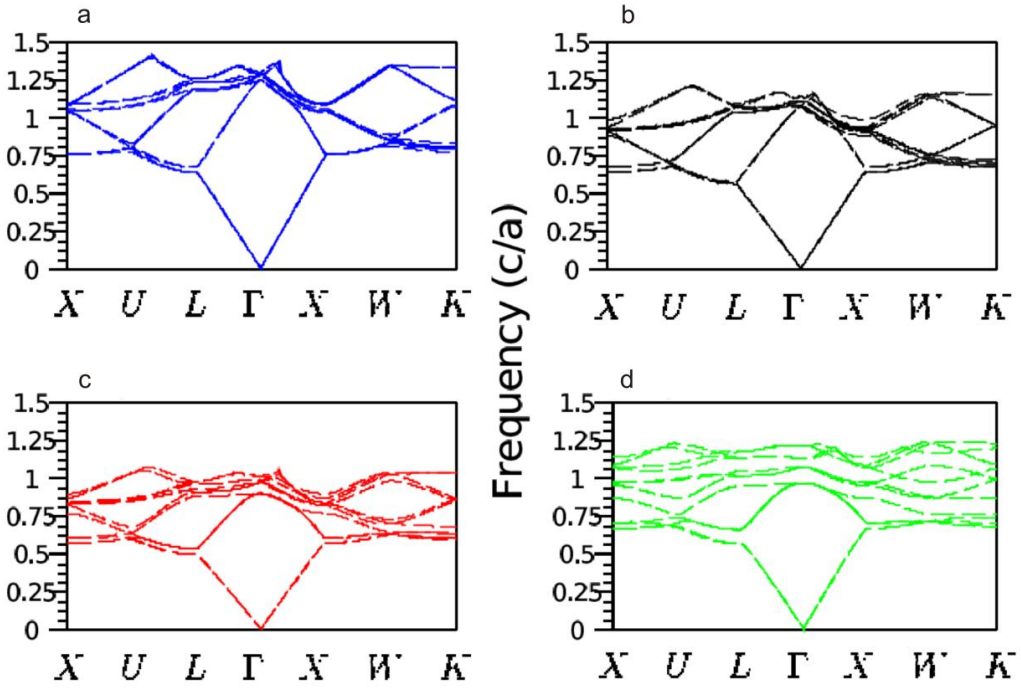

Figure III.7. Simulated band structures a) of the direct silica opal, b) of a titania partially or c) completely conformally filled silica opal and d) of a pure titania inverse opal, obtained by conformal growth of titania around the air pores. The filling fractions of titania in the anatase phase of these last three structures are r = 4.1%, r = 13.1% and r = 13.1%, respectively.

Here, $\Phi_{SiO_2} = 0.74$ and $n_{SiO_2} = 1.45$, Φ_{TiO_2} and $n_{TiO_2} = 2.7$ (anatase) or $n_{TiO_2} = 2.35$ (amorphous), Φ_{air} and $n_{air} = 1$ are the filling fractions and refractive indexes of silica, titania and air, respectively. The filling fractions are constrained to the condition that $\Phi_{SiO_2} + \Phi_{TiO_2} + \Phi_{air} = 1$. The progressive filling of the silica direct opal with anatase induces a narrowing of the Γ*L* gap width, until the PPBG vanishes at about r = 4.1% (Figure III.7b). This is followed by the appearance of the inverse PPBG, which reaches a width to position ratio of 7.45% at r = 13.1% (Figure III.7c). The monotonic decrease of the adimensional frequency together with the sequence of narrowing - disappearance - reappearance - broadening of the ΓL pseudo-gap as a function of the filling ratio r is best illustrated in Figure III.8. The simulation gives a similar result in the case of amorphous titania, with only slightly different threshold values: the PPBG disappears at r = 5.8% and the inverse photonic pseudo band gap reaches a width to position ratio of 4.9% at r = 13.1% (Figure III.8). The band diagram of the titania (anatase) pure inverse opal was also simulated. In that case, a larger width to position ratio of 14.78% is obtained at the adimensional frequency of 0.608 for a coating thickness to pore diameter ratio of r = 13.1% (Figure III.7d). The opening of the full PBG between the 8th and 9th bands for an inverse opal with an index contrast of 2.7 is clearly visible in the figure.

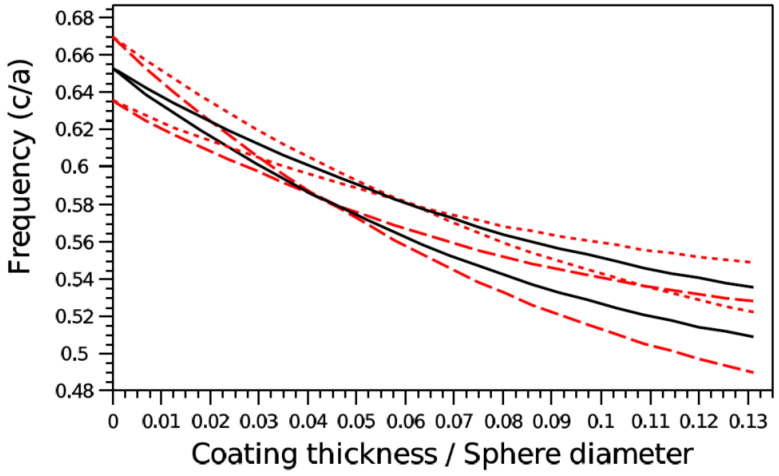

Figure III.8. Evolution of the frenquency shift (solid lines) and width (vertical interdistance between the dash or dot lines) of the Γ*L* PPBG as a function of the filling fraction r, expressed as the coating thickness divided by the sphere diameter in the cases of amorphous (solid line between dot lines) and anatase (solid line between dash lines) titania.

IV. Comparison experimental and theoretical results

In order to demonstrate the robustness of the ALD approach used in this PhD thesis, the obtained experimental results were compared to the simulated one. For better visibility theoretical and experimental spectra were plotted, in this section, next to each other.

IV.1. Case of silica opals without defects

The comparison between the theoretical and experimental plots reveals two main features. Firstly, the good quality of the grown photonic crystals becomes evident from observing the low wavelength range of the extinction spectra (Figures III.4 and III.9). The secondary periodic oscillations, so-called ‘‘Fabry–Perot’’ fringes, are due to interferences of light propagating among various optical paths back and forth in the structure. They appear in a spectral region where the dispersion relation is linear.[82] In this region, the crystal can be assimilated to a homogeneous transparent medium with an effective refractive index. Only good quality crystals, with a homogeneous optical thickness, can exhibit ‘‘Fabry–Perot’’ fringes. It is important to point out the excellent matching between the spectral positions of the fringes observed on both theoretical and experimental extinction spectra. Furthermore, a good agreement between the simulated and experimental typical positions, such as position of the PPBG of a) the direct opal, b) after the first infiltration step and c) the disappearance of the PPBG, can be visualized in the Figure III.9. As discussed above, a good “Fabry-Perot” fringes concordance can be noticed after the 1st deposition step. It appears therefore that our ALD process permits to conformally deposit metal oxide with a controlled thickness down to the nanometer.

Secondly, Figure III.9d also reveals that the theoretical spectrum shows a slightly reduced shift in the spectral position of the peaks at maximum filling. This discrepancy is due to the fact that the opal obtained by the Langmuir–Blodgett deposition is not fcc close packed, as simulated here. It is better described as a (2 + 1)D photonic crystal resulting from the stacking in a one-dimensional (1D) lattice of prepacked two-dimensional (2D) colloidal crystals.[83]

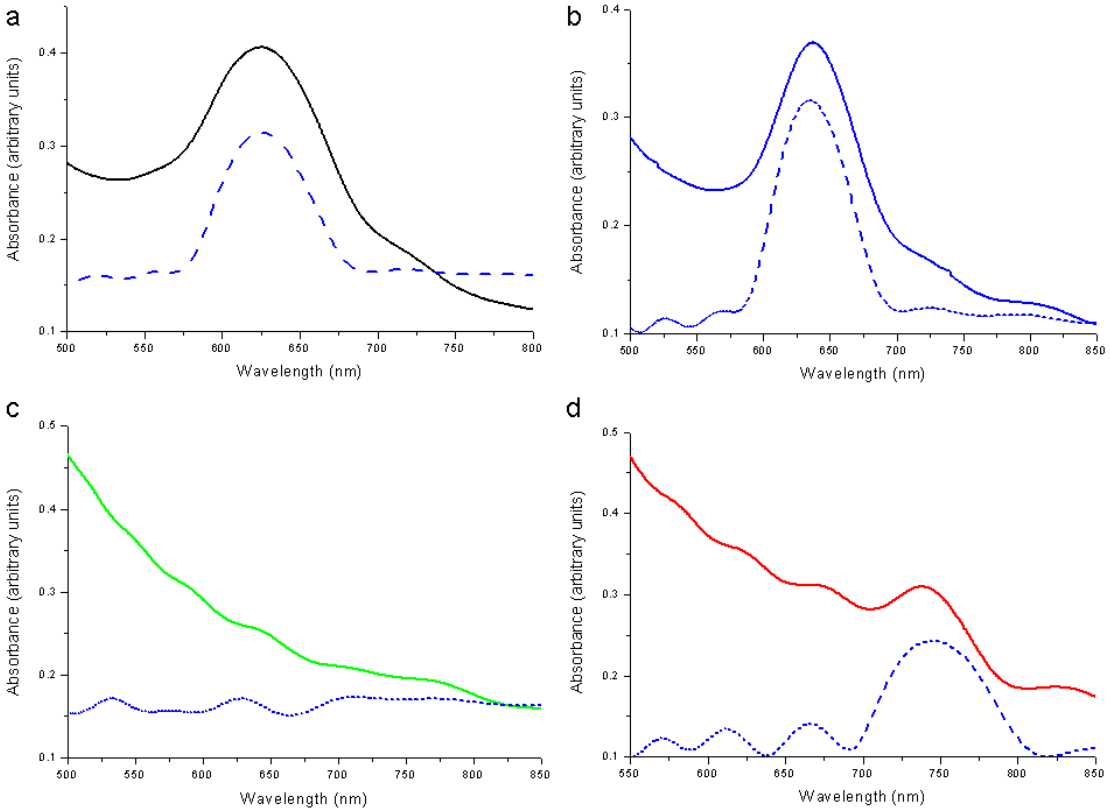

Figure III.9. Comparison of characteristic positions obtained experimentally (full lines) and theoretically (dotted lines). a) position of the PPBG of the direct opal, b) red-shift of the PPBG after the 1st infiltration step, c) disappearance of the band gap after 10 filling steps and d) position of the inverse opal after annealing.

The lack of a strict correlation between successive monolayers induces a greater d_{111} of the LB films as compared to the equivalent photonic crystal grown by controlled evaporation (fcc).[57] Consequently, a higher void volume fraction of the overall structure leads to a significantly increased composite dielectric constant, and thus to a larger shift in the Bragg peak after ALD infiltration. Evidence for this is provided by the spectra recorded from the fully filled samples after annealing (Figure III.4b, blue curve). It shows a blue shift of the extinction spectrum, which is opposed to what would be expected solely from the transformation of the amorphous titania phase into anatase, where the increased refractive index would lead to a red shift of the PPBG (cf. Figure III.8 for the evolution of the adimensional frequency in the amorphous and anatase cases). This is an indication of the fact that the relaxation/densification of the structure overcompensates the increase of the refractive index upon annealing, underlining the explanation given above.

In Figure III.10a, the comparison between the extinction spectrum of the annealed sample and the simulated spectra of silica opals conformally filled with anatase is shown. The best matching of the extinction spectra, with a maximum at λ = 740 nm, occurs for a theoretical filling ratio of 9.7%.

Such a filling fraction is larger than the theoretical maximum expected from the geometrical arrangement of silica spheres in perfectly close packed (111) planes, for which the filling would end, because of the closing of the structure, at a ratio r = 7.75%.[23] The larger filling ratio, obtained through compacting of the structure by the annealing process, is another indication of the non-fcc close packing of the direct opal.

As presented in the section II.1.2 the whole study was repeated on a silica template constituted of spheres with a diameter D = 260 nm. Figure III.10b shows the experimental extinction spectra obtained for the fully filled silica template before and after annealing, as well as the extinction spectra of a pure titania inverse opal. The latter was obtained after removal of the silica spheres by HF treatment (cf. HRTEM image, Figure III.3i). In agreement with the above, the extinction spectrum after annealing is blue-shifted. After removal of the silica template, the extinction spectrum is further blue-shifted due to the reduction of the effective refractive index. For comparison, Figure III.10b also presents the theoretical extinction spectra calculated for a conformal coating of the silica opal with anatase and the corresponding inverse opal. In excellent agreement with the results obtained in the case of the larger silica spheres, the best matching is obtained for a theoretical filling ratio of r = 10.2%.

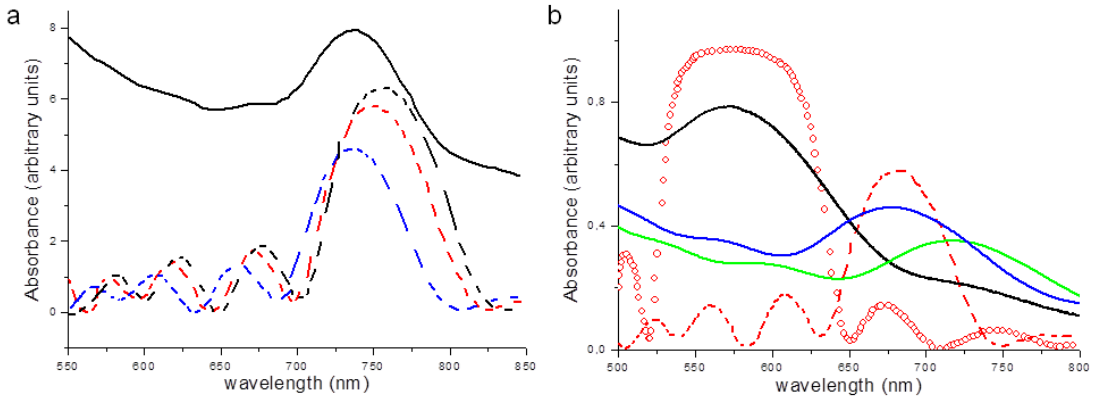

Figure III.10. Experimental and simulated extinction spectra of a) 285 nm or b) 260 nm sphere diameter direct silica opals fully filled with titania by ALD. a) The black solid curve pertains to the extinction spectrum of the opal after annealing. The dotted curves pertain to the simulated extinction spectra for anatase titania with filling fractions r ranging from 9.7 to 10.2 and 13.1% (from left to right). The best agreement between experiment and theory is found for r = 9.7%. b) The green solid line (blue solid curve) pertains to the extinction spectrum of the opal prior (after) annealing. The black solid curve pertains to the extinction spectrum of the annealed opal after HF treatment, inducing removal of the silica particles. The red curves pertain to the simulated extinction spectra of anatase titania-filled silica direct opal (dotted curve) and pure anatase titania inverse opal (circles) with a common filling fraction r = 10.2%, matching the best the corresponding experimental spectra in both cases.

IV.2. Case of silica opals containing defects

Figure III.11 shows the extinction spectra obtained both experimentally and by FDTD simulations, for SiO_2 opal containing one defect layer. The SEM transversal view of the heterostructure is also shown in Figure III.12a and a cut in the yz plane of the FDTD simulated heterostructure in Figure III.12b. The good ordering of the structure is clearly visible. A slight positional disorder generated in the layer situated on top of the guest particles layer is also observed, as already reported previously.[72]

The Figure III.12 shows the main difference between the experimentally engineered and simulated heterostructures: while the defect layer is constituted of host silica particles arranged in a hexagonally packed monolayer in the built opal, it is approximated to a block of the same thickness but with an effective refractive index material (n = 1.35) in the simulations. Although such an approximation was very successful in modeling the direct heterostructures,[72] this is not the case for the filled opal. Indeed, on the experimental side, the conformal growth will take place everywhere, including the surrounding of the host particles, while in the simulated case this conformal growth is effective only around the two guest particles, as exemplified in Figure III.12. Such a difference will have an impact on the optical properties of the system. The predicted pass band manifests as a dip at 612 nm, as seen in the extinction spectra (Figure III.11a dotted line). The simulated progressive titania ALD filling of the direct template induces a red shift of the PPBG together with its pass band (Figure III.11b, dotted lines), followed by its disappearance (Figure III.11c, dotted line), and the reappearance and red shift of the PPBG together with its pass band (Figure III.11d, dotted lines) in the inverse opal geometry. Note the monotonous red shift of the pass band as a function of the filling. The superposition between experimental (full lines) and simulated (dotted lines) curves in Figure III.11 shows a similar tendency but with slight variations (cf. section II.2.). In contrast to what happens in the simulations, after disappearance of the pass band, further filling induces a blue-shifted reappearance of the pass band within the PPBG in the inverse geometry (Figure III.11d) prior to progressively shifting more to the red as the filling fraction further increases. As a whole, the main differences between simulations and experiments are a reduced and non-monotonous red shift of the pass band as a function of the filling fraction, together with a non-complete disappearance of the PPBG (e.g. the low wavelength edge persists, cf. Figure III.11c) in the experimental extinction spectra. We tentatively attributed these discrepancies to the approximation made in order to simulate the defect layer. The increased intensity observed in the blue region of the experimental spectra is due to diffusion by unintentional defects introduced in the structure (Figure III.12a), which were not taken into account in the simulations.

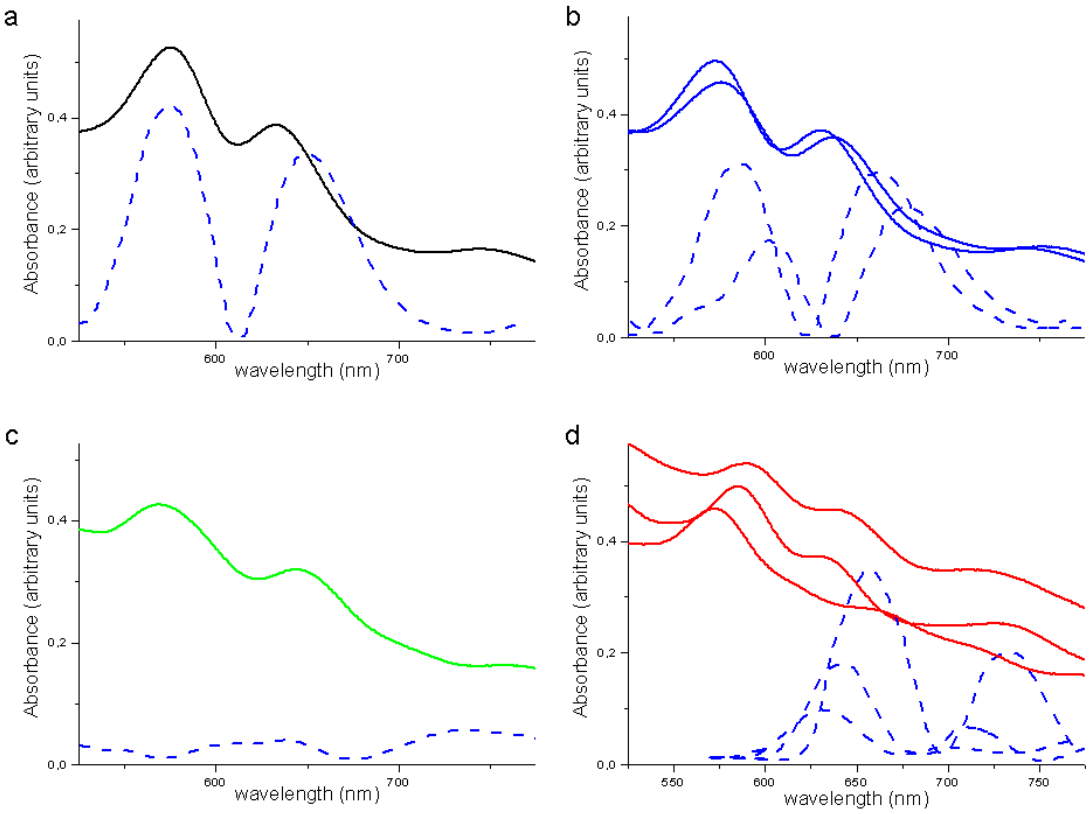

Figure III.11. Comparison of characteristic positions obtained experimentally (full lines) and theoretically (dotted lines) of a heterostructure constituted by a defect layer of 430 nm diameter guest silica particles comprised between two stacks of 5 layers of host silica particles of 280 nm diameter progressively filled with titania by ALD. a) corresponds to the opal before infiltration, the curves in b) depict the progressive red shift and reduction of the direct opal photonic pass band. The lines in c) depict its disappearance. d) depicts the progressive red shift and increasing of the titania filled silica inverse opal pass band.

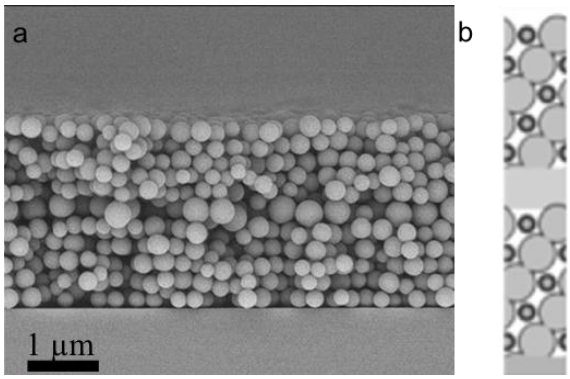

Figure III.12. a) SEM transversal view of the heterostructure constituted by a defect layer of 430 nm diameter guest silica particles comprised between two stacks of 5 layers of host silica particles of 280 nm diameter, before infiltration. b) Representative of simulated heterostructure, cut in the yz-plane.

V. Infiltration of silica opals for nanostructured particle elaboration

Nanostructured core-shell and hollow particles can be elaborated using the conformal ALD infiltration of opals. Indeed, each particle constituting an opal is homogeneously coated with the exception of its contact points with its neighbor remaining uncoated. By breaking the opal after ALD coating, core-shell particles are obtained, presenting a pattern of 12 holes in the shell. Subsequent removal of the opal material permits obtaining hollow nanostructured spheres.

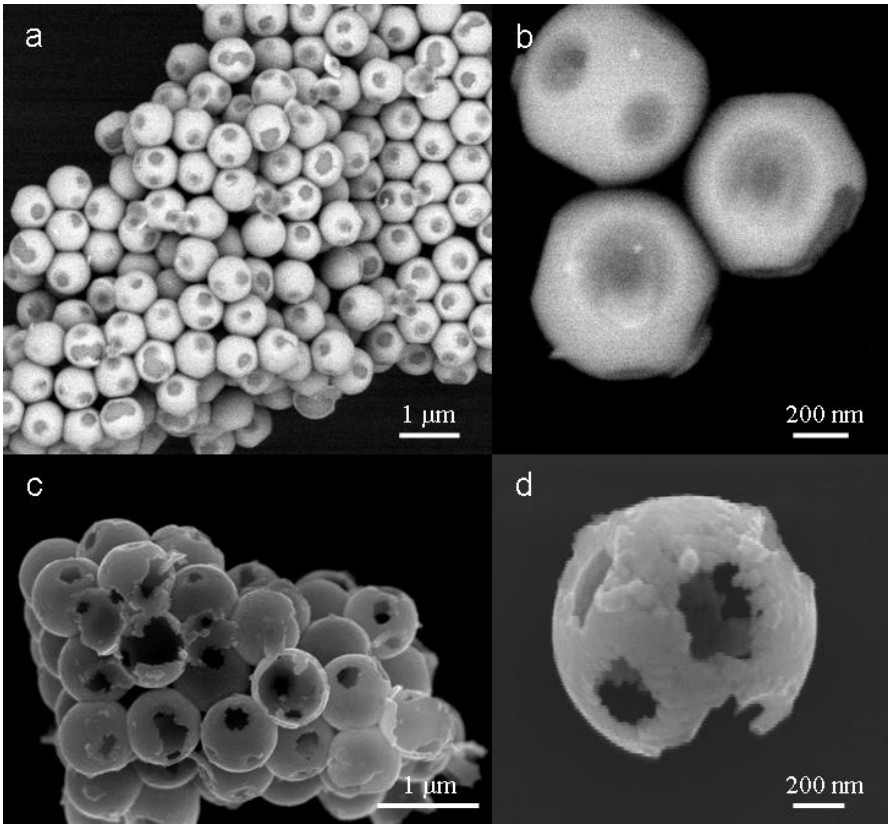

Figure III.13. a,b) SEM images in electron backscattering mode of 20 nm thick TiO_2@SiO_2 particles of 720 nm diameter. The absence of titania on specific spots is clearly visible on each silica particle, corresponding to the contact points with the neighbor particles in the fcc structure of the opal. c,d) SEM images of the TiO_2 shell after removal of the SiO_2 particles by HF etching. The initial shape of the silica remains, no collapsing of the structure is noticed leading to the formation of hollow particles with 20 nm thick wall and 720 nm of inner diameter as shown in d).

For instance, opals made of 720 nm diameter SiO_2 particles were elaborated by the Stöber method combined with LB technique, then filled with 20 nm TiO_2 by ALD and finally broken by ultra-sounds. In Figure III.13a,b, the homogeneous metal oxide layer can be nicely seen due to its bright contrast compared to the silica sphere. The darker regions visible on the surface of the particles correspond to holes in the titania shell. Actually, due to the contact points between the silica

particles in the fcc opal structure, the precursors could not diffuse and these areas remain therefore uncoated. After the silica etching by HF treatment, the titania shell remains intact forming a hollow sphere with periodic holes on the surface (Figure III.13c,d). A granular aspect of the anatase TiO_2 is visible in Figure III.13d.

Following the same principle, by surface engineering, different core-shell particle morphologies could be obtained. The PhD dissertation of Mélanie Ferrié reports on some examples of the opal infiltration used for the elaboration of nanostructured particles.[84]

VI. Conclusions

In conclusion, it was demonstrated both by simulations and experiments that the impregnation of a direct silica opal by a NHSG ALD process, allows to precisely control the optical properties of a photonic crystal. The approach further permits to modulate the photonic band structure and the ΓL pseudo-gap in a controlled manner. This is important for practical applications such as optical filtering. The agreement between theory and experiments is remarkable and demonstrates the ability of the simulations to make predictive statements. Furthermore, this work demonstrates that the ALD approach introduced by our group, based on carboxylic acids as oxygen source, is robust and can be used for precisely coating nanostructured materials with sub-nanometer thickness control. It was also shown that the combination of the Langmuir-Blodgett technique with ALD permits the controlled engineering of complex structures leading to additional features such as the control of pass bands in opals containing defects. Finally, the ALD infiltration approach can be used for the controlled elaboration of nanostructured particles.

Perspective

In the next step, the experimental results on opals containing defects, presented here, will be compared to new types of simulations combining molecular dynamics and FDTD taking into account more precisely the actual composition of the defect layer and the (2+1)D instead of the fcc structure of LB obtained colloidal crystals. Furthermore, an experimental architecture consisting in a block defect layer instead of the hexagonally packed monolayer of host particles will also be produced and compared to the herein presented calculations.

This work could be also extended to opals containing luminescent particles in order to control their emission spectra. Indeed, considering a chromophore with large emission spectra, it is of interest to be able to tailor the width and the maximum position of its emission. Thus, the tuning of the pass band appears a suitable approach.

VII. Experimental part

Opal fabrication by Langmuir-Blodgett technique

Silica particles of 260, 285 and 430 nm in diameter were synthesized following the well-known Stöber–Fink–Bohn method[85] from tetraethoxysilane (TEOS, Fluka) and ammonia (29% in water, J. T. Baker). Their functionalization with aminopropyltriethoxysilane (APTES) (Aldrich) was carried out as previously described.[73] Large excess of APTES was added to the silica particles. To ensure the anchoring of the molecule, the system was heated at 90 ºC for 2h.[73] Multilayer colloidal crystals were fabricated by the Langmuir–Blodgett technique.[71, 73] The Langmuir monolayer was compressed step-by-step at room temperature (~20 °C) until a surface pressure of ca. 6 mN m^{-1} was reached. For the transfer of the monolayer, a dipping speed of 5 mm min^{-1} was used. Under these conditions, opals consisting of 1, 5 or 10 layers of silica spheres were deposited on glass substrates.

TiO_2 infiltration by ALD

The opals were conformally coated with titania in a home-made ALD reactor working in exposure mode (shown in chapter 1). The deposition was done simultaneously on opals and on reference p-type Si (100) wafer for thickness measurements. Titanium isopropoxide and acetic acid were used as metal and oxygen precursors, respectively.[86] The deposition took place at 200 °C, while the precursor lines were maintained at 80 °C and the purge circuit at 100 °C. The metal and carboxylic acid precursors were kept in reservoirs at 80 and 30 °C, and delivered to the chamber through ALD pneumatic valves. Pure nitrogen was used as the carrier gas with a constant flow of 5 sccm. The deposition parameters were 0.03 s (1 s) for the acid (alkoxide) pulses, the residence and purge time were 20 and 15 s, respectively. The infiltration was done by 30 sets of depositions, each consisting of 20 ALD cycles with a GPC of 0.6 Å/cycle.

After complete infiltration of the opals, they were annealed for 4 h at 600 °C in a tubular oven, with a temperature ramp of 10 °C min^{-1}. The pure inverse opal was simply obtained via the removal of the silica template by immersion in a HF bath (3% concentration) during 30 min.

Optical and electron microscopy characterizations

The spectral properties of the opals were measured after each set of depositions by UV-Visible spectroscopy in extinction mode, by a Jasco V-560 spectrophotometer, over a range from 350 to 900 nm. The thickness of the as-deposited titania film on the reference Si wafer was measured by X-Ray reflectometry, using a Philips X'Pert MRD X-ray diffractometer with a copper radiation and a graphite monochromator for the selection of pure Kα radiation. The X-ray tube was operated at

40 kV and 50 mA. A 1 mm slit was used in order to reduce the scattered X-ray intensity. Measurements were performed in low-resolution experimental set up with the following instrumental configuration: divergence slit at the incident beam: 1/8 in.; step width: 0.005°; acquisition time: 1 s. The samples were structurally characterized by high resolution scanning electronic microscopy prior to and after the complete infiltration, as well as after removing the silica template. The SEM characterization was performed using a JEOL JSM 6700-F and a Hitachi SU-70 SEM, operated at 5 kV and 15 kV, respectively, in secondary electron and backscattering electron mode. The samples were Au-coated and observed in cross-section. High resolution transmission electron microscopy and electron energy loss spectroscopy measurements were performed using a CM200FEG (Philips) microscope operated at 200 kV. The microscope is equipped with a field emission gun and a GATAN Tridiem postcolumn electron energy loss spectrometer.

Simulation details

Simulations were performed in two steps. Firstly, in order to determine the photonic band structure of the various samples, fully-vectorial eigenmodes of Maxwell's equations with periodic boundary conditions were computed by preconditioned conjugate- gradient minimization of the block Rayleigh quotient in a planewave basis, using a freely available software package.[87] The eigenfrequencies up to the twelfth band were computed for 100 equally spaced k points along each high frequency direction (XULΓXWK) of the first Brillouin Zone. The irreducible Wigner–Seitz cell (WSC) was divided into 32 768 segments, defining the spatial resolution. Similar simulations were performed to calculate the photonic local density of states in direct silica opals.[88] Secondly, in order to calculate the optical extinction spectra, finite-difference time-domain (FDTD) simulations were performed,[89] using a freely available software package with subpixel smoothing for increased accuracy.[90] The computational cell, in which the incoming wave propagates along the z direction, has been implemented with periodic boundary conditions in the x and y directions, and perfectly matched layers (PMLs) in the z direction. The resolution of the grid has been refined such that the convergence of the results was ensured. In all simulations, the direct opals have been represented by monodisperse spheres of a given size (285 or 260 nm) and dielectric constant ($\varepsilon = 2.1$) in an arrangement corresponding a face-centered cubic (fcc) lattice.[72] In the FDTD simulations, the lattice has been limited to 10 planes normal to the direction [111], in agreement with the planned experimental conditions. The resulting crystal was placed on a substrate with a dielectric constant of 2.3. In order to simulate the growth of titania (amorphous with $\varepsilon = 5.52$, anatase with $\varepsilon = 7.29$) in the pores left by the direct opal during the ALD process, the original silica spheres were surrounded by interpenetrating titania shells of higher radius.

VIII. References

1. B. Lange, F. Fleischhaker and R. Zentel, *Macromol. Rapid Commun.*, 2007, **28**, 1291-1311.
2. D. P. Gaillot and C. J. Summers, in *Atomic Layer Deposition of Nanostructured Materials*, eds. N. Pinna and M. Knez, Wiley-VCH, 2011, pp. 345-376.
3. V. L. Colvin, *MRS Bull.*, 2001, **26**, 637-641.
4. J. F. Galisteo-López, M. Ibisate, R. Sapienza, L. S. Froufe-Pérez, A. Blanco and C. López, *Adv. Mater.*, 2011, **23**, 30-69.
5. L. González-Urbina, K. Baert, B. Kolaric, J. Pérez-Moreno and K. Clays, *Chem. Rev.*, 2011, 2268-2285.
6. C. López, *Adv. Mater.*, 2003, **15**, 1679-1704.
7. F. Marlow, Muldarisnur, P. Sharifi, R. Brinkmann and C. Mendive, *Angew. Chem. Int. Ed.*, 2009, **48**, 6212-6233.
8. J. H. Moon and S. Yang, *Chem. Rev.*, 2010, **110**, 547-574.
9. A. Stein, F. Li and N. R. Denny, *Chem. Mater.*, 2008, **20**, 649-666.
10. S. John, *Phys. Rev. Lett.*, 1987, **58**, 2486-2489.
11. E. Yablonovitch, *Phys. Rev. Lett.*, 1987, **58**, 2059-2062.
12. J. D. Joannopoulos, R. D. Meade and J. N. Winn, *Photonic Crystal,. Molding the flow of Light*, Princeton University Press, 2008.
13. K. Busch, G. von Freymann, S. Linden, S. F. Mingaleev, L. Tkeshelashvili and M. Wegener, *Phys. Rep.*, 2007, **444**, 101-202.
14. S. G. Romanov, N. P. Johnson, A. V. Fokin, V. Y. Butko, H. M. Yates, M. E. Pemble and C. M. S. Torres, *Appl. Phys. Lett.*, 1997, **70**, 2091-2093.
15. J. E. G. J. Wijnhoven and W. L. Vos, *Science*, 1998, **281**, 802-804.
16. H. M. Yates, W. R. Flavell, M. E. Pemble, N. P. Johnson, S. G. Romanov and C. M. Sotomayor-Torres, *J. Cryst. Growth*, 1997, **170**, 611-615.
17. A. Blanco, E. Chomski, S. Grabtchak, M. Ibisate, S. John, S. W. Leonard, C. López, F. Meseguer, H. Míguez, J. P. Mondia, G. A. Ozin, O. Toader and H. M. van Driel, *Nature*, 2000, **405**, 437-440.
18. Y. A. Vlasov, X.-Z. Bo, J. C. Sturm and D. J. Norris, *Nature*, 2001, **414**, 289-293.
19. R. Fenollosa and F. Meseguer, *Adv. Mater.*, 2003, **15**, 1282-1285.
20. F. García-Santamaría, M. Ibisate, I. Rodríguez, F. Meseguer and C. López, *Adv. Mater.*, 2003, **15**, 788-792.
21. H. Míguez, N. Tétreault, S. M. Yang, V. Kitaev and G. A. Ozin, *Adv. Mater.*, 2003, **15**, 597-600.
22. A. Rugge, J. S. Becker, R. G. Gordon and S. H. Tolbert, *Nano Lett.*, 2003, **3**, 1293-1297.
23. J. S. King, D. P. Gaillot, E. Graugnard and C. J. Surnmers, *Adv. Mater.*, 2006, **18**, 1063-1067.
24. J. S. King, E. Graugnard and C. J. Summers, *Adv. Mater.*, 2005, **17**, 1010-1013.

25. S. H. Park, D. Qin and Y. Xia, *Adv. Mater.*, 1998, **10**, 1028-1032.

26. B. Li, J. Zhou, L. Li, X. J. Wang, X. H. Liu and J. Zi, *Appl. Phys. Lett.*, 2003, **83**, 4704-4706.

27. B. Li, J. Zhou, Q. Li, L. Li and Z. Gui, *J. Am. Ceram. Soc.*, 2003, **86**, 867-869.

28. P. Yang, T. Deng, D. Zhao, P. Feng, D. Pine, B. F. Chmelka, G. M. Whitesides and G. D. Stucky, *Science*, 1998, **282**, 2244-2246.

29. F. Meseguer, A. Blanco, H. Míguez, F. García-Santamaría, M. Ibisate and C. López, *Colloid Surf. A*, 2002, **202**, 281-290.

30. A. Blanco, P. D. Garca, D. Golmayo, B. H. Jurez and C. López, *Selected Topics in Quantum Electronics, IEEE Journal of*, 2006, **12**, 1143-1150.

31. A. Blanco and C. López, *Adv. Mater.*, 2006, **18**, 1593-1597.

32. B. H. Juárez, P. D. García, D. Golmayo, A. Blanco and C. López, *Adv. Mater.*, 2005, **17**, 2761-2765.

33. H. M. Yates, M. E. Pemble, A. Blanco, H. Míguez, C. López and F. Meseguer, *Chem. Vap. Deposition*, 2000, **6**, 283-285.

34. P. D. García and C. López, *J. Appl. Phys.*, 2006, **99**, 046103-046103.

35. H. Míguez, E. Chomski, F. García-Santamaría, M. Ibisate, S. John, C. López, F. Meseguer, J. P. Mondia, G. A. Ozin, O. Toader and H. M. van Driel, *Adv. Mater.*, 2001, **13**, 1634-1637.

36. N. Tétreault, A. Mihi, H. Míguez, I. Rodríguez, G. A. Ozin, F. Meseguer and V. Kitaev, *Adv. Mater.*, 2004, **16**, 346-349.

37. M. Ibisate, D. Golmayo and C. López, *J. Opt. A: Pure Appl. Opt.*, 2008, **10**, 125202-125207.

38. A. Bielawny, J. Upping, P. T. Miclea, R. B. Wehrspohn, C. Rockstuhl, F. Lederer, M. Peters, L. Steidl, R. Zentel, S. M. Lee, M. Knez, A. Lambertz and R. Carius, *Phys. Status Solidi A*, 2008, **205**, 2796-2810.

39. M. Knez, K. Niesch and L. Niinistö, *Adv. Mater.*, 2007, **19**, 3425-3438.

40. Z. A. Sechrist, B. T. Schwartz, J. H. Lee, J. A. McCormick, R. Piestun, W. Park and S. M. George, *Chem. Mater.*, 2006, **18**, 3562-3570.

41. J. S. King, C. W. Neff, S. Blomquist, E. Forsythe, D. Morton and C. J. Summers, *Phys. Status Solidi B*, 2004, **241**, 763-766.

42. J. S. King, C. W. Neff, C. J. Summers, W. Park, S. Blomquist, E. Forsythe and D. Morton, *Appl. Phys. Lett.*, 2003, **83**, 2566-2568.

43. E. Graugnard, J. S. King, S. Jain, C. J. Summers, Y. Zhang-Williams and I. C. Khoo, *Phys. Rev. B*, 2005, **72**, 4.

44. J. S. King, E. Graugnard and C. J. Summers, *Appl. Phys. Lett.*, 2006, **88**, 3.

45. J. S. King, D. Heineman, E. Graugnard and C. J. Summers, *Appl. Surf. Sci.*, 2005, **244**, 511-516.

46. J. S. King, E. Graugnard, O. M. Roche, D. N. Sharp, J. Scrimgeour, R. G. Denning, A. J. Turberfield and C. J. Summers, *Adv. Mater.*, 2006, **18**, 1561-1565.

47. C. J. Summers, E. Graugnard, D. P. Gaillot and J. S. King, *J. Nonlinear Opt. Phys. Mater.*, 2006, **15**, 203-218.

48. C. J. Summers, E. Graugnard, D. P. Gaillot, T. Yamashita, C. W. Neff and J. Blair, *J. Nonlinear Opt. Phys. Mater.*, 2008, **17**, 1-14.

49. D. P. Gaillot and C. J. Summers, *J. Appl. Phys.*, 2006, **100**, 113118-113127.

50. E. Graugnard, J. S. King, D. P. Gaillot and C. J. Summers, *Adv. Funct. Mater.*, 2006, **16**, 1187-1196.

51. E. Graugnard, D. P. Gaillot, S. N. Dunham, C. W. Neff, T. Yamashita and C. J. Summers, *Appl. Phys. Lett.*, 2006, **89**, 181108.

52. A. Rugge, J.-S. Park, R. G. Gordon and S. H. Tolbert, *J. Phys. Chem. B*, 2005, **109**, 3764-3771.

53. I. Alessandri, M. Zucca, M. Ferroni, E. Bontempi and L. E. Depero, *Cryst. Growth Des.*, 2009, **9**, 1258-1259.

54. H. Noh, M. Scharrer, M. A. Anderson, R. P. H. Chang and H. Cao, *Phys. Rev. B*, 2008, **77**, 115136-115144.

55. M. Scharrer, X. Wu, A. Yamilov, H. Cao and R. P. H. Chang, *Appl. Phys. Lett.*, 2005, **86**, 151113-151113.

56. M. Scharrer, A. Yamilov, X. Wu, H. Cao and R. P. H. Chang, *Appl. Phys. Lett.*, 2006, **88**, 201103-201103.

57. I. M. Povey, M. Bardosova, F. C. Dillon, F. Chalvet, M. E. Pemble and K. Thomas, *Thin Solid Films*, 2008, **517**, 811-813.

58. I. M. Povey, D. Whitehead, K. Thomas, M. E. Pemble, M. Bardosova and J. Renard, *Appl. Phys. Lett.*, 2006, **89**, 104103-104103.

59. Z. A. Sechrist, R. Piestun and S. M. George, *AIP Conf. Proc.*, 2008, **992**, 507-512.

60. S. K. Karuturi, L. Liu, L. T. Su, Y. Zhao, H. J. Fan, X. Ge, S. He and A. T. I. Yoong, *J. Phys. Chem. C*, 2010, **114**, 14843-14848.

61. I. Alessandri, M. Zucca, M. Ferroni, E. Bontempi and L. E. Depero, *Small*, 2009, **5**, 336-340.

62. L. Liu, S. K. Karuturi, L. T. Su and A. I. Y. Tok, *Energy Environ. sci.*, 2011, **4**, 209-215.

63. A. Mihi, C. Zhang and P. V. Braun, *Angew. Chem. Int. Ed.*, 2011, **123**, 5830-5833.

64. N. Tétreault, E. Arsenault, L.-P. Heiniger, N. Soheilnia, J. Brillet, T. Moehl, S. Zakeeruddin, G. A. Ozin and M. Grätzel, *Nano Lett.*, 2011, **11**, 4579-4584.

65. Z. Yang, S. Gao, W. Li, V. Vlasko-Vlasov, U. Welp, W.-K. Kwok and T. Xu, *ACS Appl. Mater. Interfaces*, 2011, **3**, 1101-1108.

66. C. Cheng, S. K. Karuturi, L. Liu, J. Liu, H. Li, L. T. Su, A. I. Y. Tok and H. J. Fan, *Small*, 2011, **8**, 37–42.

67. L. Liu, S. K. Karuturi, L. T. Su, Q. Wang and A. I. Y. Tok, *Electrochem. Commun.*, 2011, **13**, 1163-1165.

68. I. Alessandri and M. Ferroni, *J. Mater. Chem.*, 2009, **19**, 7990–7994.

69. I. Alessandri, M. Ferroni and L. E. Depero, *ChemPhysChem*, 2009, **10**, 1017-1022.

70. W. Mu, D.-K. Hwang, R. P. H. Chang and J. B. Ketterson, *J. Raman Spectrosc.*, 2011, **42**, 941-944.

71. P. Massé, G. Pouclet and S. Ravaine, *Adv. Mater.*, 2008, **20**, 584-587.

72. P. Massé, R. A. L. Vallée, J.-F. Dechézelles, J. Rosselgong, E. Cloutet, H. Cramail, X. S. Zhao and S. Ravaine, *J. Phys. Chem. C*, 2009, **113**, 14487-14492.

73. S. Reculusa and S. Ravaine, *Chem. Mater.*, 2003, **15**, 598-605.

74. C. Marichy, J.-F. Dechézelles, M.-G. Willinger, N. Pinna, S. Ravaine and R. Vallée, *Nanoscale*, 2010, **2**, 786-792.

75. F. Marlow and W. Dong, *ChemPhysChem*, 2003, **4**, 549-554.

76. Y. A. Vlasov, V. N. Astratov, O. Z. Karimov, A. A. Kaplyanskii, V. N. Bogomolov and A. V. Prokofiev, *Phys. Rev. B*, 1997, **55**, R13357-R13360.

77. P. Massé, S. Reculusa, K. Clays and S. Ravaine, *Chem. Phys. Lett.*, 2006, **422**, 251-255.

78. R. Pozas, A. Mihi, M. Ocaña and H. Míguez, *Adv. Mater.*, 2006, **18**, 1183-1187.

79. P. Massé and S. Ravaine, *Chem. Mater.*, 2005, **17**, 4244-4249.

80. E. Yablonovitch, *J. Opt. Soc. Am. B*, 1993, **10**, 283-295.

81. W. Setyawan and S. Curtarolo, *Comput. Mater. Sci.*, 2010, **49**, 299-312.

82. J. F. Galisteo López, L. Palacios, E., M. Castillo, E. and C. López, *Phys. Rev. B*, 2003, **68**, 115109-115116.

83. S. G. Romanov, M. Bardosova, D. E. Whitehead, I. M. Povey, M. Pemble and C. M. S. Torres, *Appl. Phys. Lett.*, 2007, **90**, 133101-133103.

84. M. Ferrié, *Design de particules plasmoniques pour le contrôle de l'absorption et de l'émission de lumière*, Bordeaux 1, 2011, 121 pages.

85. W. Stöber, A. Fink and E. Bohn, *J. Colloid Interface Sci.*, 1968, **26**, 62-69.

86. E. Rauwel, M. G. Willinger, F. Ducroquet, P. Rauwel, I. Matko, D. Kiselev and N. Pinna, *J. Phys. Chem. C*, 2008, **112**, 12754-12759.

87. S. Johnson and J. Joannopoulos, *Opt. Express*, 2001, **8**, 173-190.

88. R. A. L. Vallée, K. Baert, B. Kolaric, M. Van der Auweraer and K. Clays, *Phys. Rev. B*, 2007, **76**, 045113-045111.

89. A. Taflove and S. C. Hagness, *Computational Electrodynamics: The Finite-Difference Time-Domain Method*, Artech House, Inc., Norwood, MA, 2005.

90. A. Farjadpour, D. Roundy, A. Rodriguez, M. Ibanescu, P. Bermel, J. D. Joannopoulos, S. G. Johnson and G. W. Burr, *Opt. Lett.*, 2006, **31**, 2972-2974.

Chapter IV:

Coating of carbon nanotubes and labeling and monitoring their anchoring sites distribution by ALD

Contents:

The novel SnO_2 process, introduced in Chapter II, was applied for the coating of carbon and BN nanotubes. It allows the coating of the inner and outer surface of multiwalled carbon nanotubes with a highly conformal film of controllable thickness. However, a certain degree of defects and/or functional surface groups is required to initiate the film growth, as demonstrated by the remained uncoated CNT ends, being highly graphitic, and the inhomogeneous coating of the BN nanotubes. Indeed, the chemical inertness of graphite and, in the case of tubes, of rolled up few layer graphene sheets, requires some degree of "defect engineering" for the fabrication of carbon-based heterostructured materials. It is shown that atomic layer deposition provides a means to specifically label anchoring sites and can be used to characterize the surface functionality of differently treated carbon nanotubes. Direct observation of deposited titania by analytical transmission electron microscopy reveals the location and density of anchoring sites as well as structure related concentrations of functional groups on the surface of the tubes. Controlled functionalization of the tubes therefore allows to tailor the distribution of deposited material and hence, the fabrication of complex heterostructures.

I. Introduction

As shown in Chapter I, atomic layer deposition provides an elegant, efficient and well controllable way to coat high aspect ratio nanostructures with a homogeneous and conformal film of precisely defined thickness.[1-3] As such, it is ideally suited for the fabrication of complex heterostructures and functional materials.[4-6] Due to their outstanding properties, carbon nanotubes constitute ideal components for such heterostructures. As a matter of fact, as presented in the introduction chapter, ALD has already been successfully applied for the coating of CNTs.[7-14] However, since the initiation of film growth requires the presence of functional surface groups and defect sites that act as anchoring and nucleation sites,[15, 16] the inert nature of high quality tubes with graphitic surface leads to non- or incomplete coating. Depending on the density and nature of functional surface species principally two ALD growth modes can be expected.[3] If the density of surface anchoring sites is high enough to allow the ALD precursors to completely react with the substrate, a 2D growth mode is favored. Otherwise, an island growth mode is favored. In this case, the subsequent material is preferentially deposited onto the ALD material already deposited in preceding cycles. In intermediate cases, the growth mode may be first island growth, and when the islands have coalesced to form a continuous layer, 2D growth may occur. Therefore, controlled tailoring of the type, degree and density of functionalization of the CNTs surface would allow to tune the coating from selectively decorated to fully coated CNTs. This is certainly of interest for applications

requiring functional materials based on heterostructured CNTs. Principally, two types of surface functionalization can be distinguished: covalent and non-covalent. The most commonly employed type (prior to ALD) is the covalent functionalization by treatment of pristine CNTs with mineral acids such as HNO_3 or other strongly oxidizing agents (e.g. O_3). It permits to generate oxygenated functional surface groups such as alcohol, ketone, ether, carboxylic acid and ester, which pave the way to an endless possibility of further attachments.[17, 18] On the other hand, non-covalent functionalization is mainly based on supramolecular complexation using various adsorptive and anchoring forces, such as van der Waals and π-π interactions, hydrogen bonding and electrostatic forces. As a prominent example, defect free suspended SWCNTs could be conformally coated with Al_2O_3 by ALD, after a NO_2 pretreatment. In this case, NO_2, which reversibly physisorbs on the SWNTs, acts as anchoring site for further oxide growth.[8, 9]

The study of the location of defects on CNTs was already carried out using different approaches either for the labeling or for the monitoring. Labeling can be pursued by several techniques such as electrodeposition,[19] nanoparticle attachment in solution[20, 21] and exposure to gas phase reactants.[22] Each of these techniques shows some limitations in terms of accuracy; nanoparticles can be also deposited onto the non-functionalized part of the nanotube and not all of the functional groups would react with a nanoparticle. In the case of processing, electrodeposition requires the CNTs to be contacted at multiple positions by lithography, for example. Furthermore, monitoring defects by spectroscopy techniques e.g. Raman[23] or photoluminescence[21] do not offer a spatial resolution high enough to map the defects at the nanometer scale. Alternative techniques that provide atomic resolution such as scanning tunneling microscopy (STM) or AFM are limited in the study of complex nanostructured materials and allow to only scan a small region of the sample.[19, 20]

In this chapter, in order to demonstrate the versatility of the novel tin dioxide ALD approach, the coating of CNTs and boron nitride (BN) nanotubes will be presented. A conformal granular as-deposited tin dioxide layer was observed except at the tube ends, which are too graphitic to allow a growth initiation. This finding was further confirmed by the BN nanotube coating. Using TiO_2 deposition, we will demonstrate that ALD, in combination with high resolution and analytical transmission and scanning electron microscopy, appears the technique of choice to map anchoring sites on nanostructured supports and to study the distribution of functional groups as a function of structure and functionalization treatment. Finally, the tuning of the CNT surface functionalization will be applied to tailor SnO_2 and ZnO ALD deposition. The interest for application-directed design of functional heterostructured CNT based materials will be therefore established.

II. Elaboration of SnO_2@CNT heterostructures

The novel tin oxide process, introduced in Chapter II, was applied to the coating of commercial stacked-cup carbon nanotubes (from Pyrograf Products, grade PR-24-PS). It allows the coating of the inner and outer surface of carbon nanotubes with a highly conformal film of controllable thickness.[24] Prior to ALD, CNTs were functionalized with nitric acid at 100 ºC for 2 h. The coated CNTs were characterized by SEM and TEM. A homogeneous coating of the tubes is indicated by the SEM and EDS observation (Figure IV.1). The CNTs tend to form balls, as shown in Figure IV.1a. In the EDS mapping, Figure IV.1b, the Sn element, represented by the green color, is homogeneously localized on the CNT balls and does not seem present in the area of the picture where the CNTs are absent. Furthermore, no CNT appears uncoated. Additional details about the deposited films are revealed by the TEM investigations (Figure IV.2). In these images, the distribution of the heavier (higher atomic number) SnO_2 on the surface can be clearly observed. Especially, high angle annular dark field imaging in STEM is suitable, as the contrast can be chosen such that the carbon support remains nearly invisible whilst the coating can clearly be seen. This is shown for the case of a final compartment of a bamboo like carbon nanostructure and for a fish-bone carbon nanotube in Figures IV.2a and c, respectively. For comparison, high-resolution TEM images recorded from similar structures are also shown (Figure IV.2b,d). While the dark contrast, due to the coating of the surface, is relatively homogeneous in the HRTEM images, a granular and particulate aspect of the deposited film can be seen in the dark field STEM images (Figure IV.2a,c).

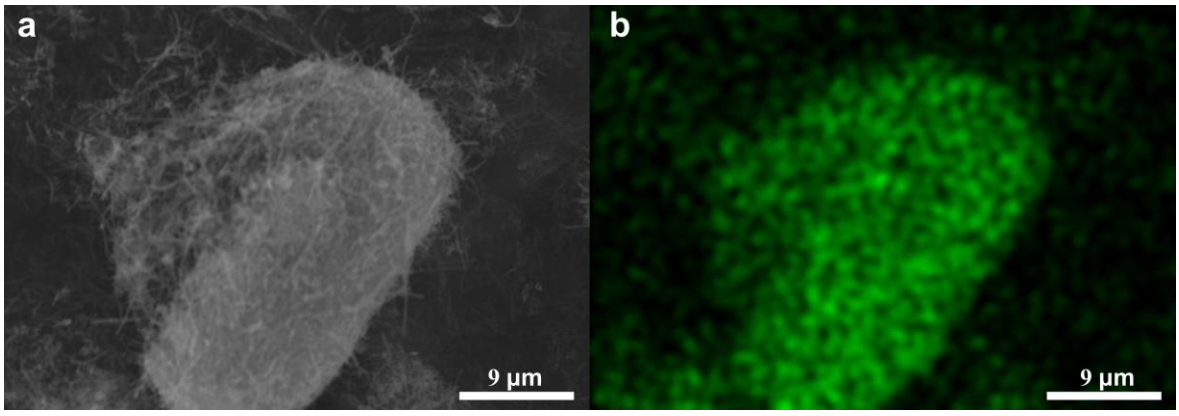

Figure IV.1. SEM image of coated carbon nanotubes and nanofibers is shown in a), the corresponding EDS map in b) shows the distribution of Tin, color coded in green.

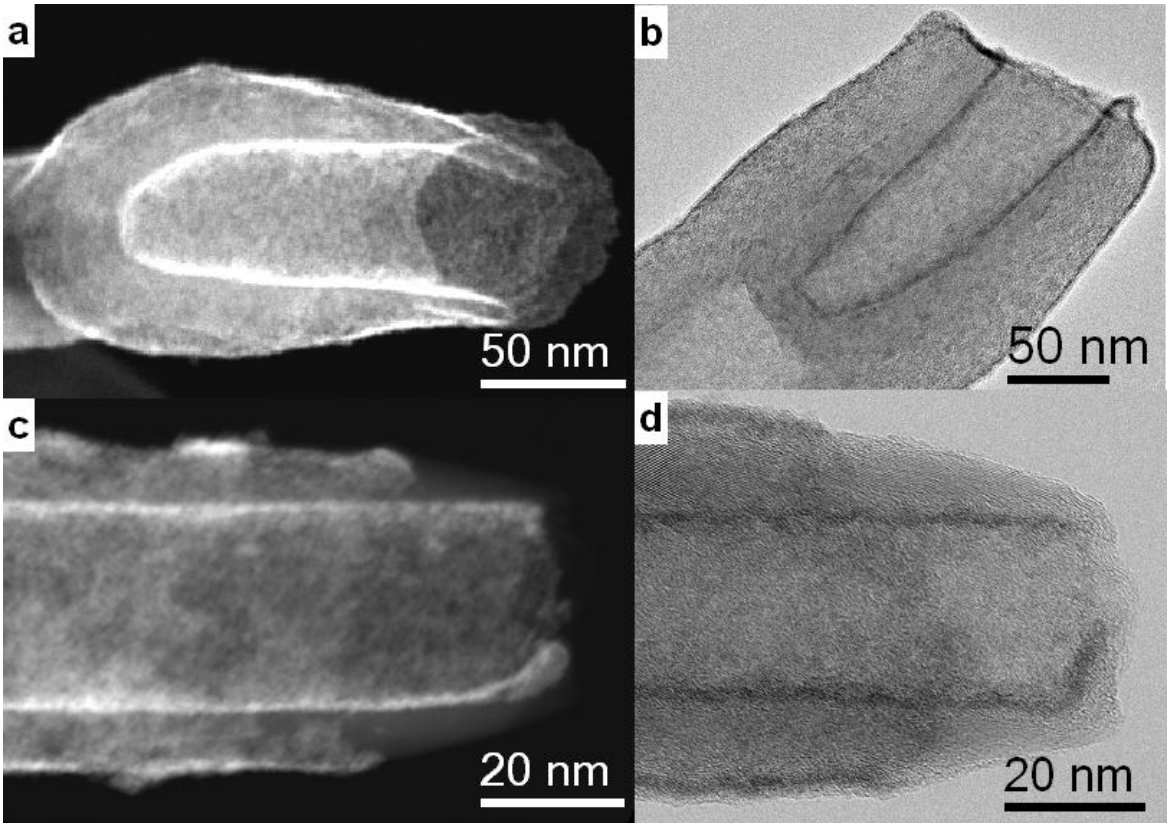

Figure IV.2. a) Dark field STEM image recorded with a high angle annular dark field detector and b) a high resolution TEM image recorded from a bamboo like CNT reveal the presence of a thin layer of electron dense material on the inner and outer surface of the final compartment. In c) and d) the distribution of the SnO_2 is shown for the case of a hollow carbon nanotube.

The particulate structure of the film is confirmed by high resolution TEM images that were recorded in regions where the thickness of the supporting carbon structure is very low (Figure IV.3b). Close inspection reveals small contrast variations due to lattice fringes of nanometer sized crystalline SnO_2 particles. Only the HRTEM observations and Fourier filtered images show the nanocrystallinity of the film and allow the conclusion of the formation of tetragonal phase SnO_2, certainly embedded into an amorphous phase. Indeed, XRD patterns recorded on coated carbon nanotubes did not reveal any peak related to tin oxide. Due to the crystallite size and the broad background signal of the possible SnO_2 amorphous phase, the broad expected reflections probably remain blended with the background.

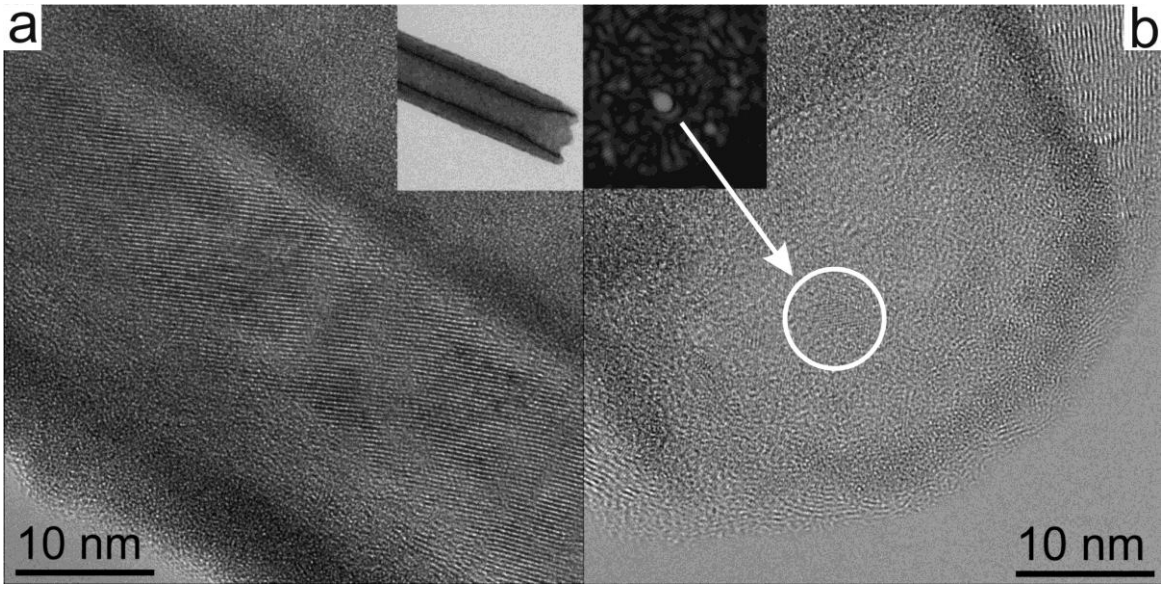

Figure IV.3. High-resolution TEM images showing the coated inner and outer surface of the fish-bone structured hollow carbon nanotube. Inset of panel a) overview TEM image of the tube shown in a). In thin regions, where the background contrast due to the carbon substrate is weak, fringes of the crystalline SnO_2 nanoparticles can be observed. It is enhanced in the Fourier filtered inset of panel b), generated using the 200 d-spacing of rutile SnO_2. The deposition temperature was 200 °C.

The thickness of the tin oxide layer, estimated from the high resolution TEM images, is around 3-3.5 and 2.5 nm in Figures IV.2a,b and IV.2c,d, respectively. In comparison, the thickness extracted from XRR on flat silicon substrates was 20 nm and 11 nm, respectively (Figure IV.4). The dotted red curves in Figure IV.4 correspond to simulated curves of 20 and 11 nm thick SnO_2 films. The position of the interference fringes of the measured samples are in good agreement with the theoretical fringes for films of equivalent thicknesses. The experimental critical angles present an important variation compared to the simulation. Indeed, due to the experimental set up of the diffractometer, its shape and position are not accurate. Therefore, it cannot be considered for fitting and the determination of the material density. Interestingly, the measured thickness was always lower in the case of the coated tubes compared to the values obtained from reflectometry measurements performed on flat silicon substrates. Hence, even though both were coated during the same deposition processes, different growths per cycle were obtained for the tubes and the Si wafer. The reason for this behavior is not yet fully understood. The observation is also in disagreement with previous results obtained for a similar ALD process, where TiO_2, HfO_2, and V_2O_4 showed the same growth on a wafer and nanotubes.[13, 25]

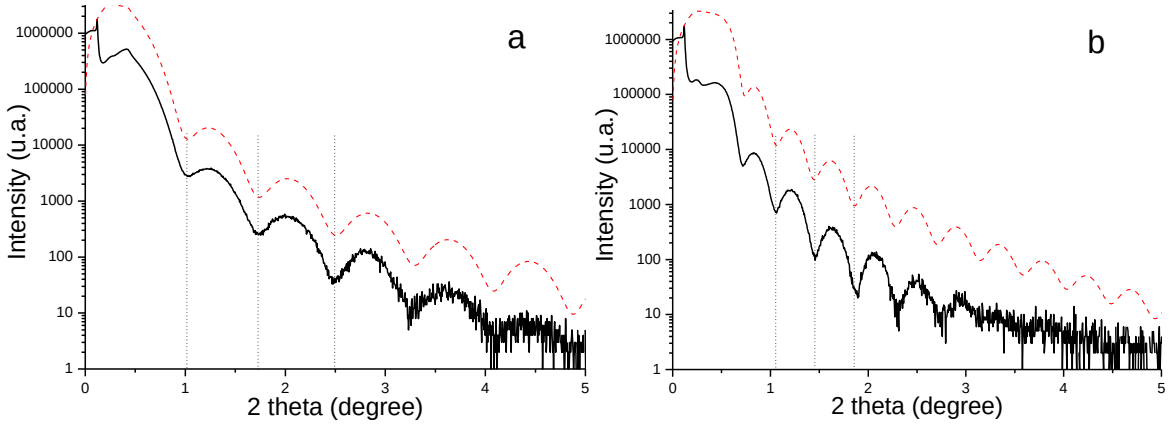

Figure IV.4. XRR curves of SnO_2 films on Si wafer (full lines) with a thickness of a) 11 nm and b) 20 nm, respectively, the dotted lines correspond to the simulated curves for samples with equivalent thicknesses.

In the case of the hollow carbon nanotubes, which are the main constituents of the Pyrograf Products (CNTs coated in this work), the walls are made up of stacked graphite cones. The oblique stacking of the graphene layers, with respect to the fiber axis, gives rise to the fish-bone like aspect of graphitic planes in high-resolution TEM. As a consequence of the stacking, the surface of the tubular structures terminates with graphitic planes only at the beginning and ending (cf. Figure IV.3a). While the presence of pyrolitic carbon is noticed on the surface of the CNT walls, the tips appear nearly free of amorphous carbon. As evidenced by the Figures IV.2c and IV.2d, the coating is homogeneous on the inner and outer walls of the tubes, whereas the exposed graphitic planes often remain uncoated. This demonstrates very well that the initiation of film growth requires a certain degree of functionalization or the presence of defects in order to create anchoring points, as previously noticed by Cavanagh *et al.*[7]

The requirement of an anchoring site for the initiation of film growth is also nicely demonstrated by coated boron nitride tubes. No treatment of the tubes was performed prior to ALD deposition. Inhomogeneity of the deposited film, such as those observed in the Figures IV.5a and IV.5b, could be related to the distribution of defective sites on the surface of the tubes. Similar observation of the relation between film growth and presence of defects was observed by Ferguson *et al.* in the SiO_2 ALD onto BN nanoparticles.[26]

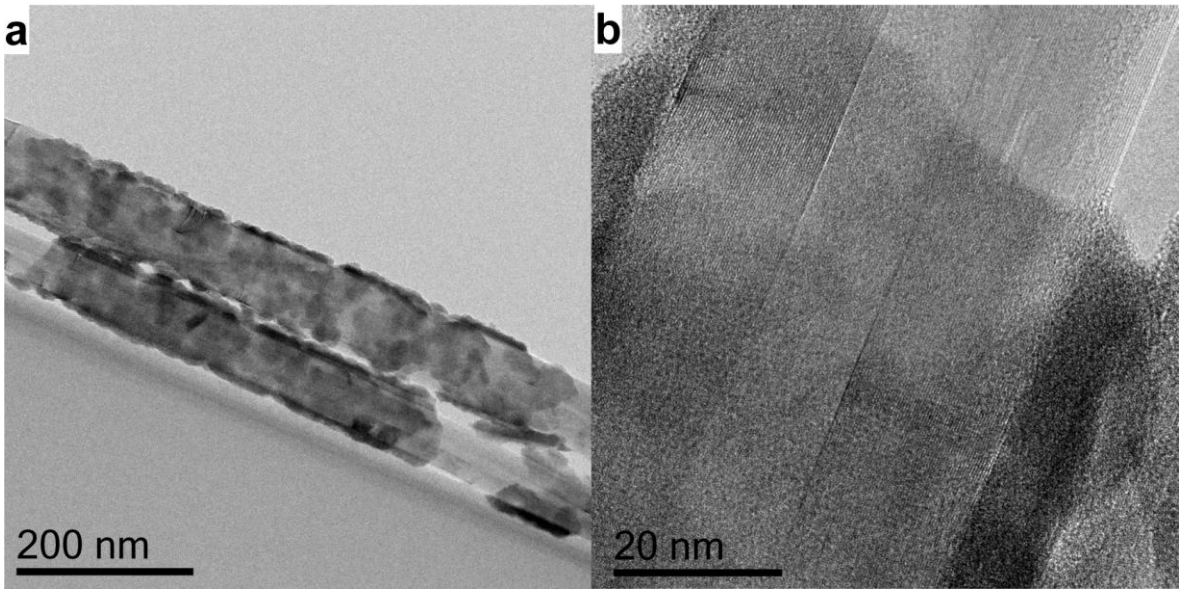

Figure IV.5. Boron nitride tubes after deposition of SnO_2 at 200 °C. The darker contrast in the TEM images is due to SnO_2. As shown in the overview image in a) and at high resolution in b), the film is not homogeneous, indicating that the density of anchoring sites is insufficient for a complete and homogeneous coating of the tubes.

By the novel SnO_2 approach presented in Chapter II, the coating of CNTs and boron nitride nanotubes can be achieved. The deposition allows the coating of the inner and outer walls of carbon nanotubes by a SnO_2 film. Due to the growth type, a particulate homogeneous film, made of embedded rutile crystalline phase nanoparticles, was obtained. Nevertheless, the film growth requires the presence of anchoring sites as indicated by the absence of coating on exposed graphitic layers and on defect free regions of the boron nitride nanotubes.

III. Labeling and monitoring of CNT defects with TiO_2 ALD

The chemical inertness of graphite and, in the case of tubes, of rolled up few layer graphene sheets, requires some degree of "defect engineering" for the rational fabrication of CNT-based materials. Tessonnier *et al*.[27] demonstrated that the degree of graphitization of the tube walls influences the type and density of surface groups created during the functionalization by nitric acid treatment. In collaboration with Dr. J.P. Tessonnier, we demonstrated that our ALD process can be used as a means to specifically label the anchoring sites (CNT defect and/or functional surface groups) on differently pre-treated tubes.[28] In this part of the thesis, it is shown that differences in initiation of film growth can be well monitored by analytical electron microscopy. Direct observation of

deposited material reveals the location and density of anchoring sites as well as structure related concentrations of functional groups on the surface of the tubes. The study therefore provides a direct feedback on the degree of functionalization as a function of CNT pre-treatment.

III.1. Presentation of CNTs used for this work

In order to characterize the surface functionality of differently treated CNTs, three commercial stacked-cups carbon nanotubes (see scheme Figure IV.6) were purchased from Pyrograf Products. The different grades correspond to a particular heat treatment, i.e. product PR24-PS treated at 700 °C, PR24-LHT at 1500 °C and PR24-HHT at 3000 ºC. The CNTs exhibit average outer and inner diameters of 85 and 40 nm, respectively, independently of the applied annealing temperature. Before ALD deposition, the CNTs were functionalized by acidic treatment. For the sake of clarity, the oxidized PR24-PS, PR24-LHT and PR24-HHT samples were labeled CNT700, CNT1500 and CNT3000. Part of the CNT700 sample was further partially defunctionalized and therefore labeled CNT700D.

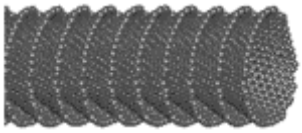

Figure IV.6. Pyrograf Products stacked-cups carbon nanotubes.[29]

Commercial stacked-cup CNTs possess several main advantages over other nanocarbons for the present work and were therefore chosen as a starting material. First, the as-grown CNTs are wrapped with a layer of pyrolytic carbon which finds its origin in the particular synthesis conditions of these CNTs. This layer consists of small graphene sheets, so called basic structural units (BSU), which are only few nm in size. They are interconnected by sp^2 and sp^3 carbon chains and assembled in concentric layers. From a structural and chemical point of view, the layer of pyrolytic carbon can be seen as a model surface representative of various nanocarbons such as carbon nanofibers, SWCNTs and MWCNTs, which allows us to extend the scope and the impact of this work. Tessonnier *et al.* used the same stacked-cup CNTs as a model material to develop a technique to selectively deposit metal particles either inside or outside CNTs.[30] This selective deposition technique was successfully employed by different groups on various CNTs since then.[31-33] Secondly, the layer of pyrolytic carbon exhibits a high concentration of structural defects (see below) which can be tuned by annealing in an inert atmosphere (graphitization). Therefore, these materials offer a large playground to study the effect of the defect density and of the surface chemistry on the ALD. Finally, it was demonstrated that MWCNTs exhibit a large number of carbonaceous debris on their surface, which are hard to characterize, but which significantly

interfere during the functionalization,[34] or the use of the MWCNTs in catalytic reactions.[35] In contrast, the surface of the stacked-cup CNTs is well-defined.[27]

The three commercial products used were functionalized with concentrated HNO_3 at 100 °C for 10 h in order to create oxygen-containing surface functional groups, which can be later used as anchoring points for TiO_2 ALD. As demonstrated by the previous work of Tessonnier *et al.*,[27, 36] with increasing annealing temperature, the degree of graphitization of the surface rises and as a consequence, the impact of the classic nitric acid treatment on the functionalization of the wall surface is altered. The thermogravimetry mass spectroscopy (TG-MS) and XPS (Figure IV.7) characterizations revealed that the formation of carboxylic acid and anhydrides, which typically are the most abundant functional groups for this kind of oxidizing treatment, seems to be disfavored when the structural order of the carbon material increases.[27] As a consequence, the pH of aqueous dispersions of CNT700 and CNT1500 increases, and the CNT3000 solution eventually turns basic. In addition, the concentration of surface functional groups created during the HNO_3 treatment decreases when increasing the graphitization temperature, as a result of the lower defect density (as observed from the evolution of the D/G ratio in Raman spectra, cf. Ref. [27]). An alternative modification of the nature and density of surface groups was achieved through a partial defunctionalization of the CNT700 sample in Ar at 800 ºC. This post-treatment removes 89% of the oxygen, as determined by XPS, but without significantly modifying the defect density.[27] The surface oxygen-containing groups and the Raman characterization results realized on the different kinds of CNTs are summarized in Table IV.1.

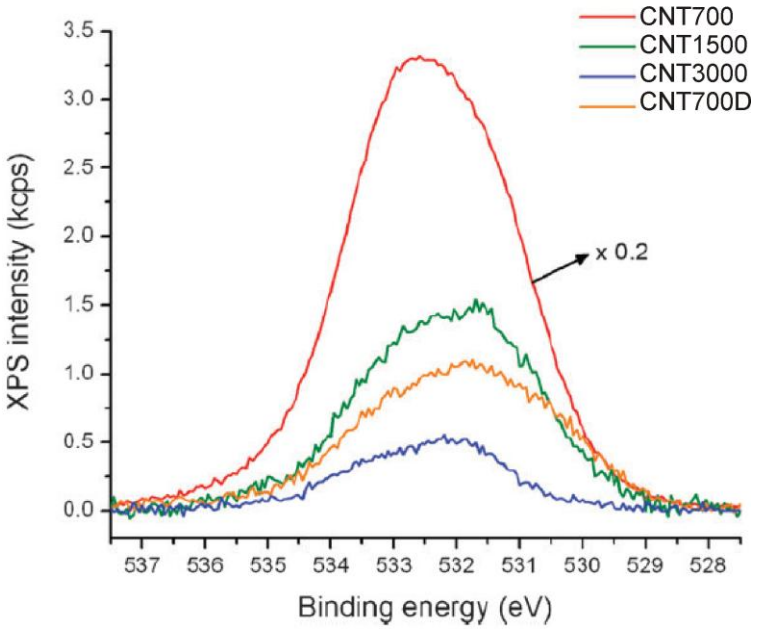

Figure IV.7. XP O1s spectra of the oxidized CNTs. Taken from Ref.[27].

Table IV.1. Characterization of the CNTs used in this work: carboxylic acid and phenol concentrations were determined by acid–base titration with NaOH (in µmol g^{-1}), and the total oxygen concentration was determined by XPS and D/G ratios (D band intensity over G band intensity, I_D/I_G) calculated from Raman spectra. Data taken from Ref.[27].

Sample Name	Carboxylic acid [a]	Phenols [a]	O/C [b]	I_D/I_G [c]
CNT700	130	180	0.099	3.6
CNT1500	27	32	0.012	1.0
CNT3000	0	18	0.005	~0
CNT700D	0	22	0.011	

[a] Determined by acid–base titration. [b] Measured by XPS. [c] calculated from Raman spectra on CNTs materials prior to acid treatment.

The high resolution transmission electron micrographs show the evolution of the structural defects and of the graphitization as a function of annealing temperature (cf. Ref.[37]). The CNT700 are characterized by a structural disorder of the outer and inner surface layer of the tubes (Figure IV.8a,b). The annealing at 1500 °C prior to the nitric acid treatment leads to the appearance of some connections between the inner rims of subsequently stacked cups (see arrow) and only a thin layer of structurally ill defined carbon is present on the exposed graphitic faces of the outer wall (Figure IV.8c,d). Finally the annealing at 3000 °C results in a straightening of the graphitic sheets and highly graphitized walls, which show connections between stacked cones. Those form steps on the inner and outer surface, which are decorated with some defective fullerene-like carbon (Figure IV.8e,f). This is not observed after nitric acid treatment and ALD coating (see Table IV.1). SEM images of the uncoated tubes are presented in Figure IV.9.

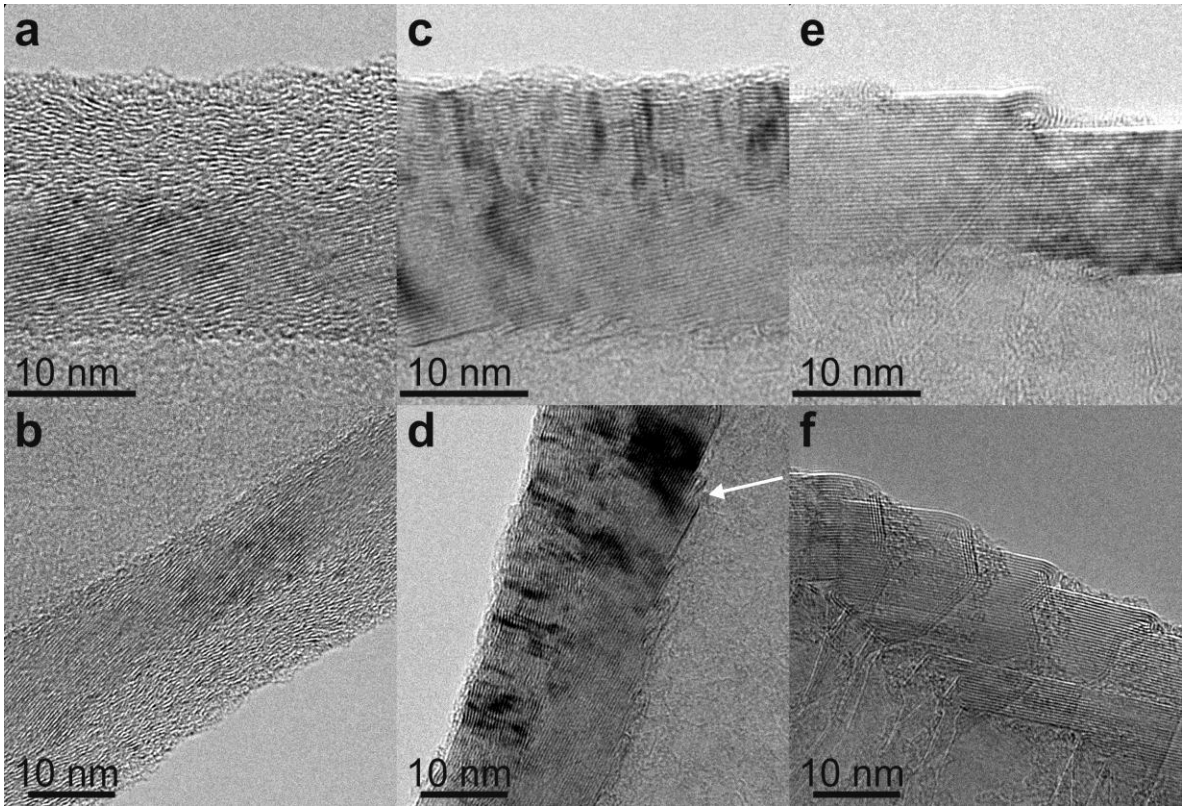

Figure IV.8. HRTEM images of the different CNTs prior to TiO_2 ALD. a, b) CNT700, c, d) CNT1500 and e, f) CNT3000, the latter before nitric acid treatment.

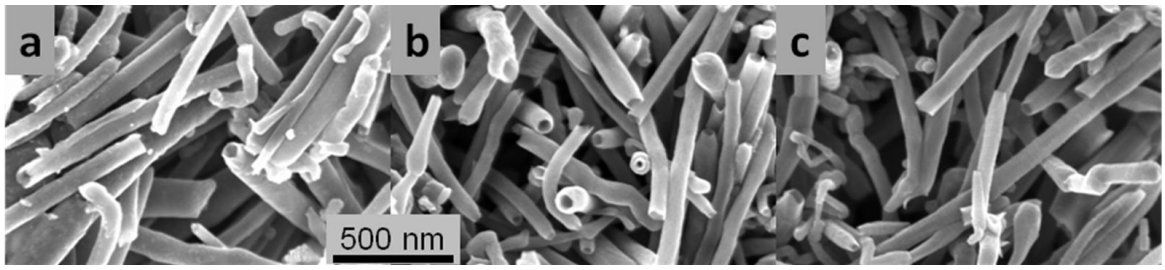

Figure IV.9. SEM images of the uncoated CNTs, a) CNT700, b) CNT1500, and c) CNT3000.

III.2. TiO_2 ALD: motivation and elemental characterization

III.2.1. Motivation for the choice of TiO_2 ALD for this study

As presented in the introductory chapter, the ALD of various metal oxides onto CNT700 was already reported by our group. Briefly, it was shown that TiO_2, V_2O_4 and HfO_2 form a conformal and homogeneous amorphous film at deposition temperatures in the range between 50-250 °C.[13, 25] The coating, only a few nanometers thick, is uniform along the whole surface of the tubes and presents approximately the same thickness at the inner and outer surface. HRTEM and electron

diffraction experiments showed that the as-deposited films are amorphous and can be grown directly on the graphitic surface of the nitric acid treated CNTs.[13, 25]

On the other hand, as shown above, it was found that the ALD of SnO_2 forms a granular film composed of sub-5 nm nanoparticles.[24] In this particular case, HRTEM studies revealed that the particulate film formation can be attributed to the property of SnO_2 to directly form nanoparticles during the deposition, even at temperatures as low as 150 °C. Indeed, the same particulate growth pattern was obtained from SnO_2 on silicon wafers passivated with native silicon oxide (cf. Chapter II). However, independent of the metal oxide that was deposited on the tubes, it was generally observed that no growth occurs on exposed graphitic planes. It can therefore be concluded that the initiation of film growth requires defects and anchoring sites at the surface of the tube.

The coating of CNTs with these metal oxides by the carboxylic acid route appears well defined, with a controllable thickness, and homogeneous on the outer and inner part of the walls.

For the present study, TiO_2 ALD was chosen for the coating as it is known to result in a very homogeneous growth of an amorphous film on the CNT700 and is therefore expected to be most suitable to detect small variations in the distribution of anchoring sites at high spatial resolution.

III.2.2. EELS characterization of TiO_2@CNTs

In order to analyze the chemical composition and purity of the deposited metal oxide, electron energy loss spectrometry was used.[25] The intensity of the EELS spectrum, recorded across the diameter of a coated tube, and spectra abstracted at different positions are shown in Figure IV.10. The figure reveals the development of the Ti-L, O-K and C-K signals across the tube. Due to the high ionization cross-section for the carbon 1s electrons, EELS is very sensitive to carbon. This is evident from the spectrum taken from the central region of the tube, where the integrated area of the carbon signal dominates the spectrum. In the surface region, on the other hand, the spectrum shows a small carbon signal. Elemental quantification of the spectrum abstracted from the surface region reveals a carbon content of less than 5%. This is a rough estimate for the upper limit of carbon in the film, since some carbon signal might also be due to the close proximity of the tube walls plus contamination due to exposure to ambient air. The shape and intensities of the Ti and O features in the EELS spectra correspond to TiO_2. It must be stressed here that the shape and intensity of the ionization edges in EELS are very sensitive to the local chemical surrounding of the ionized species. The correspondence of the shape to what is expected for TiO_2 therefore indicates a high purity of the as-deposited film.

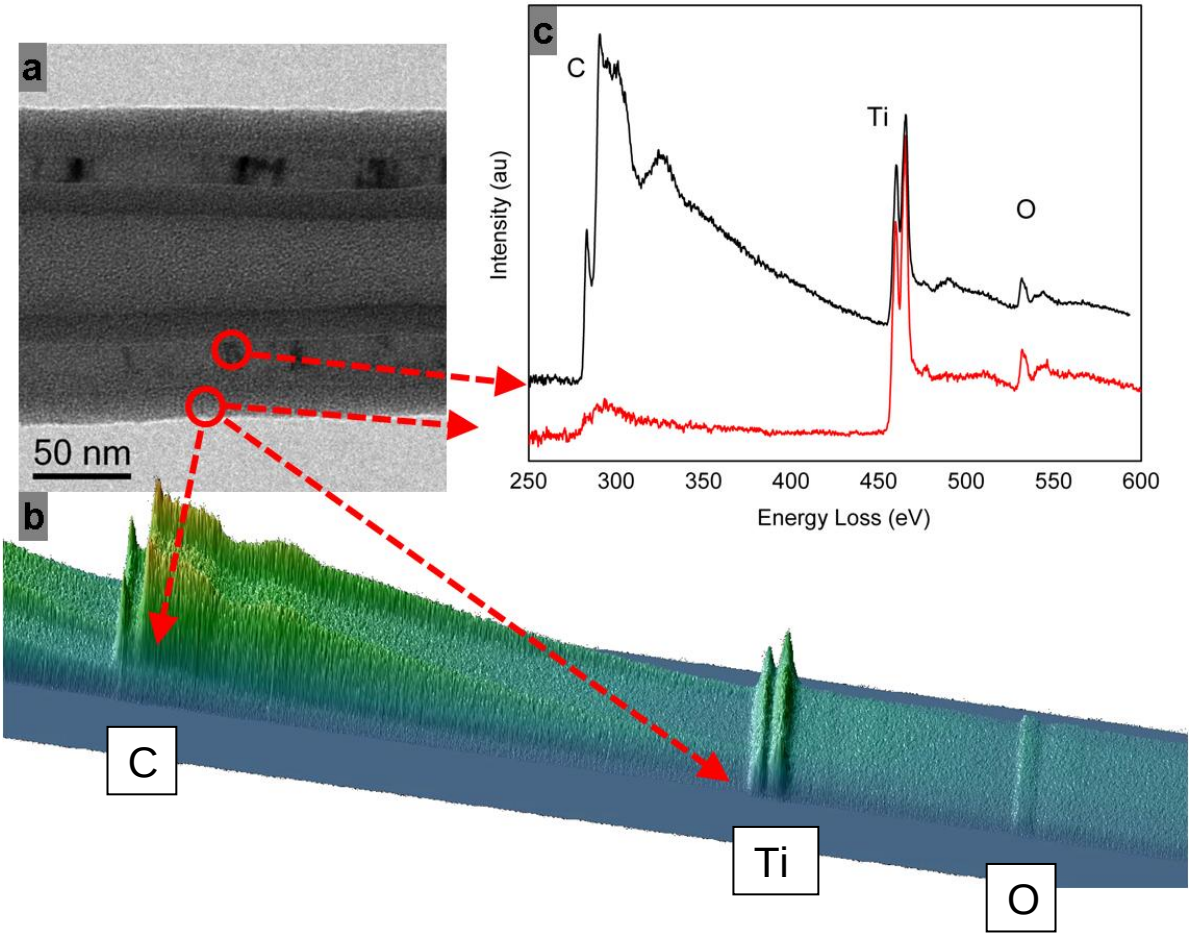

Figure IV.10. a) shows the section of a TiO_2-coated CNT from where the EELS signal was recorded (film thickness ~ 16 nm). The recorded intensity is shown in b) as a three-dimensional plot in the energy dispersive plane. It reveals the development of the C-K, Ti-L and O-K edges across the tube. The EELS spectra abstracted from the coating (red) and from a region where the signal includes the films on the top and bottom surface plus the CNT walls (black) are shown in c).

III.3. Electron microscopy characterization of TiO_2 coating on the different CNTs

In each ALD deposition process, the four differently functionalized tubes were simultaneously coated in the same chamber in order to have exactly the same deposition conditions. Figure IV.11 shows the resulting coatings obtained as a function of the CNT type. As expected, a homogeneous thin film growth was observed on the surface of CNT700 (Figure IV.11a). As compared to the morphology of the film on the CNT700, the TEM image of the CNT1500 reveals a more granular aspect (Figure IV.11b). Indeed, a pronounced particulate structure can be seen on the inside and outside walls of the carbon material. The surface of the CNT3000 is characterized by steps around the tubes surface (cf. Figure IV.8e,f). TEM investigation after ALD deposition reveals that the highly graphitic walls remain mostly uncoated, whilst TiO_2 deposition and growth can be observed

at the cone edges (Figure IV.11c). Finally, the coating of the CNT700 after partial defunctionalization (CNT700D) appears more granular than in the case of the CNT700 (Figure IV.11d). As expected, this is a result of a reduction in the oxygen containing surface groups and hence, a reduced availability of anchoring sites.

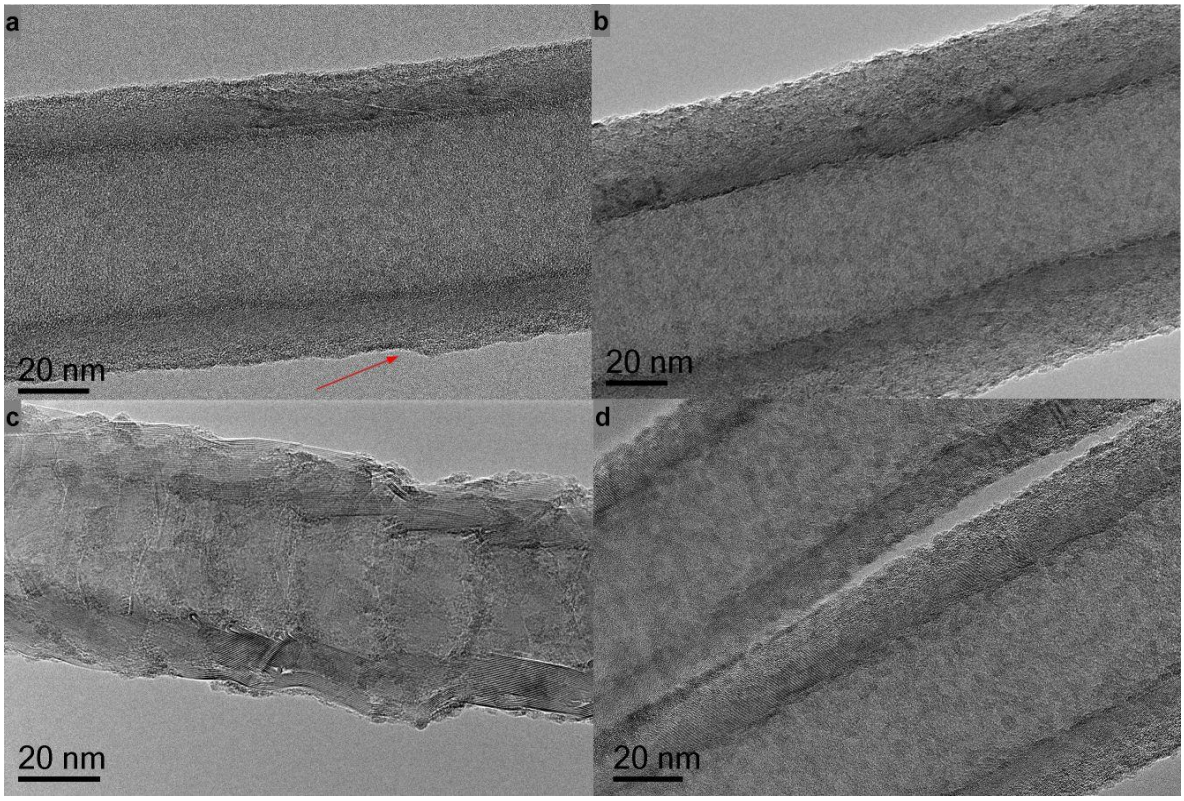

Figure IV.11. Overview TEM images of CNTs coated with TiO_2 by ALD. a) CNT700 (100cycles), b) CNT1500 (50cycles), c) CNT3000 (50cycles), d) CNT700D (100cycles).

In the following, a more detailed characterization of the various coatings will be presented for each CNT type.

III.3.1. TiO_2@CNT700

The homogeneous coating on CNT700 is shown in Figure IV.11a and in Figure IV.12 for a film obtained after 100, 50 and 500 ALD cycles, respectively. Slight variations of the contrast in the central region are due to the projection of thickness variations (dents and hills) and structural inhomogeneities in the amorphous carbon layer of the tube wall. The latter can be nicely seen on the outer surfaces of the wall. Contrast variations seen in the central region might also be due to inhomogeneities of the film itself. However, when looking at the surface regions where the electron beam passes perpendicular to the surface normal of the graphitic walls, the titania film appears as a

thin layer of darker contrast on the inner and outer surface of the tube. It smoothly follows all the hills and valleys of the tube surface in a conformal way and with relatively constant thickness (see Figure IV.12a and arrow in Figure IV.11a).

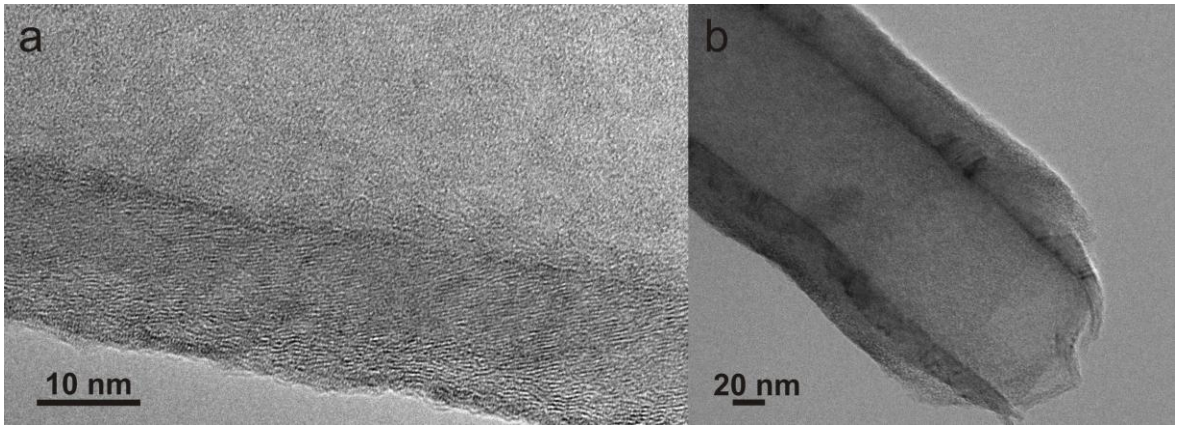

Figure IV.12. TiO_2 coating on CNT700 after a) 50 cycles and b) 500 cycles.

SEM images of CNT700 coated with 65 TiO_2 ALD cycles support these findings (Figure IV.13). The homogeneous contrast indicates a very smooth coating of the surface, which is only interrupted by occasional defects in the film (cf. also the SEM image of the uncoated tube in Figure IV.9).

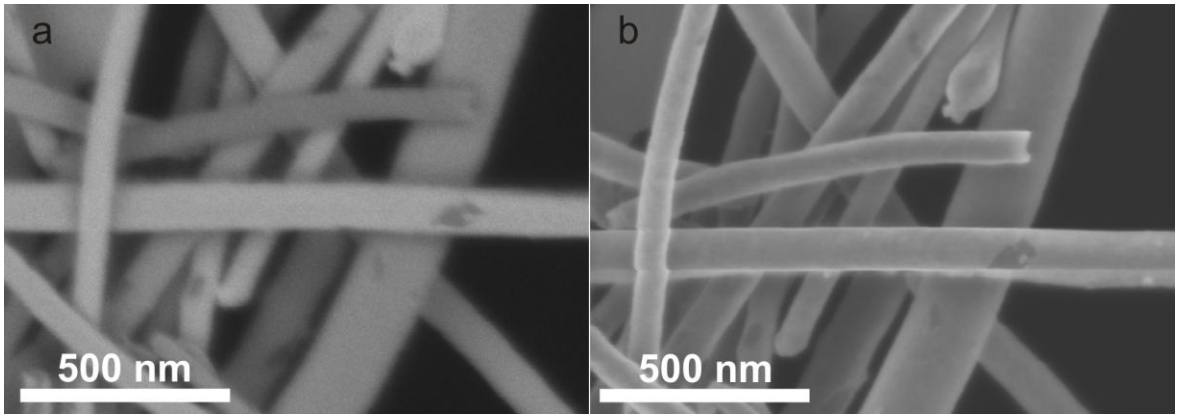

Figure IV.13. SEM images of the CNT700 coated with 65 TiO_2 ALD cycles recorded using a) secondary electrons and b) backscattered electrons.

III.3.2. TiO_2@CNT1500

As previously noted, a granular morphology of the film is observed on the CNT1500. At higher magnification, HRTEM imaging confirms the different and more granular aspect of the grown films when compared to the smooth coating observed in the case of the CNT700. The particulate structure can be seen on the inner and outer part of the carbon material for the CNT1500 (Figure IV.14). Especially, at the outer CNT surface, where the film can be observed without the disturbing background, the formation of titania clusters is clearly visible (arrows in Figure IV.14a), for

example. They measure a few nm in size and grow on the curved carbon crystallites, i.e. in defective areas. The same growth mode is also evident in the SEM image shown in Figure IV.14b. It reveals titania particles as bright dots that are randomly distributed on the surface of the CNT. The SEM image (Figure IV.14b) also shows relatively large regions that remain completely uncoated. These uncoated regions are still observed after an increase of the number of cycles as shown in the TEM (Figure IV.14c,d) and the HAADF-STEM images (Figure IV.14e,f). This phenomenon will be discussed in the next part. Similar to the coated CNT700, the exposed graphitic planes at the end of the CNT1500 remain uncoated as shown in Figure IV.14c.

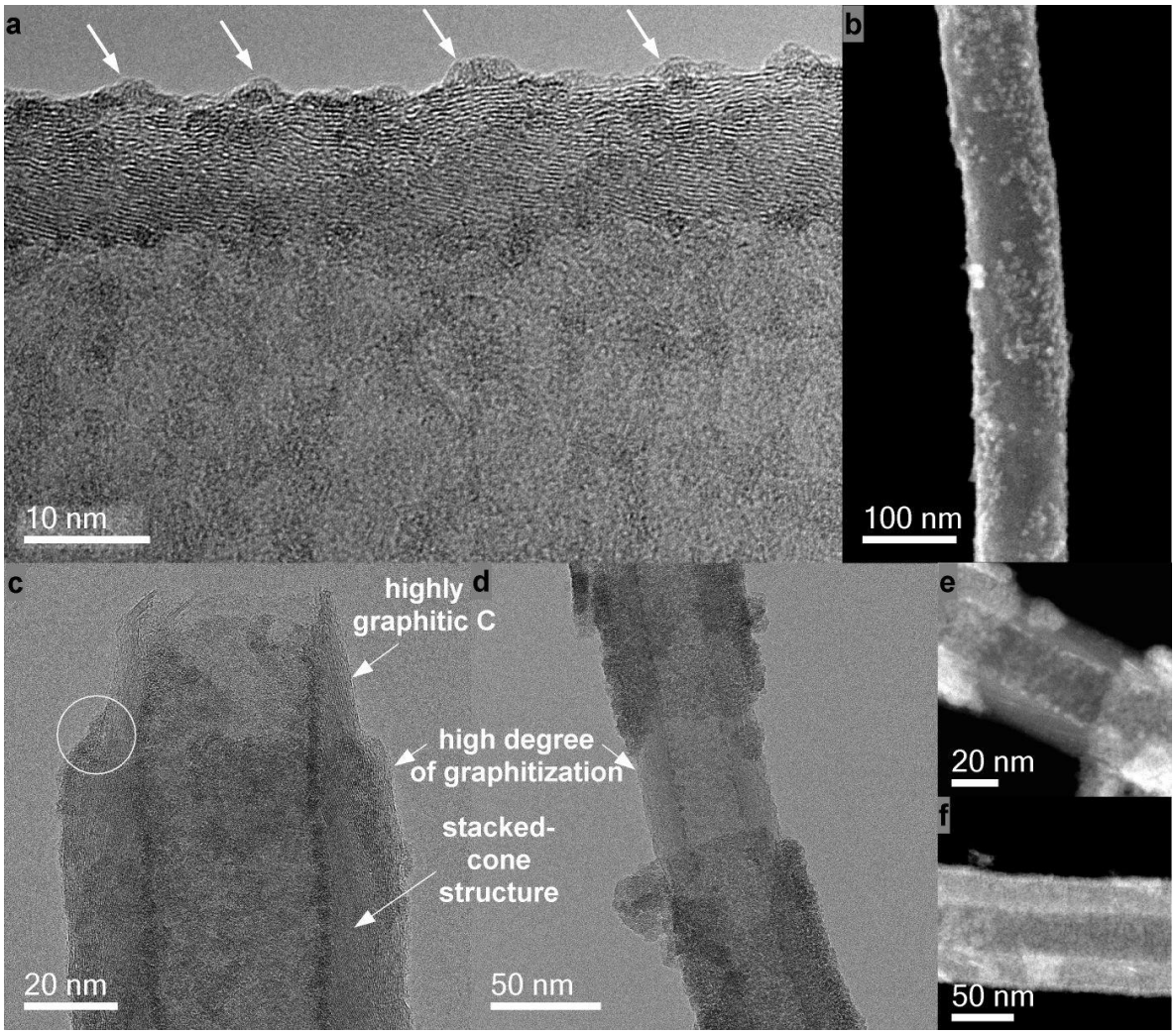

Figure IV.14. a) HRTEM and b) SEM images recorded from the CNT1500 after 50 TiO_2 cycles. c,d) HRTEM and e,f) HAADF-STEM images of uncoated regions recorded from tubes after 100 cycles.

III.3.3. TiO_2@CNT3000

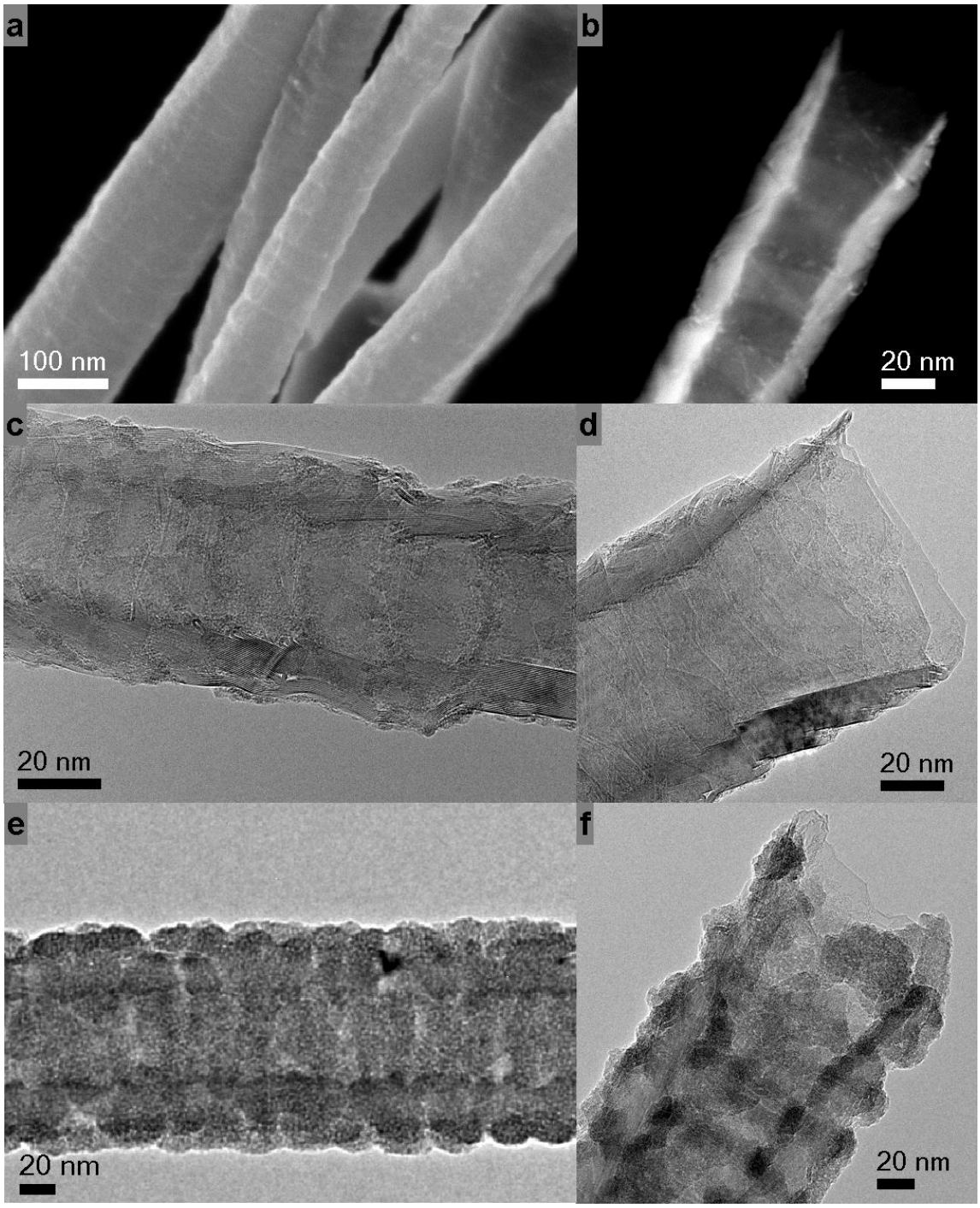

Figure IV.15. a) SEM, b) HAADF-STEM, c,d) HRTEM and e,f) TEM images of the CNT3000 coated with b) 25, a,c,d) 50 and e,f) 500 TiO_2 ALD cycles.

As demonstrated by HRTEM prior to ALD processing, the CNT3000 shows a particular structure made of steps, walls and flat terraces that are highly graphitic (cf. Figure IV.8e,f), in agreement with Paredes *et al.* STM investigations.[38] Figure IV.15a shows a SEM image of several CNTs

coated with 100 ALD cycles. As expected, the exposed graphitic parts remain mostly undecorated, and deposition only takes place at the edges of the connected cones. The ALD leads to rings of TiO_2 films wrapped around the CNTs. These structures are clearly visible on the high angle annular dark field STEM image (Figure IV.15b) and can also be seen in the HRTEM images (Figure IV.15c-f). The increase of the cycle number to 500 cycles does not fade out the morphology of TiO_2 to a continuous film; its "ring-structure" can nicely be observed in Figure IV.15e and f.

III.3.4. TiO_2@CNT700D

Similar to the case of the CNT1500, coating of the defunctionalized tubes (CNT700D) leads to a granular aspect of the film (Figures IV.16 and IV.17). The particulate structure is clearly observed on the inner and outer part of the carbon material. Compared to the CNT1500, the average particle size is slightly smaller and the coating more homogeneous. Especially, the SEM and STEM images (Figures IV.16b and IV.17a) show that the particle density is higher and more regular, i.e. without large regions that remain completely uncoated. After many ALD cycles, the film becomes conformal due to the transition from an island to a 2D growth mode. Figure IV.17b-e shows the growth transition. While after 100 ALD cycles a granular thin film can be noted (Figure IV.17c), with an increase number of cycles to 400 and 1000 cycles, a complete TiO_2 layer starts to appear (Figure IV.17d) and a smooth homogeneous coating (Figure IV.17e) is obtained, respectively. This is in contrast to what is observed for the CNT1500 support, where the coating does not reach the same degree of conformality and remains rough. Electron microscopy investigation furthermore reveals that the large uncoated regions, frequently observed in the case of the CNT1500 support, are absent in the case of the CNT700D tubes.

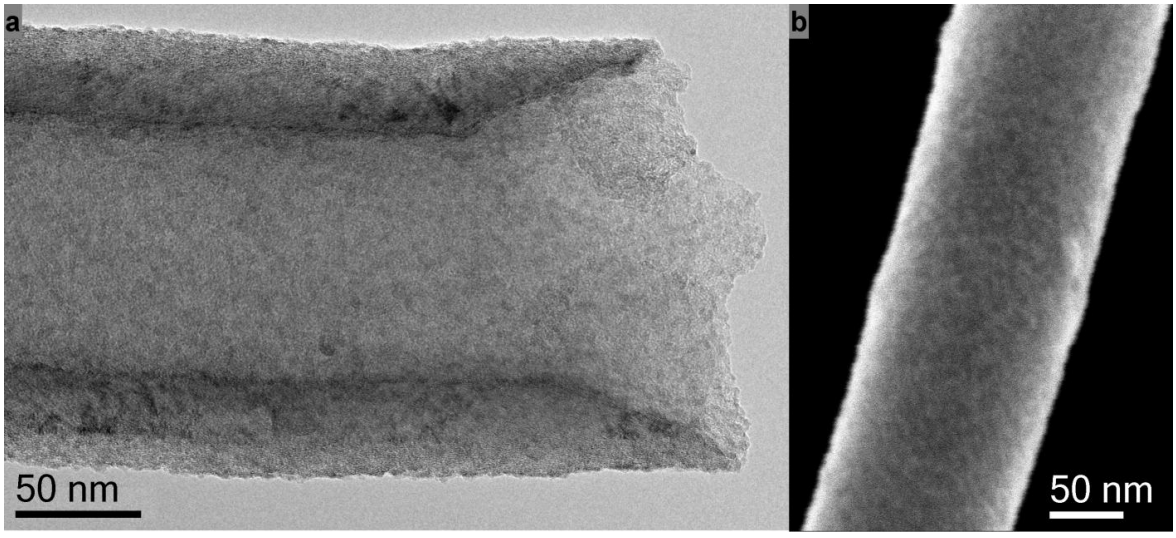

Figure IV.16. a) HRTEM and b) SEM images of CNT700D coated with 50 TiO_2 ALD cycles.

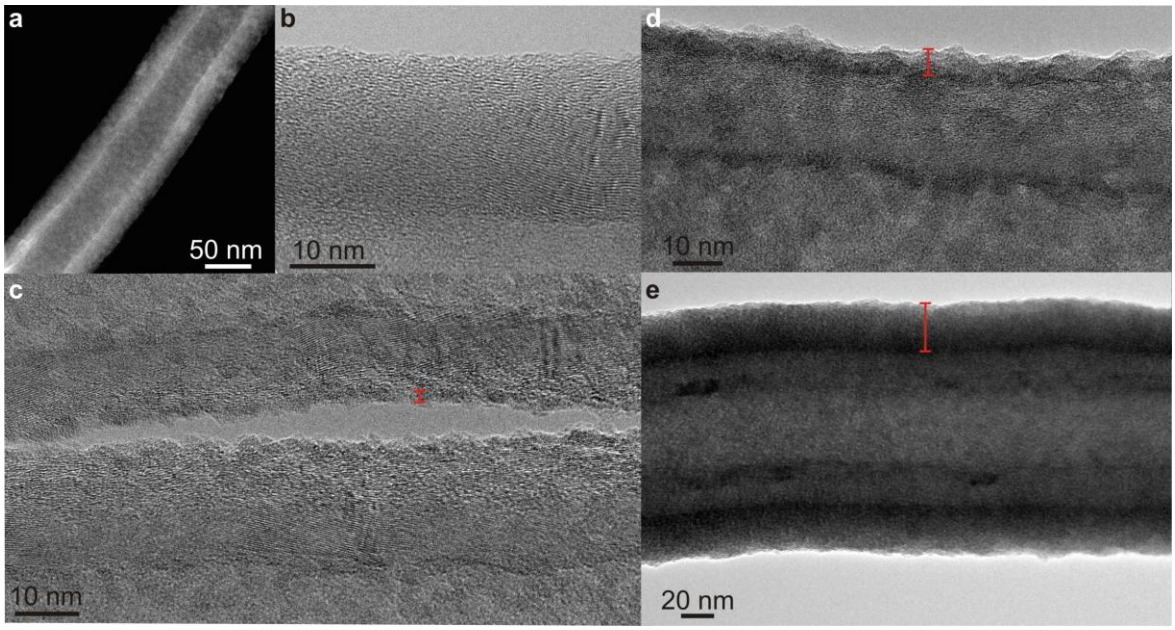

Figure IV.17. a) HAADF-STEM image of CNT700D coated with 100 TiO_2 ALD cycles. HRTEM images of CNT700D coated with b) 0, c) 100, d) 400 and e) 1000 TiO_2 ALD cycles. N.B. in c) two neighboring tubes are imaged.

III.4. Discussion

While a conformal and homogeneous coating is observed on CNT700, a granular aspect and large uncoated areas are noticed on CNT1500 (as shown in Figure IV.18a). We have already shown that the precursor vapors used in the present ALD process are able to diffuse into small pores and lead to a complete coating even on the inner walls throughout long tubes. If we exclude mechanical peeling off of the film after deposition due to weak connections between film and tube, we can conclude that regions that remain uncoated are either due to a covering of the respective region during the ALD process (touching tubes or connections with the support) or due to a lack of growth initiation events. This is consistent with previous observations[24] that have shown that no growth occurs on defect free graphitic planes (cf. also Figure IV.14c-f and HRTEM images for 100 and 500 TiO_2 ALD cycles in Figure IV.18b,c). It can therefore be concluded that the differences observed between the CNT700 and CNT1500 tubes in terms of the aspect of the coating is directly related to the different density and distribution of suitable initiation sites. At 1500 °C, the small graphitic domains or graphene sheets (BSUs) grow to form larger crystallites of sp^2-hybridized carbon.[39] Paredes *et al.*[38] investigated the pristine cup-stacked CNTs used in the present work and they observed by scanning tunneling microscopy the formation of flat terraces after annealing at 1500 °C. These domains are defect-free, hence they do not provide any anchoring point during the ALD of TiO_2. The latter is no longer able to grow as a film but instead it forms nanoparticles centered on defective areas, rich in O-containing surface functional groups.

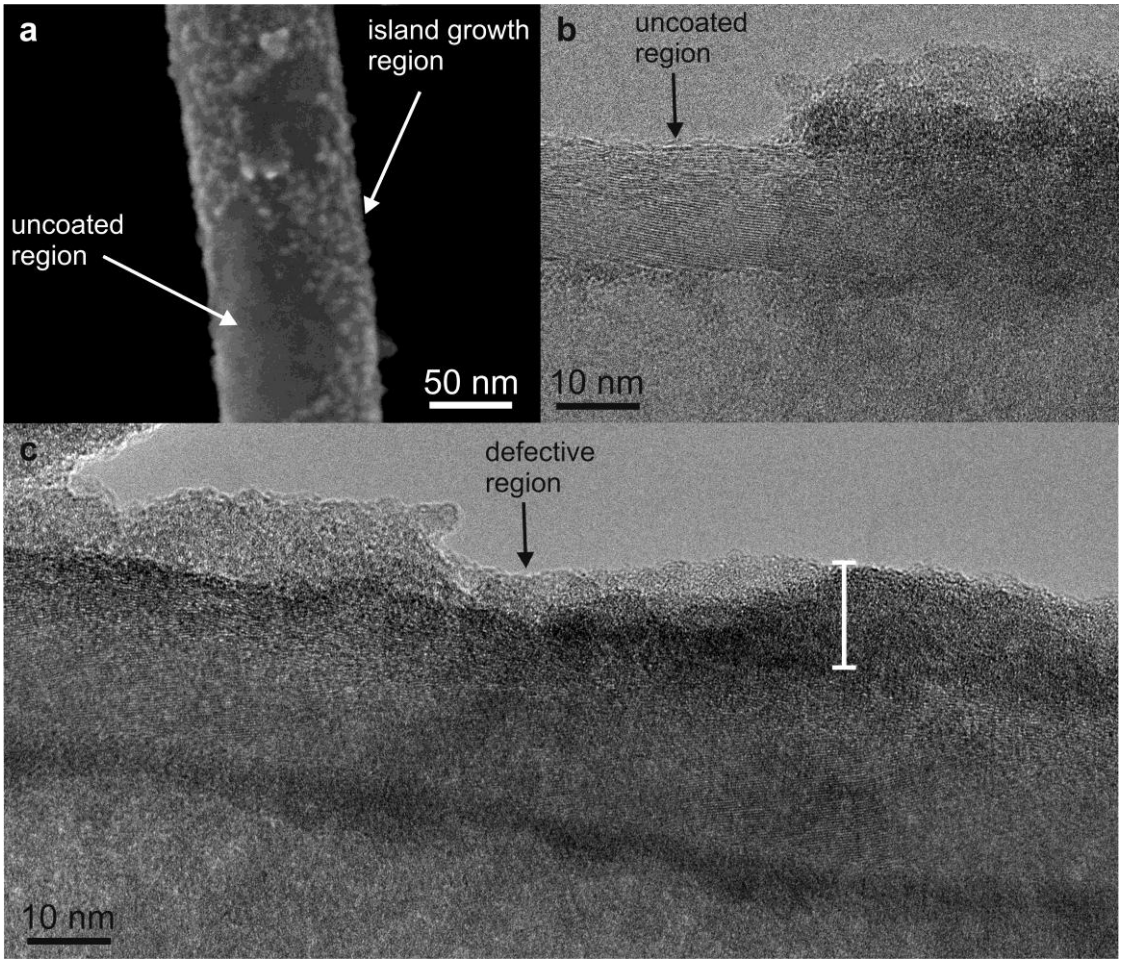

Figure IV.18. a) HRSEM image recorded from the CNT1500 coated during 50 cycles. HRTEM images recorded from tubes coated during b) 100 and c) 400 cycles.

In order to study the development of the growth mode, the number of deposition cycles was increased to 100 (Figure IV.14c-f and IV.18b) and 500 (Figure IV.18c). The initiation of the growth appears to follow an island growth that tends to transform to a 2D growth with increasing number of cycles, leading to a homogenization of the thickness. This is already observed after 100 cycles (Figure IV.14c-f and IV.18b). However, even in thick films, domains that remain uncoated can be found (Figure IV.18b). Generally, uncoated regions are found at the endings of the tubes, where the catalytically grown graphitic surface is observed to protrude from the pyrolytic layer (sword-in-sheath failure), and, similarly, on the inner surface, in the region where the last stacked cone of the structure exposes graphitic planes. In analogy, uncoated areas observed along the tubes surface are due to the absence of anchoring site, preventing the initiation of film growth.

With the increase of the graphitization of the carbon nanotubes, a peculiar and more granular aspect of the as-deposited metal oxide is noticed. Indeed, the TiO_2 ALD on CNT3000 leads to the

formation of particles at the edge of connected cones present on the material. The reason for this is the high curvature at the edge, which involves the presence of structural defects (5-membered rings) and strained C-C double bonds. In these regions, the sp^2-hybridized carbon atoms easily react to become sp^3-hybridized and thus release the strain. HNO_3 is typically used to open SWCNTs and MWCNTs because it preferentially reacts with the curved tips of the tubes. Similarly, while the oxidizing power of HNO_3 is not strong enough (in our reaction conditions) to break C-C double bonds and functionalize the graphitic terraces, it reacts and creates O-containing functional groups on the curved graphene sheets between two cones. As a result of the preferential deposition at the edges, the formation of TiO_2 rings occurs around the CNTs (Figure IV.15c-f). In the Figure IV.19, the edge initiation is clearly visible and pointed out by arrows. Moreover, HAADF performed after 25 ALD cycles (Figure IV.15b) demonstrated the formation of nanoparticles on the transversal axis of CNTs. A reference image before coating can be seen in Figure IV.21. The series of HRTEM images acquired from CNT3000 coated with a varying number of TiO_2 ALD cycles, i.e. 50 (Figure IV.19a,b and IV.15), 100 (Figure IV.19d) and 500 (Figure IV.19c), clearly shows the defective regions where the TiO_2 growth initiates. From these observations it can be concluded that the acidic treatment on the high temperature (3000 °C) treated CNTs leads only to an oxidation at the edges, where the carbon sheets are highly curved or are abruptly terminated. The titania deposition clearly demonstrates this functionalization. At low magnification, TEM permits to ascertain that these defects are homogeneously distributed all along the tubes. This is shown in Figure IV.20, where two tubes present TiO_2 clusters that are related to the surface structure of the tubes (see edges in the SEM image of Figure IV.15a).

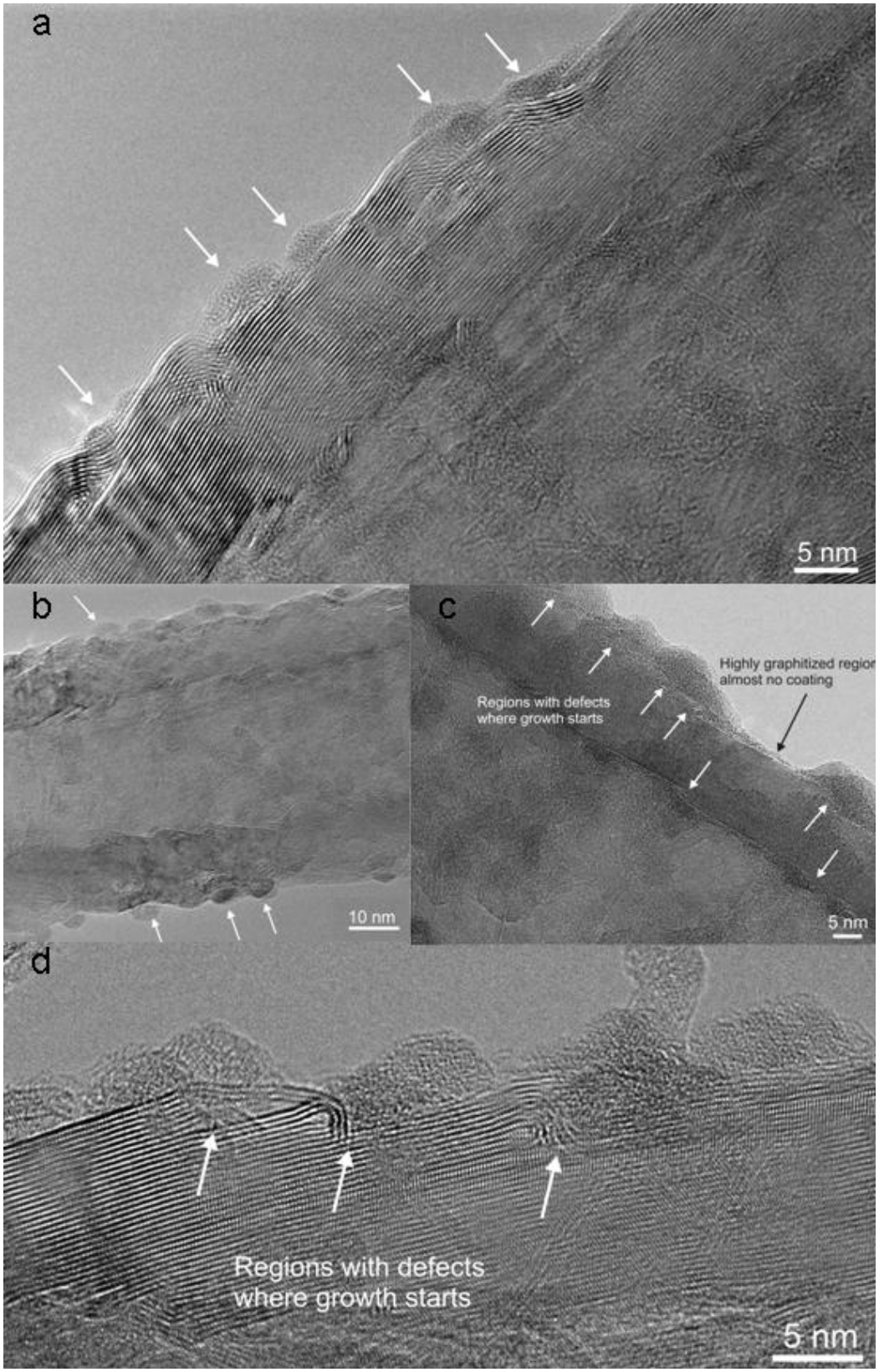

Figure IV.19. HRTEM image of the CNT3000 coated with a, b) 50, c) 500 and d) 100 TiO_2 ALD cycles.

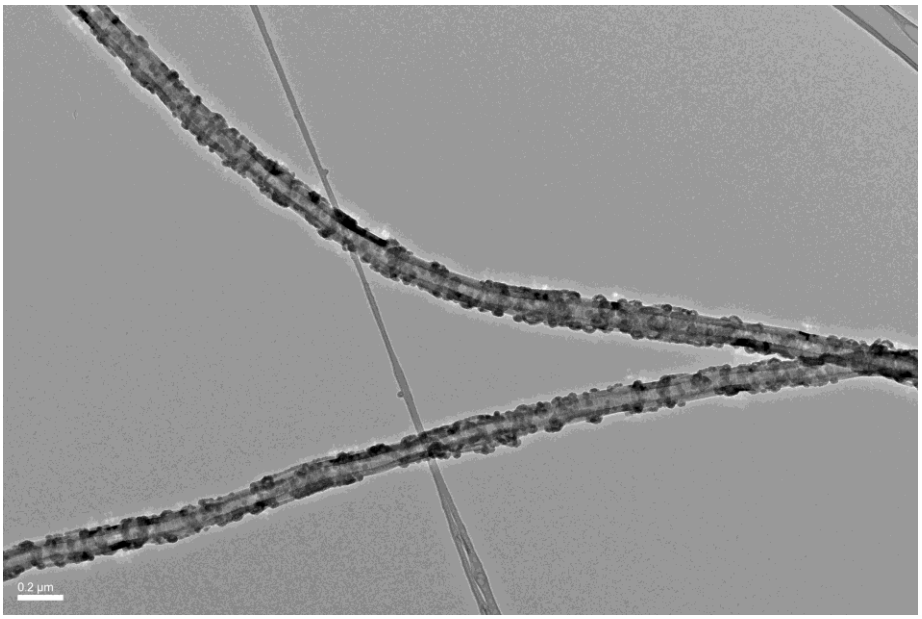

Figure IV.20. Low resolution TEM image of the CNT3000 coated with 400 TiO_2 ALD cycles showing the nucleation at defect sites which is similar at different regions of the CNT3000.

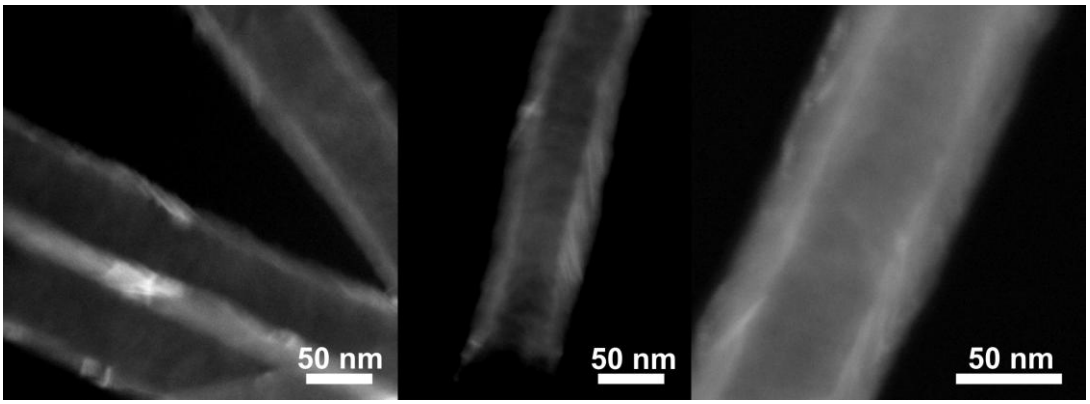

Figure IV.21. HAADF-STEM images of uncoated CNT3000.

Concerning the deposition on CNT700D, a higher and more uniform particle distribution was noticed than on the CNT1500. This observation is consistent with the X-ray photoelectron spectroscopy (Figure IV.7) analysis of both supports prior to ALD. Here, the O/C ratios for the CNT1500 and CNT700D, determined from XPS spectra, are very similar, i.e. 0.012 and 0.011, respectively (cf. Table IV.1 and Ref.[27]). It can be concluded that for the CNT1500 support, defective areas with a high concentration of O-containing groups are dispersed within a patchwork of (non-functionalized) graphitic regions. In contrast, for the CNT700D support, the oxygen concentration is lower but the groups are more homogeneously dispersed throughout the surface. This is also confirmed with a series of HRTEM images acquired after coating with 0 to 1000 cycles of TiO_2 ALD (Figure IV.16a and IV.17b-e).

IV. Engineering of MO_x@CNT by CNT surface functionalization

In order to elaborate well controlled MO_x@CNT heterostructures, the SnO_2 and ZnO ALD coatings of the differently functionalized CNTs were investigated. The capability of tailored surface functionalization to influence the ALD coating and the defect mapping will therefore be confirmed.

IV.1. Case of SnO_2 deposition

IV.1.1. SnO_2@CNT700.

CNT700, from the same batch as the one used for the labeling study (cf. section III), were firstly coated by our novel SnO_2 ALD approach. Figure IV.22 shows CNT700 coated with a varying number of ALD cycles. After 60 cycles (Figure IV.22a), the continuous coating on the inner and outer walls is visible; the granular aspect, as described in section II, can nicely be seen. As expected, with the increase of the number of cycles, a relatively homogeneous and smooth film is obtained (Figure IV.22b,c), similar to the SnO_2-coated CNTs previously presented in Figure IV.2.

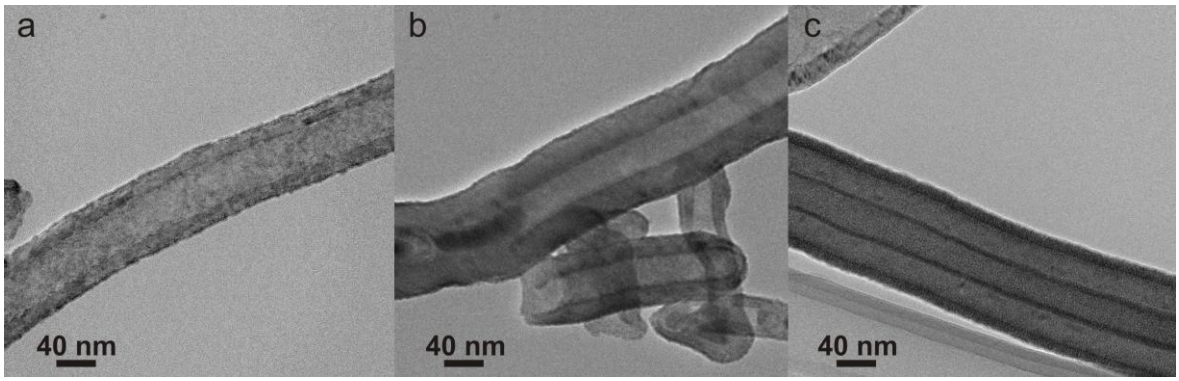

Figure IV.22. TEM images of SnO_2@CNT700 after a) 60, b) 200 and c) 400 ALD cycles reveal a conformal and continuous coating.

IV.1.2. SnO_2@CNT3000.

CNT3000 were also coated with 50, 100, 400 or 1000 SnO_2 ALD cycles. After 50 cycles, small particles nucleating on the curved graphene sheet between two cones initiate the formation of rings wrapped around the CNT (Figure IV.23a). This particular structure is well observed after a thicker deposition (Figure IV.23b-d). Particles tend to form clusters, resulting in a continuous wrapping, while the highly graphitic planes remain uncoated. HRTEM confirms the initiation at the step edge and corroborates the conclusion drawn for the TiO_2 deposition on the defect localization. Indeed, in Figure IV.24, the arrows clearly point to particles nucleating on defective spots of the tubes. Each of them can be correlated to either an edge or a dip in the graphitized carbon. Identical metal oxide ring structures, wrapped around CNTs, are obtained for both titanium- and tin oxide, demonstrating

the capability of surface groups and defects engineering to tailor the coating morphology independent of the intrinsic growth mode characteristic of the ALD process chosen. Finally the dotted circle in Figure IV.24b highlights the presence of lattice fringes.

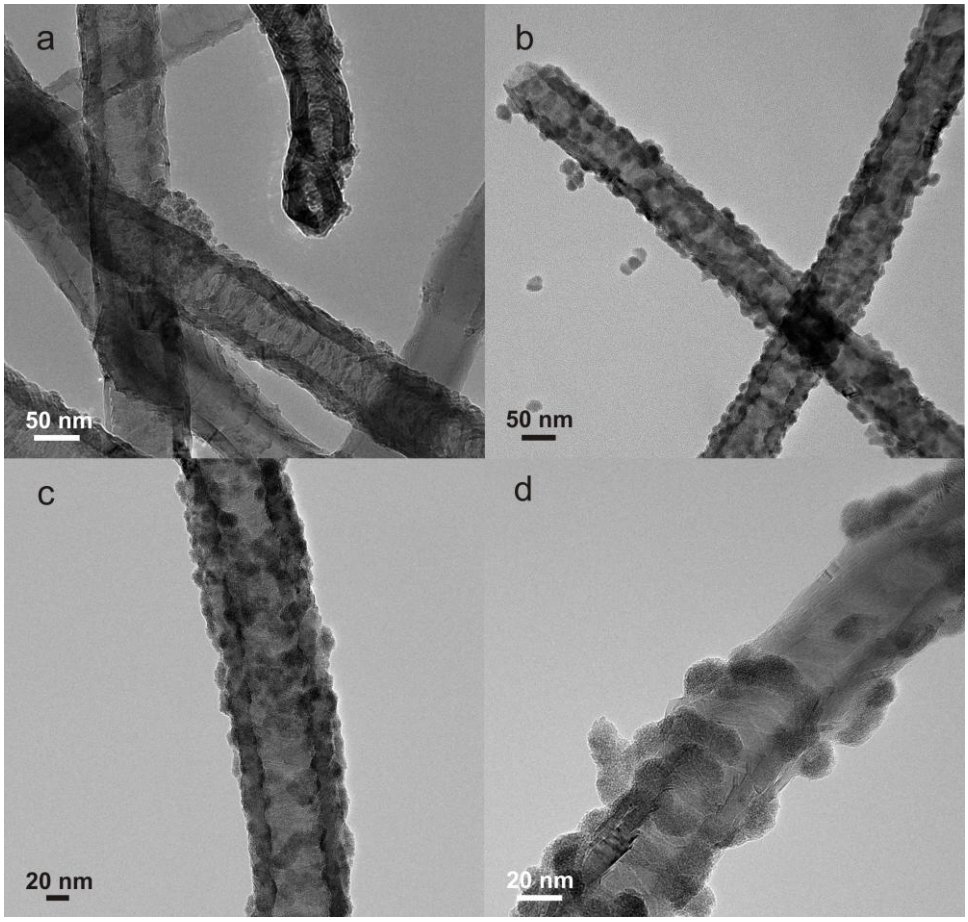

Figure IV.23. TEM images of CNT3000 coated with a) 50 cycles and b-d) 400 SnO_2 ALD cycles. Loose particles, resulting most likely from a mechanical removal, are observed in b).

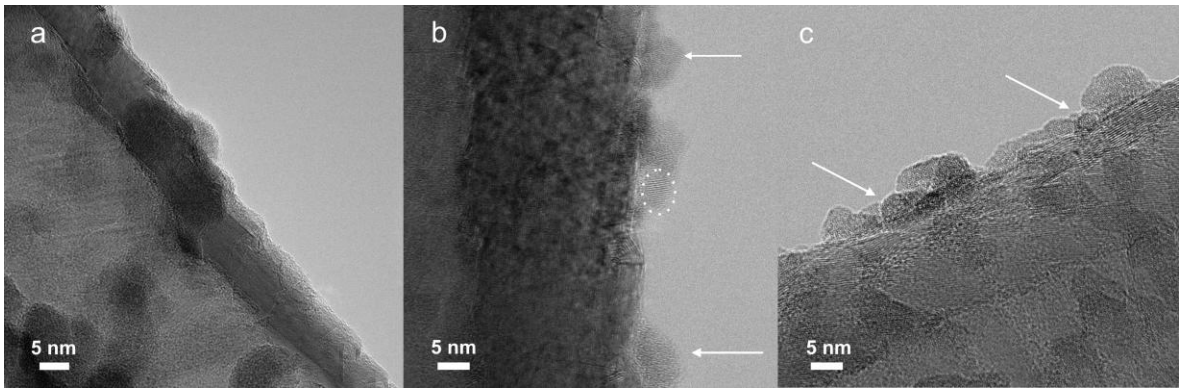

Figure IV.24. HRTEM images of SnO_2@CNT3000 after a) 400cycles, b and c) 50 cycles. The arrows point to some particles nucleating at defect sites and the dotted circle underlines lattice fringes related to SnO_2 rutile phase.

IV.1.3 Study of the crystallinity of the as-deposited SnO_2

As previously established (cf. section II and Chapter II), the as-deposited tin dioxide shows an onset of crystallinity that could not be elucidated by XRD. Only HRTEM and Fourier filtered images permitted to enlighten the presence of SnO_2 in a tetragonal phase. These findings were explained by the presence of sub-10 nm crystallites embedded into an amorphous phase leading to a strong XRD background. Therefore, only electron microscopy performed on SnO_2@CNT700 where the supporting carbon is very thin allowed the observation of some lattice fringes. HRTEM studies of the SnO_2@CNT3000 show also some crystallinity. Problably due to mechanical removal during the dry TEM grid preparation, detached particles were also observed in the images, offering ideal conditions for the study of the crystallinity. The power spectra of the TEM image were realized on detached particles. The diffraction spots visible on the power spectra shown in Figure IV.25, are indexed to the crystal plane (110) of the tetragonal rutile phase. Its calculated plane spacing is 3.34 Å and 3.44 Å for the full and area selected power spectrum, respectively (Figure IV.25b,c). These values are in agreement with the crystallographic data (JCPDS card nº 04-015-3277).

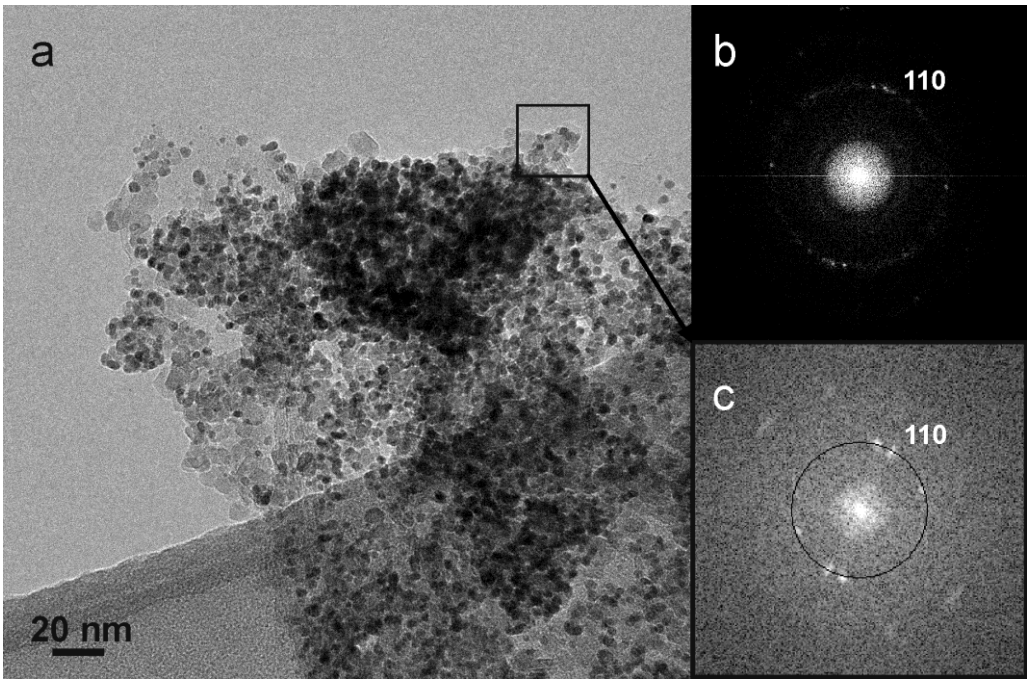

Figure IV.25. a) TEM image of SnO_2 particles, on a holey carbon grid, detached from the CNT3000, with visible lattice fringes, b) the corresponding power spectrum and c) the power spectrum of the area selected by the square.

From the fast Fourier transform (FFT) of a HRTEM image (Figure IV.26a), Fourier filtered images using the spacing (002) of the graphitized carbon and the (200) and (101) of the rutile tin dioxide

(Figure IV.26b-d), were realized. SnO_2 particles are visible in the Fourier filtered image, which is a sign of the presence of lattice fringes corresponding to the (200) and (101) planes. In Figure IV.26d, the arrow points to a particle observed in an area where the carbon contribution is low and the difference in contrast between the CNT and the metal oxide is therefore weak. This avoids any potential ambiguity on the particle appearance due to a difference of contrast and not of presence of the selected spacing.

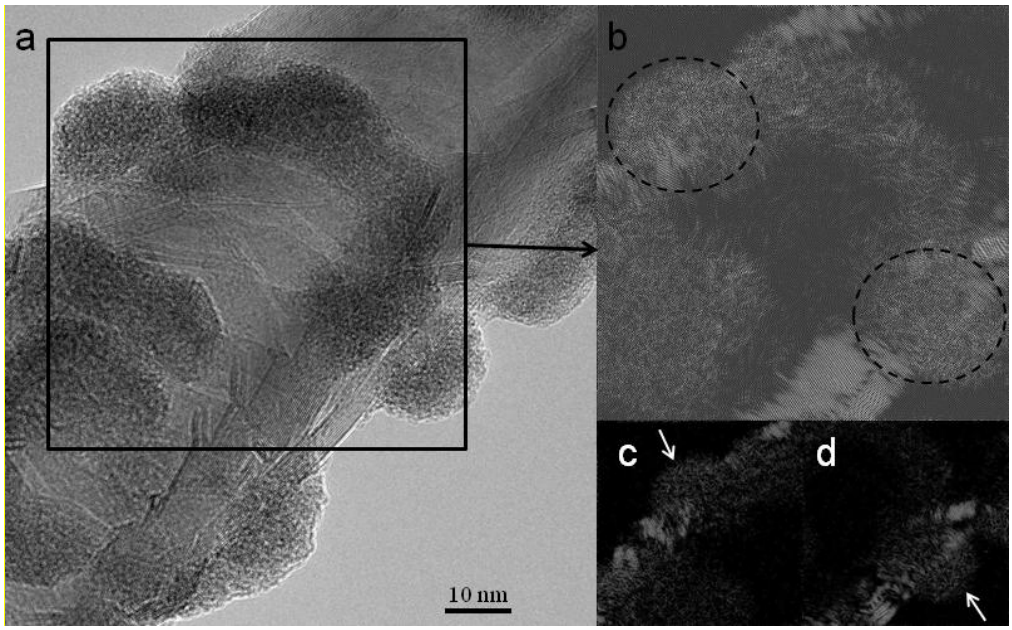

Figure IV.26. a) HRTEM image of a SnO_2-coated CNT3000 and b) its Fourier filtered image, generated using a mask including the (002) spacing of the graphitized carbon and the (101) and (200) d-spacing of the rutile SnO_2, which demonstrates the presence of some crystallites. The dashed circles show the particles on the surface. The white arrows in c) and d) Fourier filtered images (using the same spacing than in b) point to particles, indicating the presence of some lattice fringes of tin dioxide. In bright contrast, the CNT wall is also visible due to the width of the filter used and the proximity between the spacing of the carbon and of the tin dioxide.

IV.2. Case of ZnO deposition

Finally, the three types of CNTs were also coated with ZnO from diethylzinc (DeZn) and water at 100 ºC. The work on zinc oxide was realized by KyeongHwan Lee, master student at the Seoul National University, South Korea, whom I co-supervised.

IV.2.1. Electron microscopy characterization

IV.2.1.1. ZnO@CNT700

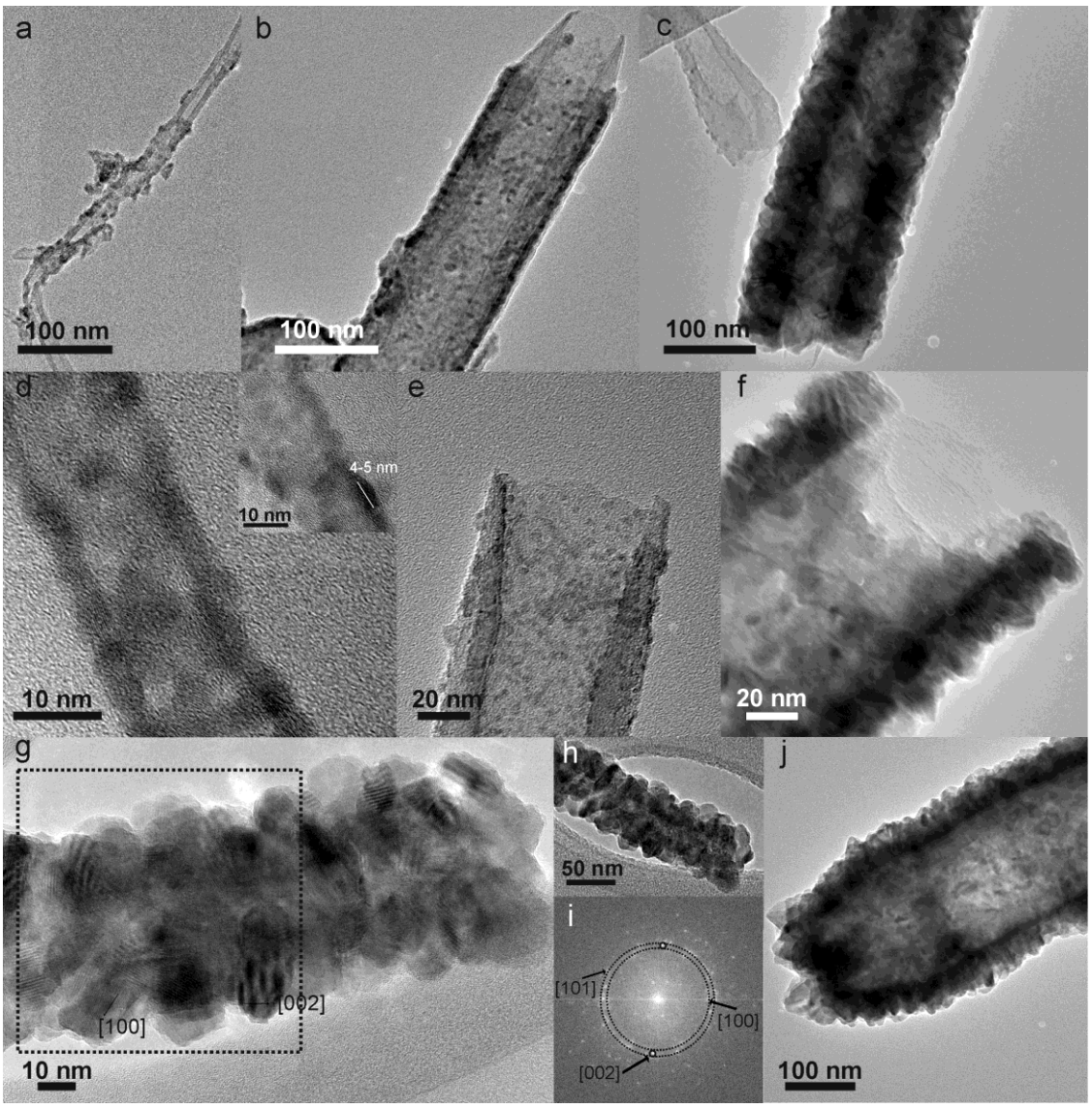

Figure IV.27. TEM images of CNT700 coated with ZnO after a,d) 20, b,e) 50, g,h) 100 and c,f,j) 200 ALD cycles. At higher magnification, d) after 20 cycles, 4-5 nm diameter size particles are visible, as shown in the inset and f) after 200 cycles, 25 nm thick film is deposited, in agreement with a GPC of ~1.2 Å/cycle. In g) the coated tube, corresponding to the one shown at low magnification in h), present lattice fringes attributed to the different planes of crystalline ZnO. In i) the corresponding power spectrum of the region delimited by the dotted square in g) corresponds to the hexagonal ZnO phase (JCPDS card nº 04-015-0825).

The obtained coated CNT700 present a rough shell of crystalline metal oxide particles (Figure IV.27). Actually, after 20 cycles, distinct 4-5 nm sized particles are formed on the walls (Figure

IV.27a and d), while when the cycle number increases to 50, isolated spherical particles (Figure IV.27e) and a continuous layer of 5-6 nm (Figure IV.27b) coexist. ZnO island growth occurs first, before a transition to 2D growth mode. Not all the particles are nucleating at the same time; in some area with less anchoring sites, a longer nucleation time is required, delaying the coalescence and then the transition to a 2D growth, which explains two simultaneous growth types in an early stage. After 100 (Figure IV.27g,h) and 200 cycles (Figure IV.27c,f,j), despite some remaining uncoated areas, the CNTs are fully covered with a homogeneous and thick polycrystalline shell. Lattice fringes are visible (Figure IV.27g) and can be attributed to the ZnO hexagonal wurtzite phase (JCPDS card nº 04-015-0825). Interesting elongated particles appear on the outer wall as shown in Figure IV.27f and j.

IV.2.1.2. ZnO@CNT1500

Although, like CNT700, CNT1500 are decorated with ZnO particles of 4-5 nm diameter size (Figure IV.28a-c), the transition from an island to a 2D growth takes place at a larger number of cycles. Indeed, less anchoring sites are present on the surface, delaying the formation of a continuous film (Figure IV.28d-f). Nevertheless, when 2D growth occurs, similar thicknesses are obtained in both carbon supports. Figure IV.28d shows in the inset a 16 nm thick film obtained after 100 cycles. As observed in the case of TiO_2 deposition, a large uncoated area remained due to an absence of functional surface group and defect.

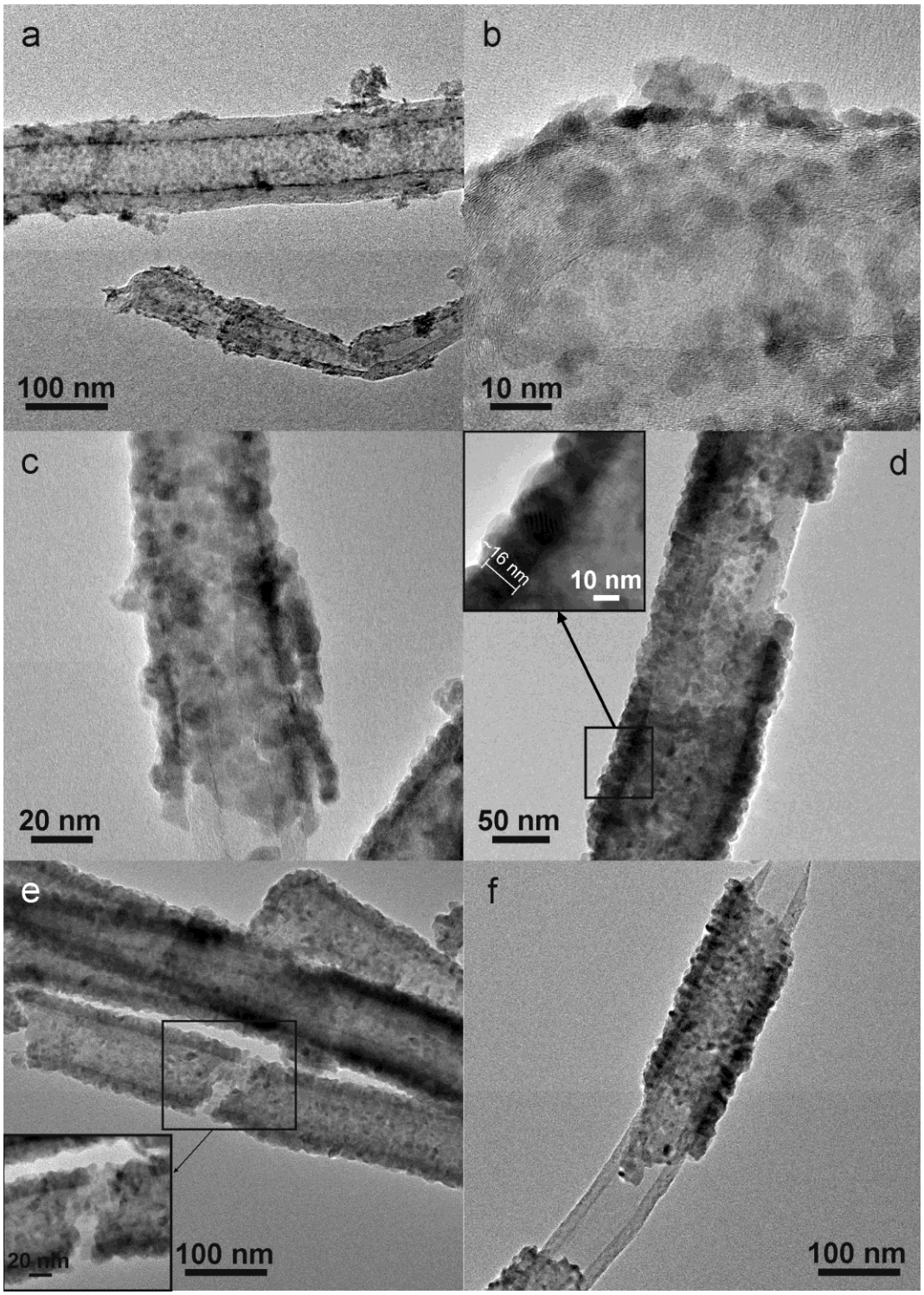

Figure IV.28. TEM images of ZnO@CNT1500 after a,b) 20, c) 50, d,e) 100 and f) 200 ALD cycles. At higher magnification, b) lattice fringes can be observed. A crystalline ~16 nm thick ZnO film was deposited onto CNT1500 as visible in the inset in d). Inset in e) shows a magnified image of the coating defect. In f) a large uncoated area is shown.

At higher magnification, crystalline particles are observed. Lattice fringes that are indexed in particular to the (002) plane of the ZnO hexagonal wurtzite phase can be observed in Figure IV.29c,d.

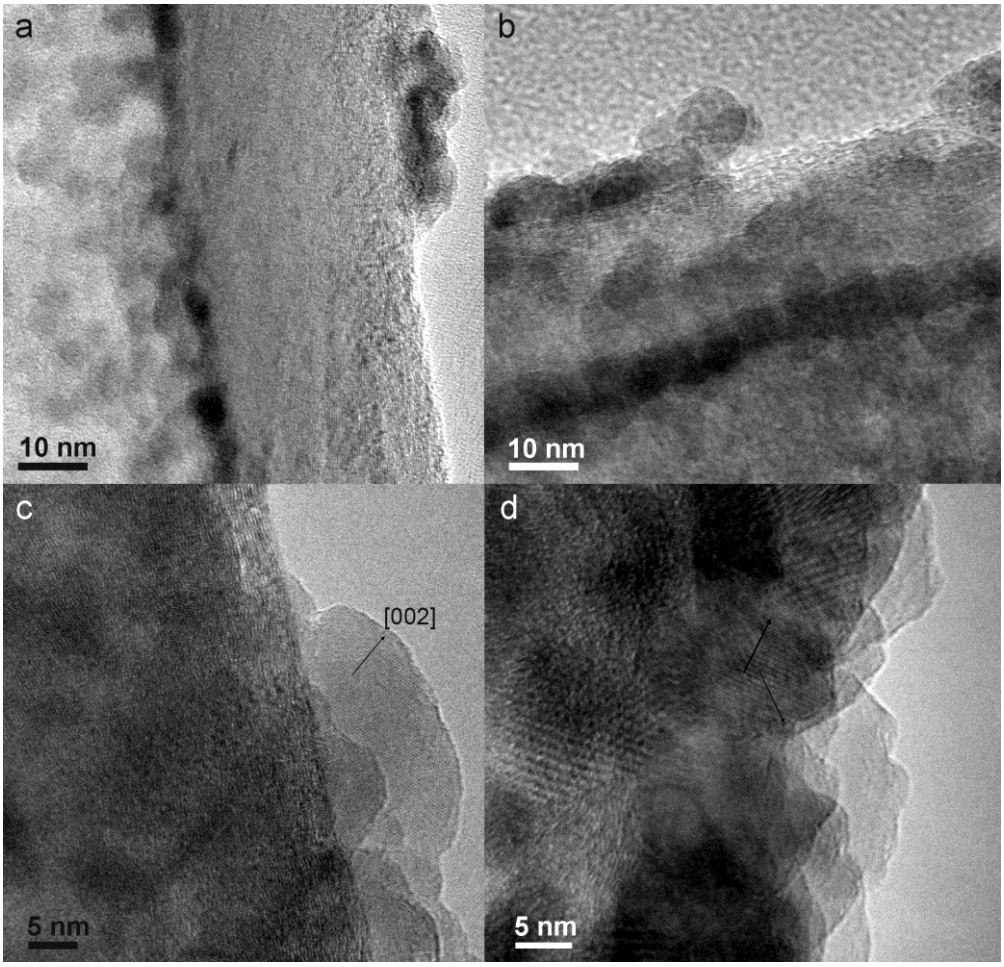

Figure IV.29. HRTEM images of CNT1500 coated with ZnO after a) 20, b) 50 and c,d) 100 ALD cycles. One can observe lattice fringes in c) and d) attributed to the crystallographic plane (002) of ZnO hexagonal phase (JCPDS card nº 04-015-0825).

IV.2.1.3. ZnO@CNT3000

Once more the coating of CNT3000 reveals a typical ring morphology of the as-deposited metal oxide. Figure IV.30 shows tubes decorated with various numbers of ALD cycles. The formation of rings transversally to the CNT axis is clearly visible in Figures IV.30c, d and e. Particles are also formed at the inner rims of the tubes (Figure IV.30e). Therefore, some parts of the outer walls of CNT3000 remain uncoated, while the inner ones are well decorated, as shown in the upper corner of the TEM image in Figure IV.30e. Similar to the SnO_2 deposition, ZnO ALD coating confirms the nucleation at the edge of the stacked cones of the CNT3000 and further proves the versatility of the surface functionalization approach for tailoring the ALD deposition.

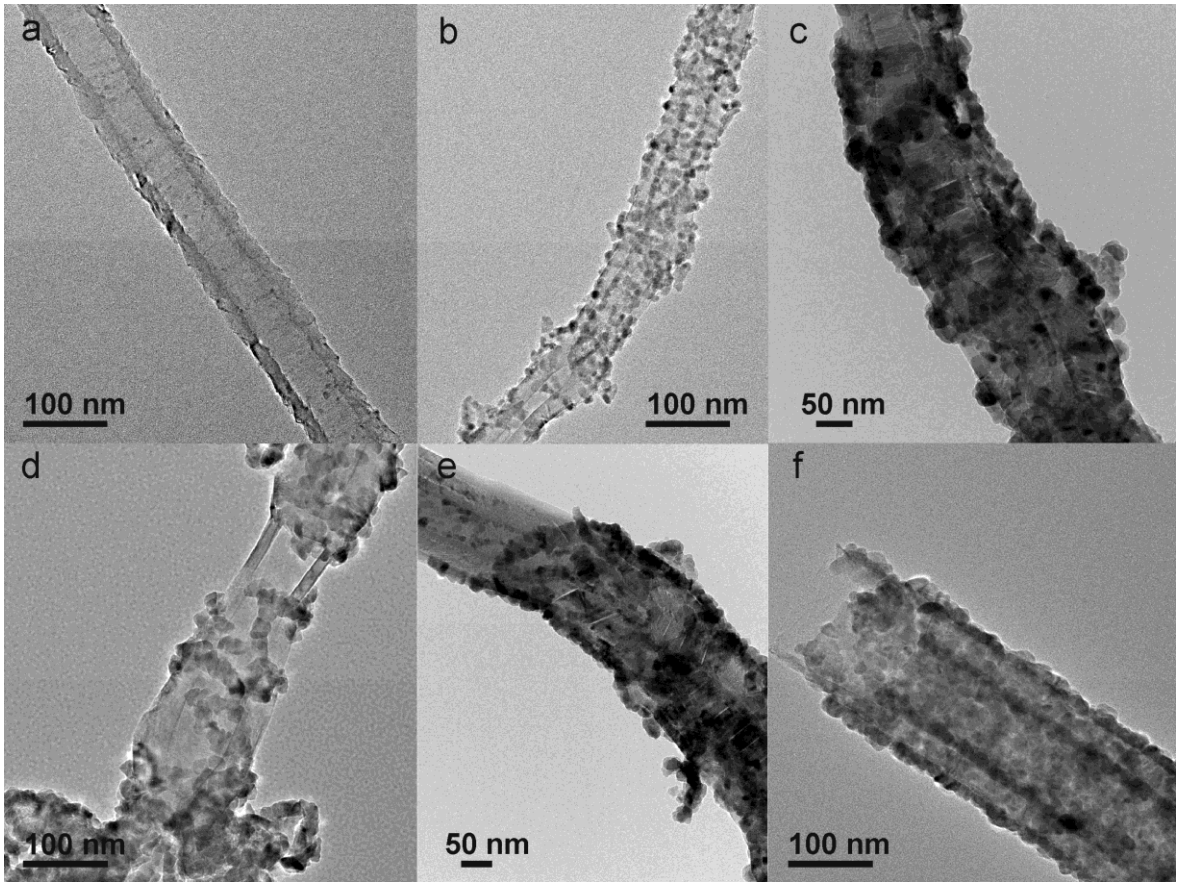

Figure IV.30. TEM images of ZnO-coated CNT3000 with a) 20, b) 50, c,d,e) 100, f) 200 ALD cycles.

At higher magnification, TEM images (Figure IV.31) clearly highlight the nucleation at the edges of the connected cones. After 20 cycles (Figure IV.31a), small particles are visible at the cone edges of the outer walls as well as on the inner rims. In Figure IV.31c,d, arrows point to some particular particles growing from those edges. The arrow in Figure IV.31b points to a curvature defect on the CNT surface on which particles are grown. These HRTEM images clearly show the particle localization on the structural defects of the tubes that preferentially consist in the sites functionalized by the nitric acid treatment, as previously mentioned. Therefore, besides being structurally ill defined, they also most probably present some O-containing surface groups, ideal for the growth initiation.

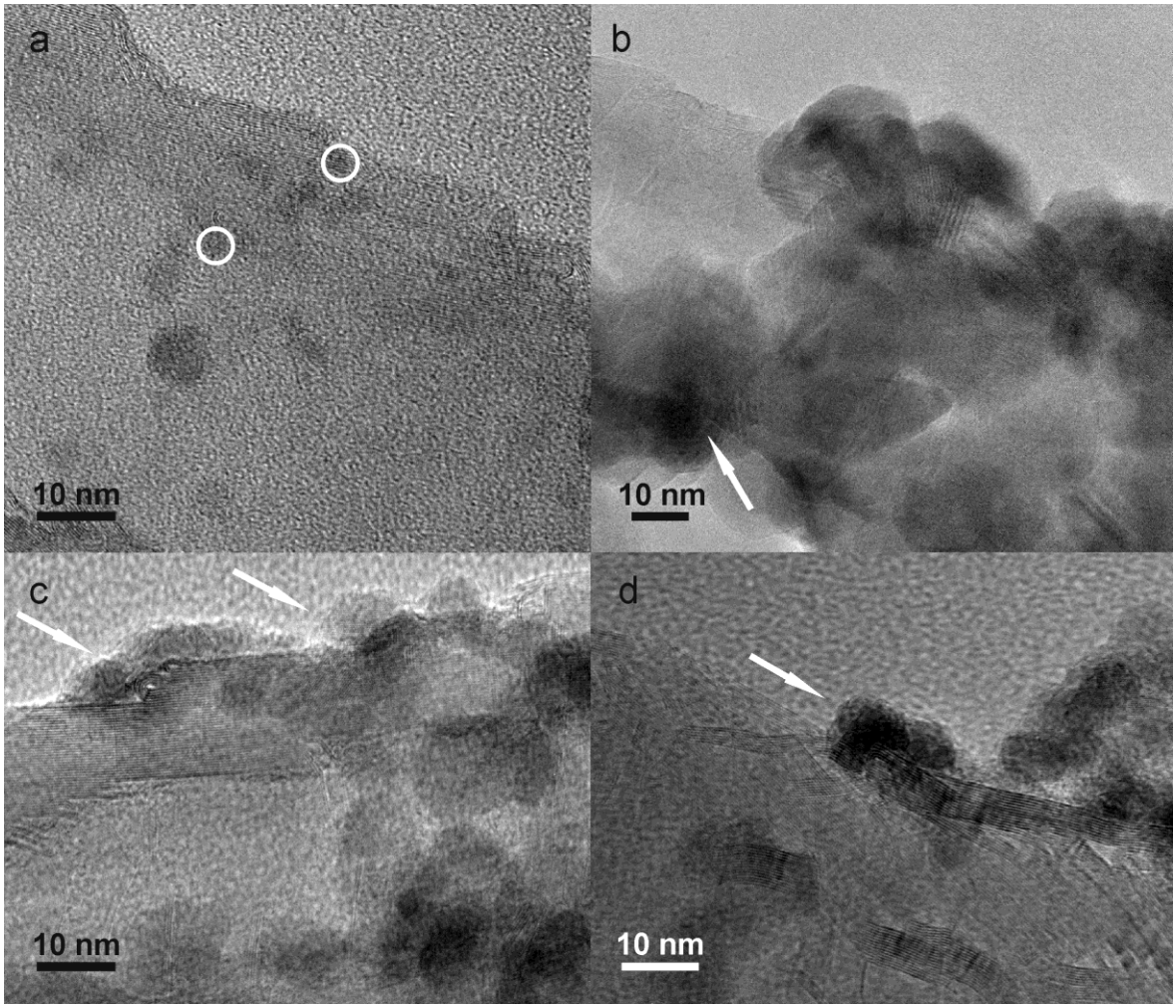

Figure IV.31. TEM images of ZnO@CNT3000 after a) 20, b) 100, c-d) 50 ALD cycles. Arrows on the images show particles nucleated at connections between rims of subsequently stacked cups or defective areas.

IV.2.2. Study of the crystallinity of the particles

In order to elucidate a possible influence of the graphitization degree on the ZnO crystallinity, HRTEM was performed in ZnO@CNT1500 and ZnO@3000. As previously reported, due to the strong influence of the surface properties of the support on the ZnO growth and a preferential orientation of the nanocrystal toward the *c*-axis at the initial stage, ZnO ALD on unfunctionalized MWCNTs leads to irregular coating.[40]

Selected area electron diffraction patterns were acquired from the ZnO-coated CNT1500 (Figure IV.32a) to investigate the crystallinity of the metal oxide. The two broad spots visible are indexed to the (002) plane of the graphitized carbon sheet (JCPDS card nº 00-058-1638), having a lattice spacing of 3.4 Å. Moreover, random reflection is noted by the presence of diffraction rings. Those spots are indexed to the crystallographic planes (100), (002), (101) and (200) of the ZnO hexagonal

phase, according to the crystallographic data (JCPDS nº 04-015-0825). In figure IV.32b, by spacing measurement the lattice fringes are attributed to the (100), (002) and (101) ZnO crystallographic planes. Figure IV.33 shows HRTEM images of ZnO@CNT3000 after 100 ALD cycles and their corresponding power spectrum obtained by FFT. The spots are indexed to the crystallographic planes (100), (002) and (101) of the ZnO hexagonal phase. On the TEM images, a direct measurement of the spacings was also performed to attribute the visible fringes to the corresponding planes. In case of Figure IV.33a, only the (002) plane was indexed even if other spacings are visible. Due to the curvature of the CNTs and the "superposition" of the ZnO nanocrystals, no evidence of a preferential orientation can be highlighted.

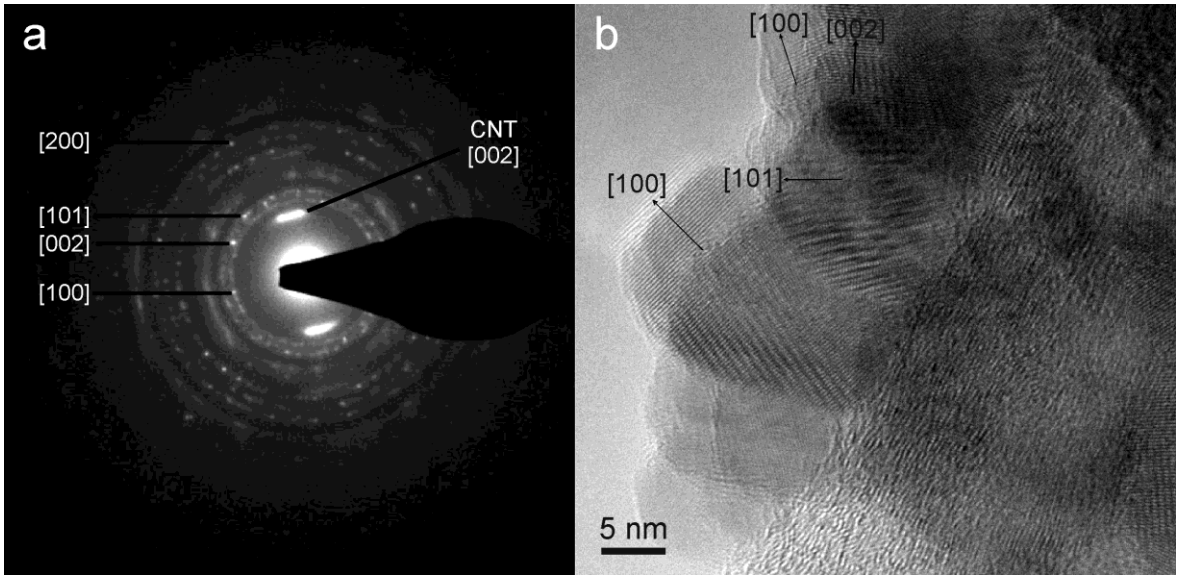

Figure IV.32. a) selected area electron diffraction and b) HRTEM image of ZnO-coated CNT1500 with 100 ALD cycles. The diffraction spots in a) are indexed to the crystallographic planes (200), (101), (002) and (100) of the ZnO hexagonal phase and the largest spots to the crystallographic plane (002) of graphitized carbon. The lattice fringes visible in b) are attributed to the (100), (101) and (002) ZnO planes.

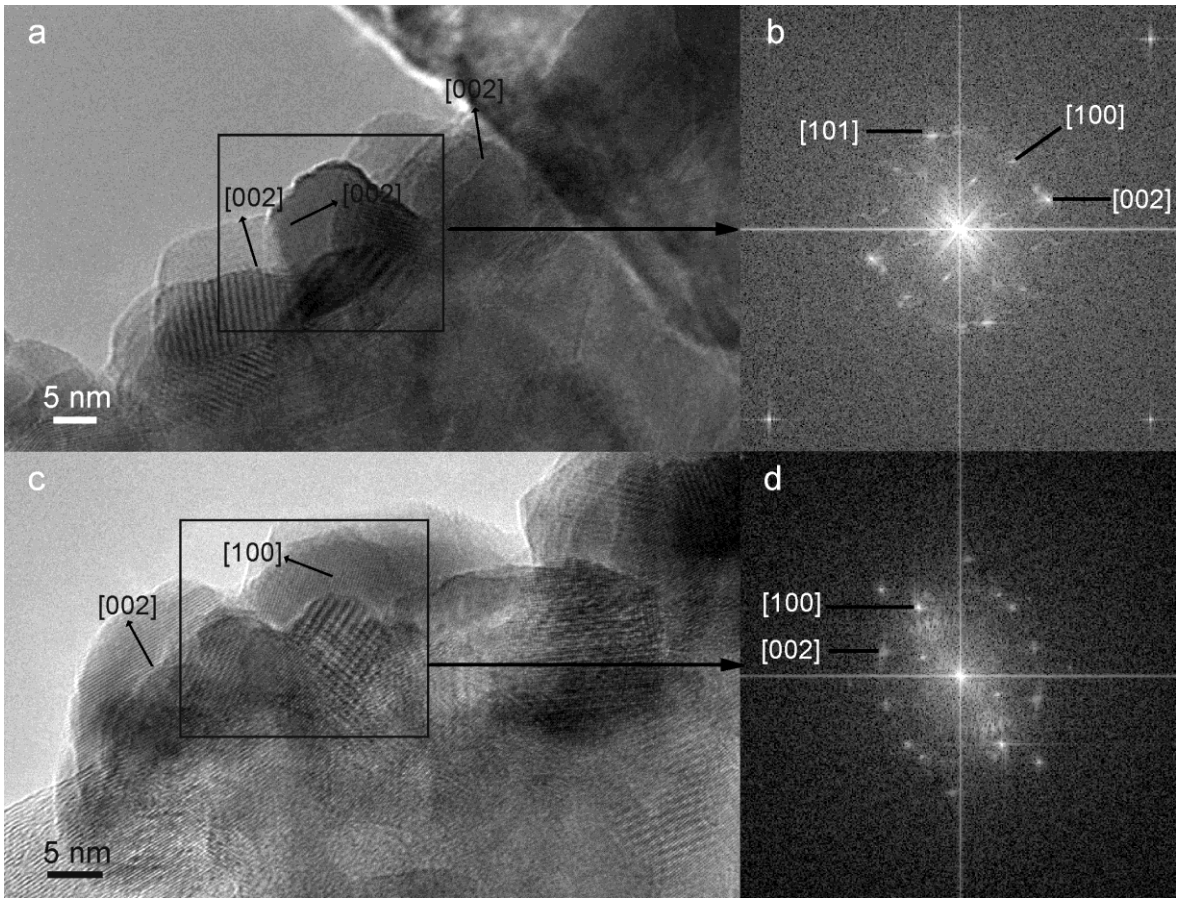

Figure IV.33. a,c) TEM images of ZnO@CNT3000 after 100 ALD cycles and b,d) their corresponding power spectra. Lattice fringes corresponding to the (002) and (100) crystallographic planes of ZnO are clearly visible.

V. Conclusions

By the novel tin dioxide ALD approach developed during this PhD, the coating of CNTs and boron nitride nanotubes was successfully carried out. The deposition allows the coating of the inner and outer walls of carbon nanotubes with SnO_2. Due to the type of growth, a particulate homogeneous film, made of crystalline nanoparticles, was obtained. Nevertheless, the film growth requires the presence of anchoring sites as indicated by the absence of coating on exposed graphitic layers and on defect free regions of the boron nitride nanotubes.

Moreover, it was shown that the growth mode of TiO_2 ALD onto CNTs strongly depends on the various chemical and thermal treatments of the substrate. 2D and island growth modes could be tuned by the surface functionalization of the CNTs as well as the transition from island to 2D growth mode, which depends on the number of ALD cycles. In the case of high temperature treated

stacked-cups nanotubes, a peculiar ring-shaped nanostructured coating could be obtained due to the pattern of the surface functional groups induced by the thermal and chemical treatments. All in all, it was shown that atomic layer deposition provides a means to specifically label anchoring sites and that it can be used to characterize the spatial distribution of surface functionality of differently treated carbon nanotubes. The requirement of the presence of anchoring sites for the initiation of film growth in ALD makes this method, in combination with HRTEM imaging, suitable for studying the spatial distribution of functional sites on high surface area supports. In fact, ALD appears as the technique of choice to map anchoring sites on nanostructured supports and to study the distribution of functional groups as a function of structure and functionalization treatment. In comparison, Raman spectroscopy does not offer a spatial resolution high enough to map the defects at the nm scale. Alternative techniques that provide atomic resolution, such as STM, are limited in the study of complex nanostructured materials and allow to scan a small region of the sample only.
Finally, the approach introduced in the present work was successfully applied to SnO_2- and ZnO-coated CNTs, corroborating the findings with TiO_2 deposition. The possibility to obtain either a homogeneous or nanostructured coating, as a function of the support functionalization, was demonstrated. Actually, homogeneous decoration of the CNTs with metal oxide particles and peculiar ring structure were achieved in a controlled manner. These findings are of great interest for the fabrication of various carbon-based nanostructures and other hetero-nanostructures in general.

Perspective

The XPS analysis of the pristine cup-stacked carbon nanotubes, as well as of commercial multiwalled carbon nanotubes (NC-3100 from Nanocyl and Baytubes from Bayer), revealed that even untreated carbon nanomaterials exhibit O-containing functional groups on their surface.[36] Those groups were formed when the materials were exposed to air after synthesis, as their defects reacted with O_2 and H_2O.[41] The calculated O/C ratio for the pristine nanocarbons ranged between 0.005 and 0.034, similar to the O/C ratios found for CNT700D, CNT1500 and CNT3000. We therefore expect to also be able to mark the defects in any nanocarbon, without any additional chemical treatment, by ALD. Preliminary experiments on the pristine cup-stacked CNTs and on pristine MWCNTs were conclusive.
We foresee that the labeling of defects in nanocarbons by ALD will play a role in better understanding of the relation between structure and defects as well as their relation to the physical and electronic properties like, for example, the study of the grain boundaries in graphene.[42] In addition, we believe that ALD will help to understand why MWCNTs, which seem to be structurally similar, exhibit different chemical, physical and electronic properties.[43]

Finally, the importance of this work on tailored CNT surface groups will be highlighted in the following chapters. Indeed, this is of great interest for the design of functional heterostructures. We will apply the heterostructures presented in this chapter to gas sensing. SnO_2 is a well-known material for gas sensor and its sensing properties will be tested toward O_2 and NO_2 target gases. TiO_2- and ZnO-coated CNT nanostructures will also be investigated. Finally, we will focus on the application of this approach to the functionalization and coating of electrospun carbon fibers, which allows a fine control of the electrocatalyst activity.

VI. Experimental part

Functionalization of carbon nanotubes

Stacked-cups carbon nanotubes were purchased from Pyrograf Products (USA). The CNTs were synthesized by catalytic chemical vapor deposition (CCVD) using the floating catalyst method described in details elsewhere.[44] Briefly, CH_4 and $Fe(CO)_5$ were fed simultaneously in a horizontal reactor maintained at 1100 °C. The thermal decomposition of the iron precursor generated iron nanoparticles which subsequently catalyzed the growth of the nanotubes. Because of the high reaction temperature, methane was also thermally decomposed (pyrolysis) on the CNT walls, leaving a relatively thick layer of disordered pyrolytic carbon.

After synthesis, the CNTs were heat treated in inert atmosphere at either 700 °C (product PR24-PS), 1500 °C (PR24-LHT) or 3000 °C (PR24-HHT) in order to graphitize the layer of pyrolytic carbon, hence decrease the density of structural defects in a controlled manner. The CNTs exhibit average outer and inner diameters of 85 and 40 nm, respectively, independently on the applied annealing temperature. The three commercial products were subsequently oxidized with concentrated nitric acid (70 %) at 100 °C for 10 h. The temperature was deliberately kept low, significantly under the boiling point of HNO_3 (120 °C) in order to prevent any structural damages to the CNTs which could modify their structural properties. The mixture was then allowed to cool down to room temperature and the functionalized CNTs were filtered and rinsed with 1 L distilled water. For the sake of clarity, the oxidized PR24-PS, PR24-LHT and PR24-HHT samples were labeled CNT700, CNT1500 and CNT3000. Part of the CNT700 sample was further heat treated in Ar at 800 °C to remove a fraction of the oxygen-containing functional groups. This sample was labeled CNT700D (defunctionalized). With increasing annealing temperature, the degree of graphitization of the surface rises and as a consequence, the impact of the classic nitric acid treatment on the functionalization of the wall surface is altered.

The first CNTs PR24-PS coated with SnO_2 were functionalized with HNO_3 in an autoclave at 100ºC for 2h. They were washed with deionized water until a neutral pH was reached.

Chemical characterizations of functionalized CNTs

The TG-MS and XPS characterizations revealed that the formation of carboxylic acid and anhydrides, which typically are the most abundant functional groups for this kind of oxidizing treatment, seems to be disfavored when the structural order of the carbon material increases (Table IV.1, section III.1.).[27] As a consequence, the pH of aqueous dispersions of CNT700 and CNT1500 increases, and the CNT3000 solution eventually turns basic. In addition, the concentration of surface functional groups created during the HNO_3 treatment decreases when increasing the graphitization temperature, as a result of the lower defect density (as observed from the evolution of the D/G ratio in Raman spectra, cf. Ref.[27] and Table IV.1). An alternative modification of the nature and density of surface groups was achieved through a partial defunctionalization of the CNT700 sample in Ar at 800 ºC. This post-treatment removes 89% of the oxygen, as determined by XPS, but without significant increase of the defect density.[27]

Atomic layer deposition

SnO_2 deposition

Tin dioxide was first deposited simultaneously on silicon wafer (used as reference) and carbon nanotubes (in a first run, Pyrograf PR-24-PS, non-functionalized and functionalized for 2h and in a second run CNT700 and CNT3000 were used) and boron nitride nanotubes, previously deposited on a Si wafer by drop casting. BN nanotubes were synthesized by the laboratory of multi-materials and interface, at the University of Lyon, France.[45] Tin tert-butoxide (STREM) and acetic acid (Aldrich) were used as metal and oxygen precursors, respectively. The depositions took place at 200 ºC in an exposure mode reactor of the home-made ALD tool schematized Figure I.13. The same procedure as described in the Chapter II was used. Typically ALD valves were opened for 0.03 and 1 s for the acetic acid and tin ter-butoxide, respectively. The residence time after each precursor pulse was set to 20 s, followed by a nitrogen purge during 15 s. The number cycles varied from 50 to 1000.

TiO_2 deposition

Titanium dioxide was deposited simultaneously on the CNTs exposed to the various treatments and on a silicon wafer. The latter was used as reference substrate for film thickness measurement. Prior to the ALD, CNTs were deposited by drop-deposition on a silicon wafer from dispersions in

ethanol. In order to remove the ethanol adsorbed at the surface of the CNTs, the samples were treated at 200 °C at 1 mbar under a stream of nitrogen for 15 min inside the ALD chamber prior to the first deposition cycle. The four types of carbon material were inserted and coated at the same time, in the same chamber, in order to have exactly the same deposition conditions. Titanium isopropoxide and acetic acid were used as metal and oxygen sources, respectively. The depositions took place at 200 °C in a home-made ALD reactor, which operated in exposure mode (cf. Chapter I). Metal precursor and acetic acid were introduced subsequently by pneumatic ALD valves from their reservoirs, which were kept at 80 and 30 ºC, respectively. Pure nitrogen was used as a carrier gas at a constant flow rate of 5 sccm. The ALD valves were opened for 0.03 and 1.2 s for the oxygen source and titanium precursor, respectively. The residence time after each precursor pulse was set to 20 s, followed by a nitrogen purge during 15 s. In order to study the nucleation of the oxide and to monitor the growth behavior as a function of the density of functional surface groups, different numbers of ALD cycles were realized in order to deposit various thicknesses. The number of cycles was chosen between 25 and 1000 with a nominal growth per cycle of 0.6 Å.[46]

ZnO deposition

Zinc oxide was deposited simultaneously on the four types of functionalized CNTs, each previously deposited on a silicon wafer from dispersions in ethanol. The depositions took place at 100 ºC in a commercial ALD equipment, a CN1 model "atomic-classic" working in exposure mode. Diethyl zinc (Aldrich, Zn, 52 wt. % min) and water were used as metal and oxygen sources, respectively, and subsequently introduced by pneumatic ALD valves from their reservoirs. Pure nitrogen was used as a carrier gas and the ALD valves were opened for 0.3 s for both the oxygen source and zinc precursor. The residence time after each precursor pulse was set to 5 s, followed by a nitrogen purge during 20 s and 30 s in the case of diethyl zinc and water, respectively. The samples were coated with 20, 50, 100 and 200 ALD cycles.

Structural Characterizations

The thickness of the as-deposited metal oxide films on the wafer substrates was measured by X-ray reflectivity using a Philips X'Pert MRD X-ray diffractometer with a copper radiation and a graphite monochromator for the selection of pure Kα radiation. The X-ray tube was operated at 20 kV and 20 mA. A 1 mm slit was used in order to reduce the scattered X-ray intensity. Measurements were performed in low-resolution experimental set up with the following instrumental configuration: divergence slit at the incident beam: 1/8 in.; step width: 0.01°; acquisition time: 1 s.

CNTs were characterized before and after ALD deposition by TEM, high-resolution transmission electron microscopy and scanning transmission electron microscopy using a JEOL EM-2010, a

JEOL JEM-2200FS, a Hitachi H9000 and a Philips CM200 FEG microscope. Electron energy loss spectra were also recorded from the TiO_2 coated carbon nanotubes and SnO_2 coated boron nitride nanotubes. Scanning electron microscopy images were recorded using a FEG-SEM Hitachi SU-70 microscope operating at 4 kV with a working distance of 2-3 mm.

SEM and TEM investigations were carried out on copper TEM grids coated with a holy carbon support film. The samples were deposited by dipping the TEM grids directly into the dry sample powder in order to avoid extra contamination.

VII. References

1. S. M. George, *Chem. Rev.*, 2010, **110**, 111-131.
2. M. Leskelä and M. Ritala, *Angew. Chem. Int. Ed.*, 2003, **42**, 5548-5554.
3. R. L. Puurunen, *J. Appl. Phys.*, 2005, **97**, 121301-121362.
4. M. Knez, K. Niesch and L. Niinistö, *Adv. Mater.*, 2007, **19**, 3425-3438.
5. C. Marichy, M. Bechelany and N. Pinna, *Adv. Mater.*, 2012, **24**, 1017-1032.
6. N. Pinna and M. Knez, *Atomic Layer Deposition of Nanostructured Materials*, Wiley-VCH, 2011.
7. A. S. Cavanagh, C. A. Wilson, W. Alan and S. M. George, *Nanotechnology*, 2009, **20**, 255602-255611.
8. D. B. Farmer and R. G. Gordon, *Electrochem. Solid State Lett.*, 2005, **8**, G89-G91.
9. D. B. Farmer and R. G. Gordon, *Nano Lett.*, 2006, **6**, 699-703.
10. C. F. Herrmann, F. H. Fabreguette, D. S. Finch, R. Geiss and S. M. George, *Appl. Phys. Lett.*, 2005, **87**, 123110-123112.
11. J. S. Lee, B. Min, K. Cho, S. Kim, J. Park, Y. T. Lee, N. S. Kim, M. S. Lee, S. O. Park and J. T. Moon, *J. Cryst. Growth*, 2003, **254**, 443-448.
12. C. Marichy, A. Pucci, M.-G. Willinger and N. Pinna, in *Atomic Layer Deposition of Nanostructured Materials*, eds. N. Pinna and M. Knez, Wiley-VCH, 2011, pp. 327-343.
13. M. G. Willinger, G. Neri, E. Rauwel, A. Bonavita, G. Micali and N. Pinna, *Nano Lett.*, 2008, **8**, 4201-4204.
14. G. D. Zhan, X. H. Du, D. M. King, L. F. Hakim, X. H. Liang, J. A. McCormick and A. W. Weimer, *J. Am. Ceram. Soc.*, 2008, **91**, 831-835.
15. Y.-S. Min, E. J. Bae, J. B. Park, U. J. Kim, W. Park, J. Song, C. S. Hwang and N. Park, *Appl. Phys. Lett.*, 2007, **90**, 263104-263103.
16. X. R. Wang, S. M. Tabakman and H. J. Dai, *J. Am. Chem. Soc.*, 2008, **130**, 8152-8153.
17. S. Banerjee, T. Hemraj-Benny and S. S. Wong, *Adv. Mater.*, 2005, **17**, 17-29.
18. A. Hirsch, *Angew. Chem. Int. Ed.*, 2002, **41**, 1853-1859.
19. Y. Fan, B. R. Goldsmith and P. G. Collins, *Nat. Mater.*, 2005, **4**, 906-911.

20. X. Li, J. Niu, J. Zhang, H. Li and Z. Liu, *J. Phys. Chem. B*, 2003, **107**, 2453-2458.
21. X. Wang, L. Cao, C. E. Bunker, M. J. Meziani, F. Lu, E. A. Guliants and Y.-P. Sun, *J. Phys. Chem. C*, 2010, **114**, 20941-20946.
22. Y. Fan, M. Burghard and K. Kern, *Adv. Mater.*, 2002, **14**, 130-133.
23. M. S. Dresselhaus, G. Dresselhaus, R. Saito and A. Jorio, *Phys. Rep.*, 2005, **409**, 47-99.
24. C. Marichy, N. Donato, M.-G. Willinger, M. Latino, D. Karpinsky, S.-H. Yu, G. Neri and N. Pinna, *Adv. Funct. Mater.*, 2011, **21**, 658-666.
25. M. G. Willinger, G. Neri, A. Bonavita, G. Micali, E. Rauwel, T. Herntrich and N. Pinna, *Phys. Chem. Chem. Phys.*, 2009, **11**, 3615-3622.
26. J. D. Ferguson, A. W. Weimer and S. M. George, *Chem. Mater.*, 2000, **12**, 3472-3480.
27. J.-P. Tessonnier, D. Rosenthal, F. Girgsdies, J. Amadou, D. Begin, C. Pham-Huu, D. Sheng Su and R. Schlögl, *Chem. Commun.*, 2009, 7158-7160.
28. C. Marichy, J.-P. Tessonnier, M. C. Ferro, K.-H. Lee, R. Schlögl, N. Pinna and M.-G. Willinger, *J. Mater. Chem.*, 2012, **22**, 7323-7330.
29. AppliedSciencesInc, A Comparison of Carbon Nanotubes and Carbon Nanofibers, http://pyrografproducts.com/carbon-nanotubes.html.
30. J.-P. Tessonnier, O. Ersen, G. Weinberg, C. Pham-Huu, D. S. Su and R. Schlögl, *ACS Nano*, 2009, **3**, 2081-2089.
31. B. Li, C. Wang, G. Yi, H. Lin and Y. Yuan, *Catal. Today*, 2011, **164**, 74-79.
32. D. Shuai, C. Wang, A. Genc and C. J. Werth, *J. Phys. Chem. Lett.*, 2011, **2**, 1082-1087.
33. W. Zheng, J. Zhang, B. Zhu, R. Blume, Y. Zhang, K. Schlichte, R. Schlögl, F. Schüth and D. S. Su, *ChemSusChem*, 2010, **3**, 226-230.
34. C. G. Salzmann, S. A. Llewellyn, G. Tobias, M. A. H. Ward, Y. Huh and M. L. H. Green, *Adv. Mater.*, 2007, **19**, 883-887.
35. A. Rinaldi, J. Zhang, B. Frank, D. S. Su, S. B. A. Hamid and R. Schlögl, *ChemSusChem*, 2010, **3**, 254-260.
36. J.-P. Tessonnier, D. Rosenthal, T. W. Hansen, C. Hess, M. E. Schuster, R. Blume, F. Girgsdies, N. Pfänder, O. Timpe, D. S. Su and R. Schlögl, *Carbon*, 2009, **47**, 1779-1798.
37. M. Endo, Y. A. Kim, T. Hayashi, T. Yanagisawa, H. Muramatsu, M. Ezaka, H. Terrones, M. Terrones and M. S. Dresselhaus, *Carbon*, 2003, **41**, 1941-1947.
38. J. I. Paredes, M. Burghard, A. Martínez-Alonso and J. M. D. Tascón, *Appl. Phys. A*, 2005, **80**, 675-682.
39. R. Schlögl, in *Handbook of Heterogeneous Catalysis*, eds. G. Ertl, H. Knözinger, F. Schüth and J. Weitkamp, Wiley VCH, Weinheim, 2007.
40. D. S. Kim, S. M. Lee, R. Scholz, M. Knez, U. Gösele, J. Fallert, H. Kalt and M. Zacharias, *Appl. Phys. Lett.*, 2008, **93**, 103108-103110.
41. R. Menzel, M. Q. Tran, A. Menner, C. W. M. Kay, A. Bismarck and M. S. P. Shaffer, *Chem. Sci.*, 2010, **1**, 603-608.
42. P. Y. Huang, C. S. Ruiz-Vargas, A. M. van der Zande, W. S. Whitney, M. P. Levendorf, J. W. Kevek, S. Garg, J. S. Alden, C. J. Hustedt, Y. Zhu, J. Park, P. L. McEuen and D. A. Muller, *Nature*, 2011, **469**, 389-392.

43. E. P. J. Parrott, J. A. Zeitler, J. McGregor, S.-P. Oei, H. E. Unalan, W. I. Milne, J.-P. Tessonnier, D. S. Su, R. Schlögl and L. F. Gladden, *Adv. Mater.*, 2009, **21**, 3953-3957.

44. G. G. Tibbetts, M. L. Lake, K. L. Strong and B. P. Rice, *Compos. Sci. Technol.*, 2007, **67**, 1709-1718.

45. M. Bechelany, S. Bernard, A. Brioude, D. Cornu, P. Stadelmann, C. Charcosset, K. Fiaty and P. Miele, *J. Phys. Chem. C*, 2007, **111**, 13378-13384.

46. E. Rauwel, G. Clavel, M. G. Willinger, P. Rauwel and N. Pinna, *Angew. Chem. Int. Ed.*, 2008, **47**, 3592-3595.

Chapter V:

MO_x@CNTs heterostructures in gas sensing

Contents:

In the previous chapter the elaboration of controlled carbon-based nanostructures by ALD was demonstrated. In order to illustrate the potential of the approach, the obtained heterostructures were applied to gas sensing. This work is the result of a collaboration with the group of Prof. Giovanni Neri at the University of Messina, Italy, who realized the gas sensing experiments. Therefore, a non-exhaustive presentation of the diverse findings will be introduced in this chapter showing the applicability of our heterostructures.

The sensing properties of the SnO_2@CNT700 and TiO_2@CNT700 structures were investigated using NO_2 and O_2 as target gas. Furthermore, SnO_2@CNT3000 and ZnO-coated CNTs sensors were tested for NO_2 monitoring. The characteristics of oxygen and nitrogen dioxide sensors made of coated CNT nanomaterials have been related to the formation of a p-n heterojunction at the interface between the CNT and the MO_x. Promising results have been obtained in case of tin dioxide-coated CNT700 and unprecedented p-type responsiveness has been observed in case of titanium oxide-coated CNT700.

I. Introduction

In view of the development of new functional materials, where desired properties of one material acting as a support are combined with complementary and desired properties of a second material, ALD is a highly suitable technique. One example for the application of such hybrid materials is gas sensing, where the response of a material to the presence of a certain reducing or oxidizing gas species is used to monitor its concentration.[1, 2] Resistive gas sensors are widely employed in many commercial applications such as, household security, industrial emission control, biomedical and agricultural domains, and automotive.[3, 4] Although sensors made of metal oxide semiconductor (MOS) nanostructures are highly attractive, their high operating temperature constitutes a strong limitation. Efforts have been devoted to combine these metal oxides with a suitable conductive support, to develop near room temperature gas sensors.

Tin oxide, titanium oxide and zinc oxide have proven to be suited for application as active layers in MOS gas sensors. Their electric resistance changes as a function of the surrounding atmosphere due to the charge carrier exchange between the adsorbed gas and the oxide surface. Since the sensing process takes place at the surface, it is crucial to have a large surface to volume ratio in order to achieve a high response. Recently, many MO_x nanostructured forms have been used for gas sensing applications. However, often it is difficult to obtain and control the shape, size and morphology of the nanostructures. By using a high surface area support, such as carbon nanotubes,

as template and ALD as a coating technique, an easy way to prepare one dimensional metal oxide/carbon nanotubes heterostructures was proposed.

The tubes ALD-coated with mostly SnO_2 but also with TiO_2 or ZnO were investigated as active component in gas-sensor devices for oxygen and nitrogen dioxide monitoring. Actually, nitrogen dioxide (NO_2) is a toxic compound produced by combustion processes in power plants, combustion engines and automobiles, and harmful for the environment as a major cause of acid rain and photochemical smog.[5] Safety guidelines recommend exposure periods not longer than 8 hours to more than 3 ppm NO_2 gas.[6] Therefore, many efforts are currently made to develop sensors that can effectively detect NO_2 even at extremely low concentrations.[7] MOS sensors for O_2 find an important application in automotive in order to replace the lambda sensor, which controls the combustion process.[3] They also have an essential place in the food industry.

In the following, CNTs are considered as p-type semiconductor, whilst the three investigated metal oxides are n-type semiconductors. Due to the formation of a p-n heterojunction between the highly conductive support (p-type) and the SnO_2 thin film (n-type) an enhancement of the gas sensing response is observed,[8] while an unexpected p-type response have been observed in the case of TiO_2-coated carbon nanotubes.[9] Responses to O_2 and NO_2 at different gas concentrations and sensor temperature were investigated. The responses towards the target gases will be presented as a function of the metal oxide investigated. Subsequently, the general sensing mechanism of such MO_x@CNTs sensors will be described.

II. SnO_2@CNTs nanostructures used as gas sensor

The CNTs (Pyrograf Product, grade PR-24-PS) previously coated with SnO_2, i.e. SnO_2@CNT700 (cf. Chapter IV, section II) were investigated as gas sensing material.[8] A comparison between their sensing behavior and the one of SnO_2@CNT3000 (cf. Chapter IV, section IV.I) will be presented. In this section, the sensitivity of the gas sensor is defined as $S = R_{gas}/R_0$ where R_{gas} is the electric resistance of the sensor at different target gas concentration and R_0 is the baseline resistance.

II.1. Electrical measurement

The electric resistance of CNTs coated with SnO_2 films of different thicknesses was investigated first. These measurements, performed in pure nitrogen, served as reference and baseline for the gas sensing tests. Figure V.1 presents the case of CNTs coated with 4 nm of SnO_2. The resistance, recorded in the temperature range between RT and 200 °C, decreases with the increasing temperature and shows a slight hysteresis upon the first heating-cooling cycle, probably due to the

evaporation of some solvent that was used for the deposition of the SnO_2@CNTs onto the sensor device.

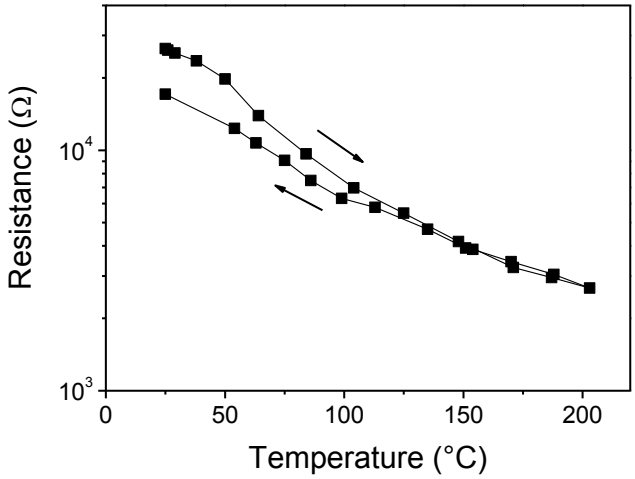

Figure V.1. Resistance *vs.* temperature of the as-prepared 4 nm SnO_2-coated nanotubes.

The device made of uncoated nanotubes shows lower electric resistance than the one made of SnO_2-coated tubes as depicted in Figure V.2. Indeed, their resistance is about 2-3 orders of magnitude higher and its value depends on the thickness of the SnO_2 coating. The resistance of the thinner film is about one order of magnitude higher than that of the thicker film. The resistance is dominated by the Schottky barrier at the surface of n-type SnO_2 film causing the formation of a depletion layer. In the case of the thinner film (SnO_2 thickness = 3.0 nm) the space-charge region extends through the whole volume of the film, i.e. the layer is fully depleted.[10] This causes a higher potential barrier at the surface, resulting in a higher resistance as compared to the case of a thicker film (SnO_2 thickness = 4.0 nm). This is in agreement with a report on SnO_2 films of different thickness deposited on α-Al_2O_3.[11]

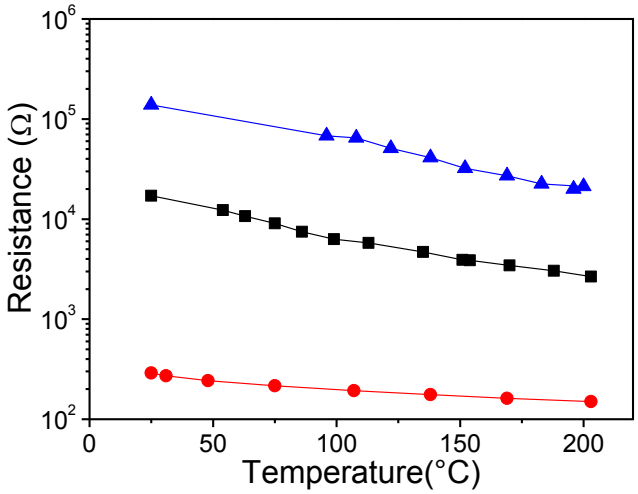

Figure V.2. Resistance *vs.* temperature of the samples investigated. Uncoated nanotubes (circles), 4.0 nm SnO_2 coating (squares) and 3.0 nm SnO_2 coating (triangles).

II.2. Oxygen sensing tests

To assess the applicability of SnO_2@CNTs heterostructures for resistive chemical sensors, their O_2 sensing properties at low-mild temperatures were investigated first. SnO_2@CNTs nanostructures have been already tested for the detection of CO,[12] NO_2,[13, 14] NH_3,[15] formaldehyde[16] and ethanol[17] but, to the best of our knowledge, no study on oxygen detection was reported before the present work.[8] Oxygen sensors operating at low-mild temperature are important in applications for the control of combustion processes and also in food industry, for example. Moreover, the study of the interaction of oxygen with the surface of semiconducting materials is of primary importance because oxygen plays a key role in the sensing mechanism of metal oxide semiconductors towards various kinds of gases. The variation of resistance as a function of the oxygen concentration at 200 °C is shown in Figure V.3a for a SnO_2 coating of 3.0 nm. A typical linear trend, extending in all the range of investigated oxygen concentration, is observed. The dynamic performance of the sensor was measured under different concentrations of oxygen (Figure V.3b). The resistance of the sensor increases upon exposure to O_2, whereas it decreases upon its removal. This behavior is in agreement with the phenomena already observed on SnO_2 nanowires. Indeed, after annealing under inert atmosphere, during exposure to oxygen, a decrease of the nanowires conductivity was observed.[18] In the present case, it is noteworthy that the response of the sensor was stable and reproducible for repeated testing cycles. Both the response and the recovery were fast at this operating temperature (200 °C). Although sensor responses were obtained down to 100 °C, the response/recovery times were longer. On the contrary, no response to oxygen was registered in the same conditions with the uncoated CNTs (not shown).

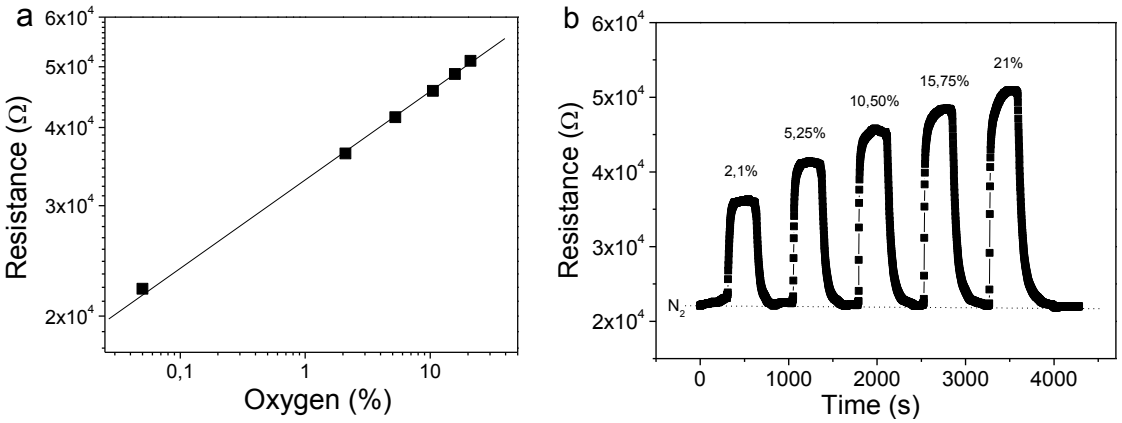

Figure V.3. a) Variation of the sensor resistance vs. oxygen concentration and b) transient response of the sensor made of SnO_2-coated carbon nanotubes exposed to different concentration of oxygen at 200 °C. The coating thickness was 3.0 nm.

The observed response to oxygen demonstrates that the SnO_2 film behaves as a n-type semiconductor. Since the CNTs used in this work behave as p-type semiconductors (see typical p-type semiconductor response to NO_2 gas of uncoated CNTs, Figure V.5, section II.3)[19, 20] a heterojunction is formed between the tin dioxide film and the CNT. In such a heterostructure two different depletion layers (and associated potential barriers) can coexist. The first depletion layer is located at the surface of the metal oxide film and the second one at the interface between CNTs and metal oxide films. While the first depletion layer is due to the adsorption of ionized oxygen at the surface of the SnO_2 film, the second one is caused by the CNTs-SnO_2 heterojunction. It appears, as also supported by the electrical response to O_2, that its adsorption on the surface of the SnO_2 film modifies the depth of the first depletion layer, which in turn alters the depletion layer at the p-CNTs-n-SnO_2 interface. This is further confirmed by the responses of the sensors with different SnO_2 coating thicknesses (Figure V.4).

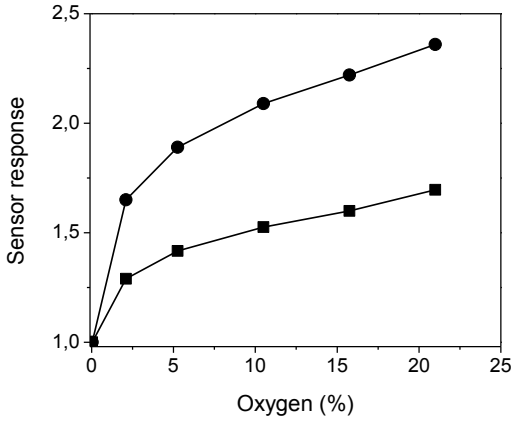

Figure V.4. Sensor response as a function of the oxygen concentration for the sensor made of SnO_2-coated CNTs with thicknesses of 3.0 nm (circles) and 4.0 nm (squares).

The sample with the thinner SnO_2 layer (3.0 nm) exhibits a higher response than the one with the thicker layer (4.0 nm). The increasing of the sensing performances with the decreasing of the coating thickness can be explained by the space-charge layer model.[21] Generally, when the grain size is reduced down to the Debye length (L_d), the sensitivity increases.[10] Since for SnO_2 the L_d is about 3 nm,[10] and hence, in the range of the thinner coating, the adsorbed oxygen molecules fully deplete electrons in the SnO_2 film. As a result, a conduction barrier is built up, leading to the observed increase of the resistance. When the sensor is exposed to pure nitrogen, oxygen will be desorbed and then the extracted electrons will be released back with a high resistance variation.

II.3. NO_2 sensing tests

The SnO_2@CNTs nanostructures, in particular the sensor with 3.0 nm SnO_2 film, were also investigated for monitoring NO_2. As shown in Figure V.5, the presence of NO_2 induces a decrease of the resistivity of the device made of uncoated CNTs. This behavior is characteristic of a p-type semiconductor and the bare CNTs present a sensitivity of ~1.1.[20]

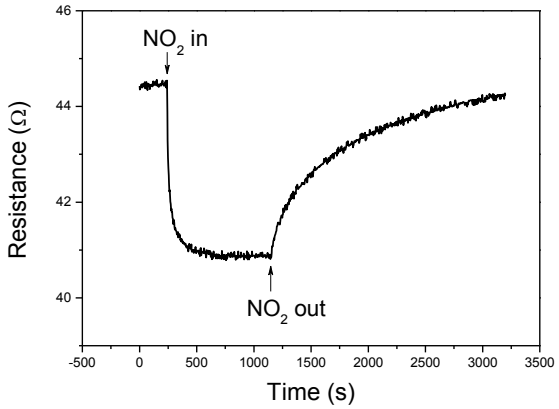

Figure V.5. Transient response of the uncoated CNTs to 6.5 ppm of NO_2 at 150 °C. A decrease of the resistance upon introduction of NO_2 is observed with a sensitivity S ~ 1.1.

Preliminary tests, aimed to find the optimal operating temperature of the sensor for NO_2 monitoring, were achieved. The highest sensor response, recorded between RT and 250 °C, was obtained at 150 °C with a sensor response S = 45 to 5 ppm NO_2 (Figure V.6).

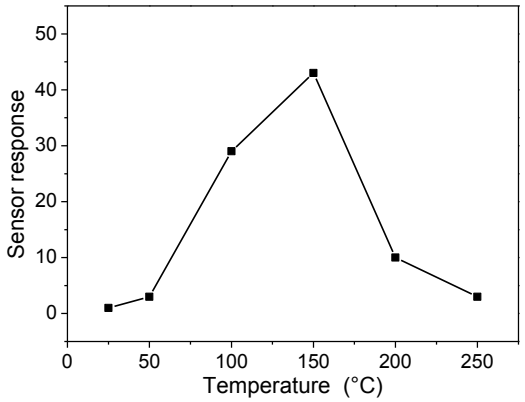

Figure V.6. Sensor response-temperature curve for the sensor made of 3.0 nm SnO_2-coated CNTs to 5 ppm of NO_2.

Taking into consideration that:

i) The uncoated CNTs-based sensor is much less sensitive to NO_2, under the same experimental conditions,[19, 20]

ii) Crystalline 2-3 nm sized SnO_2 particles synthesized in solution, using a similar non-aqueous sol-gel approach, show no sensitivity to NO_2 up to 200 °C and a much lower sensitivity above 200 °C as compared to the CNTs-SnO_2 heterostructures,[22]

iii) A comparison with published results shows that NO_2 detection at low concentration with sufficient sensitivity requires temperature higher than 200 °C or 1D nanostructure of the active material,[14, 23-28]

it can be safely concluded that the peculiar heterostructure of the SnO_2@CNTs sensor is responsible for the enhanced sensor response to NO_2. Moreover, these findings support the proposed electrical model and the response of the sensor to O_2 as discussed above.

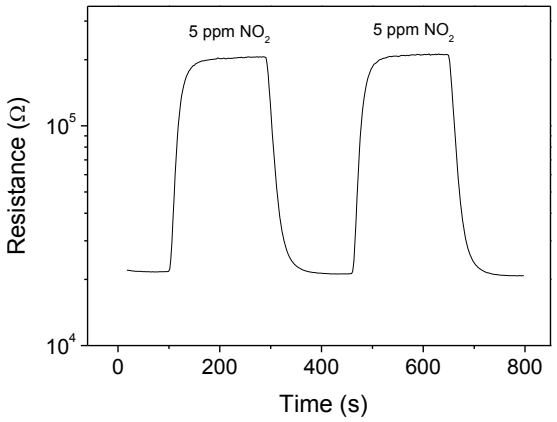

Figure V.7. Transient response of the 3.0 nm SnO_2-coated CNTs sensor to 5 ppm of NO_2 at 200 °C.

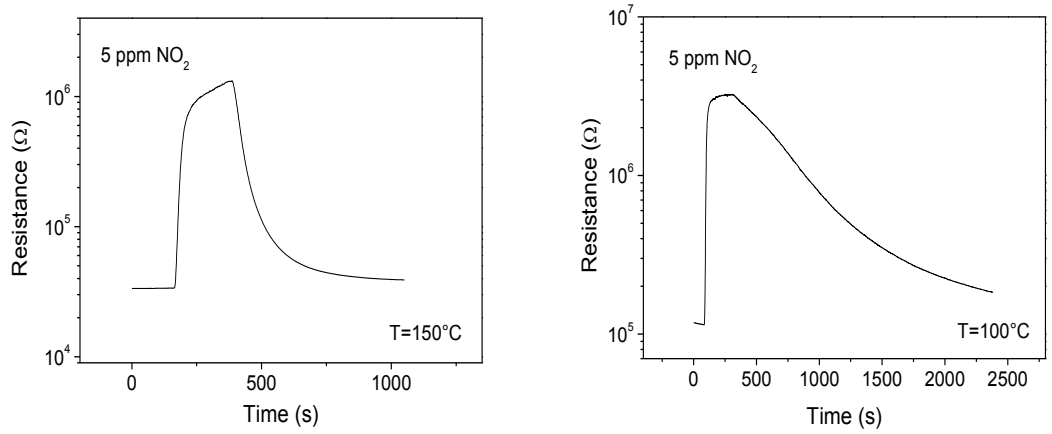

Figure V.8. Transient responses of the 3.0 nm SnO_2@ CNTs to 5 ppm of NO_2 at a) 150 and b) 100 °C.

Figures V.7 and V.8 show transient responses to 5 ppm of NO_2 at various temperatures. The response at 200 °C is fast, reversible and reproducible (Figure V.7). The increase of resistance when the sensor is exposed to NO_2 can be interpreted on the basis of the non-dissociative adsorption at the surface of n-type tin dioxide grains:

NO_2 (gas) + $e^- \rightarrow NO_2^-$ (ads)

Subsequently, the concentration of electrons at the surface of the metal oxide decreases and the resistance increases accordingly. The response time, τ_{res}, defined as the time it takes for the resistance to decrease to 90% of the minimum resistance when NO_2 is introduced into air, is 40 s. The recovery time, τ_{rec}, the time required for 90% increment in resistance when NO_2 is turned off and pure dry air is reintroduced into the chamber, is 50 s.

At lower temperatures, the response/recovery times observed are longer. To achieve complete signal recovery in a reasonable time at the optimal temperature of 150 °C, the sensor was exposed to NO_2 pulses for a short-time period. Figure V.9 shows the response of the sensor exposed to 0.5-5 ppm of NO_2 for a period of 30 s.

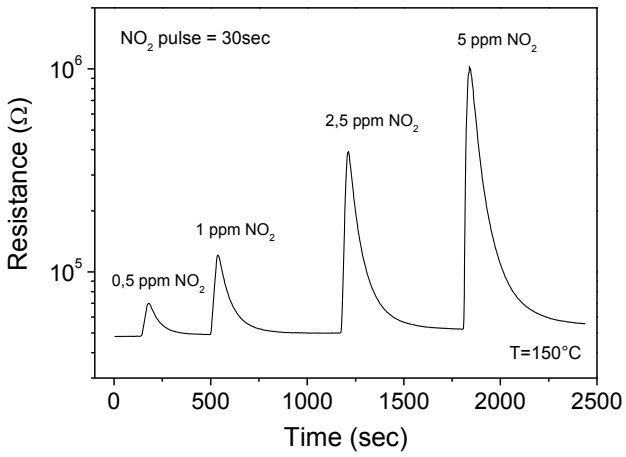

Figure V.9. Transient response of the sensor made of 3.0 nm SnO_2-coated CNTs, operating at 150 °C, exposed to 0.5-5 ppm of NO_2 for a period of 30 s.

Although sensor responses were slightly lower compared to those achieved at the saturation exposure, NO_2 at sub-ppm concentration was easily detected in just a few seconds. Moreover, in the range of the NO_2 concentration investigated the sensor response shows a linear trend as a function of the NO_2 concentration in a log-log plot (Figure V.10).

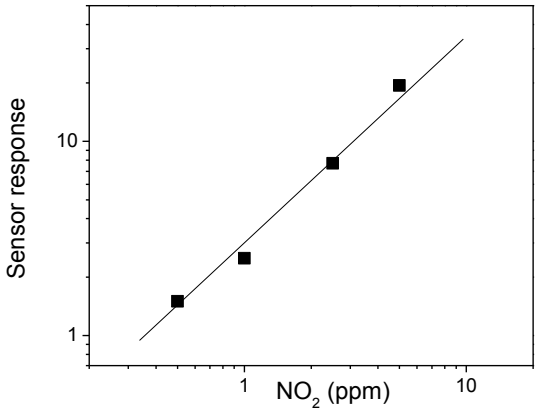

Figure V.10. Calibration curve of the of the 3.0 nm SnO_2-coated CNTs sensor, operating at 150 °C, exposed to 30 s pulses of NO_2.

The gas sensing characteristics of V_2O_4 films deposited on the same CNT support towards NO_2 were previously reported.[19, 20] On the one hand, the SnO_2 coated CNTs were found around two orders of magnitude more effective for sensing NO_2. On the other hand, it turned out that a similar mechanism must be responsible for the detection of NO_2 at such low temperatures. This confirms the key role of the metal oxide/CNT heterojunction in defining the sensor response of these composite materials.

II.4. Comparison with devices made of SnO_2@CNT3000: case of NO_2 sensing tests

II.4.1. Electrical measurement of the different types of CNTs

The resistivity of sensor devices made of CNTs was investigated as a function of the temperature and CNT type (i.e. CNT700, CNT1500 and CNT3000, Figure V.11). With the increase of the thermal treatment, a progressive decrease of the electric resistance of the CNTs was found.

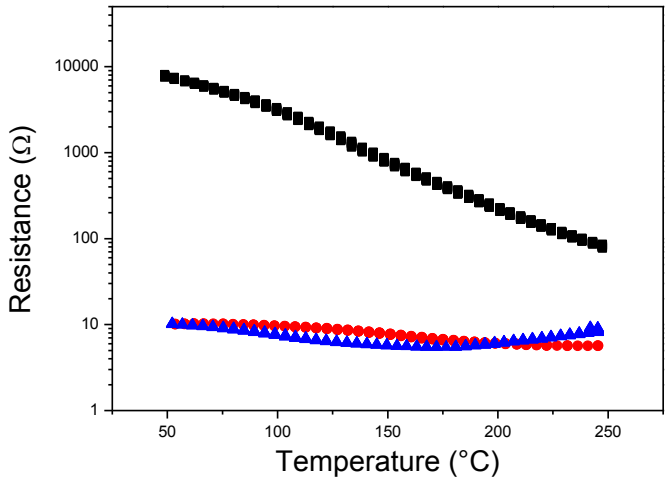

Figure V.11. Electric resistivity of the as-received CNTs heat treated at various temperatures: CNT700 (squares), CNT1500 (triangles) and CNT3000 (circles).

This difference in behavior is directly correlated to the increasing degree of graphitization of the carbon material, the presence of amorphous carbon and defects within the structure causing a decrease of conductivity.[29, 30]

II.4.2. NO_2 sensing tests of devices made of SnO_2@CNT3000

The SnO_2@CNT3000 nanostructures, presented in Chapter IV, in particular the heterostructure presenting 3 nm SnO_2 particles (cf. Figure V.13b), were investigated as NO_2 sensor, in order to study the influence of the metal oxide morphology on the MO_x@CNTs sensing properties. A decrease of the resistance of the sensing device is noticed in presence of NO_2 (Figure V.12), which is characteristic to a p-type semiconductor behavior. The sensor presents a poor sensitivity close to the uncoated CNT3000 one. The coated CNT3000 device presents an opposite response to the sensor made of SnO_2@CNT700.

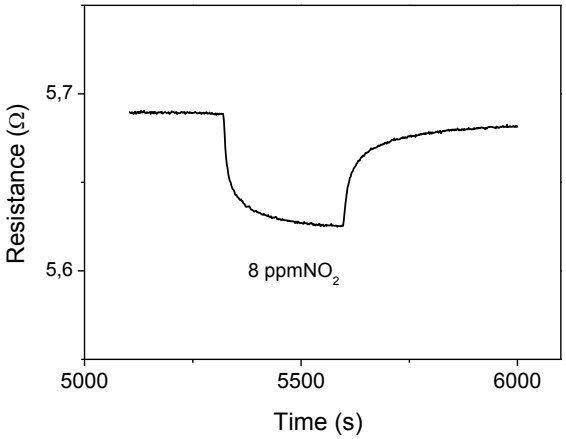

Figure V.12. Transient response of the 3.0 nm SnO_2-coated CNTs sensor to 5 ppm of NO_2 at 200 °C.

II.4.3. Comparison of the sensing behavior as a function of the CNT support

As mentioned in the Chapter IV, the ALD coating can be tuned as a function of the type of CNTs used. When CNT700 were coated, a granular but homogeneous and continuous SnO_2 film along the whole tube length was obtained (Figure V.13a), while the ALD deposition on CNT3000 leads to the formation of rings wrapped around the CNTs (Figure V.13b).

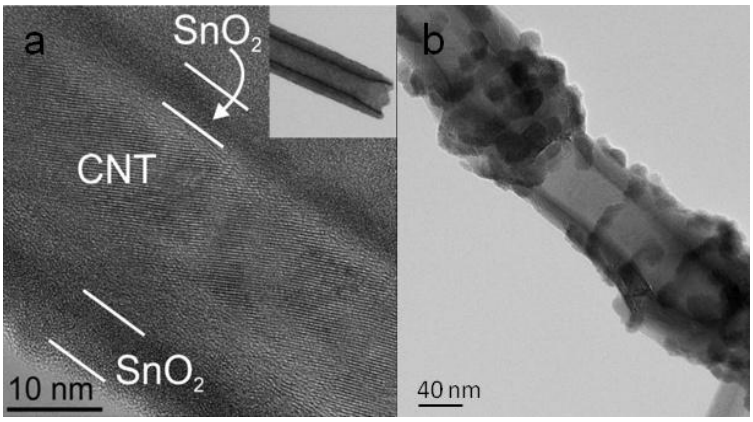

Figure V.13. TEM images of a) SnO_2@CNT700 and b) SnO_2@CNT3000.

Measurements have shown strong differences in the behavior of the various nanostructures tested. The SnO_2@CNT700 sensor responded to nitrogen dioxide with very high sensitivity (Figure V.7), whereas the response of the SnO_2@CNT3000 sensor was very poor (Figure V.12). A n-type and p-type semiconductor behavior was noted for the devices made of tin dioxide-coated CNT700 and CNT3000, respectively. The difference in response can be explained by the various junctions involved during the sensing mechanism and their influence on the electric path. Figure V.14a shows a picture of the sensor device electrodes on which coated CNTs were deposited (magnified

in Figure V.14b). As schematized in Figure V.14c, the network of the coated CNTs, randomly oriented over the electrodes, is responsible for the electric paths between the adjacent Pt electrodes. The deposited nanotubes on the device have numerous contacts among themselves, forming potential barriers at the crossing points, which can be modified by the presence of the metal oxide coating. From previous investigations, it was ascertained that MO_x coating appears to be involved in the receptor function, while the CNTs provide mainly the electronic conduction path (transducer function).[13] However, here it appears that the nature and morphological/microstructural characteristics of both coating and support also play a prominent role in addressing the sensor response. These characteristics determine the electrical transport properties thought the sensing layer, and in turns, affect the sensing properties. The difference in the SnO_2 morphology causes a different modulation of electrical conduction through the sensing layer. SnO_2 is considered n-type semiconductor, while CNTs demonstrates a p-type behavior. In the case of SnO_2@CNT700, the SnO_2 coating is continuous and electrical conduction is expected to occur through the CNT-MO_x interface. This creates a p-n heterojunction of which the barrier height is modulated by NO_2 interaction with the n-type SnO_2 layer. On the opposite, in case of the SnO_2@CNT3000, due to the partial coverage of the nanotubes, the electrical conduction flows mainly through the CNT-CNT contact, resulting in a p-type response.

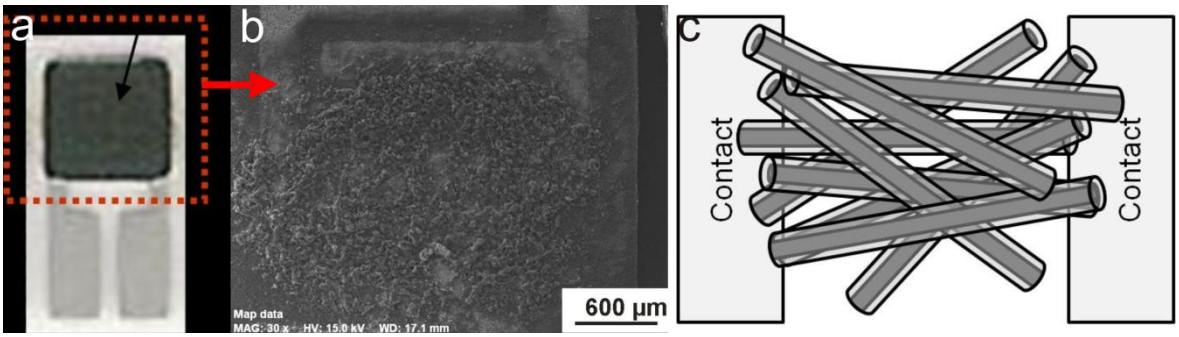

Figure V.14. a) picture of the sensor device with coated CNTs, b) SEM image at low magnification of the deposited CNTs on the interdigited Pt electrodes and c) schematic of the network formed by the CNTs on the gas sensor device.

The difference in the sensor responses observed as a function of the coating morphology is comparable to the behavior of the ZnO@CNTs photodetector observed by Lin *et al.*[31] Indeed, the role of the thickness and nanostructure of the deposited material on the properties of p-n heterojunction was demonstrated by coating CNTs (p-type) with ZnO (n-type) by ALD. ZnO crystalline nanoparticles are deposited forming a partial or full coating of the CNTs. The thus-fabricated photodetector devices exhibit a semiconducting p-type character when the coating is incomplete and a n-type character for a continuous coating. This was attributed to the different

nature of charge carriers, holes for the first and electrons for the latter case. In the present case, the modulation is realized through the metal oxide morphology determined by the type of support instead of the number of cycles applied.

III. Extension to TiO_2@CNTs and ZnO@CNTs nanostructures: preliminary results

The application to NO_2 and O_2 monitoring of TiO_2@CNTs and ZnO@CNTs heterostructures, introduced in the Chapter IV, is presented in this section as well as the electrical properties of the sensors as a function of the metal oxide thickness and the CNT type.

III.1. Electrical properties of the MO_x@CNTs devices

The electric resistance of thick films made of either pure CNTs or CNTs coated with 3.5 nm TiO_2, as a function of the operating temperature, was investigated to acquire a reference and baseline for the subsequent measurements. The resistance of CNTs coated with ZnO was studied as a function of the coating thickness and CNT type.

In Figure V.15a, the resistance of both CNTs and TiO_2@CNTs, recorded from 45 °C to 200 °C, decreases with the temperature increase, indicating a semiconductor behavior. Moreover, a much higher resistance of 10^3-10^4 ohm is observed in case of 3.5 nm TiO_2-coated CNTs compared to the uncoated carbon material (50-150 ohm). Nevertheless, when compared with the resistance value of a device made of a titania nanoparticle-based film, in the range of mega ohm, due to the insulating character of the metal oxide, the heterostructure displays a significantly lower resistance value. This behavior can be attributed to the very low thickness of the film and high conductivity of the CNTs, which provide a privileged conduction path.[9]

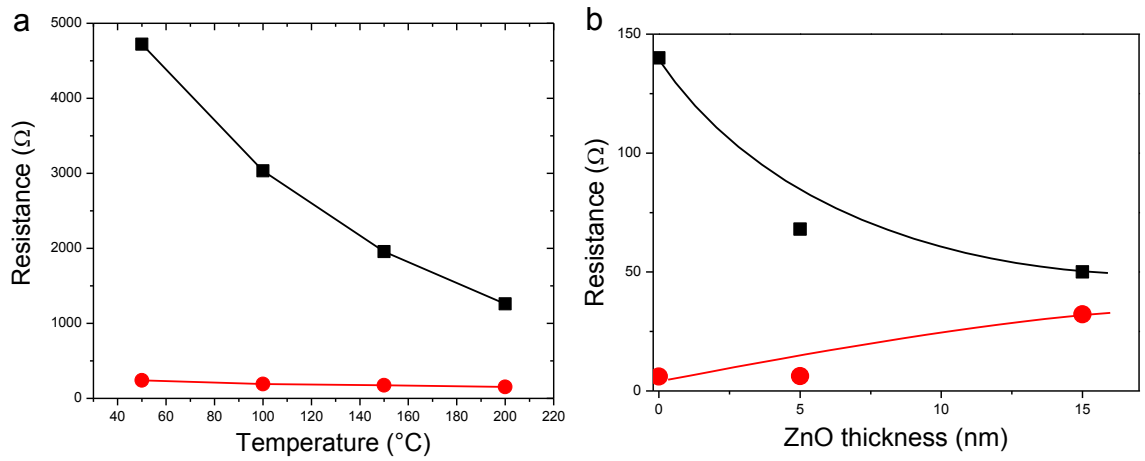

Figure V.15. a) Electric resistance of pure CNT700 (full circles) and TiO_2@CNT700 (full squares) *vs.* the operating temperature. b) Electric resistance of ZnO@CNT700 (full squares) and ZnO@CNT3000 (full circles) as a function of the ZnO thickness.

Depending on the CNT type used as a support, different evolutions of the resistance as a function of the ZnO thickness are observed (Figure V.15b). The increase of the ZnO layer on CNT700 leads to a decrease of the resistance, in respect to the CNT resistance, while an increase is noticed in case of CNT3000. This phenomenon confirms that the electrical conduction through the sensing layer is due to the potential barrier at the crossing points, which is modified in the presence of the metal oxide coating. Actually, in case of the CNT3000, at the crossing points, junctions between CNT/CNT, CNT-ZnO/ZnO-CNT and CNT/ZnO-CNT coexist, while in case of CNT700, the junctions are expected to be mainly CNT-ZnO/ZnO-CNT. In the first case, the increasing thickness therefore leads to an augmentation of the number of the contact points between CNT-ZnO/ZnO-CNT and CNT/ZnO-CNT, having a higher potential barrier than CNT/CNT, which causes an increase of resistance.

III.2. Preliminary results on gas sensing experiments

III.2.1. TiO_2@CNT700 sensor devices

The sensing properties of CNT700 coated with a 3.5 nm thick TiO_2 layer towards NO_2 were investigated as a function of the temperature. Because an unexpected p-type semiconductor response was observed, the sensor was subsequently applied to O_2 monitoring.[9]

III.2.2.1. NO_2 gas sensing tests

Preliminary experiments were realized on the 3.5 nm thick TiO_2 coated CNT700 device to determine the optimal working temperature. The sensor response reveals to be strongly influenced

by the operating temperature. A detectable response to 5 ppm of NO_2 starts from near ambient temperature (40 °C) and the response increases with the temperature, showing a maximum in the range of 100-150 °C before it decreases. The transient response to 5 ppm of NO_2 at 150 °C (Figure V.16a) shows a decrease of the resistance of the sensor in presence of the target gas. The observed response corresponds to a p-type semiconductor behavior. Both response and recovery times, i.e. τ_{red} and τ_{rec}, of the sensor, presented Figure V.16b, decrease as the function of the operating temperature. Moreover the response is faster than the recovery and even at near room temperature, the device responses in less than 4 minutes. The influence of the TiO_2 thickness on the gas response and the influence of its morphology are currently under investigation using TiO_2-coated differently treated CNTs (i.e. CNT700, CNT1500, CNT3000 and CNT700D) as sensor devices.

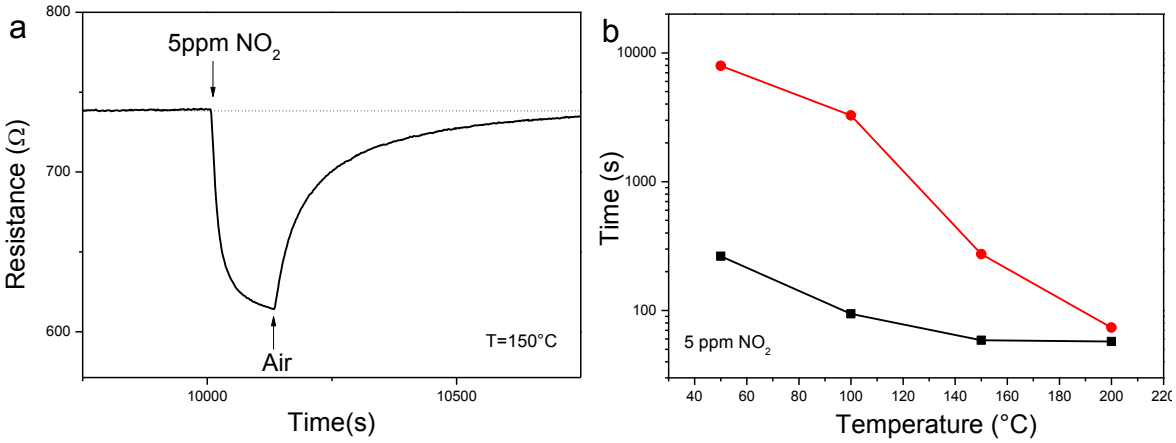

Figure V.16. a) Transient response of TiO_2@CNTs sensor at 150 °C to 5 ppm of NO_2 gas, b) response (squares) and recovery times (circles) of the sensor to 5 ppm of NO_2 gas as a function of the operating temperature.

The NO_2 sensing response of the TiO_2@CNTs material demonstrates a p-type semiconductor behavior. As NO_2 behaves as an oxidizing or reducing agent, depending on the temperature and concentration,[32] a misinterpretation of the results can occur. Therefore, in order to prove the p-type conductivity of the sensing layer, further experiments were performed with oxygen as target gas.

III.2.1.2 O_2 gas sensing tests

As in case of nitrogen dioxide, in presence of oxygen a decrease of the sensor device resistance occurs (Figure V.17). Two hypotheses can be considered to explain the observed behavior with the TiO_2@CNTs heterostructure.

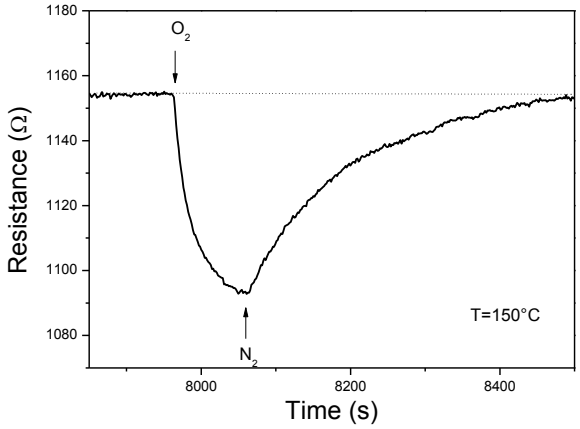

Figure V.17. Transient response of the TiO_2@CNTs gas sensor to 20% O_2 in nitrogen, at 150 °C.

On the one hand, one can consider that pure titania films in the anatase phase are generally considered n-type semiconductors, while only few reports demonstrated a p-type behavior.[33] Therefore, the presence of carbon nanotubes could favor the n- to p-type transition. Bittencourt *et al.*[34] reported that MWCNTs/WO_3 films behave either as p-type or n-type semiconductors, depending on the loading of carbon nanotubes dispersed into the WO_3 matrix. Sanchez *et al.*[35] found a reversed Ti_xO_y → adsorbate direction for the charge transfer in the interaction of NH_3 with TiO_2@CNTs, which is expected to decrease the resistance with electron-acceptor adsorbates, as observed with the present TiO_2@CNTs material in presence of NO_2 or oxygen. On the other hand, the behavior of TiO_2@CNTs structure can also be related to the very low thickness of the titania layer. Indeed, as shown with the sensors made of SnO_2@CNTs, the thickness and morphology of the metal oxide plays a fundamental role in the response type by modulating the energy barrier involved in the sensing and the electrical conduction. The experiments with different TiO_2 thicknesses and various CNT types, which are currently being carried out, will probably shed light on the involved sensing mechanism.

III.2.2. ZnO@CNT sensor devices – NO_2 sensing tests

Finally the heterostructures made of ZnO-deposited onto the different CNT types were investigated as nitrogen dioxide sensors to study the potential influence of the carbon support and metal oxide morphology on the sensing properties.

In order to test the sensitivity of the ZnO@CNT700 sensors towards nitrogen dioxide, the responses as a function of the operating temperature of the devices made of CNT700, 6 nm and 15 nm ZnO–coated CNT700 were recorded (Figure V.18). The three sensors present a very weak response to the target gas, suggesting a little sensitivity of the zinc oxide deposited on CNTs, even though structured ZnO already appears to be suitable for monitoring NO_2.[7, 36, 37]

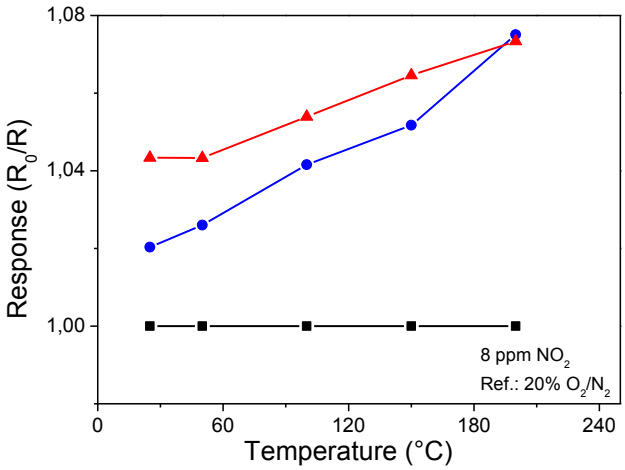

Figure V.18. Responses of the sensors made of uncoated CNT700 (triangles), 6 nm ZnO-coated CNT700 (circles) and 15 nm ZnO-coated CNT700 (squares) to 8 ppm of NO_2 as a function of the operating temperature.

This observation seems to be confirmed by the results obtained with the ZnO@CNT1500 and ZnO@CNT3000 sensors. Figure V.19 shows the transient responses of the CNT1500 and 6 nm ZnO@CNT1500 to 8 ppm of NO_2 at 150 °C. Actually, a poor sensitivity is observed for all the ZnO@CNTs-based sensors, independent of the metal oxide thickness and CNT type. The recorded sensitivity of these devices is of the same order as the one of the CNT support.

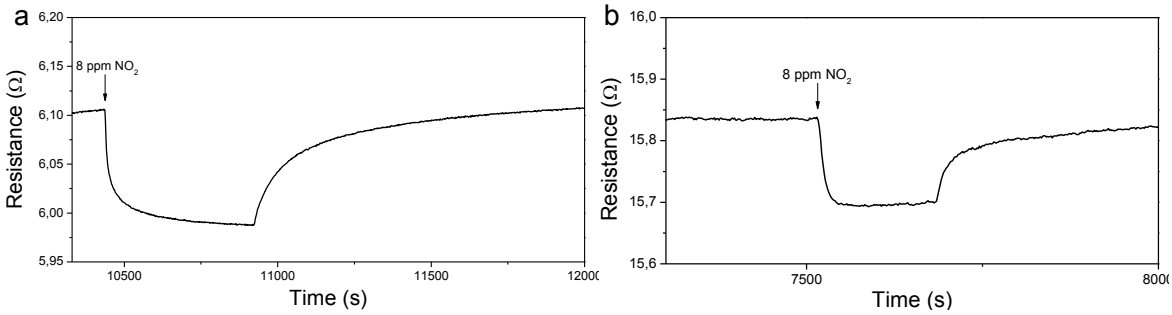

Figure V.19. Transient responses to 8 ppm of NO_2 at 150 °C of a) the CNT1500 sensor and b) 6 nm ZnO-coated CNT1500.

IV. Sensing mechanism with MO_x@CNTs nanostructures

Considering the literature,[3, 38] mainly on core-shell materials-[13, 20, 39-42] and nanowires-[25, 36] based gas sensor [42]and the obtained results, the p-n heterojunction formed between the n-type metal oxide and the p-type carbon nanotubes plays an important role in the sensing mechanism of MO_x-coated CNTs heterostructures. First of all, the sensing response is based on interactions of the target gas

with the surface of the sensing material. Based on this, the metal oxide is considered to be involved in the receptor function and the CNTs provide mainly the electronic conduction path.[13] As depicted in Figure V.20, a depletion region exists at the heterojunction of the MO_x shell and the tube and a junction is created between two coated CNTs at the networking point, creating an additional potential barrier. When an oxidizing target gas, such as NO_2, adsorbs on the surface of the metal oxide, a new depletion region is created at the surface of the shell. Indeed, the adsorbed NO_2 extracts electrons from the metal oxide modifying the width of the depletion layer at the surface of the metal oxide. This can alter the depletion layer at the n-MO_x/p-CNT junction and therefore modify the whole resistance of heterostructured sensor. Moreover, when the metal oxide shell presents a thickness inferior or equal to its Debye length, its surface is fully depleted by the gas adsorption which in turn strongly modifies the heterojunction layer. An enhanced sensitivity is therefore observed.

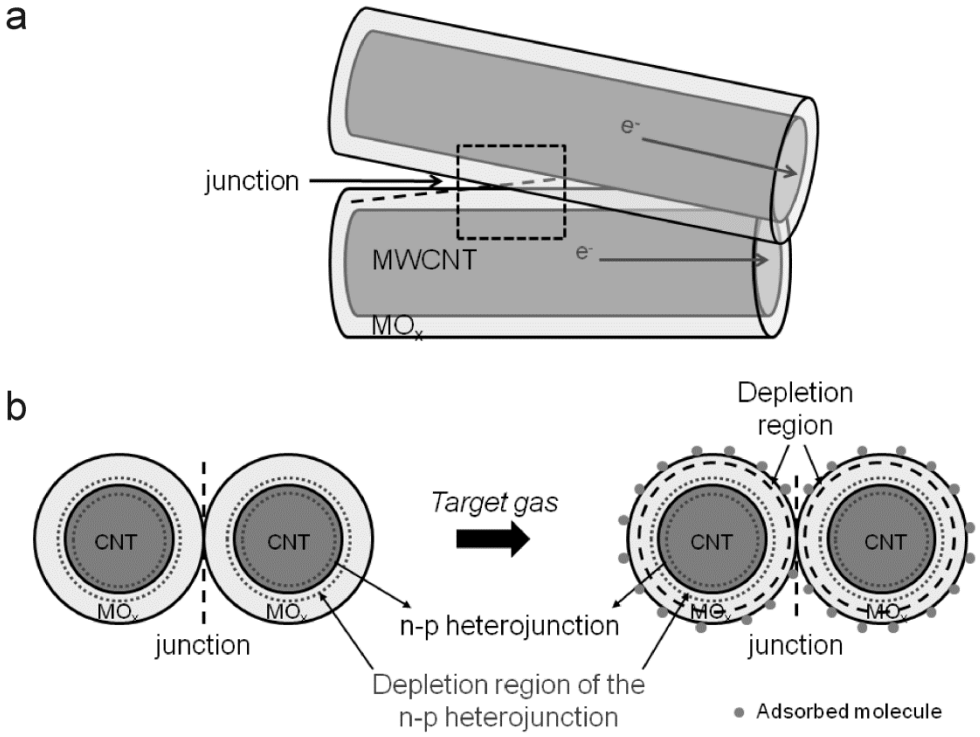

Figure V.20. Schematic illustration of the junctions involved in the sensing mechanism of the 3D structured MO_x@CNTs gas sensor. b) depicts the junction existing between the tubes of the networking at their crossing points, as shown by the dotted square in a), as well as the different depletion regions existing as a function of the presence of the target gas.

Taken from reference[13], Figure V.21 shows the changes in height of the different potential barriers occurring in presence of NO_2, d_1 (d_2) and d_3 (d_4) correspond to the width of both depletion layers, i.e. at the SnO_2 surface and SnO_2/CNTs interface, respectively, before (after) NO_2 adsorption. The

formation and height of the energy barrier is determined by the metal oxide morphology, e.g. layer compactness, thickness and degree of coverage, and the CNT characteristics.

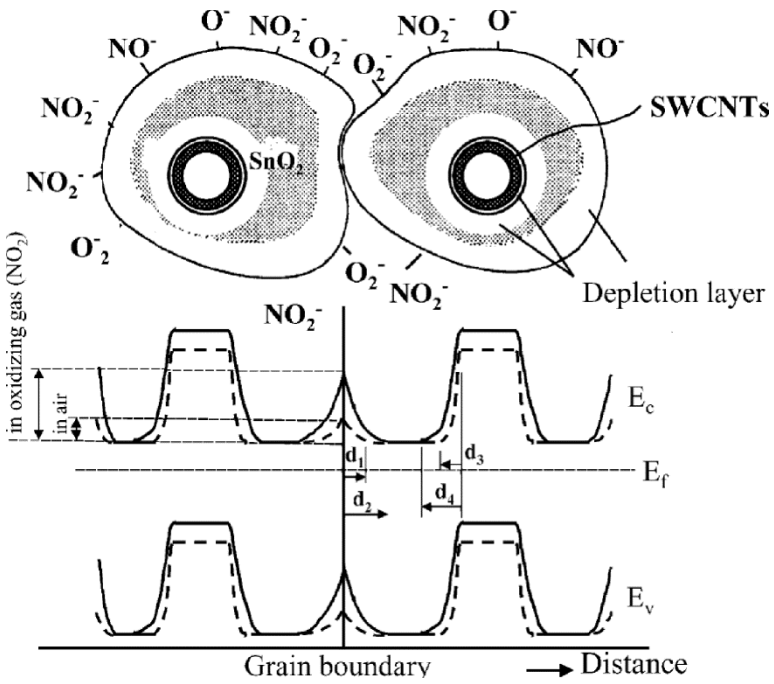

Figure V.21. Model of a potential barrier to electronic conduction at grain boundary for hybrid SWCNTs/SnO_2 sensors. (NO^- species may be formed in the reaction: $NO_2 + O^- \rightarrow NO^- + O_2$). Taken from Ref.[13].

V. Conclusions

The electrical and sensing characteristics of chemoresistive devices based on MO_x-coated CNTs heterostructures, deposited onto alumina substrates and provided with interdigitated electrodes, were investigated. The electrical characteristics of the samples can be understood in terms of a space–charge layer model. Sensing tests revealed that, unlike the bare CNTs, the resistance of a device made of SnO_2-coated CNTs is remarkably altered by its exposure to O_2 and to low concentrations of NO_2. Due to the formation of a p-n heterojunction between the p-type conductive CNTs and the n-type thin film, an enhancement of the gas-sensing response was observed. This synergetic effect, caused by the interaction of film and support, enables the detection of sub-ppm concentrations of NO_2 at low temperature (150 ºC) in just few seconds. The proportion to which this effect determines the sensing properties highly depends on the film thickness and morphology. Therefore, the highest sensitivity and sensor response is obtained for a film of which the thickness is in the range of the respective Debye length, and a continuous and conformal coating.

The 3.5 nm TiO_2-coated CNTs sensor has shown unprecedented p-type responsiveness. Hypotheses have been formulated in order to explain the p-type conductivity and the sensing behavior towards NO_2 and O_2. Further studies are currently under investigation in order to either infirm or confirm the formulated hypotheses. The ZnO-coated CNTs, independent of the metal oxide thickness and type of CNTs used, did not show significant responsiveness to NO_2.

Among all the sensors tested, the SnO_2@CNT700 based sensor has shown the most promising performance. Indeed, its detection limit is below 0.5 ppm NO_2, leading to a potential future application as an environmental nitrogen dioxide sensor.

Finally, since ALD permits a unique control of thin film deposition it also allows to modulate the performances of gas sensors as they are closely related to the thickness and the nanostructure of the active material. Therefore, the heterostructures fabricated with the CNT1500 and CNT3000 substrates, introduced in Chapter IV, are currently investigated as gas sensors. Only some preliminary results have been presented in this chapter.

VI. Experimental part

Preparation of the heterostructures

The procedure used to prepare the MO_x@CNTs was previously reported in detail in Chapter IV. Briefly, functionalized commercial CNTs (Pyrograf product), differently heat treated, were coated with SnO_2, TiO_2 or ZnO by ALD. CNTs treated at 700 °C, 1500 °C and 3000 °C were respectively labeled CNT700, CNT1500 and CNT3000, after their functionalization with concentrated nitric acid. The ALD depositions took place at either at 200 °C in the case of SnO_2 and TiO_2 or at 100 °C in the case of ZnO. Titanium isoproxide and tin tert-butoxide reacting with acetic acid and diethyl zinc reacting with water were used as precursors. The tin dioxide-coated CNT700 and CNT3000, titanium dioxide-coated CNT700 and zinc oxide-coated CNT700, CNT1500 and CNT3000 were investigated as gas sensors. The metal oxide thickness was previously determined by TEM (cf. Chapter IV).

Gas sensing experiments

The home-made sensing device used for testing consists of an alumina substrate with Pt interdigitated electrodes on one, and a Pt heater on the other side. The spacing between the Pt electrodes measures 200 microns. The active sensing layer was deposited by screen printing of an aqueous suspension with the coated nanotubes. Gas sensing tests were carried out inside a stainless-steel chamber under controlled atmosphere using an adapter as shown in Figure V.22.

Mass flow controllers were used to adjust desired concentrations of target gases in dry air. Electrical and sensing measurements were carried out in the temperature range from room temperature to 250 °C, with steps of 50 °C under a dry nitrogen/air total flow of 50 sccm. The sensor response was measured as change in resistance in four point mode using an Agilent 34970A multimeter. An Agilent E3632A dual-channel power supply was used for the heater of the sensor. The sensors were tested for monitoring O_2 and NO_2.

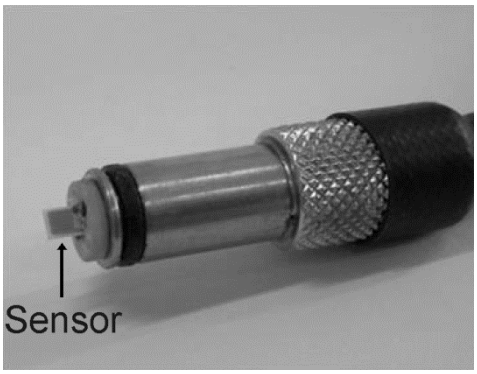

Figure V.22. Picture of the sensor device.

VII. References

1. S. Capone and P. Siciliano, *Gas Sensors from Nanostructured Metal Oxides*, American Scientific Publishers, 2004.
2. W. Gopel and K. D. Schierbaum, *Sens. Actuators, B*, 1995, **26**, 1-12.
3. G. Neri, *Sci. Adv. Mater.*, 2010, **2**, 3-15.
4. A. Tricoli, M. Righettoni and A. Teleki, *Angew. Chem. Int. Ed.*, 2010, **49**, 7632-7659.
5. J. M. Samet, *Inhalation Toxicology: International Forum for Respiratory Research*, 2007, **19**, 1021-1027.
6. B. Brunekreef and S. T. Holgate, *The Lancet*, 2002, **360**, 1233-1242.
7. C. Baratto, G. Sberveglieri, A. Onischuk, B. Caruso and S. di Stasio, *Sens. Actuators, B*, 2004, **100**, 261-265.
8. C. Marichy, N. Donato, M.-G. Willinger, M. Latino, D. Karpinsky, S.-H. Yu, G. Neri and N. Pinna, *Adv. Funct. Mater.*, 2011, **21**, 658-666.
9. N. Donato, M. Latino, G. Neri, D. Spadaro, C. Marichy, M.-G. Willinger and N. Pinna, in *2nd Carbomat Workshop*, eds. S. Scalese and A. L. Magna, Catania, 2011, pp. 37-40.
10. C. Xu, J. Tamaki, N. Miura and N. Yamazoe, *Sens. Actuators, B*, 1991, **3**, 147-155.
11. A. Rosental, A. Tarre, A. Gerst, J. Sundqvist, A. Harsta, A. Aidla, J. Aarik, V. Sammelselg and T. Uustare, *Sens. Actuators, B*, 2003, **93**, 552-555.
12. R. J. Wu, J. G. Wu, M. R. Yu, T. K. Tsai and C. T. Yeh, *Sens. Actuators, B*, 2008, **131**, 306-312.

13. B.-Y. Wei, M.-C. Hsu, P.-G. Su, H.-M. Lin, R.-J. Wu and H.-J. Lai, *Sens. Actuators, B*, 2004, **101**, 81-89.
14. Y. X. Liang, Y. J. Chen and T. H. Wang, *Appl. Phys. Lett.*, 2004, **85**, 666-668.
15. N. Van Hieu, L. T. B. Thuy and N. D. Chien, *Sens. Actuators, B*, 2008, **129**, 888-895.
16. J. Liu, Z. Guo, F. Meng, Y. Jia and J. Liu, *J. Phys. Chem. C*, 2008, **112**, 6119-6125.
17. P. M. Ajayan, *Chem. Rev.*, 1999, **99**, 1787-1800.
18. A. Kolmakov, Y. Zhang, G. Cheng and M. Moskovits, *Adv. Mater.*, 2003, **15**, 997-1000.
19. M. G. Willinger, G. Neri, A. Bonavita, G. Micali, E. Rauwel, T. Herntrich and N. Pinna, *Phys. Chem. Chem. Phys.*, 2009, **11**, 3615-3622.
20. M. G. Willinger, G. Neri, E. Rauwel, A. Bonavita, G. Micali and N. Pinna, *Nano Lett.*, 2008, **8**, 4201-4204.
21. H. Ogawa, M. Nishikawa and A. Abe, *J. Appl. Phys.*, 1982, **53**, 4448-4455.
22. G. Neri, A. Bonavita, G. Rizzo, S. Galvagno, N. Pinna, M. Niederberger, S. Capone and P. Siciliano, *Sens. Actuators, B*, 2007, **122**, 564-571.
23. C. Baratto, E. Comini, G. Faglia, G. Sberveglieri, M. Zha and A. Zappettini, *Sens. Actuators, B*, 2005, **109**, 2-6.
24. A. Chiorino, G. Ghiotti, F. Prinetto, M. C. Carotta, C. Malagù and G. Martinelli, *Sens. Actuators, B*, 2001, **78**, 89-97.
25. Y.-J. Choi, I.-S. Hwang, J.-G. Park, K. J. Choi, J.-H. Park and J.-H. Lee, *Nanotechnology*, 2008, **19**, 095508-095511.
26. E. Comini, G. Faglia, G. Sberveglieri, Z. Pan and Z. L. Wang, *Appl. Phys. Lett.*, 2002, **81**, 1869-1871.
27. Y. Cui, Q. Wei, H. Park and C. M. Lieber, *Science*, 2001, **293**, 1289-1292.
28. T. Hyodo, S. Abe, Y. Shimizu and M. Egashira, *Sens. Actuators, B*, 2003, **93**, 590-600.
29. AppliedSciencesInc, A Comparison of Carbon Nanotubes and Carbon Nanofibers, http://pyrografproducts.com/carbon-nanotubes.html.
30. Q. W. Li, Y. Li, X. F. Zhang, S. B. Chikkannanavar, Y. H. Zhao, A. M. Dangelewicz, L. X. Zheng, S. K. Doorn, Q. X. Jia, D. E. Peterson, P. N. Arendt and Y. T. Zhu, *Adv. Mater.*, 2007, **19**, 3358-3363.
31. Y.-H. Lin, P.-S. Lee, Y.-C. Hsueh, K.-Y. Pan, C.-C. Kei, M.-H. Chan, J.-M. Wu, T.-P. Perng and H. C. Shih, *J. Electrochem. Soc.*, 2011, **158**, K24-K27.
32. B. Ruhland, T. Becker and G. Müller, *Sens. Actuators, B*, 1998, **50**, 85-94.
33. F. Hossein-Babaei, M. Keshmiri, M. Kakavand and T. Troczynski, *Sens. Actuators, B*, 2005, **110**, 28-35.
34. C. Bittencourt, A. Felten, E. H. Espinosa, R. Ionescu, E. Llobet, X. Correig and J. J. Pireaux, *Sens. Actuators, B*, 2006, **115**, 33-41.
35. M. Sánchez, M. E. Rincón and R. A. Guirado-López, *J. Phys. Chem. C*, 2009, **113**, 21635-21641.
36. M. W. Ahn, K. S. Park, J. H. Heo, J. G. Park, D. W. Kim, K. J. Choi, J. H. Lee and S. H. Hong, *Appl. Phys. Lett.*, 2008, **93**, 263103-263103.
37. N. Koshizaki and T. Oyama, *Sens. Actuators, B*, 2000, **66**, 119-121.

38. C. X. Wang, L. W. Yin, L. Y. Zhang, D. Xiang and R. Gao, *Sensors*, 2010, **10**, 2088-2106.

39. G. Lu, L. E. Ocola and J. Chen, *Adv. Mater.*, 2009, **21**, 2487-2491.

40. L. Zhao, M. Choi, H.-S. Kim and S.-H. Hong, *Nanotechnology*, 2007, **18**, 445501-445505.

41. L. F. Zhu, J. C. She, J. Y. Luo, S. Z. Deng, J. Chen, X. W. Ji and N. S. Xu, *Sens. Actuators, B*, 2011, **153**, 354-360.

42. E. H. Espinosa, R. Ionescu, B. Chambon, G. Bedis, E. Sotter, C. Bittencourt, A. Felten, J. J. Pireaux, X. Correig and E. Llobet, *Sens. Actuators, B*, 2007, **127**, 137-142.

Conclusion

In this thesis, the elaboration of functional heterostructures, using atomic layer deposition, their advanced characterization and investigation of their physical properties have been presented. Based on the reaction between a metal alkoxide and a carboxylic acid, the unconventional non-aqueous approach to ALD was applied and further extended. In the first stage, the main efforts were devoted to demonstrate its versatility and to extend it to the deposition of SnO_2. Further, particular attention was given to the controlled coating of carbon nanotubes and their application as chemoresistive gas sensors.

In chapter II, a novel SnO_2 deposition was developed by reacting tin(IV) tert-butoxide with acetic acid. Low or moderate temperature depositions were achieved offering the possibility to coat thermal and/or moisture sensitive substrates. These findings pave the way to the elaboration of innovative heterostructured materials. The as-prepared films are almost free of carbon. Due to the particular growth, conformal granular thin films were deposited on various supports. Indeed, the SnO_2 films consist of well defined 2-3 nm sized-nanoparticles homogeneously dispersed on the substrate. Furthermore, this approach allows the homogeneous coating of the inner and outer walls of carbon nanotubes.

In order to prove the suitability of our non-aqueous ALD approach for the coating of high aspect ratio materials, the controlled infiltration of silica opals was realized. Langmuir-Blodgett elaborated opals were coated with titanium dioxide using a 1.2 nm deposition step in Chapter III. The investigation of their optical properties, i.e. the modification of the pseudo photonic band gap of the coated SiO_2 opals, at each infiltration step, was used to monitor the accuracy of the ALD deposition. The good agreement between experimental and simulated absorption spectra demonstrates the robustness of the approach using carboxylic acid as oxygen source.

Therefore our approach has been implemented to the fabrication of functional metal oxide-coated carbon nanotubes (Chapter IV). The homogeneous and accurate coating of the inner and outer walls of stacked-cups CNTs, functionalized by conventional nitric acid treatment, has been realized with metal oxides such as titanium-, tin- and zinc oxide, the latter was deposited from a conventional aqueous ALD route. Defects and/or functional surface groups, acting as anchoring sites, are required for the film growth initiation. Indeed, the highly graphitic ends of the tubes remained uncoated because of their chemical inertness. Based on these observations, a certain

degree of "defect engineering" is necessary for the elaboration of CNT-based nanomaterials. Controlled tailoring of the type, degree and density of functionalization of the CNT surface would therefore allow to tune the coating from selectively decorated up to fully coated CNTs. The degree of the tube graphitization strongly influences the impact of the acidic functionalization, at first, our ALD approach has been used to specifically label the anchoring sites on differently thermally and chemically pre-treated carbon nanotubes. ALD combined with high resolution electron microscopy techniques has been proven to be a powerful tool for characterizing the surface functionality of CNTs. One can foresee the extension of such an approach to other carbon-based nanostructures (e.g. graphene, carbon fibers, *etc.*). On the other hand, this is certainly of interest for application directed design of functional carbon-based nanostructures. Based on the tailored CNT functionalization, metal oxide-coated CNTs have been elaborated with a highly controlled MO_x morphology.

The elaborated MO_x@CNTs materials have been tested as active components in gas sensing devices (Chapter V). Responses to O_2 and NO_2 at different concentrations and sensor temperatures were investigated. The formation of a p-n heterojunction between the n-type tin dioxide and the p-type conductive CNT support leads to an enhancement of the gas sensing response. Because of the synergic effect caused by the interaction of film and support, the SnO_2@CNT-based sensor shows a sub-ppm detection limit of nitrogen dioxide at low temperature, i.e. 150 °C. This is promising for future environmental sensor development. The influence of the p-n junction on the gas sensing properties can be modulated by the thickness, density and morphology of the metal oxide shell. Indeed, changing the degree of coverage of CNTs from fully to partially coated, an evolution from n-type to p-type sensing behavior has been foreseen. Additional MO_x@CNTs-based sensors with the different types of CNTs, metal oxide morphology and thicknesses are currently investigated. Interesting responses towards NO_2 and O_2 have been obtained using TiO_2@CNTs-based sensor. Its observed p-type behavior can be explained by either the very low thickness of the coating or the n to p-type transition of TiO_2, favored by the interaction with CNTs. We expect that the experiments currently carried out with different thicknesses of the oxide film will fully elucidate the sensing mechanism involved. Finally, the work using the relation between the acid functionalization efficiency and the degree of graphitization as an approach for tailoring the ALD coating paves the way to a new methodology for the design of functional carbon-based materials. For example, a preliminary work has been realized on the graphitization and ALD coating of electrospun carbon fibers to enhance electrocatalyst activity and stability. The first results are presented in the following Perspective work section.

Perspective work

Use of the defect engineering of CFs to enhance electrocatalyst activity and stability

Particular attention is devoted to the development and improvement of fuel cell catalysts. The use of ALD for preparing such catalysts is discussed in Chapter I, section IV.2. Pt-based electrocatalysts have proven to be the most promising catalysts for alcohol oxidation.[1, 2] However, during the methanol electro-oxidation, occurring at the anode, additionally to the CO_2 by-product, CO is also formed, causing a poisoning of the Pt catalyst. Indeed, the carbon monoxide gets strongly adsorbed on the platinum sites, drastically decreasing the catalytic activity. Therefore, efforts have been devoted to avoid this poisoning and stabilize the Pt particles. Two approaches have been considered: On the one hand, Pt nanoparticles have been mixed with other noble metals such as Ru, Pd, known to oxidize the CO into CO_2. On the other hand, metal oxides can be added to the electrocatalyst, SnO_2 being the most common metal oxide combined with the Pt particles due to the following reasons:

i) SnO_2 adsorbs oxygen species promoting the CO oxidation; the platinum can be liberated from the carbon monoxide avoiding its poisoning and therefore the diminution of its electrocatalytic activity.[3] One of the possible routes in which SnO_2 promotes regeneration of Pt active surface with absorbed OH is the following bifunctional mechanism:[4]

$SnO_2 + OH^- \rightarrow SnO_2\,OH_{ads} + e^-$

$Pt(CO)_{ads} + OH^- \rightarrow Pt + CO_2 + H_2O + e^-$

ii) SnO_2 brings a stabilizing component toward the sintering of the Pt nanoparticles dispersed on conventional carbon black supports. This stabilization effect is also sought after by employing other metal oxide such as aluminum oxide,[5] or titanium oxide.[1]

One of the possible drawbacks of such overcoating is the potential coverage of Pt active surface. Recently, Lu *et al.*[6] published the use of Al_2O_3 ALD to stabilize the Pd particles without blocking the active sites. After investigation, they reported the formation of film porosity with the thermal treatment, enabling the access to the Pd sites.

Finally, the corrosion of the Pt support is another important concern for the electrocatalyst performance. Although carbon-supported Pt particles are widely used due to the high surface area and good electrical properties of the carbon support, the latter presents a thermodynamic instability with the electrochemical potential.[1] Particular attention is devoted to improving the corrosion resistance of these electrocatalyst supports using a passivating layer for instance.

Based on the statement that the degree of graphitization of the carbon material strongly influences the ALD growth, the pre-heat-treatment of electrospun carbon fibers (CF) was investigated in order to tune their SnO_2 and TiO_2 ALD coating. Pt nanoparticles were homogeneously dispersed onto the treated carbon fibers followed by the metal oxide ALD coating. This work is the fruit of collaboration with Dr. Sara Cavaliere, at the University of Montpellier II, France. The preparation of carbon fibers by electrospinning, Pt deposition and electrocatalytic measurements have been performed in Montpellier, while ALD depositions as well as calcinations at 1500 °C and characterizations have been done in Aveiro.
The preliminary results obtained on the elaboration of the modified electrocatalysts will be briefly presented here, to highlight the potential impact of the present PhD work. Non-exhaustive details will be given. The differently treated fibers will be first introduced before the electrocatalytic properties of the Pt-based catalysts.

Heat treatment of the carbon fibers

The CFs consist of electrospun polyacrylonitrile fibers stabilized at 280 °C and carbonized under inter atmosphere at 700 °C, 1000 °C or 1500 °C. The thermal treatment leads to the increase of the graphitization, as shown by the Raman spectra (Figure P.1). Actually, according to the I_D/I_G ratio, after the treatment at 1500 °C the obtained graphitization is similar to that of the CNT1500 discussed in Chapter IV.[7] The table P.1 summarizes the I_D/I_G ratio obtained for the differently treated fibers and tubes. For sake of clarity, the carbon fibers heat-treated at 700, 1000 and 1500 °C are labeled CF-700, CF-1000 and CF-1500 respectively.

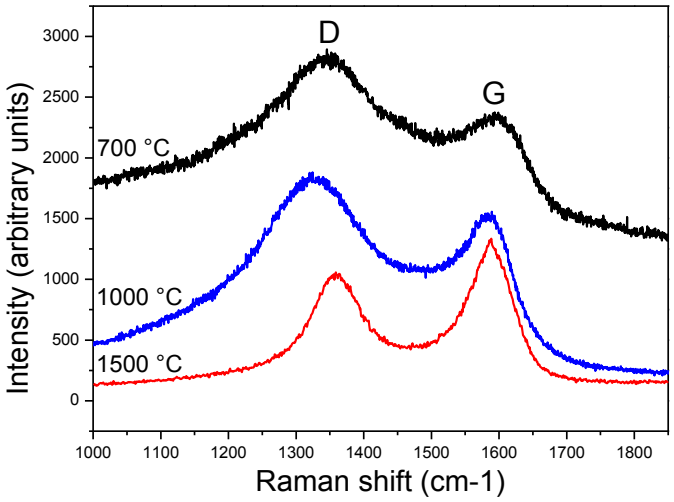

Figure P.1. Raman spectra of the treated carbon fibers at 700, 1000 and 1500 °C.

Table P.1. D/G ratios calculated from Raman spectra.

$T_{carbonization}$	I_D/I_G	CNTs	I_D/I_G
700 °C	2.2	CNT700	3.6
1000 °C	1.7	CNT1500	1
1500 °C	0.9	CNT3000	~0

The in plane electrical conductivity of a fiber pellet, as a function of the temperature, was measured by using an in-house conductivity cell with the conventional four probe method and Van der Paw calculations,[3] for the fibers CF-700 and CF-1000. A semiconductor behavior is observed in both cases and a drastic increase of the conductivity is noticed between the treatment at 700 °C and 1000 °C, as shown in Figure P.2. Actually, the CF-1000 conductivity is comparable or even higher than that of the carbon black Vulcan XC-72, a widely used electrocatalyst support, showing a metallic behavior, taken as reference.

The heat-treatment might induce a decrease of the specific surface area, therefore N_2 adsorption/desorption measurements are currently carried out in order to determine the best compromise between the surface area and the electrical properties of the fibers.

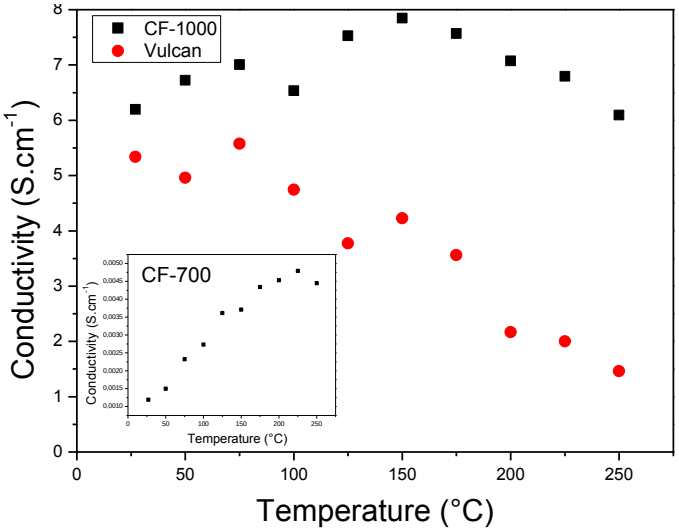

Figure P.2. Electrical conductivity of the fibers treated at 1000 °C (squares) and of the carbon black Vulcan XC-72 (circles) and, in inset, the conductivity of the fibers treated at 700 °C are presented.

Characterization of the carbon fibers-supported Pt nanoparticles

After the CF thermal treatment, Pt nanoparticles were deposited onto the fibers by the conventional polyol method.[4] A loading of 20 % was aimed, although at the moment an uncertainty remains on the effective Pt loading on the CF-1500. The degree of graphitization might have an influence not only on the ALD coating but also on the efficiency of the platinum deposition and on the overall electrochemical behavior. The TEM investigation (Figure P.3) reveals a homogeneous dispersion of 3 nm-sized nanoparticles over the fibers. A size distribution centered at 2.5 ± 0.7 nm was observed, while a particle size of 4 nm was determined by XRD.

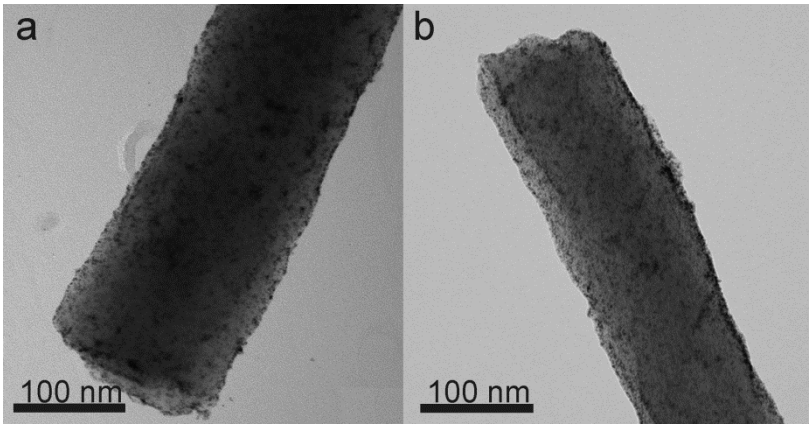

Figure P.3. TEM images of Pt nanoparticles deposited on the carbon fibers a) CF-700 and b) CF-1000.

The stability of the electrocatalyst, after its deposition on the working electrode, has been investigated by cyclic voltammetry (CV) in degassed $HClO_4$. Figure P.4 reports the relative decrease of the active surface area determined from the hydrogen adsorption/desorption as a function of the CV cycles. Unlike Pt/CF-700 and Pt/CF-1000, the electrochemical surface area of the catalyst Pt deposited on CF-1500 does not show a drastic diminution after 1000 cycles. An improvement of the stability occurs then with the graphitic character of the fiber support.

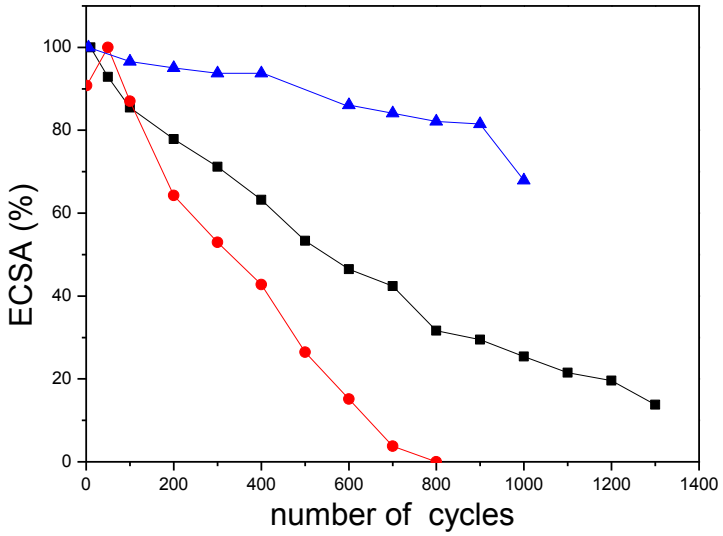

Figure P.4. Electrochemical surface area as a function of the number of CV cycles and the calcination temperature: 700 °C (full circles), 1000 °C (full squares) and 1500 °C (full triangles).

ALD coating of the Pt/CFs electrocatalysts

In order to increase the stability and the performance of the Pt/CFs, TiO_2 and SnO_2 ALD have been carried out on the different electrocatalysts, with diverse cycle numbers. The two home-made ALD tools presented in Chapter I have been used for this purpose. Briefly, the SnO_2 deposition took place at 200 °C in the exposure mode home-made ALD tool described in Figure I.13, following the process presented in Chapter II. The Pt/CFs material was hold inside the reactor with a "tea bag" made of a Kevlar mat. The number of cycles was set to either 30 or 15.

The TiO_2 deposition took place at 200 °C in the continuous flow mode home-made ALD tool described in Figure I.14. The sample powder was held in a rectangular crucible covered with a stainless steel filter allowing the precursor diffusion, while keeping the material in place. Titanium isopropoxide and acetic acid were used as metal and oxygen precursors, respectively. The metal and carboxylic acid were delivered to the chamber through ALD pneumatic valves. Pure nitrogen was used as the carrier gas with a constant flow of 100 sccm. The deposition parameters were 2 s (10 s) for the acid (alkoxide) pulses and the purge time was 20 s. Considering a GPC of 0.15 Å per cycle, either 50 or 100 cycles were realized.

To avoid the blocking of the active Pt sites and the addition of a resistive component, very low thicknesses of metal oxide are sought after. Therefore MO_x thicknesses of less than 2 nm were targeted. The number of cycles has been set to deposit either ~0.5 or ~1 nm thick films. As observed with the CNT700 and CNT1500, a growth of either a continuous film or dispersed particles is expected to occur as a function of the CF graphitization.

The electrocatalytic activity of the heterostructures toward methanol electro-oxidation and oxygen reduction reactions has been investigated. Because the ORR experiments (not presented) were not conclusive up to now, only the study on the MOR for which encouraging findings have been obtained, is presented.

Application of the electrocatalysts to the methanol electro-oxidation

The electrocatalytic activity toward methanol oxidation of the CF-700 (CF-1500)-supported Pt heterostructures coated with either 15 (30) SnO_2 or 100 TiO_2 (50) cycles was investigated. For each CF calcination temperature, the electrocatalysts, for which the CV curves are presented in Figure P.5, were prepared from the same batch of Pt/CFs as well as the same electrode surface (0.196 cm^2) and mass of materials were used, allowing a direct comparison of the catalysts as a function of the carbon support. The catalyst ink was prepared by mixing the appropriate amount of Pt catalyst (5 mg) with deionized water, ethanol and a 5%$_{wt}$ aqueous/alcoholic solution of Nafion. A 6 µl ink portion was pipetted onto the working electrode.

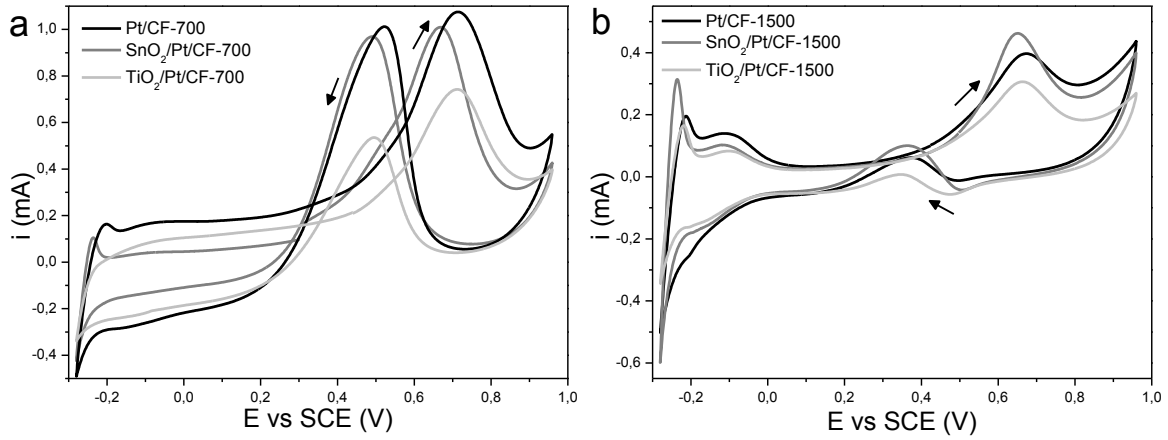

Figure P.5. Cyclic voltammogramms of the Pt/CFs (black lines), SnO_2/Pt/CFs (dark grey lines) and TiO_2/Pt/CFs (light grey lines) using as support a) CF-700 and b) CF-1500. CV curves were recorded in 0.5 M H_2SO_4 containing 1 M CH_3OH with a sweep rate of 50 $mV.s^{-1}$, using a saturated calomel electrode (SCE) as reference.

On each curve, in the forward scan, the noted sharp peak at low potential (~-0.25 V) is attributed to hydrogen desorption while the symmetric anodic peak around 0.7 V is assigned to the methanol electro-oxidation. In the backward scan, the presence of an asymmetric anodic peak is attributable to the oxidation of remaining incompletely oxidized carbonaceous species.[8, 9]

In the case of CF-700 used as carbon support, the presence of tin dioxide did not affect the current but did bring a catalytic effect compared to the Pt/CF-700. Indeed, in the forward scan, the symmetric anodic peak center at 0.71 V in case of Pt/CF-700 shifts at 0.66 V when the electrocatalyst is coated with SnO_2. Similar observation is noted with the asymmetric anodic peak in the backward scan (Figure P.5a and Table P.2). The lowering potential is attributed to a reduction of the energy barrier and therefore to an increase of the electrocatalytic activity due to SnO_2. On the contrary, the deposition of titanium dioxide led to a drop of current, the overpotential remaining identical to that of the uncoated catalyst. Two hypotheses can be formulated to explain this phenomenon. By its non-conductive nature, TiO_2 bring a resistive component thickness-dependent, which is responsible of a current lowering. On the other hand, the coverage of Pt particles by the metal oxide reduces the active surface area and leads to a decrease of the current. Both of these effects can be conjugated. HRTEM and STEM characterizations are under investigation in order to determine whether or not the Pt sites are blocked by TiO_2.

Similar trends have been observed with the CF1500-supported catalysts. A lower overpotential and furthermore higher currents were observed with the SnO_2 coating (despite the non-conducting nature of the deposited oxide layer), while the opposite behavior occurred when coated with TiO_2 (Figure P.5b and Table P.2). These results confirm the positive effect of SnO_2 on the methanol oxidation reaction. With the formation of tin dioxide particles being expected, a synergic effect[5] probably arises from the proximity of the Pt and SnO_2 nanoparticles.

Table P.2. Comparison of the performance of the different electrocatalysts as a function of the ALD coating and the heat treatment of CFs. E_f and E_b correspond to the peak potential and I_f and I_b to the peak current of the forward and backward scans, respectively.

Electrocatalyst	Forward scan		Backward scan	
	E_f (V)	I_f (mA)	E_b (V)	I_b (mA)
Pt/CF-700	0.71	1.07	0.52	1.01
30-SnO_2/Pt/CF-700	0.66	1.01	0.49	0.97
100-TiO_2/Pt/CF-700	0.71	0.74	0.49	0.53
Pt/CF-1500	0.67	0.39	0.38	0.06
15-SnO_2/Pt/CF-1500	0.65	0.46	0.36	0.10
50-TiO_2/Pt/CF-1500	0.66	0.30	0.35	0.01

In conclusion, this section aimed to demonstrate the applicability of the work realized on tailoring CNTs coating to other carbon-based material. The controlled surface graphitization of carbon fibers was briefly introduced as a pathway to control the ALD coating, which allows the enhancement of the electrocatalyst activity. The influence of thermal treatment on the CFs on the intrinsic properties of the Pt/CFs catalysts (i.e. conductivity and stability) has been demonstrated. Encouraging findings have been highlighted. Indeed, an increase of the catalytic activity toward the methanol oxidation reaction by the coating of Pt/CF with ALD SnO_2 has been noticed, the ALD-deposited tin dioxide helping to release the Pt from the adsorbed CO, decreasing the catalyst poisoning.

References

1. A. Rabis, P. Rodriguez and T. J. Schmidt, *ACS Catal.*, 2012, **2**, 864-890.
2. K.-S. Lee, I.-S. Park, Y.-H. Cho, D.-S. Jung, N. Jung, H.-Y. Park and Y.-E. Sung, *J. Catal.*, 2008, **258**, 143-152.
3. H. Zhang, C. Hu, X. He, L. Hong, G. Du and Y. Zhang, *J. Power Sources*, 2011, **196**, 4499-4505.
4. Y. Lin, S. Zhang, S. Yan and G. Liu, *Electrochim. Acta*, 2012, **66**, 1-6.

5. H. Feng, J. W. Elam, J. A. Libera, W. Setthapun and P. C. Stair, *Chem. Mater.*, 2010, **22**, 3133-3142.

6. J. Lu, B. Fu, M. C. Kung, G. Xiao, J. W. Elam, H. H. Kung and P. C. Stair, *Science*, 2012, **335**, 1205-1208.

7. J.-P. Tessonnier, D. Rosenthal, F. Girgsdies, J. Amadou, D. Begin, C. Pham-Huu, D. Sheng Su and R. Schlögl, *Chem. Commun.*, 2009, 7158-7160.

8. S.-B. Han, Y.-J. Song, J.-M. Lee, J.-Y. Kim and K.-W. Park, *Electrochem. Commun.*, 2008, **10**, 1044-1047.

9. M. C. Gutiérrez, M. J. Hortigüela, J. M. Amarilla, R. Jiménez, M. L. Ferrer and F. del Monte, *J. Phys. Chem. C*, 2007, **111**, 5557-5560.

Appendix

Publications list

1- "Nonaqueous sol–gel chemistry applied to atomic layer deposition: tuning of photonic band gap properties of silica opals"
C. Marichy, J.-F. Dechézelles, M.-G. Willinger, N. Pinna, S. Ravaine and R. Vallée, *Nanoscale*, 2010, **2**, 786 – 792.

2- "$CoFe_2O_4$-TiO_2 and $CoFe_2O_4$-ZnO Thin Film Nanostructures Elaborated from Colloidal Chemistry and Atomic Layer Deposition"
G. Clavel, **C. Marichy**, M.-G. Willinger, S. Ravaine, D. Zitoun, and N. Pinna, *Langmuir*, 2010, **26** (23), 18400–18407.

3- "Tin Dioxide Sensing Layer Grown on Tubular Nanostructures by a Non-Aqueous Atomic Layer Deposition Process"
C. Marichy, N. Donato, M.-G. Willinger, M. Latino, D. Karpinsky, S.-H. Yu, G. Neri and N. Pinna, *Adv. Funct. Mater.*, 2011,**21**, 658–666.

4- "Sol-Gel-Chemistry and Atomic Layer Deposition"
G. Clavel, **C. Marichy** and N. Pinna, *in Atomic Layer Deposition of Nanostructured Materials*, (Eds: N. Pinna, M. Knez), Wiley-VCH, 2011, 61.

5- "Coating of Carbon Nanotubes"
Catherine Marichy, Andrea Pucci, Marc Willinger and Nicola Pinna, *in Atomic Layer Deposition of Nanostructured Materials*, (Eds: N. Pinna, M. Knez), Wiley-VCH, 2011, 327.

6- "A one-pot microwave-assisted non-aqueous sol-gel approach to metal oxide/graphene nanocomposites for Li-ion batteries"
S.H. Baek, S.-H. Yu, S.-K. Park, A. Pucci, **C. Marichy**, D.-C. Lee, Y.-E. Sung, Y. Piao and N. Pinna, *RSC Adv.*, 2011, **1**, 1687-1690.

7- "Ultra simple catalyst layer preparation for the growth of vertically aligned CNTs and CNT-based nanostructures"
R. M. Silva, A. Pucci, **C. Marichy**, D. Mata, M. C. Ferro, R. F. Silva and N. Pinna, *Cryst. Eng. Comm.*, 2012, **14**, 48-52.

8- "Atomic Layer Deposition of Nanostructured Materials for Energy and Environmental Applications"
C. Marichy, M. Bechelany, N. Pinna, *Adv. Mater.*, 2012, **24**, 1017–1032.

9- "Labeling and monitoring the distribution of anchoring sites on functionalized CNTs by atomic layer deposition"
C. Marichy, J.-P. Tessonnier, M. C. Ferro, K.-H. Lee, R. Schlögl, N. Pinna and M.-G. Willinger, *J. Mater. Chem.*, 2012, **22**, 7323-7330.